

Alma Mater Studiorum – Università di Bologna

DOTTORATO DI RICERCA IN

CHIMICA

Ciclo XXVII

Settore Concorsuale di afferenza: 03/C2 - CHIMICA INDUSTRIALE

Settore Scientifico disciplinare: CHIM/04 - CHIMICA INDUSTRIALE

**SAFETY BY DESIGN: PRODUCTION OF ENGINEERING SURFACE
MODIFIED NANOMATERIALS**

Presentata da: Camilla Delpivo

Coordinatore Dottorato

Prof. Aldo Roda

Relatore

Prof. Angelo Vaccari

Co-relatori

Dott.ssa Anna Luisa Costa

Prof.ssa Stefania Albonetti

Esame finale anno 2015

ABSTRACT

This PhD thesis focused on nanomaterial (NM) engineering for occupational health and safety, in the frame of the EU project “Safe Nano Worker Exposure Scenarios (SANOWORK)”. Following a safety by design approach, surface engineering (surface coating, purification process, colloidal force control, wet milling, film coating deposition and granulation) were proposed as risk remediation strategies (RRS) to decrease toxicity and emission potential of NMs within real processing lines.

In the first case investigated, the PlasmaChem ZrO₂ manufacturing, the colloidal force control applied to the washing of synthesis reactor, allowed to reduce ZrO₂ contamination in wastewater, performing an efficient recycling procedure of ZrO₂ recovered.

Furthermore, ZrO₂ NM was investigated in the ceramic process owned by CNR-ISTEC and GEA-Niro; the spray drying and freeze drying techniques were employed decreasing NM emissivity, but maintaining a reactive surface in dried NM.

Considering the handling operation of nanofibers (NFs) obtained through Elmarco electrospinning procedure, the film coating deposition was applied on polyamide non-woven to avoid free fiber release. For TiO₂ NF the wet milling was applied to reduce and homogenize the aspect ratio, leading to a significant mitigation of fiber toxicity.

In the Colorobbia spray coating line, Ag and TiO₂ nanosols, employed to transfer respectively antibacterial or depolluting properties to different substrates, were investigated. Ag was subjected to surface coating and purification, decreasing NM toxicity. TiO₂ was modified by surface coating, spray drying and blending with colloidal SiO₂, improving its technological performance.

In the extrusion of polymeric matrix charged with carbon nanotube (CNTs) owned by Leitat, the CNTs used as filler were granulated by spray drying and freeze spray drying techniques, allowing to reduce their exposure potential.

Engineered NMs tested by biologists were further investigated in relevant biological conditions, to improve the knowledge of structure/toxicity mechanisms and obtain new insights for the design of safest NMs.

ACKNOWLEDGEMENTS

I would like to express my gratitude to my academic advisor, Prof. Angelo Vaccari, for his excellent guidance, and to my academic co-advisors, Prof. Stefania Albonetti, for her encouragement and suggestion during my doctoral research period.

I'm very grateful to Dr. Anna L. Costa for the opportunity to carry out my PhD in the context of the EU project SANOWORK. I would like to thank all my colleagues and staff of the Institute for Science and Technology for Ceramics - National Research Council - of Faenza (IT), in particular to Simona, Magda, Davide and Michele, for their support and for the moments shared together.

I would also like to thank all the SANOWORK partners, for their collaboration and the high quality work carried out: it was great for me visit your Company and/or your Lab, and work together with you all. A special thanks to Prof. Tofail Syed of University of Limerick for accepting me in his research group during the Marco Polo fellowship and for made me feel very welcome.

Moreover, I feel all the time in debt to my partner Michele, my sisters Domitilla and Lucilla and my parents for their overwhelming love and for having faith in me. I will never thank them enough.

GLOSSARY

- AAS** flame atomic absorption spectrometer
- APS** aerodynamic particle sizer
- ATR-IR** attenuated total reflection infrared
- BET** Brunauer-Emmett-Teller method
- BSA** bovine serum albumin
- BSA/PBS** bovine serum albumin in phosphate buffered saline
- CFC** colloidal force control
- CFE** colony forming efficiency
- CFU** centrifugal filter unit
- CNR-ISTEC** National Research Council - Institute for Science and Technology for Ceramics
- CNT** carbon nanotube
- CPC** condensation particle counters
- DCFH** dichlorofluorescin oxidation assay
- d_H** hydrodynamic diameter
- DLS** dynamic light scattering
- DMEM** Dulbecco's modified Eagle's medium, culture medium
- DSC/TGA** differential scanning calorimetry thermal gravimetric analysis
- DTG** differential gravimetric analysis
- EA** exposure assessment
- EDS** energy dispersive x-ray spectrometry detector
- E_g** band gap energy
- ELS** electrophoretic light scattering
- ENM** engineered nanomaterial
- EPR** electron paramagnetic resonance
- FBS** fetal bovine serum
- GSH** reduced glutathione
- Ham's F-12**, nutrient mixture added in culture medium
- HR-TEM** high resolution
- ICP-OES** inductively coupled plasma-optical emission spectroscopy
- IEP** isoelectric point

IOM Institute of occupational medicine

LA-ICP-MS laser ablation-inductively coupled plasma-mass spectrometry

LDH lactate dehydrogenase

LPS lipopolysaccharide

MEM minimum essential medium, culture medium

MPS mini particle sampler

MWCNT multi-walled carbon nanotube

NAS nano aerosol sampler

NF nanofibre

NM nanomaterial

NP nanoparticle

P25 aerioxide P25

PA polyamide 6

PC protein corona

PDM optical particle counter

PEG 600 polyethylene glycol 600

PL processing line

PL 1 processing line 1

PL 2 processing line 2

PL 3 processing line 3

PL 4 processing line 4

PL 5 processing line 5

PL 6 processing line 6

PNC plastic nano-composite

PP polypropylene

PVP polyvinylpyrrolidone

RhB Rhodamine B

ROS reactive oxygen species

RRS risk remediation strategy

SbyD safety by design

SC solvent-resistant stirred cell

SEM scanning electron microscope

SEM-FEG SEM with field emission gun

SERS surface enhanced Raman spectroscopy

SPR surface plasmon resonance

SSA specific surface area

STEM-HAADF high angle annular dark field scanning transmission electron microscopy

SWCNT single-walled carbon nanotube

TBARs thiobarbituric acid reactive substances assay

TEM transmission electron microscope

TEM-BF TEM in bright field mode

TEM-EDS TEM with an energy dispersive x-ray spectrometry detector

TEOS tetraethylorthosilicate

TG thermal gravimetric analysis

WP work package

XPS X-Ray photoelectron spectroscopy

XRD X-ray diffraction

XRF X-ray fluorescence

z-b zero-background

ZP zeta potential

Zr-Pr Zirconium-praseodymium

TABLE OF CONTENTS

ABSTRACT	i
ACKNOWLEDGEMENTS	ii
GLOSSARY	iii
TABLE OF CONTENTS	vi
LIST OF TABLES	xii
LIST OF FIGURES	xv
1. Introduction	1
1.1 Safety by design concept	1
1.1.2 The NM surface engineering as RRS	2
1.2 European project SANOWORK.....	3
1.2.1 Contest.....	3
1.2.2 Consortium	4
1.2.3 Approach.....	6
1.3 References	8
2. Processing line 1: washing/disposal line (ZrO ₂ nanopowder).....	10
2.1 Introduction	10
2.1.1 ZrO ₂ nanomaterials.....	10
2.1.2 Description of Processing line 1.....	10
2.1.3 Critical step identified and RRS proposed	12
2.1.3.1 Reactor washing.....	12
2.1.3.2 Sedimentation.....	12
2.1.3.3. Recycle	13
2.2 Experimental.....	13
2.2.1 Preliminary Characterization of ZrO ₂ nanopowder	13
2.2.2 Application of RRS at lab-scale level.....	13
2.2.2.1 Reactor washing.....	13
2.2.2.2 Sedimentation.....	14
2.2.3 Implementation of RRS within Processing line 1.....	15

2.2.3.1 Recycle	15
2.2.4 Characterization of ZrO ₂ dispersion in biological medium	15
2.3 Results and Discussion	16
2.3.1 Preliminary characterization of ZrO ₂ nanopowder	16
2.3.2 Application of RRS at lab-scale level.....	19
2.3.2.1 Reactor washing.....	19
2.3.2.2 Sedimentation.....	21
2.3.3 Implementation of RRS within Processing line 1.....	22
2.3.3.1 Recycle and quality of ZrO ₂ nanopowder	22
2.3.4 Toxicity outcomes	24
2.3.5 Characterizations of ZrO ₂ in biological medium	26
2.3.6 Exposure assessment: on-site measurements	27
2.3.7 Cost/benefit analysis	28
2.4 Conclusions	29
2.5 References	29
3. Processing line 2: ceramic process line (ZrO ₂ nanopowder).....	31
3.1 Introduction	31
3.1.1 ZrO ₂ nanomaterials.....	31
3.1.2 Description of Processing line 2.....	31
3.1.3 Critical step Identified and RRS proposed	32
3.1.3.1 Wet formulation drying	33
3.1.3.2 Uniaxial Pressing	33
3.1.3.3 Zircon pigment manufacturing	33
3.2 Experimental.....	33
3.2.1 Preliminary characterization of ZrO ₂ nanopowder	33
3.2.2 Application of RRS at lab scale / pilot scale level	33
3.2.2.1 Wet formulation drying	33
3.2.2.2 Uniaxial pressing	34
3.2.2.3 Zircon pigment manufacturing	35
3.3 Results and Discussion	36
3.3.1 Application of RRS at lab scale / pilot scale level	36
3.3.1.1 Wet formulation drying	36

3.3.1.2 Uniaxial pressing	37
3.3.1.3 Zircon pigment manufacturing	38
3.3.2 Exposure assessment: off-line measurement	39
3.4 Conclusions	41
3.5 References	42
4. Processing line 3: electrospinning line (polyamide nanofibres)	43
4.1 Introduction	43
4.1.1 Polyamide nanofibres	43
4.1.2 Description of Processing line 3.....	43
4.1.3 Critical step identified and RRS proposed	44
4.1.3.1 Handling and manufacturing	45
4.2 Experimental.....	45
4.2.1 Preliminary characterization of polyamide nanofibres	45
4.2.2 Application of RRS at lab-scale level.....	45
4.2.2.1 Handling and manufacturing	45
4.3 Results and discussion	46
4.3.1 Preliminary Characterization of polyamide nanofibres.....	46
4.3.2 Application of RRS at lab-scale level.....	46
4.3.2.1 Handling and manufacturing	46
4.3.3 Exposure assessment: off-line and on-site measurements.....	47
4.4 Conclusions	48
4.5 References	48
5. Processing line 4: electrospinning line (TiO ₂ nanofibres).....	50
5.1 Introduction	50
5.1.1 TiO ₂ nanofibres	50
5.1.2 Description of the Processing line 4	51
5.1.3 Critical step identified and RRS proposed	52
5.1.3.1 Handling and manufacturing	52
5.2 Experimental.....	52
5.2.1 Preliminary characterization of TiO ₂ nanofibres	52
5.2.2 Application of RRS at lab-scale level.....	53

5.2.2.1 Handling and manufacturing	53
5.3 Results and discussion	53
5.3.1 Preliminary characterization of TiO ₂ nanofibres	53
5.3.2 Application of RRS at lab-scale level.....	55
5.3.2.1 Handling and manufacturing	55
5.3.3 Toxicity outcomes.....	59
5.3.4 Exposure assessment: off-line and on-site measurements.....	61
5.4 Conclusions	62
5.5 References	63
6. Processing line 5: spray coating line (Ag and TiO ₂ nanosol).....	65
6.1 Introduction	65
6.1.1 Ag and TiO ₂ nanomaterials	65
6.1.2 Description of Processing line 5.....	66
6.1.3 Critical step identified and RRS proposed	67
6.1.3.1 Spray coating	67
6.2 Experimental.....	67
6.2.1 Preliminary characterization of involved nanosols	67
6.2.1.1 Preliminary characterization of Ag sample.....	67
6.2.1.2 Preliminary characterization of TiO ₂ sample	69
6.2.2 Application of RRS at lab-scale level.....	69
6.2.2.1 Ag samples	69
6.2.2.2 TiO ₂ samples	70
6.2.3 Implementation of RRS within the Processing line 5	71
6.2.3.1 Ag samples	71
6.2.3.2 TiO ₂ samples.....	71
6.2.4 Characterization of Ag and TiO ₂ dispersion in biological media.....	72
6.2.4.1 Interaction between AgNPs and BSA.....	73
6.3 Results and Discussion	74
6.3.1 Preliminary characterization of pristine Ag and TiO ₂ nanosols.....	74
6.3.1.1 Ag sample.....	74
6.3.1.2 TiO ₂ sample	78
6.3.2 Application of RRS at lab-scale level.....	79

6.3.2.1 Ag samples	79
6.3.2.2 TiO ₂ samples	83
6.3.3 Implementation of RRS within Processing line 5.....	89
6.3.3.1 Ag samples	89
6.3.3.2 TiO ₂ samples	95
6.3.4 Toxicity outcomes.....	96
6.3.4.1 Ag samples	97
6.3.4.2 TiO ₂ samples	98
6.3.5 Characterizations of Ag and TiO ₂ in biological media.....	99
6.3.5.1 Ag samples	99
6.3.5.1.1 Interaction between AgNPs and BSA.....	102
6.3.5.2 TiO ₂ samples	107
6.3.6 Exposure assessment: on-site measurements	109
6.3.7 Cost/benefit analysis	110
6.4 Conclusions	112
6.5 References	114
7. Processing line 6: plastic composite line (CNT).....	117
7.1 Introduction	117
7.1.1 CNT.....	117
7.1.2 Description of Processing line 6.....	118
7.1.3 Critical step identified and RRS proposed	119
7.1.3.1 Feed preparation, degassing molten polymers and cleaning process	119
7.2 Experimental.....	119
7.2.1 Preliminary characterization of CNTs	119
7.2.2 Application of RRS at lab-scale level.....	120
7.2.3 Application of RRS at lab-pilot scale level.....	120
7.3 Results and discussion	121
7.3.1 Preliminary characterization of CNT	121
7.3.2 Application of RRS at lab-scale level.....	122
7.3.3 Application of RRS at pilot-scale level	125
7.3.4 Toxicity outcomes.....	127

7.3.5 Exposure assessment: off-line and on-site measurements.....	129
7.3.6 Cost/benefit analysis	131
7.4 Conclusions	132
7.5 References	133
8. Final Conclusions	135
Curriculum Vitae.....	137
Work in progress based on this thesis	138
Peer-reviewed publication based on this thesis	138
Conference presentation based on this thesis	138
Other peer-reviewed publication.....	140

LIST OF TABLES

1. Introduction

Table 1 - Partner involved in SANOWORK Project and WP in which they are involved.....	5
Table 2 - NM involved, its risk determinant properties and RRS proposed.	6
Table 3 - SANOWORK processing line, company involved, nano-manufacturing process and NM application.	7

2. Processing line 1: washing/disposal line (ZrO₂ nanopowder)

Table 1 - Characterization data for the samples involved in the introduction of RRS in PL 1. 20	
Table 2 - Characterization data of the samples involved in the sedimentation study.....	21
Table 3 - Characterization data of the samples involved in the introduction of the RRS.	22
Table 4 - ZP, mean diameter and Pdl of ZrO ₂ samples and P25 dispersed at 125 µg/ml in deionized water and complete culture medium. Data in italics, of not sufficiently good quality, were reported only to establish a general trend.	26
Table 5 - Toxicity, exposure and risk data and remediation costs for the step considered in PL1.	28

3. Processing line 2: ceramic process line (ZrO₂ nanopowder)

Table 1 - Pellets densities after cold die pressing or sintering	37
Table 2 - Summary of the colorimetric measurement.....	38
Table 3 - Summary of main results of the dustiness tests on ZrO ₂ powders.....	41

4. Processing line 3: electrospinning line (polyamide nanofibres)

Table 1 - Summary of the air permeability measurement.	47
--	----

5. Processing line 4: electrospinning line (TiO₂ nanofibres)

Table 1 - Summary of AR determination for the TiO ₂ NF samples.	56
Table 2 - E _g of the TiO ₂ NF samples.....	58

6. Processing line 5: spray coating line (Ag and TiO₂ nanosol)

Table 1 – XRF measurement of total and ionic Ag content in pristine sample	76
---	----

Table 2 - XRF measurement of total and cationic Ag content in pristine sample	77
Table 3 – DLS measurement of pristine TiO ₂ sample.....	78
Table 4 – XRF and XRD results of pristine TiO ₂ sample.....	79
Table 5 - Primary particle size distribution data obtained from TEM images	80
Table 6 - Mean d _H , Pdl and ZP of modified Ag samples diluted up to 128 µg/ml in deionized water.....	81
Table 7 - Results of Ag ⁺ separation and determination in pristine and modified Ag samples.	81
Table 8 - Data of Ag samples employed and antibacterial activity results.....	82
Table 9 - Primary particle size distribution data obtained from TEM images	85
Table 10 - Mean d _H , Pdl and ZP of modified TiO ₂ samples diluted up to 125 µg/ml in deionized water.....	85
Table 11 - Summary of BET and XPS data for the spray dried TiO ₂ _15_NP_SD sample.....	86
Table 12 - RhB degradation efficiency % after 60 min of reaction of pristine TiO ₂ _6_sol and modified TiO ₂ _15_NP_SD, TiO ₂ _18_sil_sol (TiO ₂ 3 wt.%), TiO ₂ _18_sil_sol (solid 3 wt.%) and TiO ₂ _36_cit_sol samples.....	88
Table 13 - Data obtained for microbial tests on treated ceramic tiles	89
Table 14 - pH, ZP, mean size diameter by intensity and Pdl of Ag samples dispersed at 128 µg/ml in deionized water and complete culture media DMEM and Ham’s F-12.	101
Table 15 - Quantification from survey XPS spectra	106
Table 16 - Quantification from HR-TEM XPS spectra	106
Table 17 - pH, ZP, mean size diameter by intensity and Pdl of TiO ₂ samples dispersed at 125 µg/ml in deionized water and complete culture medium DMEM. Data in italics, of not of sufficiently good quality data, were reported only to evidence a general trend.	107
Table 18 - Toxicity, exposure and risk data and remediation costs for the spraying operation of Ag NPs in PL5, considered a high risk task for workers.....	110
Table 19 - Toxicity, exposure and risk data and remediation costs for the spraying operation of TiO ₂ NPs in PL5, considered a high risk task for workers.....	111

7. Processing line 6: plastic composite line (CNT)

Table 1 - Summary of BET results of pristine C_1_NT sample.	122
Table 2 - Summary of the CNT samples AR determination.	123
Table 3 - Summary of BET results of modified CNT samples.	123
Table 4 - Summary of the main parameters in DSC.....	126
Table 5 - Summary of result obtained on PNC flexural properties.	127

Table 6 - PNC tensile properties.....	127
Table 7 - Summary of the main results on the dustiness tests on pristine C_1_NT and modified CNT	130
Table 8 - Toxicity, exposure and risk data and remediation costs for the spraying operation of Ag NPs in PL5, considered a high risk task for workers.	132

LIST OF FIGURES

1. Introduction

Figure 1 - Conceptual framework driving the design of safe NMs	1
Figure 2 - Surface engineering proposed as RRS	3
Figure 3 - Partners involved in the EU SANOWORK project and their location.....	4
Figure 4 - The SANOWORK approach.....	7

2. Processing line 1: washing/disposal line (ZrO₂ nanopowder)

Figure 1 - PlasmaChem synthetic procedure.	11
Figure 2 - Scheme of processing line 1, showing process steps in which RRS were applied and evaluated.	12
Figure 3 - Pristine powder morphology by SEM-FEG images.	16
Figure 4 - TEM image of pristine powder (left) and crystalline ZrO ₂ phase (right).....	17
Figure 5 - TEM image with underlined the spot used for EDS determination.....	17
Figure 6 - XRD spectra of pristine sample and powders calcined at 400°C and 1 000°C.....	17
Figure 7 - Raman spectra of pristine zirconia.	18
Figure 8 - DSC-TGA analysis of pristine ZrO ₂ powder.	19
Figure 9 - ZP versus pH titration curves for the different ZrO ₂ samples.....	20
Figure 10 - Picture of the samples involved in the sedimentation study.	21
Figure 11 - Raman and optical spectra of ZrO ₂ particles obtained from wastes; the blu line represented the pristine sample ZrO ₂ _PCHEM_sol, while the black and red line represented the ZrO ₂ _CHEM_sol_1 and ZrO ₂ _PCHEM_sol_2, respectively.....	23
Figure 12 - TG (left) and DTG (right) analyses of ZrO ₂ NMs obtained from zirconium wastes.	23
Figure 13 - Cell viability, measured by CFE assay, in A549. Cells were exposed for 24, 48 and 72 h to increasing concentrations (1.25 - 80 µg/cm ²) PL 1 ZrO ₂ NM. Data are presented as mean % CFE normalized to the untreated control (C-; black bar) ± standard error of the mean (SEM), n = 9. * p < 0.05, ** p < 0.01, *** p < 0.001. C+: 1µM Na ₂ CrO ₄ that induced 0 % CFE (data not shown).....	24
Figure 14 - Photos of grid during background measurement, sampling from fume hood containing the sol-gel reactor.....	27

3. Processing line 2: ceramic process line (ZrO₂ nanopowder)

Figure 1 - Main steps in the production of ceramic bodies.	31
Figure 2 - Scheme of PL 2, showing the process steps in which RRS was applied and evaluated	32
Figure 3 - Morphology of a) pristine ZrO ₂ _1_NP, b) spray dried ZrO ₂ _9_NP_SD and c) freeze dried ZrO ₂ _12_NP_SD samples observed by SEM-FEG at different magnification.	36
Figure 4 - Picture of the pellets obtained by pressing and sintering; from the top to the bottom: i) pristine CP ZrO ₂ _1_NP, ii) spray dried CP ZrO ₂ _9_NP_SD, and iii) freeze dried CP ZrO ₂ _12_NP_SD samples.....	37
Figure 5 - XRD patterns of pristine ZrO ₂ _14_SilPr_NP (black) and modified ZrO ₂ _15_SilPr_NP_SD (red) pigments	39
Figure 6 - Scheme of experimental set-up for dustiness test.....	40
Figure 7 - ZrO ₂ particles from aerosol generated from (left to right): i) pristine ZrO ₂ _1_NP, ii) ZrO ₂ _1_NP, ZrO ₂ _9_NP_SD and iii) ZrO ₂ _12_NP_FD samples.....	40

4. Processing line 3: electrospinning line (polyamide nanofibres)

Figure 1 - Main step in PA electrospinning procedure	44
Figure 2 - Scheme of processing line 3, showing process step in which RRS were applied and evaluated	44
Figure 3 - Pristine PA_4.1_gel sample morphology by SEM images.....	46
Figure 4 - Morphology of the gelatine coated PA_4.1_gel (left) and washed PA_4.1_gel_W1 (right) samples by SEM images.....	46
Figure 5 - Sampling grid image showing two area subjected to EDS analysis and respective spectra.....	48

5. Processing line 4: electrospinning line (TiO₂ nanofibres)

Figure 1 - Main steps in TiO ₂ electrospinning procedure	51
Figure 2 - Scheme of PL 4, showing the process step in which RRS were applied and evaluated	52
Figure 3 - Pristine TiO ₂ _1_NF sample morphology by a) TEM-BF and b) STEM- SE images...	54
Figure 4 - Pristine TiO ₂ _1_NF sample morphology and AR distribution by SEM images.	54
Figure 5 – XRD spectrum of pristine TiO ₂ _1_NF sample.....	54
Figure 6 - TGA/DSC analysis of pristine TiO ₂ _1_NF sample.....	55

Figure 7 – Morphology of the ball milled a) TiO ₂ _8_NF, b) TiO ₂ _9_NF, c) TiO ₂ _10_NF, d) TiO ₂ _11_NF samples and their AR distributions calculated from SEM-FEG images.....	56
Figure 8 - EPR signal intensity after co-incubation with long TiO ₂ _1_NF, ball milled TiO ₂ _8_NF, UICC crocidolite and P25. Results are expressed as mean +/- standard error of the mean (sem) (n = 3). *** p < 0.001, ** p < 0.01, * p < 0.05 versus vehicle control.	57
Figure 9 - Representative EPR spectra after co-incubation with long TiO ₂ _1_NF, ball milled TiO ₂ _8_NF, UICC crocidolite and P25	58
Figure 10 - Characterization of cell/materials interactions by SEM. Macrophages were seeded on coverslips and treated for 24 h with the indicated materials at 10 µg/cm ² . The preparations were fixed and dehydrated before being mounted on stub for SEM analysis. Representative images at increasing magnification were taken a) untreated cells, b) UICC crocidolite, c) pristine TiO ₂ _1_NF sample, d) modified TiO ₂ _8_NF sample, e) P25.....	61
Figure 11 - Temporal monitoring of particle concentration evolution during preliminary campaign by Elmarco.....	62

6. Processing line 5: spray coating line (Ag and TiO₂ nanosol)

Figure 1 - Colorobbia Ag (left) and TiO ₂ (right) nanosol synthetic scheme	66
Figure 2 - Scheme of PL 5, showing process steps in which RRS were applied and evaluated.....	67
Figure 3 - HR-TEM images of pristine Ag nanosol.....	74
Figure 4 - HR-TEM image of pristine Ag (left) and its crystalline phase (right)	75
Figure 5 - HR-TEM image with underlined the spot used for EDS determination.....	75
Figure 6 – Particle size distribution based on HR-TEM images.....	75
Figure 7 - Image of SC device	76
Figure 8 - Image of CFU device.....	76
Figure 9 - DTA-TGA analysis of pristine and purified Ag sample	77
Figure 10 - Pristine Ag nanosol shape by HR-TEM images.....	78
Figure 11 - Particle size distribution from HR-TEM images	78
Figure 12 - Images by HR-TEM of modified Ag samples: a) Ag_15_sil_sol, b) Ag_31_sol_UF, c) Ag_35_sil_sol and its related EDS pattern	80
Figure 13 - Modified TiO ₂ sample, a) SEM-FEG, bright field TEM and EDS of TiO ₂ _15_NP_SD, b) bright field TEM, STEM-HAADF images and STEM-EDS line scan of TiO ₂ _18_sil_sol, c) bright field TEM, STEM-HAADF images and STEM-EDS line scan of TiO ₂ _36_cit_sol.....	84
Figure 14 - BET analysis of spray dried TiO ₂ _15_NP_SD sample	86
Figure 15 - EPR signal intensity after co incubation with pristine TiO ₂ _6_sol and modified TiO ₂ _36_cit_sol, TiO ₂ _15_NP_SD, TiO ₂ _18_sil_sol samples. Signal intensity of a silica SiO ₂ _2_NP_SD sample and the benchmark control Aeroxide® P25 were also reported for	

comparison. Results were expressed as mean +/- standard error mean (n = 3). *** P < 0.001, **P < 0.01, * P < 0.05 vs. vehicle control; ####P < 0.001, ## P < 0.01 vs. pristine TiO₂_6_sol..... 86

Figure 16 - Representative EPR spectra after 1 h of co-incubation of the spin trap Tempone-H with pristine TiO₂_6_sol and modified TiO₂_36_cit_sol, TiO₂_15_NP_SD, TiO₂_18_sil_sol samples. Spectra of the silica SiO₂_2_NP_SD sample and the benchmark Aeroxide® P25 were also reported for comparison..... 87

Figure 17 - RhB degradation efficiency % of pristine TiO₂_6_sol and modified TiO₂_15_NP_SD, TiO₂_18_sil_sol (TiO₂ 3 wt.%), TiO₂_18_sil_sol (solid 3 wt.%) and TiO₂_32_cit_sol samples. 88

Figure 18 - Typical set up for microbial tests on treated ceramic tiles..... 89

Figure 19 - Uncoated ceramic tile spectra (blank), 9 measurement point belonging to one line raster..... 90

Figure 20 - CT Ag_1_sol spectra, a) 6 point line raster, b) 7 point line raster, c) 8 point line raster, d) 9 point line raster, e) 10 point line raster. Three consecutive ablations for each raster were reported. 92

Figure 21 - Comparison of the signal intensity of the first ablation for each line raster considered in the pristine CT Ag_1_sol sample. 92

Figure 22 - CT Ag_31_sol spectra, a) 4 point line raster, b) 5 point line raster, c) 6 point line raster, d) 7 point line raster, e) 8 point line raster. Three consecutive ablations for each raster were reported. 94

Figure 23 – Comparison of the signal intensity of CT Ag_1_sol, CT Ag_31_sol and blank. 94

Figure 24 - NO and NO_x conversion tests on treated ceramic tiles: a) Blank, uncoated tile, b) CT TiO₂_6_sol, c) CT TiO₂_18_sil_sol and d) CT TiO₂_36_cit_sol..... 95

Figure 25 - NO and NO_x conversion tests on treated ceramic tiles coated with pristine TiO₂_6_sol (TiO₂ content 1 wt.%, black), modified TiO₂_18_sil_sol (TiO₂ content 1 wt.%, red) and CT TiO₂_18_sil_sol (total solid content 1 wt.%, TiO₂ content 0,25 wt.%, blue). 96

Figure 26 - Cell viability, measured by Resazurin assay using RAW 264.7. Cells were exposed for 24 h to increasing concentrations (1.25 – 80 µg/cm²) of PL 5 Ag NM..... 97

Figure 27 - Cell viability, measured by CFE assay, in A549. Cells were exposed for 24, 48 and 72 h to increasing concentrations (1.25 – 80 µg/cm²) of TiO₂ NMs. Data are graphically presented as mean % CFE values normalized to the untreated control (0 µg/cm²; black bar) ± standard error mean (SEM); n = 9. * p > 0.05; ** p < 0.01; *** p < 0.001. C+: 1µM Na₂CrO₄ that induced 0 % CFE (data not shown). 98

Figure 28 - Schematic representation of PC formation moving from a lab-system to a bio-system..... 100

Figure 29 - DLS sizes of Ag samples dispersed in Milli-Q water, DMEM and Ham's F-12. For each solvent, from the top to the bottom, the samples were Ag_1_sol, Ag_15_sil_sol, Ag_31_sol_UF and Ag_35_sil_sol.....	101
Figure 30 - Scheme of Ag-BSA conjugation and purification tests	102
Figure 31 - UV-vis spectra of Ag and Ag-BSA samples after 0, 24, 48, 72 h of interaction with BSA.....	103
Figure 32 - UV-vis spectra of purified Ag and Ag-BSA samples after 0, 24, 48, 72 h of interaction with BSA.....	104
Figure 33 - ATR-IR spectrum of Ag and Ag-BSA samples after 24 h of interaction with BSA	105
Figure 34 - DLS size graph of TiO ₂ samples dispersed in Milli-Q water, DMEM and Ham's F-12. For each solvent, from top to bottom, the samples were TiO ₂ _6_sol, TiO ₂ _18_sil_sol, TiO ₂ _36_cit_sol and P25.....	107
Figure 35 - Evolution of the particle calculation (particules/cm ³) during spray coating operation and TEM images of the particles in each step.....	109

7. Processing line 6: plastic composite line (CNT)

Figure 1 - Main step in PNC production	118
Figure 2 - Scheme of processing line 6, showing process step in which RRS were applied and evaluated.	119
Figure 3 - Pristine CNT sample morphology by HR-TEM images.	121
Figure 4 - Pristine CNT sample morphology by SEM images.	121
Figure 5 - Morphology of modified a) freeze dried C_3_FG and b) spray dried C_4_FG samples from TEM and SEM-FEG images.....	122
Figure 6 - EPR signal intensity after co incubation with pristine C_1_NT or modified forms C_3_FG and C_4_SD. Results are expressed as mean +/- sem (n=3). *** p<0.001, **p<0.01, vs. vehicle control; # p<0.05 vs. Pristine (C_1_NT).....	124
Figure 7 - Representative EPR spectra after 1 h of co-incubation of the spin trap Tempone-H with pristine C_1_NT and modified, C_3_FG and C_4_SD, samples.....	124
Figure 8 - SEM images of a) pristine PP-pCNT pellet surface by SEM, b) modified PP-mCNT pellet surface by SEM c) inner part of pristine PP-pCNT pellet by TEM and d) inner part of PP-mCNT pellet by TEM.....	125
Figure 9 - TGA analysis of pristine C_1_NT (green pattern) and modified C_4_SD (blue pattern) samples.....	126
Figure 10 - Cell viability in cells treated with pristine C_1_NT. Resazurin. Data are average of 18 determinations in 3 separate experiments. *** p< 0.001 (upper panel). Cell viability in	

cells treated with modified C_3_FG and C_4_SD samples. Resazurin. Data are average \pm SD of 6 determination. *, **, *** p<0.05, p<0.01, p< 0.001..... 128

Figure 11 - Temporal monitoring of particle concentration evolution during preliminary campaign at Leitat 129

Figure 12 - CNT particles from aerosol generated from a) pristine C_1_NT and b) modified C_3_FG samples. 131

1. Introduction

1.1 Safety by design concept

The SbyD may be defined as an approach that encourages to deeply define health and safety risks during material planning and/or development. In such a way, along with product or process quality and efficiency, also the related health and safety issues, may be determined and managed during the early planning stage^[1, 2], to reduce or avoid the likelihood of risks to emerge at a further step. This concept, arising from construction sector, may be extended to other fields, including that of nanotechnology, being a novel way to control and manage the risk related to NM, production, use and disposal.

The NM engineering following the SbyD concepts was highlighted as a strategic and priority area in the European Nanosafety Cluster and in the EU Nano-Safety Strategy 2015-2025 Agenda^[3]. Such as reported in this latter, the development and implementation of SbyD control strategies, with its primary prevention value of risk management, represents one of the biggest challenge of nanotechnology that should guarantee its sustainable development. The SbyD approach in nanotechnology, suggests to focus on the design for safety during the development and application of new NMs, to control risks that may arise at a later stage. The key features that drive to design safe NMs follow the conceptual framework^[4] schematized in figure 1.

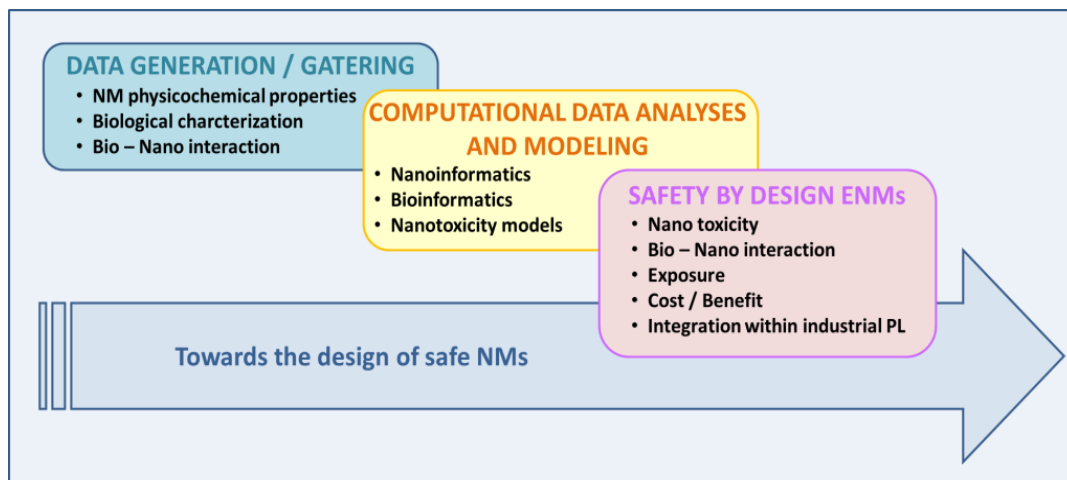


Figure 1 - Conceptual framework driving the design of safe NMs

At a first level, the design of safe NMs started from data generation/gathering; it included the investigation of NM physicochemical properties and toxicity, to understand the mechanism that governed both the adverse effects of NMs on biological systems and the NMs emission/exposure potential. At a second level, the observed evidences on NM emission, exposure pathway and bio-nano interaction, should be supported by predicting models. Finally, at a third level, the design of safe NMs should be implemented within real industrial

processing lines, allowing a cost/benefit analysis and the promotion of SbyD risk control measure.

1.1.2 The NM surface engineering as RRS

From the first investigation on NMs [5, 6, 7, 8], the research field of nanotechnology experienced an impressive growth [9], giving rise to many related research fields. Among them, the NM engineering was aimed to obtain, manipulate and integrate NMs into more complex structure, creating novel materials with new or improved technological features [10]. In parallel, with the development of nanotechnology, the nanotoxicology emerged as new research field aimed to investigate the toxicity, environmental, health and safety issues related to NMs [11].

In recent years, taking advantage from the experience gained and shared within this new research field, great attention was posed on the identification of some NM property/activity relationships, that allowed the control of NM hazard properties. Although these relationships are not yet fully understood and elucidated, it is now commonly accepted that some physicochemical properties of NMs may influence their uptake, transport and fate. These include NM size, shape, surface chemistry and stability under some environmental and biological conditions (e.g., acquisition of a PC) [12].

To date, different strategy and surface engineering were developed to decrease and control NM toxicity and emission potential, improving therefore their biocompatibility. In the case of nanofibrous materials, that trigger the toxicity mechanism due to their shape (e.g., high aspect ratio), it was found a toxicity paradigm that dictated if a fiber must be considered an hazardous material. Following the “fiber pathogenicity paradigm”, a safe fibrous material should have a certain diameter and length and, moreover, should be not biopersistent [13]. An aerodynamic diameter $> 3 \mu\text{m}$, did the NM too thick to be inhalable, being the cut-off for inhalation in humans around $5 \mu\text{m}$ as aerodynamic diameter (for fibers, the aerodynamic diameter may be approximately evaluate as 3-times the actual diameter) [14]. A fiber length $< 5 \mu\text{m}$ was demonstrated to be a value that hindered frustrated phagocytosis [14, 15]. Finally, a NF should be not biopersistent to undergo a rapid dissolution in the lungs.

For NM that exerted a toxicity mechanism due to dissolution phenomena and ion leaching, a different surface engineering was exploited. As reference, for ZnO NP the control of particle solubility/dissolution were achieved by ion doping [16]. For Ag NP, the control of ion release from Ag NP surface were obtained through surface modification on Ag particles, including peroxidation, sulfidation and thiol ligand exchange [17]. Moreover, surface modifications, including surface coating, surfactant and ligand addition, were widely investigated to improve biocompatibility and successfully accomplished biomedical applications of Au [18] and iron oxide NPs [19]. Following a SbyD approach, different NM surface engineering was investigated in SANOWORK project as a tool to control the risk related to NMs (Fig. 2).







Surface engineering strategy	Schematic representation
Surface coating	
Control of colloidal forces	
Spray drying and freeze spray drying techniques	
Immobilization by organic film coating deposition	
Purification	
Wet milling	

Figure 2 - Surface engineering proposed as RRS

The surface coating and purification strategy were aimed to control the surface chemistry of NMs. The control of colloidal forces, spray drying and freeze drying were employed to consolidate nanosized particles in bigger aggregates. The immobilization by film coating deposition and the wet milling were investigated, respectively, to control free NF release or their aspect ratio. Due to their character of preventive measures and their contextualization within real industrial scenarios, surface engineering of NMs investigated in the SANOWORK project were considered and identified as RRS.

1.2 European project SANOWORK

1.2.1 Contest

Strong nanotechnology proponents, such as Lux Research ^[20], anticipate that nanotechnology applications will affect nearly each type of manufactured assets in the next few years. Nevertheless, the promise of a significant contribution by nanotechnology to boost the economy, live standards and improve the quality of life may be outweighed by the perceived occupational, environmental, health and safety risks. The fast development of nanotechnology raises occupational, environmental, health and safety concerns and among the possible exposure locations, the workplaces where NMs are intentionally produced, used, disposed and recycled, pose specific risk assessment and management challenges ^[21, 22]. These worrying issues were considered to be of primary importance for the European Commission, that has introduced the call NMP.2011.1.3-2 inviting European researchers to cooperate, focusing their efforts on “worker protection and exposure risk management strategies for nanomaterial production, use and disposal”.

In this context, the European project “Safe nano worker exposure scenarios (**SANOWORK**)” was aimed to develop and implement RRS, that consist in NM surface engineering, with a balanced approach between design for manufacturing and for safety, proposed to prevent workers from exposure and/or potential hazards related to NMs.

1.2.2 Consortium

The SANOWORK consortium brings together large and medium size enterprises together with private research centers, academics and public entities, that possess considerable experience in the field of NM occupational health and safety. Partners involved and their location in the European community are shown in figure 3.

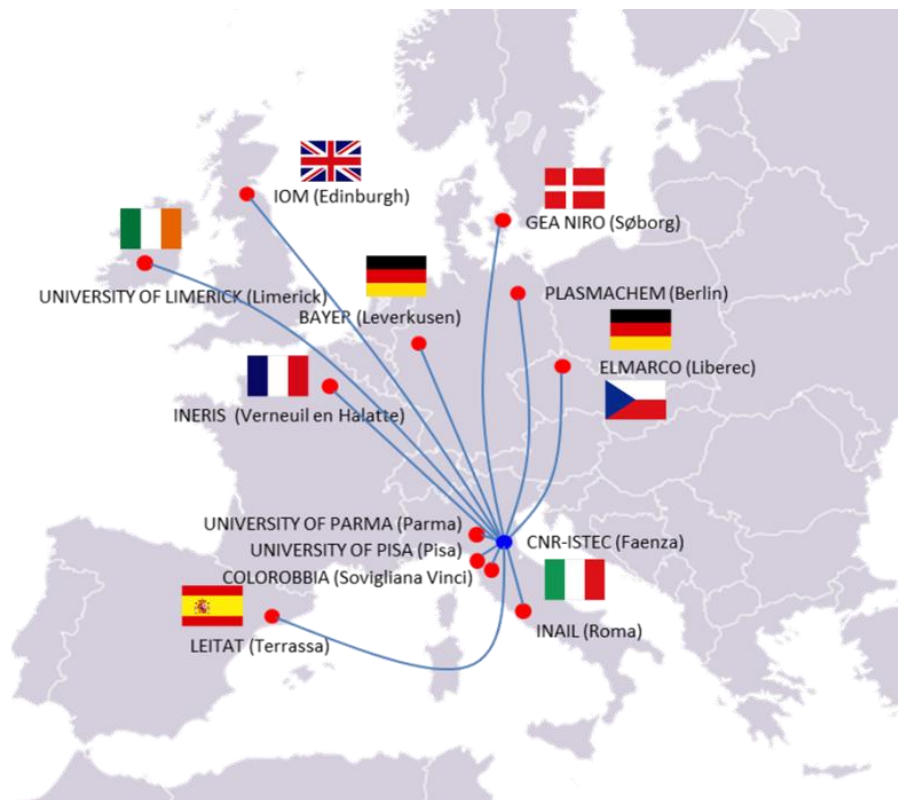


Figure 3 - Partners involved in the EU SANOWORK project and their location

CNR-ISTEC, a governmental organization for scientific research in the field of traditional, structural, bio and functional ceramic materials, coordinated the project and provided expertise in NM synthesis, NM surface functionalization and implementation of RRS within processing line. The industrial partners, **PlasmaChem**, **GEA-Niro**, **Elmarco**, **Bayer** and **Colorobbia**, extensively involved in R&D and industrial production, let available their processing lines for the implementation of RRS and provided the worker exposure scenario. **IOM**, a private research center in the fields of occupational and environmental health, hygiene and safety, was involved in the toxicological investigation, especially concerning fibrous NMs. **Leitat**, a private technological center, provided a pilot-scale set up for the implementation of RRS and the related exposure scenario. Moreover Leitat performed physico-chemical and

mechanical characterization of plastic materials produced within its PL. The **University of Parma and University of Pisa** collaborated performing cytotoxicity and genotoxicity assays for the toxicological characterization of NMs involved. The **University of Limerick**, performed NM surface characterization and insurance risk quantification. **Ineris**, a French public research body, offered its expertise and performed the EA. **Inail**, the Italian workers compensation authority, provided information on the rules and regulations in the fields of occupational health and safety.

In relation to know-out and facilities available, each partner was involved in different tasks, that were organized in 7 WP, area highlighted in blue in table 1 show the contribution from each partner to the different WPs.

Table 1 - Partner involved in SANOWORK Project and WP in which they are involved.

WP / Partner	WP1	WP2	WP3	WP4	WP5	WP6	WP7
	Administrative & scientific management	Risk analysis	Exposure assessment	Design for risk control	Toxicological hazard assessment	Implementation in PL	Dissemination & exploitation activity
CNR-ISTEC							
IOM							
PlasmaChem							
Elmarco							
GEA-Niro							
Colorobbia							
Bayer							
Ineris							
University of Limerick							
University of Parma							
University of Pisa							
Leitat							
Inail							

1.2.3 Approach

In SANOWORK project, five target NMs (ZrO_2 , Ag, TiO_2 , polyamide and CNT), corresponding to three different nanostructured samples (nanoparticles, nanofibers, nanotubes) and including main risk determinant properties were considered (Table 2).

Table 2 - NM involved, its risk determinant properties and RRS proposed.

NMs	Form	Possible risk determinant properties	RRS proposed
ZrO_2	Nanoparticles	<ul style="list-style-type: none"> Nanosize Photoreactivity High charged surface 	<ul style="list-style-type: none"> Spray and freeze drying Surface coating CFC
Ag		<ul style="list-style-type: none"> Nanosize Reactivity Solubility (Ag^+ leaching) 	<ul style="list-style-type: none"> Surface coating Purification
TiO_2		<ul style="list-style-type: none"> Nanosize Photoreactivity High charged surface 	<ul style="list-style-type: none"> Spray drying Surface coating Blending with colloidal SiO_2
Polyamide	Nanofibers	<ul style="list-style-type: none"> High aspect respirable particle 	<ul style="list-style-type: none"> Film coating deposition
TiO_2		<ul style="list-style-type: none"> High aspect respirable particle Photoreactivity High charged surface 	<ul style="list-style-type: none"> Wet ball milling
CNT	Nanotubes	<ul style="list-style-type: none"> High aspect respirable particle Redox reactivity 	<ul style="list-style-type: none"> Spray and freeze spray drying Surface coating

Depending on structural alerts of involved NMs and exposure critical steps identified within their nano-manufacturing processing lines, different RRS based on NM surface engineering were proposed. The resulting ENMs were developed to control key risk relevant properties (structural alerts), exposure and hazard potential, still maintaining the desired performance in NMs or final products. Such RRS were integrated in the involved processing lines, that identify industrially relevant sectors and applications (Table 3).

Table 3 - SANOWORK processing line, company involved, nano-manufacturing process and NM application.

SANOWORK PL	Company	Nano-manufacturing process	NM application
1	PlasmaChem	ZrO ₂ production	Optical materials
2	CNR-ISTEC & GEA-Niro	Ceramic ZrO ₂ material production & ZrO ₂ spray drying	Ceramic pigments
3	Elmarco & BAYER	PA sheet production	Air filter materials
4	Elmarco & BAYER	TiO ₂ NF production	Photocatalytic materials
5	Colorobbia	Ag and TiO ₂ sol production	Functionalized surface coatings
6	Leitat & GEA-Niro	Plastic nano-composite production	Plastic nano-composites

As shown in figure 4, following the introduction and application of RRS within PLs, two different situations have been outlined, the **BEFORE** and **AFTER** one: in the former, pristine NMs were produced by the original process, while in the latter, modified ENMs were obtained through RRS application, introducing novel production steps.

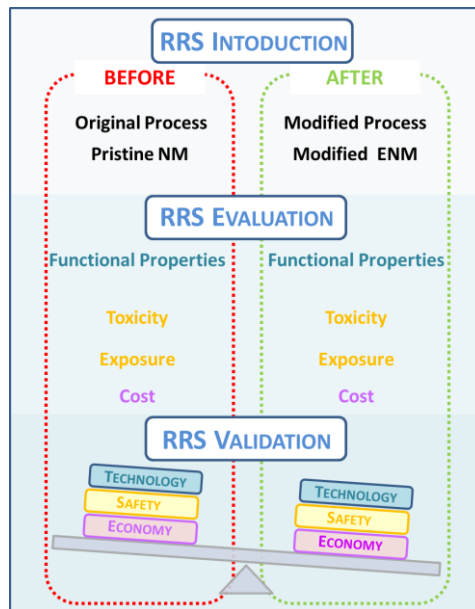


Figure 4 - The SANOWORK approach.

In SANOWORK approach, to evaluate RRS effectiveness, different parameters, concerning respectively technology, safety and economics aspects, were considered in the BEFORE and AFTER situations. Relevant NMs performance were evaluated to ensure that RRS did not results detrimental for NM production/application. NMs toxicity was assessed by

biologist and correlated with NM characterization performed in biological conditions, to define a sound structure-toxicity mechanisms. Exposure to NMs in each PL during the critical step were investigated directly on-site or through off-line experiments. A cost/benefit analysis of NM production was performed to correlate the cost of introduction of RRS with the benefit arising from their application, to promote a safest industrial use of ENMs.

1.3 References

- [1]. R. Korman, *Eng. News-Rec.*, **2001**, 31, 26 - 29
- [2]. M. Behm, *Safety Sci.*, **2005**, 43, 589 - 611
- [3]. K. Savolainen, U. Backman, D. Brouwer, B. Fadeel, T. Fernandes, T. Kuhlbusch, R. Landsiedel, I. Lynch, and L. Pylkkänen, and members of the NanoSafety Cluster “Nanosafety in Europe 2015-2025: Towards Safe and Sustainable Nanomaterials and nanotechnology Innovations”, Copyright 2013 Finnish Institute of Occupational Health, http://www.ttl.fi/en/publications/Electronic_publications/Nanosafety_in_europe_2015-2025/Documents/nanosafety_2015-2025.pdf.
- [4]. A. L. Costa, **2014**, Chapter 3, Rational Approach for the safe Design of Nanomaterials. Book: Nanotoxicology - Progress Towards Nanomedicine. ISBN: 978-1-4822-0387-5
- [5]. R. P. Feynman, *Eng. Sci.*, **1960**, 23, 22 - 36
- [6]. K.H. Bennemann and J. Koutecky, *Proc. 3rd Int. Meet. on Small Particles and Inorganic Clusters*, West Berlin, July 9 - 13, **1984**
- [7]. M. D. Morse, *Chem. Rev.*, **1986**, 86, 1049 - 1109
- [8]. A. Henglein, *Chem. Rev.*, **1989**, 89, 1861 - 1873
- [9]. R. Paull, J. Wolfe, P. Hébert and M. Sinkula, *Nat. Biotechnol.*, **2003**, 21, 1144 - 1147
- [10]. H. Goesmann and C. Feldmann, *Angew. Chem. Int. Ed.*, **2010**, 49, 1362 - 1395
- [11]. A. D. Ostrowski, T. Martin, J. Conti, I. Hurt, B. Herr Harthorn, *J. Nanopart. Res.*, **2009**, 11, 251 - 257
- [12]. M. Zhu, G. Nie, H. Meng, T. Xia, A. Nel, and Y. Zhao, *Acc. Chem. Res.*, **2013**, 46, 622 - 631
- [13]. K. Donaldson, F. Murphy, A. Schinwald, R. Duffin and C. A. Poland, *Nanomedicine*, **2011**, 6, 143 - 156
- [14]. K. Donaldson, *Crit. Rev. Toxicol.*, **2009**; 39, 487 - 500
- [15]. K. Donaldson, F. A. Murphy, R. Duffin, C. A Poland, *Part. Fibre Toxicol.*, **2010**, 7:5, 1 - 17
- [16]. T. Xia, Y. Zhao, T. Sager, S. George, S. Pokhrel, N. Li, D. Schoenfeld, H. Meng, S. Lin, X. Wang, M. Wang, Z. Ji, J. I. Zink, L. Mädler, V. Castranova, S. Lin, and A. E. Nel, *ACS Nano*, **2011**, 5, 1223 - 1235
- [17]. J. Liu, D. A. Sonshine, S. Shervani, and R. H. Hurt, *ACS Nano*, **2010**, 4, 6903 - 6913
- [18]. K. Kobayashi, J. Wei, R. Iida, K. Ijiro and K. Niikura, *PJ*, **2014**, 46, 460 - 468
- [19]. A. K. Gupta, M. Gupta, *Biomaterials*, **2005**, 26, 3995 - 4021
- [20]. Lux Research Inc., **2005**, Nanotechnology: Where Does the U.S. Stand?: Hearing Before the Subcomm. on Research of the H. Comm. on Sci., 109th Cong. 1 (statement of Matthew M. Nordan, Vice President of Research)

- [21]. R. J. Aitken, K. S. Creely, and C. L. Tran, **2004**, Nanoparticles: An Occupational Hygiene Review. HSE Books. ISBN: 0-7176-2908-2 www.hse.gov.uk/research/rrhtm/rr274.htm
- [22]. K. Thomas, P. Aguar, H. Kawasaki, J. Morris, J. Nakanishi, and N. Savage, *Toxicol. Sci.*, **2006**, 92, 23 - 32

2. Processing line 1: washing/disposal line (ZrO₂ nanopowder)

2.1 Introduction

2.1.1 ZrO₂ nanomaterials

Different synthetic procedures have been developed and reported in literature to obtain ZrO₂ nanopowders and colloids with desired properties, including sol–gel ^[1,2] and co-precipitation processes ^[3,4], microwave assisted synthesis ^[5, 6], microwave assisted combustion synthesis ^[7], spray pyrolysis ^[8] and two phases route reaction ^[9]. Various properties of ZrO₂ were enhanced by its nanoscale and among these the photocatalytic properties, mechanical resistance, electro-chemical and electro-optical properties, make ZrO₂ one of the most attractive oxides for several applications.

ZrO₂ exhibits photocatalytic activity in many reactions due to its relatively wide E_g value and the high negative value of the conduction band potential ^[10]. The E_g shows a value range between 3.25 and 5.1 eV, depending on the synthetic preparation technique, and the most frequent and accepted value is 5.0 eV ^[1]. ZrO₂ has been widely employed as photocatalyst in different reactions such as the decomposition of water, the reduction of carbon dioxide ^[11], the photodegradation of organic compounds as nitrophenol ^[12] or the exchange of isotopic oxygen ^[13]. Pd over ZrO₂ catalyses the methanol decomposition to carbon monoxide and hydrogen ^[14], while nanocomposite Au/ZrO₂ has been used as catalyst for CO oxidation ^[15].

Due to its high conductivity, long-term durability and high dispersion, ZrO₂ has been employed as solid proton conductor for fuel cell electrodes ^[16]. ZrO₂ possesses adequate chemical and mechanical properties to be an excellent bio-inert ceramic material for medical devices ^[17] especially in those applications that require highly strength and toughness as dentistry ^[18].

For nano ZrO₂ photocatalytic and oxidizing/reducing surface properties are known and considered potentially very interesting, mainly for nano heterogeneous catalysis ^[11, 19]. Furthermore, the high dispersion in aqueous medium of this oxide does it very useful for a lot of different applications, nevertheless make it as well a potentially hazardous material because of the easy mechanism of transport and uptake in aqueous cellular systems.

Especially when applications in medical fields are envisaged, hazardous properties of NMs should be considered. As reported, within toxicological paradigms nano size dimension ^[20], presence of contaminant ^[21], high aspect ratio shape ^[22], redox and acidic/basic properties as well as surface charge ^[23] may influence NMs toxicity.

2.1.2 Description of Processing line 1

PL 1 represents the manufacturing procedure owned by PlasmaChem, that provided ZrO₂ NMs as well as information on synthetic procedure, letting available the industrial scenario for the evaluation and implementation of RRS. PlasmaChem ZrO₂ NPs were synthesized by forced hydrolysis and hydrothermal treatment in acidic environment, starting

from different zirconium (IV) alkoxides, nitric acid and distilled water. The main steps of sol-gel synthetic procedure are reported in figure 1.

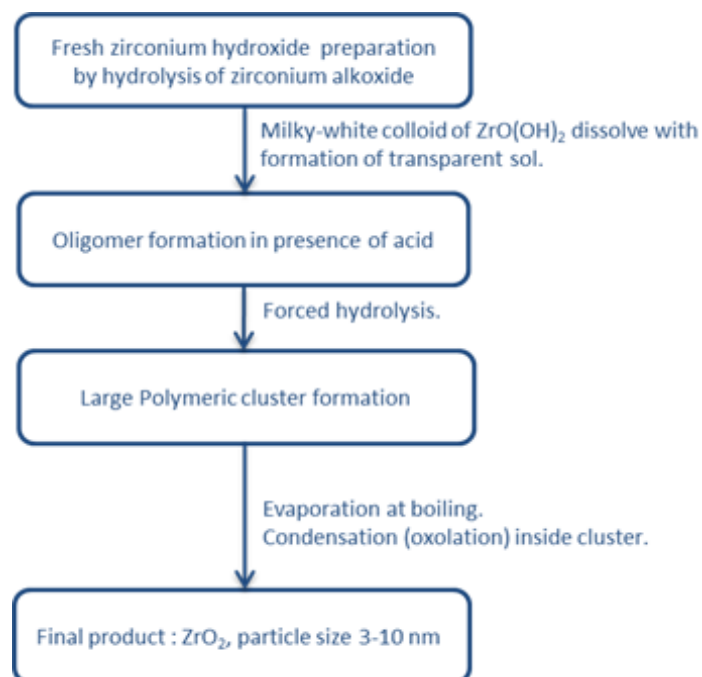


Figure 1 - PlasmaChem synthetic procedure.

Zirconium hydroxide was prepared by a drop-wise addition of zirconium alkoxide to water in a tank. Once formed, Zr(OH)₄ was left to settle down over 1 - 2 h, then the clear supernatant was discarded by decantation and the precipitate washed by distilled water to remove alcohol produced from alkoxide hydrolysis. In a second step, the Zr(OH)₄ suspension was transferred into a round-bottom glass reactor and nitric acid was added. The obtained reaction mixture was left to boil for 24 h, leading to the formation of tetramers or octamers [Zr_xO_y(OH)_(4x-2y)·(x-2y)H₂O, where y > x and x = 4, 8] and their clusters with size > 0.5 nm. The formation of hydrous zirconia colloids during boiling was revealed by the change in solution transparency that turned from an initial milk-like appearance to transparent one. Further removal of ca. 90 % v/v of water by distillation led to the formation of a viscous yellowish suspension, which was then transferred and dried at above 100 °C in an oven. Oxolation reactions proceeded leading to 1 - 2 nm sized particles, with ca. 4.0 g/cm³ density (for comparison, ZrO(OH)₂ density is ca. 3.2 g/cm³). As last step, particles were crystallized for few days at 105 °C. Picnometric density, refractive index and Raman spectra of nanoparticles were checked at 12 h time intervals as monitoring parameters and ZrO₂ aging was ended when the refractive index of particles achieves values of 1.9 - 2.0.

2.1.3 Critical step identified and RRS proposed

A general scheme of the PL 1 was reported in figure 2.

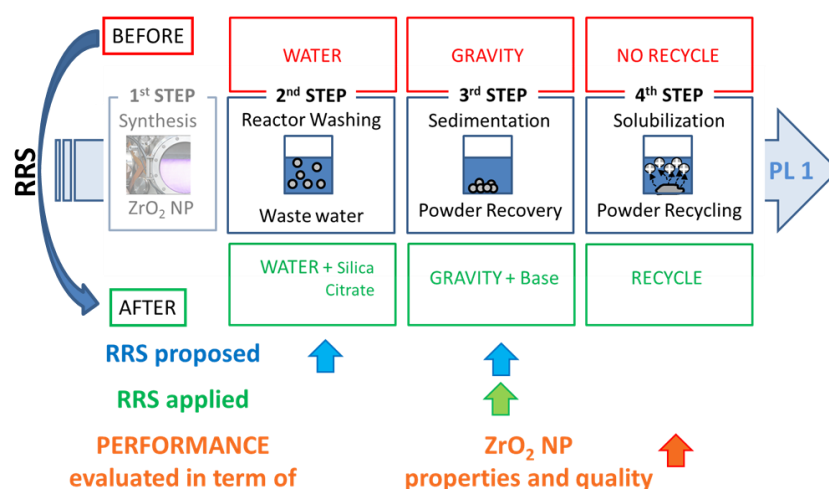


Figure 2 - Scheme of processing line 1, showing process steps in which RRS were applied and evaluated.

Along PL 1, the relevant steps for health hazard and EA were the synthetic reactor washing, the sedimentation and the following waste water disposal and recycle operations. The two scenarios that took shape with the introduction of RRS are defined as BEFORE and AFTER one, in which the RRS were implemented.

2.1.3.1 Reactor washing

The first critical step to be monitored was the washing of the synthesis reactor due to the relevant amount of ZrO₂ stuck on the walls. During this step, the RRS of CFC was proposed to increase the washing efficiency by improving ZrO₂ water dispersion adding stabilizing agents. The introduction of RRS may lead to an higher recovery of ZrO₂ NM produced, with the possibility to perform a recycling procedure. Moreover, from the process point of view, the control of the dispersion state may also be useful for those production steps that require the best degree of powder dispersion. The BEFORE scenario was represented by the washing of the synthesis reactor only by water, while the AFTER scenario was represented by the reactor washing performed by water added of dispersing agent.

2.1.3.2 Sedimentation

The second critical step to be monitored is referred to the sedimentation of ZrO₂ material contained in waste water produced during the reactor washing. ZrO₂ suspensions should be allowed to settle down, to separate supernatant (waste water) from solid sediment that, once formed, has a lower exposure potential. Nevertheless this process requires long times and may not be effective if ZrO₂ particles are stable and do not aggregate, hindering the sedimentation. RRS based on the CFC were proposed to force the sedimentation process and achieve a better sedimentation efficiency that may lead to a faster phases separation, without

ZrO₂ NPs contamination in the supernatant. Moreover, ZrO₂ sediment recovered may be solubilized with mineral acid and employed as inorganic salt precursor for further applications. In the BEFORE scenario, NMs dispersions were let to sediment by gravity, before water discharge; in the AFTER one, the sedimentation by gravity was enhanced varying pH, to obtain a faster and more efficient process.

2.1.3.3. Recycle

The last step considered in PL 1 was the recycle of the ZrO₂ collected after the sedimentation. During this step the introduction of RRS were evaluated taking into account both quality and recycle efficiency of regenerated ZrO₂. The BEFORE scenario was realized through the discarding of the waste water without its regeneration, while the AFTER one was represented by the recycle of the ZrO₂ gel produced applying the RRS in the previous steps, followed by a mineral acid treatments to recover a solution of inorganic precursor that may be employed again for further synthesis.

2.2 Experimental

2.2.1 Preliminary Characterization of ZrO₂ nanopowder

Pristine ZrO₂ NPs, encoded as **ZrO₂_1_NP**, was provided by PlasmaChem and subjected to preliminary characterizations. Powder morphology was at first observed by SEM-FEG (Zeiss Gemini, GE) taking images at different magnifications, using low current acceleration. HR-TEM (JEOL JEM-2100F, USA) was used to assess the presence of a smaller particle fraction as well as to evaluate the presence of a crystalline phase. Crystalline phase was investigated by XRD (D8 ADVANCE, Bruker AXS, GE) and Raman Spectroscopy (Renishaw RM 1000, UK). Thermal behavior was evaluated by thermal analysis (PL-STA 1500, PL Thermal Science, UK).

2.2.2 Application of RRS at lab-scale level

2.2.2.1 Reactor washing

To better disperse pristine ZrO₂ during reactor washing, two different stabilizing agent were tested at lab scale level: a commercial silica colloidal dispersion, Ludox-HS40, and Trisodium Citrate Dihydrate. Samples involved in the simulation of the synthesis reactor washing were described and listed below.

- Pristine ZrO₂ nanosol, encoded as **ZrO₂_2_sol**, was obtained dispersing pristine ZrO₂ powder in distilled water by ultrasonic method. The nominal ZrO₂ concentration of 3 wt.% was chosen in accordance with PlasmaChem to reproduce the typical ZrO₂ concentration in the washing water. This sample represents the BEFORE situation and simulates the ZrO₂ dispersion obtained by reactor washing performed only with water.
- Modified sample, **ZrO₂_7_sil_sol**, was obtained by mixing pristine ZrO₂ nanosol with commercial colloidal SiO₂ (SiO₂/ZrO₂ = 4; total solid concentration 3 wt.%) and then ball milling for 24 h the sample to promote homogenization. This sample represents the AFTER

situation and simulates the ZrO₂ dispersion obtained from the reactor washing performed with water and colloidal silica as dispersing agent.

- Modified sample, **ZrO₂_10_cit_sol** was obtained by mixing pristine ZrO₂ nanosol with Trisodium Citrate Dihydrate (ZrO₂/Citrate weight ratio = 1/0.01; total solid concentration 3 wt.%) and then ball milling for 24 h the sample to promote homogenization. This sample represents the AFTER situation and simulates the ZrO₂ dispersion obtained from the reactor washing performed with water and citrate salt as dispersing agent.
- Modified sample, **ZrO₂_13_cit_sol** was obtained by mixing pristine ZrO₂ nanosol with Trisodium Citrate Dihydrate (ZrO₂/Citrate weight ratio = 1/1; total solid concentration 3 wt.%) and then ball milling for 24 h the sample to promote homogenization. This sample represents the AFTER situation and simulates the ZrO₂ dispersion obtained from the reactor washing performed with water and citrate salt as dispersing agent.

Samples underwent ZP titrations versus pH using an AcoustoSizer (Colloidal Dynamics, AU), equipped with a titrating system that employ 1 M KOH or HCl solutions for pH variations. Samples were analyzed at 3 wt.% concentration and moving the dispersion by means of a peristaltic pump, to achieve sample homogenization.

2.2.2.2 Sedimentation

To force the sedimentation of ZrO₂ NMs both pristine ZrO₂ (ZrO₂_2_sol) or SiO₂ modified sample from previous step (ZrO₂_7_sil_sol) were considered. The ZP vs pH titrations showed that in both cases the colloidal stability decreased towards basic pH. Therefore the sedimentation of samples was forced through base addition. Samples involved in the simulation of forced sedimentation were reported below:

- Pristine ZrO₂ nanosol **ZrO₂_2_sol**, described in the above paragraph.
- Modified sample **ZrO₂_14.2_sol** (composed of ZrO₂_14.2_gel and ZrO₂_14.2_SURN) was obtained by adding NaOH 10 M to ZrO₂_2_sol until pH≈11. **ZrO₂_14.2_SURN** sample was collected by decanting (after 48 h) the supernatant water, while **ZrO₂_14.2_gel** sample was collected from the bottom of the flask. These samples simulates the AFTER situation where the ZrO₂ dispersion to sediment was obtained by washing the reactor with water and then adding a base to force the sedimentation.
- Modified sample **ZrO₂_7_sil_sol**, described in the above paragraph.
- Modified sample **ZrO₂_15_sil_sol** (composed of ZrO₂_15_sil_gel and ZrO₂_15_sil_SURN) was obtained by adding NaOH 10 M to ZrO₂_7_Sil_sol until reaching pH≈11. **ZrO₂_15.2_Sil_SURN** sample was collected by decanting (after 48 h) the supernatant water, while **ZrO₂_15.2_Sil_gel** sample was collected from the bottom of the flask. These samples simulates the AFTER situation where the ZrO₂ dispersion to sediment was obtained by washing the reactor with water plus SiO₂ as dispersing agent and then adding a base to force the sedimentation.

The presence of ZrO₂ in the decanted water measured by XRF (Panalytical Axios Advanced, NL), sedimentation rate were determined from visual observations.

2.2.3 Implementation of RRS within Processing line 1

2.2.3.1 Recycle

Both washing and sedimentation steps previously tested at lab scale level were implemented by PlasmaChem at pilot scale level. Then, a recycling procedure was performed. By this way the introduction of RRS in the PL has been evaluated in terms of quality and improved recycle efficiency of recovered ZrO_2 . To simulate the recycle procedures, the materials used were:

- Pristine ZrO_2 sample, encoded as **ZrO₂_PCHEM_sol** (nominal [ZrO_2] 10 wt.%) represented the BEFORE situation, where the ZrO_2 wasn't recycled.
- Modified samples **ZrO₂_PCHEM_sol_1** and **ZrO₂_PCHEM_sol_2** represent the AFTER situation where the ZrO_2 recycle was performed as follows: Na_2CO_3 0,5 M was added to the wastes containing ZrO_2 nanoparticles (concentration is variable, normally in the range of 0.001-0.05%) until reaching $pH \approx 10-11$ obtaining a gel that (after ca. 1 day) formed a precipitate, which could be easily separated from the supernatant. The supernatant was collected by decantation and discharged (contamination with ZrO_2 is not detected as reported above). One half of the sample was dissolved in a small amount of 65% HNO_3 (sample **ZrO₂_PCHEM_sol_1**), and another half in a small amount of 36% HCl (sample **ZrO₂_PCHEM_sol_2**). The undissolved particles (ca. 1% from the total dry weight) were collected by centrifugations and discarded as chemical wastes. For both batches, the remaining solutions were diluted and hydrolyzed by ammonia yielding zirconium hydroxide, which was further used as a reagent according to the original manufacturing procedure. These samples simulate the after situation where the ZrO_2 recycle was performed starting from a gel and using HNO_3/NH_3 or by HCl/NH_3 to recover the ZrO_2 precursor of the synthesis.

2.2.4 Characterization of ZrO_2 dispersion in biological medium

Samples considered by biologists for toxicological characterizations, described above (pristine **ZrO₂_2_sol** and modified **ZrO₂_7_sil_sol**, **ZrO₂_10_cit_sol** and **ZrO₂_13_cit_sol**), were also subjected to some chemical-physical characterizations performed in "biological conditions". To understand processes occurring during NMs-biological interactions, chemical-physical characterization should be contextualized and, therefore, performed in conditions (timing, temperature, NMs concentration, solvents, pH,...) that closely simulated those of the systems in which NMs will move and react.

Being the dispersion state and stability relevant parameters for the NMs-biological interactions, an investigation on both size and ZP of pristine and modified ZrO_2 NMs dispersed in both deionized water and complete cell culture medium were performed. d_H and ZP were obtained by DLS technique (Zetasizer nano ZSP, UK). The standard operating procedure described hereafter was followed for all samples. ZrO_2 dispersion was ultrasonic treated for 15 min and two set of samples were prepared. For samples dispersed in culture medium, aliquots of ZrO_2 dispersions were first added to BSA/PBS [0.05 %, v/v] to obtain an intermediate which was then added to cell culture medium supplemented with FBS [10 %, v/v] to reach a final ZrO_2 concentration of 125 $\mu g/ml$.

The further set of ZrO₂ samples were prepared diluting, with MilliQ water, up to 125 µg/ml ZrO₂ dispersions. Dispersion were left to equilibrated for 1 h, then were vortex-mixed to ensure samples homogenization before size and ZP measurements. d_H were obtained from DLS data expressed by intensity, in backscattering detection mode (scattering angle of 173 °) and setting measurement duration on automatic. After 2 min of temperature equilibration at 25 °C, 1 ml of sample volume was subjected to three consecutive measurements which were averaged to obtain d_H .

After particle size determination, samples underwent ZP measurement by ELS. The Smoluchowski approximation [24], consistent with the high dielectric constant of water, main component of all above specified solvents, was applied to convert the electrophoretic mobility to ZP. Measurements were performed on 700 µl of sample, measurement duration was set to automatic as well as attenuator position and applied voltage. After 2 min of temperature equilibration, samples underwent five measurements spaced out by 120 sec delay to avoid Joule heating. Before and after ZP analysis, a size measurement was performed to check that the samples have not changed. Analyses of NMs dispersed in cell culture medium were collected in monomodal mode due to the high medium conductivity, thus obtaining a mean ZP value.

2.3 Results and Discussion

2.3.1 Preliminary characterization of ZrO₂ nanopowder

Pristine powder morphology was at first observed by SEM-FEG taking images at different magnifications, using low current acceleration. As shown in figure 3, powder had a broad size distribution being composed by both aggregates of few microns and small nanometers particles.

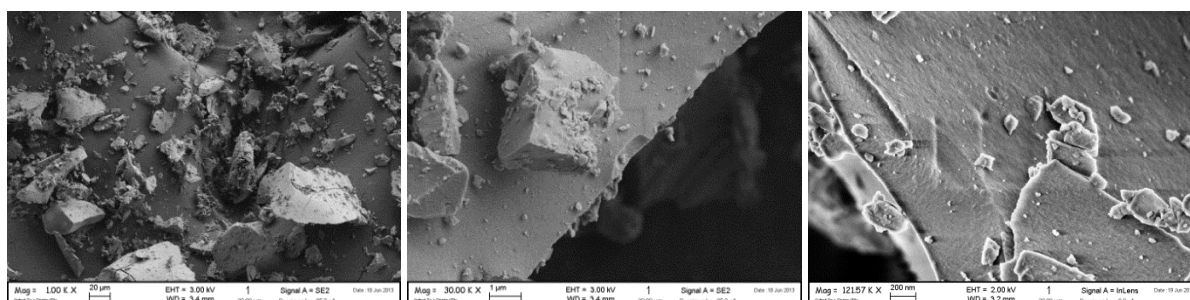


Figure 3 - Pristine powder morphology by SEM-FEG images.

Sample was observed by HR-TEM with a field emission source operating between 80 - 200 kV, figures 4 and 5, to assess the presence of a smaller particles fraction as well as to evaluate the presence of a crystalline phase.

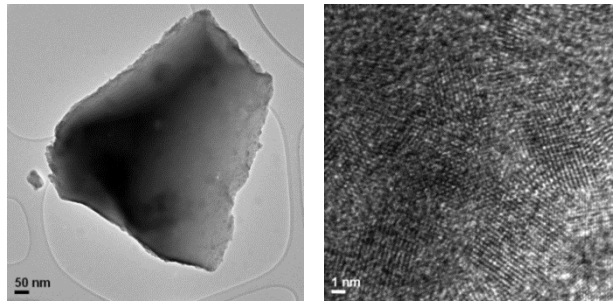


Figure 4 - TEM image of pristine powder (left) and crystalline ZrO₂ phase (right).

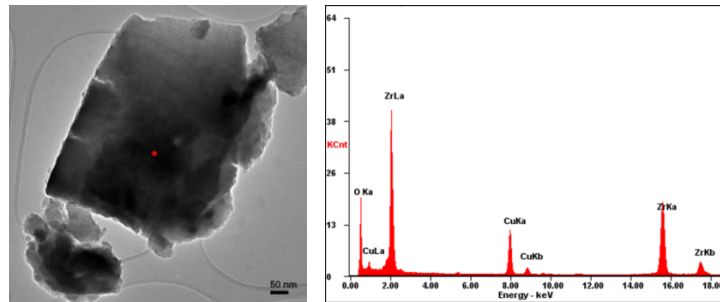


Figure 5 - TEM image with underlined the spot used for EDS determination.

HR-TEM lattice images obtained at different magnifications, confirmed that the presence of a crystalline phase, while the TEM-EDS spectrum obtained by spot mode showed the presence of Zr and O. The crystalline phase of pristine sample was investigated by XRD (Cu K α radiation; 10 - 80 ° 2 θ range, scan rate 0.02 2 θ , 185 s equivalent per step) and the spectra of pristine sample and powders after 1h calcination at 400°C and 1 000° C are reported, from up to down, in figure 6.

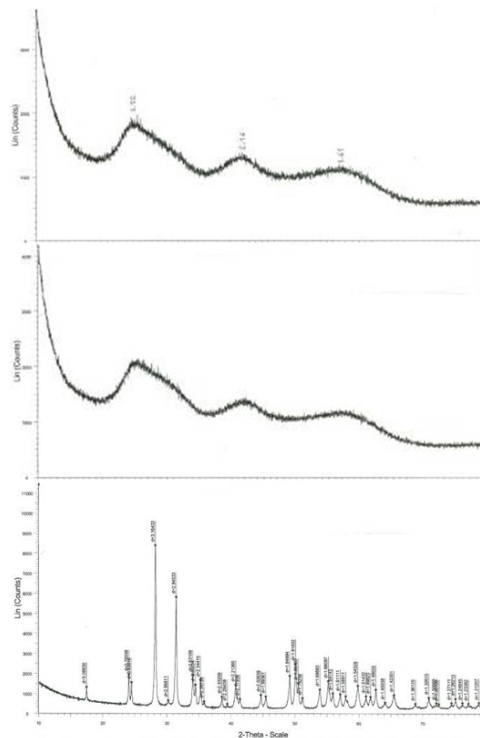


Figure 6 - XRD spectra of pristine sample and powders calcined at 400°C and 1 000°C.

Pristine and calcined (1h at 400°C) powders showed XRD spectra that did not match bulk monoclinic ZrO₂ structure; in fact, only after 1h of calcination at 1 000°C the sample showed the structure of bulk, monoclinic ZrO₂. Pristine sample spectrum showed a broadened diffraction patterns typical of NMs, but hardly comparable with those reported in literature [25], probably due to very small crystallite size. Due to marked peak broadening, it was not possible to calculate the crystallite size, but according to the literature, also Raman spectroscopy may be employed to investigate both crystalline phase [26] and size [25] of NMs. Raman spectrum of pristine sample was obtained using a laser Raman microscope equipped with Argon 514 nm and Diode 785 nm lasers for excitation in the frequencies range 0 – 1 300 cm⁻¹ (Fig. 7).

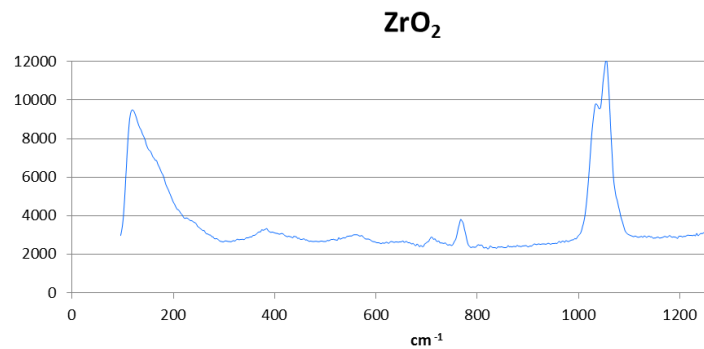


Figure 7 - Raman spectra of pristine zirconia.

Raman spectrum of pristine sample showed the typical features of a nano-sized ZrO₂ material. As previously reported [25], for sample with size under 20 nm, a new Raman peak at 1 035 cm⁻¹ arised attributable to surface vibrational mode, that strengthened and shifted toward higher frequencies (1 050 cm⁻¹) as the grain size decreases up to 5 nm. As further reported, the crystalline size of nano ZrO₂ may be calculated from the intensity 1 050 cm⁻¹/475 cm⁻¹ peak ratio. Exploiting this phenomenon, ZrO₂ NMs yielded a calculated diameter of 2 - 3 nm.

Pristine sample was subjected to DSC/TGA analysis to check the thermal behavior (Fig. 8).

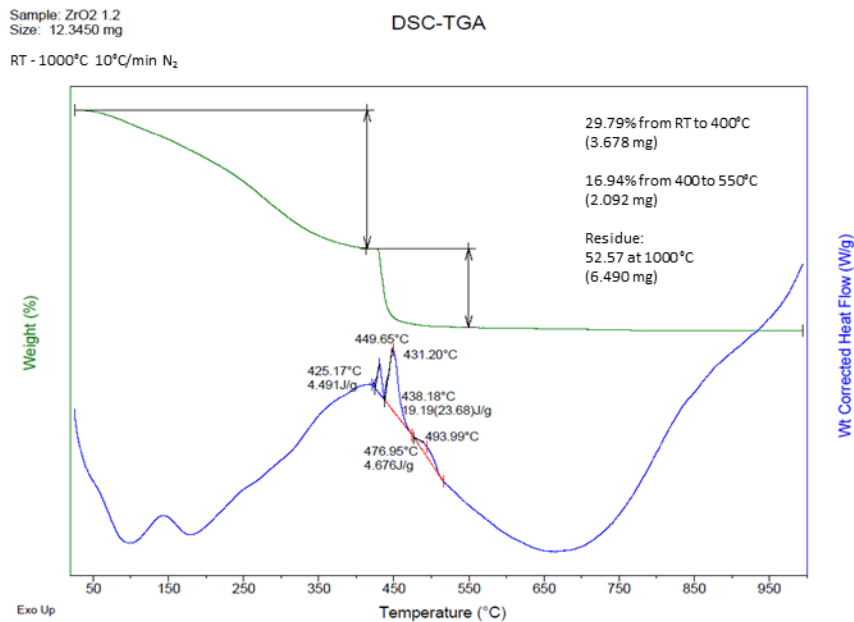


Figure 8 - DSC-TGA analysis of pristine ZrO₂ powder.

Figure 8 showed a slow weight loss of ca. 30 wt.% up to 400 °C, then in the temperature range 400 - 500 °C, the sample lost ca. 17 wt.%; this weight lost was associated with two exothermic peaks probably due to the nitrate thermal decomposition. Heating the sample until 1 000 °C, it was detected a further weight loss of 47 wt.%, with a residue of ~ 53 wt.%.

2.3.2 Application of RRS at lab-scale level

2.3.2.1 Reactor washing

The washing procedures efficiency was related to the ZrO₂ colloidal dispersion stability, evaluated in term of ZP. Actually, it is a general rule of thumb that an absolute ZP value above 60 mV yields an excellent stability, above 30 results in a good stability, above 20 an acceptable short term stability and a value less than 5 mV generally leads to particle aggregation and phase separation [27]. There are two fundamental mechanism that affect dispersion stability: the steric and electrostatic stabilization. Steric repulsion usually involves the use of polymers that, adsorbing on the particle surfaces, avoid their close contact and prevent agglomeration and/or aggregation phenomena. Electrostatic stabilization is achieved adding charged molecules or ions that modify the particle interaction, due to the distribution of charged species in the system. Each mechanism presents advantages and disadvantages; polymers used in steric stabilization provided the best effect, but may be expensive. Generally, their adsorption on the surfaces is an irreversible process and, thus, it is difficult to subsequently destabilize the system if required. Thus, for these reasons, their use are limited to those applications in which the presence of polymer does not affect the final product properties.

The electrostatic or charge stabilization, involving an alteration of the ions in solution, may be potentially inexpensive, reversible and moreover it may be used both to stabilize and destabilize the system.

To simulate the reactor washing, two different dispersing agents, colloidal SiO₂ and Trisodium Citrate Dihydrate, were employed exploiting, respectively, steric and electrostatic stabilization. Table 1 reported some of the characterizations performed on sample involved in the simulation of reactor washing.

Table 1 - Characterization data for the samples involved in the introduction of RRS in PL 1.

Sample code	pH	[ZrO ₂] wt.% (nominal)	Dispersing agent/ZrO ₂ weight ratio	Z potential ² [mV]	Isoelectric point (IEP)
ZrO ₂ _2_sol	1.62	3.00	-	+ 50	No, positive
ZrO ₂ _7_sil_sol	2.44	0.60	4	+ 164	5.04
ZrO ₂ _13_cit_sol	6.53	3.00	1	-32.8	No, negative

¹ Measures performed at pH reported

Pristine and modified samples were subjected to ZP vs pH titration and the curves obtained were compared to identify the pH region in which the ZrO₂ dispersion was improved (ZP ≥ ± 50 mV in comparison to the pristine sample) or in which the system destabilization occurred (around IEP). Figure 9 showed the ZP vs. pH titration curves of pristine and modified samples.

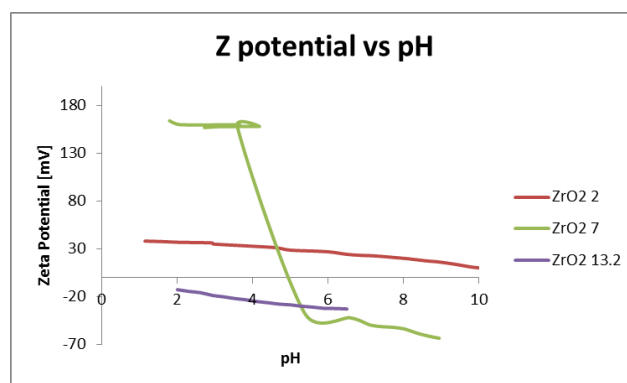


Figure 9 - ZP versus pH titration curves for the different ZrO₂ samples

Pristine sample ZrO₂_2_sol gave rise to a translucent, stable dispersion at acid pH (ZP >30 mV at pH < 5), while at higher pH values dispersion started to destabilize, forming a gel network at pH > 8. SiO₂ modified sample, ZrO₂_7_sil_sol, was a whitish, stable dispersion in the range 3 < pH < 7 (ZP > 100 mV for pH < 3 and ZP > 50 mV for pH > 7), while in the range 4 < pH < 7 the dispersion reach the IEP and solid material dispersed, started to aggregate and precipitate. Citrate modified sample, ZrO₂_13_cit_sol, was a translucent with a good stability in pH range taken into account (Z potential ~ -30 mV for pH 2 to 7), showing no IEP.

According to the data obtained, pristine ZrO₂ was really water-dispersible and stable, also without any dispersant. The addition of an unnecessary dispersing agent represented a

useless extra cost and may negatively affect the following steps. On other hand, modified materials may result less toxic respect to the pristine one and, from data obtained, SiO₂ addition improves the ZrO₂ dispersion stability. Thus, it was decided to study next sedimentation step employing both pristine and SiO₂ modified samples.

2.3.2.2 Sedimentation

To force the sedimentation process, colloidal dispersion was destabilized by means of pH variation towards sample IEP. Basing on ZP vs pH measurements, the pH region for destabilization and gel formation was identified and sedimentation rates were compared for both pristine and modified samples. After phase separation (Fig. 10) the amount of precipitate was evaluated and the presence of ZrO₂ in the decanted water measured by XRF.

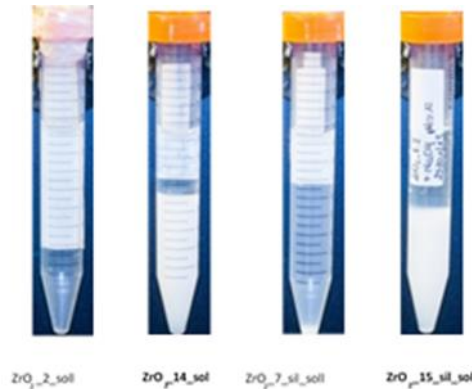


Figure 10 - Picture of the samples involved in the sedimentation study.

Table 2 - Characterization data of the samples involved in the sedimentation study.

Sample Code	[ZrO ₂] wt.% (nominal)	[ZrO ₂] wt.% (XRF)	pH	ZP [mV]	Sedimentation rate [h]
ZrO ₂ _2_sol	3.00	1.88	1.6	+ 50	>168
ZrO ₂ _14_gel	3.00	-	11	+ 10*	48
ZrO ₂ _14_SURN		0.00			
ZrO ₂ _7_sil_sol	0.60	0.33	2.4		>168
ZrO ₂ _15_sil_gel	0.60	-	11	-70*	48
ZrO ₂ _15_sil_SURN		0.00			

*ZP measurement performed on the sample before liquid from solid separation

The aim of the sedimentation process was the separation of the solid-rich phase from the decanted waste-water. To evaluate the efficiency of RRS, two parameters were considered: the material sedimentation rate and the purity of the decanted waste water (samples supernatant).

Pristine sample ZrO₂_2_sol was a very stable dispersion at pH = 1.6 obtained using water as solvent; in this condition the dispersion formed a very small amount of precipitate only after a week (168 h). Thus it was impossible to measure the sedimentation rate of pristine material as well as the purity of the supernatant obtained. ZP of modified samples ZrO₂_14_sol

was measured just before gel formation; liquid was let to separate and precipitate to sediment. The formation of a compact precipitate, that facilitate the separation of waste water, was considered for sedimentation rate determination. ZrO₂ in precipitate samples (ZrO₂_14_gel) was about 6 wt.%. ZrO₂_14_SURN sample, that represent the decanted waste water, was analyzed by XRF and no ZrO₂ was identified (detection limit about 10 ppm), obtaining a clean decanted waste water. Modified sample ZrO₂_15_sil_sol was treated as the previous one showing comparable sedimentation rate and obtaining a good phase separation. ZrO₂ in precipitate material (ZrO₂_15_sil_gel) collected was about 7 wt.%, also in this case was not found any ZrO₂ contamination in the supernatant.

Once ZrO₂ sediment was collected, it was studied the possibility to solubilize it using a mineral acid and recover a solution of inorganic salt precursor, that may be recycled for further applications. Considering the possibility to recycle the precipitate material, ZrO₂_14_gel sample was selected, because of the possibility to obtain a ZrO₂ without a further purification step that may be required for ZrO₂_15_sil_gel sample that contained also SiO₂. It was so decided to integrate silica coating strategy only if the results of toxicological characterization may justify the presence of a less toxic NMs.

2.3.3 Implementation of RRS within Processing line 1

2.3.3.1 Recycle and quality of ZrO₂ nanopowder

The recycling procedures was aimed to obtain, after the introduction of the RRS, a ZrO₂ material with the same properties of the ZrO₂ produced using the PlasmaChem manufacturing procedures. This objective was used to evaluate process and product performances. In table 3 were reported some data referred to both pristine and modified materials.

Table 3 - Characterization data of the samples involved in the introduction of the RRS.

Sample Code	[ZrO ₂] wt.%	pH	Hydrodynamic diameter [nm] ¹	Refractive index	Loss on tempering at 900 °C ² [wt.%]
ZrO ₂ _PCHEM	10	≈ 1	2.4	1.9	36.7
ZrO ₂ _PCHEM_sol_1	10	≈ 1	2.4	1.9	33.4
ZrO ₂ _PCHEM_sol_2	10	≈ 1	3.8	1.9	32.7

¹ by number ; ² for 30 min

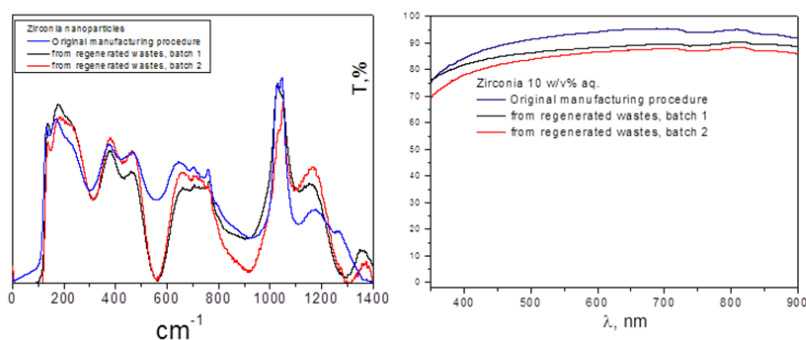


Figure 11 - Raman and optical spectra of ZrO_2 particles obtained from wastes; the blue line represented the pristine sample $ZrO_2_PCHEM_sol$, while the black and red line represented the $ZrO_2_CHEM_sol_1$ and $ZrO_2_PCHEM_sol_2$, respectively.

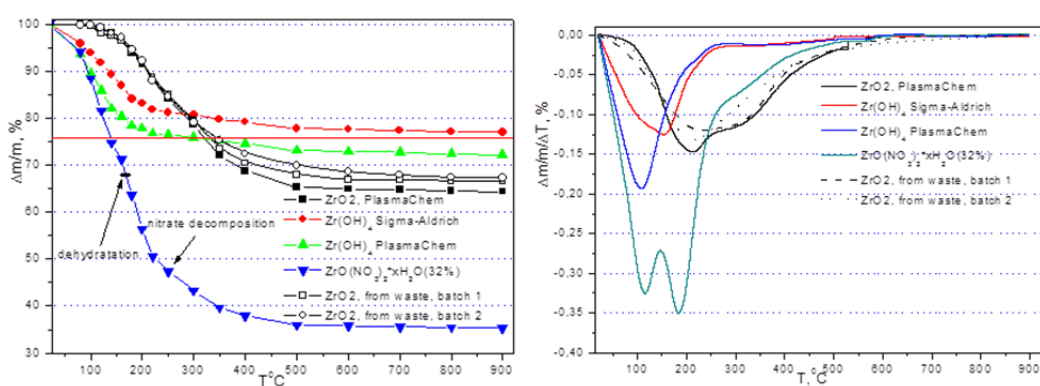


Figure 12 - TG (left) and DTG (right) analyses of ZrO_2 NMs obtained from zirconium wastes.

Figure 11 reported the Raman and optical spectra of the three ZrO_2 samples in order to compare their properties. The parameters of crystallographic structure, optical transparency and refractive properties were of primary importance for this material, which was used in optical applications. Raman spectra indicate a monoclinic structure of the nanoparticles [26]: peaks at ca. 110 cm^{-1} , 181 cm^{-1} , $380 - 475\text{ cm}^{-1}$ and $615 - 760\text{ cm}^{-1}$ and especially that at 1050 cm^{-1} , evidenced the presence of particles of crystalline size below 20 nm [25]. The relatively low intensity and broadening of the peaks were typical for NMs. The intensity $1050\text{ cm}^{-1}/475\text{ cm}^{-1}$ peak ratio may be used to calculate the crystallite size, that in case of these particles yielded to a calculated diameter of $2 - 3\text{ nm}$. This value correlated very well with DLS mean diameter for all three samples. By comparison of the spectra reported, the use of HNO_3 during reagent regeneration delivered slightly better results than HCl .

Figure 12 showed the TG analysis of PlasmaChem ZrO_2 , of ZrO_2 synthetic precursors as $Zr(OH)_4$ and $ZrO(NO_3)_2 \cdot xH_2O$ and of ZrO_2 samples obtained after the recycling procedures. To better detect the weight losses of the different zirconia samples, the TG curves were differentiated obtaining the DTG ones. Few peaks in DTG curves appeared at about 100°C , $150 - 200^\circ\text{C}$ and $300 - 350^\circ\text{C}$. The first two peaks may be associated with the loss of water and the third one to the elimination of nitrates. Weight loss above $400 - 450^\circ\text{C}$ dealt with crystallization

and crystal growth. From curves obtained, the samples prepared from zirconia waste displayed a thermal behavior comparable with that of original ZrO₂ particles.

2.3.4 Toxicity outcomes

An important parameter to evaluate the health hazard reduction following the introduction of RRS was the toxicity of pristine and modified NMs towards cells. Cell lines employed have been chosen by biologists in relation to involved industrial scenario and NMs application. In all processing lines the exposure was supposed to occur mainly via inhalation, thus for viability and cytotoxicity tests, two cell lines were selected: A549 and RAW 264.7 cells, alveolar epithelial cells and macrophages, respectively. Both cell types were typically encountered by NMs upon inhalation and their interaction determined the biological outcome of the exposure. As a result of prolonged exposure to nanomaterial, genotoxicity tests were performed with Balb/3T3 cells, mouse embryonic fibroblasts. Samples considered in the reactor washing step, pristine **ZrO₂_2_sol** and modified **ZrO₂_7_sil_sol**, **ZrO₂_10_cit_sol**, **ZrO₂_13_cit_sol** samples, were in-vitro tested by biologists partners of SANOWORK EU project. ZrO₂ materials, along the range of dose tested (1.25 to 80 µg/cm²), exerted no or low toxicity towards epithelial cells A549, as shown in figure 13.

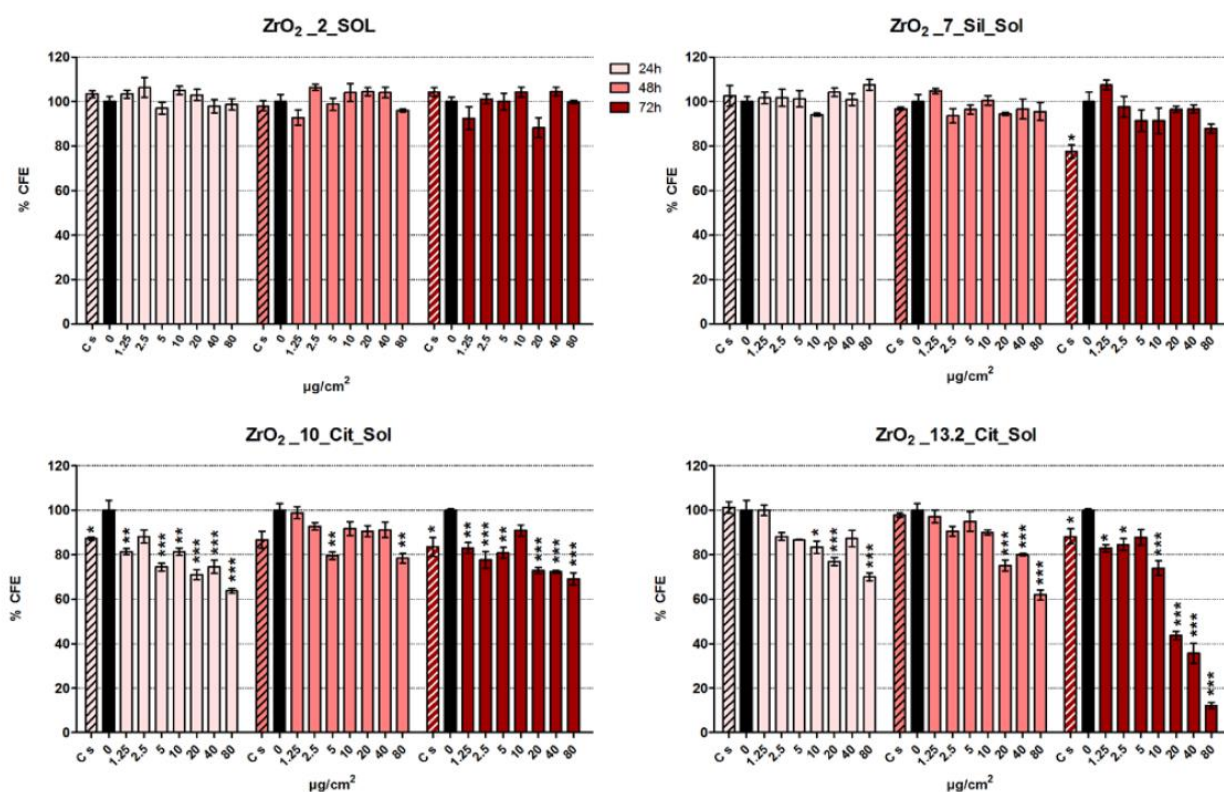


Figure 13 - Cell viability, measured by CFE assay, in A549. Cells were exposed for 24, 48 and 72 h to increasing concentrations (1.25 - 80 µg/cm²) PL 1 ZrO₂ NM. Data are presented as mean % CFE normalized to the untreated control (C-; black bar) ± standard error of the mean (SEM), n = 9. * p < 0.05, ** p < 0.01, *** p < 0.001. C+: 1µM Na₂CrO₄ that induced 0 % CFE (data not shown).

In addition, oxidative stress, an imbalance between anti-oxidant and oxidant in cells, and pro-inflammatory activity were taken into account in the toxicity evaluation. Oxidative stress determined in cell free conditions suggested that ZrO₂ NMs were not able to self-generate ROS. By contrast, in epithelial cells, pristine material significantly induced oxidative stress and ZrO₂_10_Cit_Sol slightly increased it. Nevertheless, no cell lipid peroxidation, another effect of oxidative stress, were evidenced after incubation with ZrO₂ NMS. Pro-inflammatory activity, assessed as increase in NO production by macrophages, was significant, although modest, in both pristine and modified ZrO₂ NMs.

To investigate the effect of prolonged exposure to nanomaterial, genotoxicity tests were performed with Balb/3T3 cells. From results obtained all ZrO₂ samples induced comparable genotoxicity in vitro. Taking into account the carcinogenic potential, high doses of modified ZrO₂_10_cit_sol and ZrO₂_13_cit_sol samples showed more severe effects than pristine and silica modified ZrO₂_7_sil_sol ones, but the presence of silica seemed to protect Balb/3T3 from morphological transformation, characteristic of tumorigenic cells.

To discriminate between NMs and other components contribution to genotoxicity, solvent control experiments ^[28] were performed, filtering out NMs from solvent and testing only the latter toward cells. Despite NMs were removed from samples to be tested, they showed genotoxic and carcinogenic effect, suggesting that observed genotoxic potential might not be due exclusively to NMs, but also to their solvent that may contain “toxic contaminants”. From the toxicological data reported here, the toxicity of pristine NM was comparable with those of modified ZrO₂ samples, obtained following RRS application. Therefore RRS of CFC through the employ of stabilizing agent as colloidal silica or sodium citrate, were not able to decrease ZrO₂ NM toxicity, only maintaining the NM toxicological profile.

2.3.5 Characterizations of ZrO₂ in biological medium

A further goal was to find a relationship between toxicological response and chemical-physical property (as size and ZP) of NMs such as tested in biological systems. Table 4 showed the results of wet state characterizations (pH, ZP and mean d_H by intensity) of pristine ZrO₂_2_sol, and modified ZrO₂ samples ZrO₂_7_sil_sol, ZrO₂_10_cit_sol and ZrO₂_13_cit_sol, dispersed in deionized water and complete culture medium, at 125 µg/ml.

Table 4 - ZP, mean diameter and Pdl of ZrO₂ samples and P25 dispersed at 125 µg/ml in deionized water and complete culture medium. Data in italics, of not sufficiently good quality, were reported only to establish a general trend.

Sample Code	MilliQ water				MEM			
	pH	ZP (mV)	d _H (nm)	Pdl	pH	ZP (mV)	d _H (nm)	Pdl
ZrO ₂ _2_sol	3,6	41.0	261	0.36	7.4	-10.9	1 376	0.84
Std. Dev.		2.0	79	0.08		0.4	460	0.28
ZrO ₂ _7_sil_sol	4,6	40.4	276	0.38	7.5	-10.2	172	1.00
Std. Dev.		1.8	85	0.08		0.4	3	0.00
ZrO ₂ _10_cit_sol	3,4	40.3	83	0.76	7.3	-10.9	1 713	0.79
Std. Dev.		2.7	32	0.22		0.3	236	0.20
ZrO ₂ _13_cit_sol	6,5	-47.0	173	0.39	7.4	-11.1	36	0.47
Std. Dev.		0.0	13	0.08		0.1	0	0.00
P25	4,1	37.4	286	0.30	7.7	-11.5	468	0.44
Std. Dev.		0.9	4	0.04		0.3	16	0.02

For most of ZrO₂ samples investigated, in both solvents, it was impossible to obtain sound size data due to samples polydispersity and the presence of large, settling particles during the analyses. These size data suggested poor samples stability and presence of aggregation phenomena at investigated conditions. Only ZrO₂_13_cit_sol, upon dispersion in culture medium, showed good quality data; its DLS graph by intensity showed two peak at 11 nm and 73 nm diameter size, the relative abundance of which, from the particle size distribution by volume, was respectively 97 % and 3 %. Comparing pristine and citrate modified samples, the presence of citrate in ZrO₂_13_cit_sol seemed to prevent ZrO₂ from aggregation in biological media. The ZP of all the samples in water were, as absolute value, higher than 40 mV, that stated a good colloidal stability. ZrO₂ samples dispersed in medium showed lower stability than in water and their ZP levelled off at values of -10/-11 mV. This levelling effect may be related to protein adsorption on NM surface or to PC formation, being ZP measured close to the values of serum proteins at the same pH. The observed ZP encouraged to investigate other parameter inherent to NMs-biological interactions, such as quantity, identity and secondary structure of adsorbed proteins, that may be related to the presence of designed surface modification and toxicity exerted by NMs [29].

2.3.6 Exposure assessment: on-site measurements

Being inhalation one of the main way of exposure to NMs, in all processing lines the EA were focused on contamination by NMs in air. EA started from a "basic measurement campaign" within PL 1 to verify the exposure to NMs during the steps supposed to be critical. Measurements were carried out in PlasmaChem workplace, during different process operations like as the transport of a ZrO₂ suspension in the laboratory or the handling of final ZrO₂ powder under the fume hood. The instruments used were the CPC and the TEM grid sampler system. The CPC were used between main potential sources and outlets, to determine, in real time the total particle concentration in number, from 10 nm down to one μm. The TEM grid sampler used was used to measure particles near to the respiratory system; in this instrument, through a sampling pump, particles were sampled on specific TEM grids, which were observed.

Measurement of the background ambient aerosol was performed before to start with the tests during process operations, to discern for the specific contributions by the process to air pollution. For background, due to maintenance operation on the air handling system, the concentration in number measurement were not analyzed being the particle concentration fluctuations probably affected by changes in the air system. Thus, only results from microscope image analysis were taken into account. From sampling grids used during background measurement, different particle sizes were observed (Fig. 14).

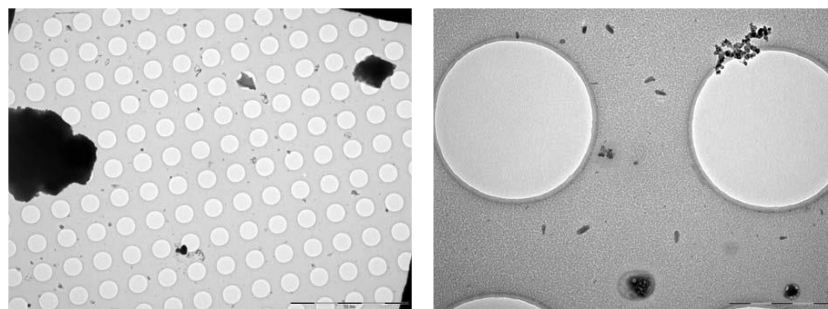


Figure 14 - Photos of grid during background measurement, sampling from fume hood containing the sol-gel reactor

From the data reported, particles larger than 1 μm (left) were composed by the chemical elements characteristic of construction materials. Around a half of the population in the 0.1 - 1 μm range were find to be soot (right photo, particles in the top right) and an high number of particles degraded under microscope beam. From EDS analyses, small particles were composed mainly by carbon, calcium, sodium and silicium. No particle containing zirconium were detected in the grid analysis. Data obtained showed that ZrO₂ handling under the fume hood and transport of ZrO₂ suspension in the laboratory did not influence NM concentration in number, as recorded by CPC. The EDS analyses of material collected on the grids used during sampling confirmed the absence of ZrO₂ NMs.

2.3.7 Cost/benefit analysis

For PL 1, a qualitative cost/benefit analysis was carried out by UL in collaboration with partners involved in SANOWORK project. Table 5 show hazard, exposure, toxicity and associated cost data in relation to the reactor washing, sedimentation and recycling operation. Exposure data were taken from the measurement campaign carried out by INERIS, while toxicity data derived from the tests performed by biologists. ZrO₂ properties, production time and costs were evaluated together with the partner PlasmaChem.

Table 5 - Toxicity, exposure and risk data and remediation costs for the step considered in PL1.

Involved step	Manufacturing	Reactor washing		Sedimentation	Recycling
Sample Code	ZrO ₂ _2_sol	ZrO ₂ _7_sil_sol	ZrO ₂ _13_cit_sol	ZrO ₂ _gel	ZrO ₂ _PChem
RRS	None, unmodified CNT	SiO ₂ blending	Citrate coating	Control of colloidal forces	-
Exposure	Human exposure low because the NPs are in a wet form	Human exposure low because the NPs are in a wet form	Human exposure low because the NPs are in a wet form	-	Reduced environmental exposure since the waste water has been cleaned and ZrO ₂ recovered
Toxicity	Similar to reference material P25	No influence on the toxicological profile	Higher effects both in terms of oxidative stress and NO production	-	-
Functional Change	None by definition	-	-	None	None
Cost [KWh/Kg]	674	-	-	-	627
Production Time [h/Kg]	2.7-4.4	No significant impact on washing efficiency in terms of ZrO ₂ dispersion in wastewater		5, together with clear waste water after sedimentation with positive environmental impact	1.2

For processing lines 6, the RRS targeted on the reduction of wastes production during manufacturing of ZrO₂ has been developed and successfully implemented at pilot scale, achieving a reduction of production self cost by 7 %. Moreover RRS application resulted to lower both the production times and costs without affecting the ZrO₂ quality and properties.

2.4 Conclusions

Technological, safety and economics aspects were taken into account to evaluate the RRS effectiveness. RRS of CFC were applied on ZrO₂ NMs during different process steps and implemented at pilot-scale level. The reactor washing and ZrO₂ sedimentation steps were improved by the application of RRS as demonstrate by faster and higher ZrO₂ recovery, further obtaining clean waste water. The introduced recycling step gave a ZrO₂ NM with quality and properties comparable with those of ZrO₂ produced by the original manufacturing procedure, achieving a reduction of wastes quantity, production time and cost.

To evaluate an health hazard potential mitigation due to RRS application, pristine and modified samples toxicity were evaluated and compared. From in vitro tests, all ZrO₂ NMs exerted no or low cytotoxicity, slight oxidative stress and modest pro-inflammatory activity. Moreover, ZrO₂ samples and their respective solvent controls induced genotoxic and carcinogenic effect, suggesting a genotoxicity for both solvents and dissolved materials. On the basis of the results obtained, tested RRS did not seem to influence the toxicological profile of pristine ZrO₂ NMs. To find a relationship between toxicological response and NM chemical-physical properties, size and ZP of ZrO₂ NMs were investigated in “biological condition”. Size data sowed aggregation and destabilization in biological medium, with the exception of ZrO₂_13_cit_sol sample. The ZP levelling, which underwent samples after dispersion in cell culture media, suggested the formation of PC.

In term of exposure, no ZrO₂ NM contamination in air, either in the background or during the considered process steps, were found in a basic measurement campaign. The sol-gel synthesis procedure prevent worker from ZrO₂ NM inhalation, which may occur when the final product was dried and handled without the proper engineering control measures.

2.5 References

- [1]. J.A. Navìo, M.C. Hidalgo, G. Colòn, S. G. Botta, and M. I. Litter, *Langmuir*, **2001**, 17, 202 - 210
- [2]. M. Mizuno, Y. Sasaki, S. Lee, and H. Katakura, *Langmuir*, **2006**, 22, 7137 - 7140
- [3]. J. Duh, H. Dai, W. Hsu, *J. Mat. Sci.*, **1988**, 23, 2786 - 2791
- [4]. H. Armendàriz, M. A. Cortes, I. Hernández, J. Navarrete and A. Vázquez, *J. Mat. Chem.*, **2003**, 13, 143 - 149
- [5]. J. Liang, Z. Deng, X. Jiang, F. Li, and Y. Li, *Inorg. Chem.*, **2002**, 41, 3602 - 3604
- [6]. N.T. Kalyana Sundaram, T. Vasudevan, A. Subramania, *J. Phys. Chem. Solids*, **2007**, 68, 264 - 271
- [7]. N. C. Sagaya Selvam, A. Manikandan, L. J. Kennedy, J. J. Vijaya, *J. Colloid Interf. Sci.*, **2013**, 389, 91 - 98
- [8]. P. Murugavel, M. Kalaiselvam, A. R. Raju and C. N. R. Rao, *J. Mat. Chem.*, **1997**, 7, 1433 - 1438
- [9]. N. Zhao, D. Pan, W. Nie, and X. Ji, *J. Am. Chem. Soc.*, **2006**, 128, 10118 - 10124

- [10]. F. Juillet, F. Lecomte, H. Mozzanega, S. J. Teichner, A. Thevenet and P. Vergnon, *Faraday Symp. Chem. Soc.*, **1973**, 7, 57 - 62
- [11]. K. Sayama and H. Arakawa, *J. Phys. Chem.*, **1993**, 97, 531 - 533
- [12]. N. Assi, A. A. Mehrdad Sharif, Q. S. Manuchehri Naeini, *Int. J. Nano Dimension*, **2014**, 5, 387 - 391
- [13]. D. Martin and D. Duprez, *J. Phys. Chem.*, **1996**, 100, 9429 - 9438
- [14]. Y. Matsumura, M. Okumura, Y. Usami, K. Kagawa, H. Yamashita, M. Anpo and M. Haruta, *Catal. Lett.*, **1997**, 44, 189 - 191
- [15]. X. Zhang, H. Wang, and B. Xu, *J. Phys. Chem*, **2005**, B109, 9678 - 9683
- [16]. S. Tominaka, N. Akiyama, F. Croce, T. Momma, B. Scrosati, T. Osaka, *J. Pow. Sources*, **2008**, 185, 656 - 663
- [17]. J. Chevalier, L. Gremillard, *J. Eur. Ceram. Soc.*, **2009**, 29, 1245 - 1255
- [18]. P. F. Manicone, P. Rossi Iommetti, L. Raffaelli, *J. Dentistry*, **2007**, 35, 819 - 826
- [19]. Y. Nakano, T. Lizuka, H. Hattori, K. Tanabe, *J. Catal.*, **1979**, 57, 1 - 10
- [20]. G. Oberdörster, J. Ferin, and B. E. Lehnert, *Env. health persp.*, **1994**, 102, 173 - 179
- [21]. K. Donaldson, D. M. Brown, C Mitchell, M Dineva, P. H. Beswick, P. Gilmour, and W. MacNee, *Env. health persp.*, **1997**, 105, 1285 - 1289
- [22]. Dufresne, M. Harrigan, S. Massé, R. Bégin, *Am. J. Ind. Medicine*, **1995**, 27, 581 - 592
- [23]. Nagy, A. Steinbrück, J. Gao, N. Doggett, J. A. Hollingsworth, and R. Iyer, *ACS Nano*, **2012**, 6, 4748 - 4762
- [24]. M. Smoluchowski, *Ann. Phys.*, **1906**, 21, 756 - 780
- [25]. G. G. Siu, M. J. Stokes, Y. Liu, *Phys. Review B*, **1999**, 59, 3173 - 3179
- [26]. A. Martim, J. C. Poignet, J. Fouletier, M. Allibert, D. Lambertin, G. Bourgès, *J. Appl. Electrochem.*, **2010**, 40, 533 - 542
- [27]. P. R. Mishra, L. Al Shaal, R. H. Müller, C. M. Keck, *Int. J. Pharm.*, **2009**, 371, 182 - 189
- [28]. R. Coradeghini, S. Gioria, C. P. García, P. Nativo, F. Franchini, D. Gilliland, J. Ponti, F. Rossi, *Toxic. Lett.*, **2013**, 217, 205 - 216
- [29]. Lynch, K. A. Dawson, *Nanotoday*, **2008**, 3, 40 - 47

3. Processing line 2: ceramic process line (ZrO₂ nanopowder)

3.1 Introduction

3.1.1 ZrO₂ nanomaterials

Different synthetic procedures have been developed and reported in literature to obtain ZrO₂ directly in form of NPs, like spray pyrolysis^[1], microwave assisted combustion^[2] and gas-solid reaction^[3, 4]. In other procedures, particles are obtained by different wet synthetic routes, separate by precipitation^[5], filtration^[6] or centrifugation/decantation^[7] and then dried, to obtain the NMs in form of powder.

Main ZrO₂ applications have been reported in chapter 2, whereas further applications were proposed recently. ZrO₂ thin film was deposited on different substrates, to confer them hardness^[8] photoluminescence^[9] and optical properties^[10]. ZrO₂-polystyrene hybrid nano composite was recently investigated as adsorbents for lead in environmental application^[11]. In ceramic field, nano ZrO₂ was mainly employed as bio-inert component for medical devices^[12], but it was also used to synthesize coloring pigment for ceramic glazes^[13, 14].

3.1.2 Description of Processing line 2

PL 2 is a process that employ ZrO₂ NMs provided by PlasmaChem for ceramics applications. This processing line were reproduced at lab-scale level by CNR-ISTEC, that provided information on experimental procedure and set-up. The main steps involved in the production of ceramic bodies are reported in figure 1.

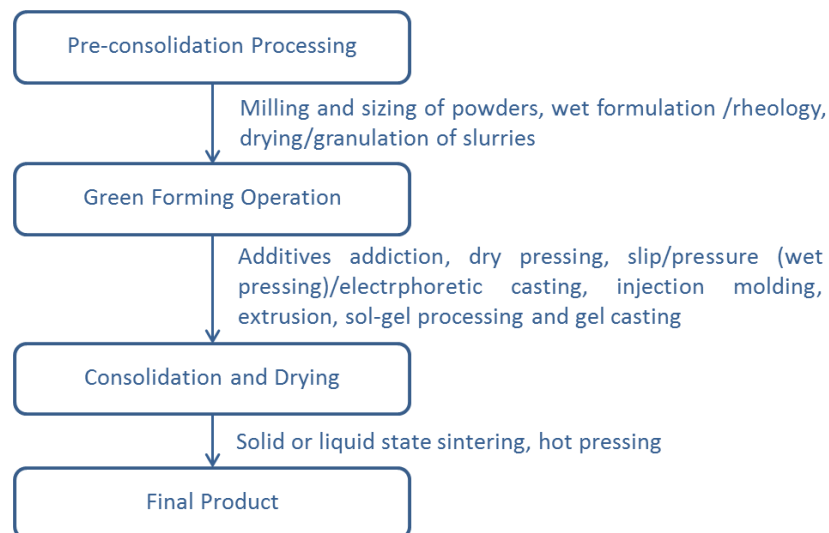


Figure 1 - Main steps in the production of ceramic bodies.

The manufacturing of a ceramic products may be summarized in three main steps: i) pre-consolidation processing, ii) green forming and iii) consolidation. During pre-consolidation, materials are treated to provide specific properties to final ceramics and to

obtain a suitable materials for the next forming operations. Milling and sizing were employed to decrease average particle size and shrink particle size distribution of ceramic powders. In wet formulation, slurry dispersion state and composition were defined by adding proper amount additives, plasticizer and binders. In the following step, slurry obtained was dried using different techniques, forming powders by decantation/filtration/centrifugation and drying them in an oven, by freezing or by spray drying. The latter was both a drying and granulation process, and was widely diffused due to the good control of powder quality standards, as particle size distribution and shape, residual moisture content and bulk density.

In green forming, ceramic materials were formed to obtain desired near net shape before densification. Before forming, other specific additives were added. Then powders were dry pressed and the slip, a blend of powders and additives, subjected to slip casting, wet pressing, freeze casting, injection molding or extrusion processes. Hot consolidation was achieved by firing at high temperature the shaped green body; during this step solid or liquid state sintering and hot pressing were the most commonly employed techniques. Following consolidation a rigid, finished product was obtained [15].

3.1.3 Critical step Identified and RRS proposed

A general scheme of the PL 2 is reported in figure 2.

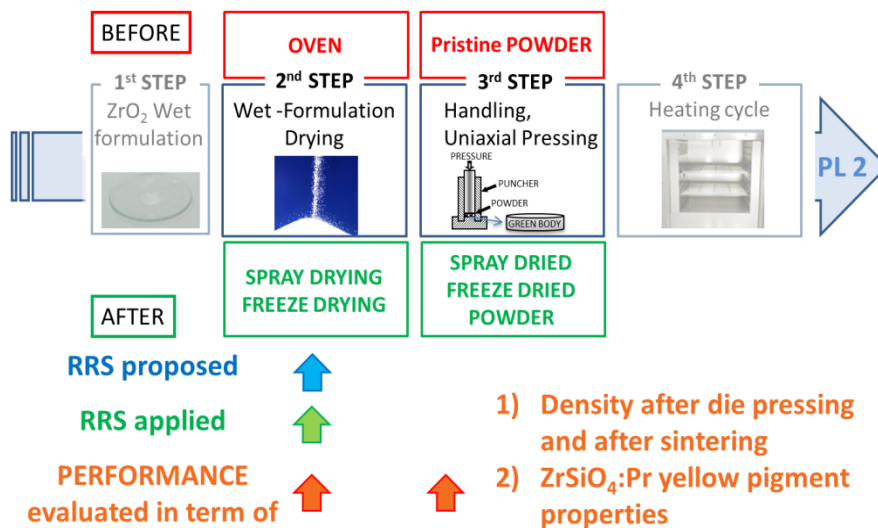


Figure 2 - Scheme of PL 2, showing the process steps in which RRS was applied and evaluated

Along PL 2, the relevant steps for health hazard and EA were the wet formulation drying, the handling and uniaxial pressing operations. The two scenarios that took place with the introduction of RRS, were defined as the BEFORE and the AFTER one, in which the RRS were implemented.

3.1.3.1 Wet formulation drying

The first critical step to be monitored was referred to the wet formulation drying due to the possible dispersion by aerosol of nano ZrO₂, that became a potential source of NMs exposure. During this step the RRS proposed were two alternative drying techniques, the freeze drying and spray drying, aimed to decrease NMs emission in the workplace. The introduction of RRS may lead to a ZrO₂ powder with controlled size distribution, residual moisture content, density and shape, all relevant parameters for final ceramic quality. The BEFORE scenario was represented by the drying of ZrO₂ NMs in an oven, while in the AFTER scenario ZrO₂ NMs was dried by freeze or spray drying.

3.1.3.2 Uniaxial Pressing

The second critical step to be monitored, referred to ceramic processing operations, like uniaxial pressing, due to possible NMs inhalation by the workers. During this step, the control of powder characteristics (size distribution, residue humidity and particles shapes), obtained after RRS application, may lead to a process improvement in term of decreasing potential exposure to NMs and improving ceramic product quality. The BEFORE scenario was represented by the employ of ZrO₂ NM dried in an oven, while the AFTER scenario, involved ZrO₂ NMs dried by freeze or spray drying.

3.1.3.3 Zircon pigment manufacturing

Another step considered and proposed as possible application of ZrO₂ NM, was the Zr-Pr yellow pigment manufacturing. During this step, the control of potential exposure to NMs by the colloidal synthetic route together with the spray drying technique as RRS, may lead to a process improvement in term of both decreasing potential exposure to NMs and improving quality of ceramic pigment. The BEFORE scenario was represented by preparation of Zr-Pr pigment by traditional mechanical mixing of powders, while in the AFTER scenario, Zr-Pr pigment were synthesized by colloidal route and spray drying.

3.2 Experimental

3.2.1 Preliminary characterization of ZrO₂ nanopowder

Pristine ZrO₂ NM, encoded as **ZrO₂_1_NP**, was provided by PlasmaChem and employed for both PL 1 and PL 2. Powder preliminary characterizations have been reported in chapter 2.

3.2.2 Application of RRS at lab scale / pilot scale level

3.2.2.1 Wet formulation drying

The study of drying step of the ZrO₂ wet formulation was performed at pilot-scale level by GEA-Niro using a spray drier (Mobile Minor, GEA-Niro) and at lab-scale level by CNR-ISTEC

using a freeze drier (MDF0.1, 5Pascal). For the spray drying, the process parameters were optimized by GEA-Niro to obtain a dry, non-sticking and micron-sized powder. For freeze drying, the freezing cycle was performed at $-37\text{ }^{\circ}\text{C}$ for 5 h, then the temperature was increased up to $25\text{ }^{\circ}\text{C}$ under vacuum. Samples involved in the wet formulation drying step, are described below:

- Pristine ZrO_2 powder, encoded as **ZrO₂_1_NP**, was the PlasmaChem NM dried in an oven and used as BEFORE material.
- Modified sample, **ZrO₂_9_NP_SD**, was prepared dispersing pristine ZrO_2 powder in distilled water by ultrasonication. The dispersion obtained were spray dried giving a granulate powder, that was considered as modified sample for following process operation performed in the AFTER scenario.
- Modified sample, **ZrO₂_12_NP_FD**, was prepared dispersing pristine ZrO_2 powder in distilled water by ultrasonication. The dispersion obtained was freeze dried giving a white translucent needle-like powder, that was considered as modified sample for following process operation performed in the AFTER scenario.

Samples were observed by SEM-FEG (Zeiss, DE) and employed as raw ceramic material for the following consolidation step.

3.2.2.2 Uniaxial pressing

The study of cold consolidation step was performed at lab-scale level by CNR-ISTEC due to the know-how and facilities existing. For the die pressing, the materials obtained and compared are described below:

- Pristine sample was a ceramic pellet obtained employing pristine powder and encoded as **CP ZrO₂_1_NP**. Pristine powder was sprayed with an aqueous solution of PEG 600 (10 wt.%) to facilitate the densification and then sieved ($250\text{ }\mu\text{m}$) to remove the coarser fraction. An amount of 1.5 g was used to fill the mold (15 mm diameter) for the cold die pressing, performed applying a $P = 1\text{ }000\text{ kg/cm}^2$. After pressing, the ceramic pellet, or “green body”, was removed from the mold and finally sintered in an oven at $1\text{ }200\text{ }^{\circ}\text{C}$ (in air, heating rate = $100\text{ }^{\circ}\text{C/h}$; residence time = 1 h; cooling by inertia) giving rise to a consolidate ceramic pellet.
- Modified sample was a ceramic pellet obtained employing modified powder $\text{ZrO}_2_9_NP_SD$ and encoded as **CP ZrO₂_9_NP_SD**. Modified powder was wetted with an aqueous solution of PEG 600 (10 wt.%) to facilitate the densification and then sieved ($250\text{ }\mu\text{m}$) to remove the coarser fraction. An amount of 1.5 g were used to fill the mold (15 mm diameter) for the cold die pressing, performed applying a $P = 1\text{ }000\text{ kg/cm}^2$. After pressing, the ceramic pellet, or “green body”, was removed from the mold and finally sintered in an oven at $1\text{ }200\text{ }^{\circ}\text{C}$ (in air, heating rate = $100\text{ }^{\circ}\text{C/h}$; residence time = 1 h; cooling by inertia) giving rise to a consolidate ceramic pellet.
- Modified sample was a ceramic pellet obtained employing modified powder $\text{ZrO}_2_{12_NP_FD}$ and encoded as **CP ZrO₂_12_NP_FD**. Modified powder was wetted with

an aqueous solution of PEG 600 (10 wt.%) to facilitate the densification and then sieved (250 μm) to remove the coarser fraction. An amount of 1.5 g were used to fill the mold (15 mm diameter) for the cold die pressing, performed applying a $P = 1\,000\text{ kg/cm}^2$. After pressing, the ceramic pellet, or “green body”, was removed from the mold and finally sintered in an oven at 1 200 °C (in air, heating rate = 100 °C/h; residence time = 1 h; cooling by inertia) giving rise to a consolidate ceramic pellet.

Density of each materials after cold die pressing and after sintering were calculated from pellet volume and weight. Pellets were weighted using an analytical balance (ED 224-5, Sartorius) and pellets height and diameter were measured trough calipers.

3.2.2.3 Zircon pigment manufacturing

A further investigated process was the Zr-Pr pigment manufacturing, being a possible application of ZrO_2 NM in ceramic field. The study of the above mentioned ceramic application with pristine and modified materials were performed at lab-scale level exploiting CNR-ISTEC facilities. For Zr-Pr pigment production, samples compared were:

- Pristine sample, encoded as **ZrO₂_14_SilPr_NP**, was obtained by the traditional method of mechanical mixing of a right amount of ZrO_2 NM, SiO_2 fused (CE MINERAL 44 CSS) and Pr_6O_{11} dry powders, followed by calcination in closed alumina crucibles, using an electric kiln in static air, at the maximum temperature of 1 000 °C, to obtain the yellow Zr-Pr pigment.
- Modified sample, encoded as **ZrO₂_15_SilPr_NP_SD**, was obtained by mixing ZrO_2 [pristine powder dispersion, 3 wt.%], colloidal SiO_2 [LudoxHS-40, 3 wt.%] in 1:1 molar ratio, the chromophore Pr_6O_{11} [0.05 atoms per formula unit] and LiF [5 wt.%], used as mineralizer. Sample was mixed and ball milled for 24 h to promote homogenization. The dispersion was then dried in a lab scale atomizer (spray dryer SD-05, Lab-Plant) obtaining a granulated powder which was then calcined in closed alumina crucibles, using an electric kiln in static air, at the maximum temperature of 1 000 °C, to give the yellow Zr-Pr pigment.

XRD (Bruker D8 ADVANCE) equipped with a LynxEye detector, set to discriminate $\text{Cu K}\alpha_{1,2}$ radiation, in the 10 - 80° 2θ angle range, with an equivalent counting time of 16 s per 0.02° 2θ step, was used to investigate the pigment reaction yield through crystalline phases determination. Quantitative interpretation of full pattern was performed by Rietveld refinement using the GSAS-EXPGUI software package. Colour was measured on ground Zr-Pr pigment by diffuse reflectance spectroscopy (HunterLab Miniscan MSXP4000) and data are expressed as $L^*a^*b^*$ coordinates.

3.3 Results and Discussion

3.3.1 Application of RRS at lab scale / pilot scale level

3.3.1.1 Wet formulation drying

Pristine freeze and spray dried powders morphology was observed by SEM-FEG taking images at different magnifications, using low current acceleration (Fig. 3).

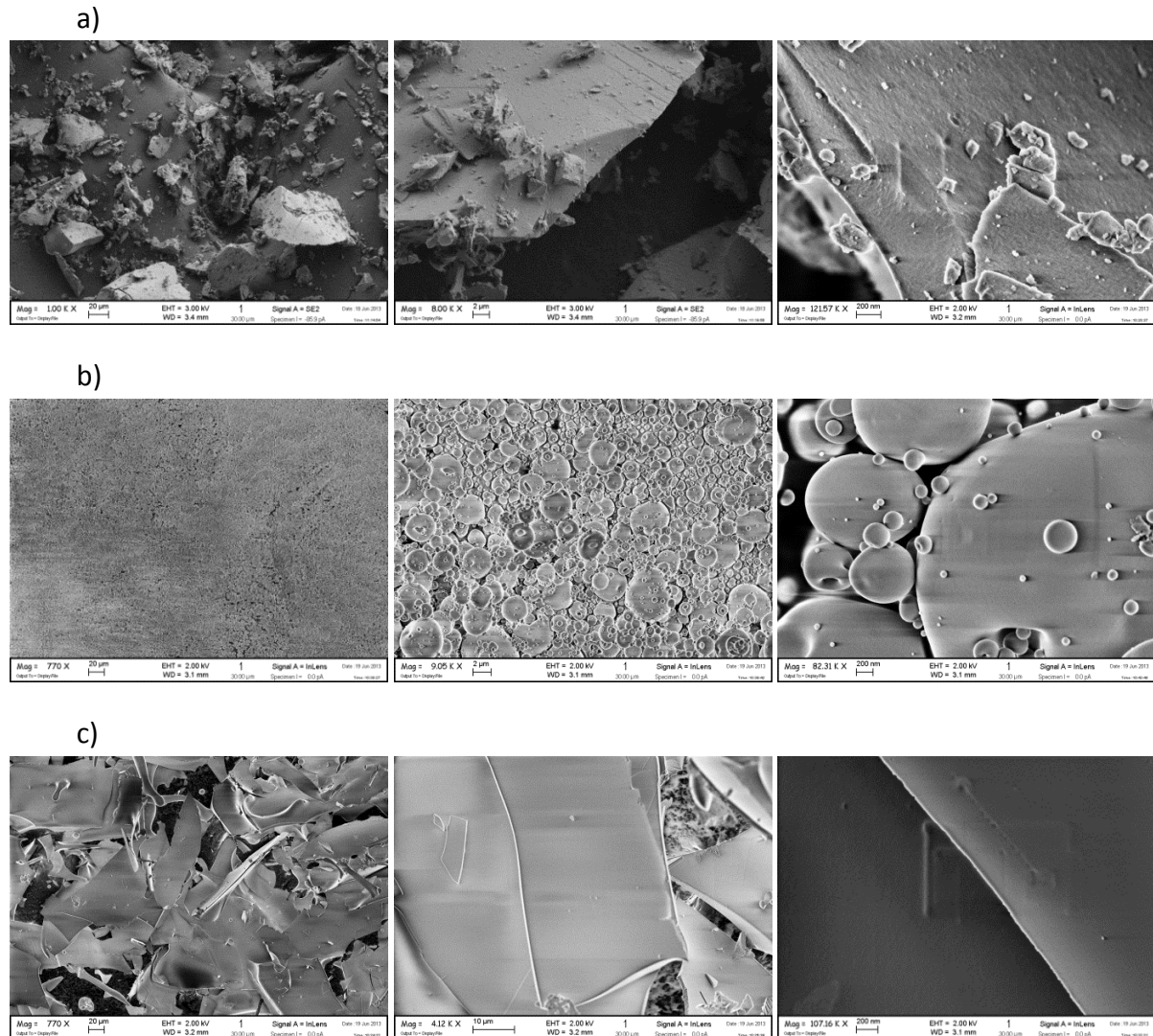


Figure 3 - Morphology of a) pristine ZrO₂_1_NP, b) spray dried ZrO₂_9_NP_SD and c) freeze dried ZrO₂_12_NP_SD samples observed by SEM-FEG at different magnification.

As shown in figure 3, panel a, pristine powder had an irregular morphology and a broad size distribution being composed by both aggregates of few microns and small nanometer particles. Sample obtained by spray drying (Fig. 3, panel b), was composed by granules of spherical shape typical of spray dried materials. Freeze dried sample (Fig. 3, panel c) exhibited thin and irregular sheet-like particles, showing that in this case the expected granulation process did not occur.

3.3.1.2 Uniaxial pressing

Dried samples obtained in previous step underwent uniaxial pressing obtaining ceramic pellets, that was weighted and measured before and after sintering, for density determination. Picture of representative pellets sample and results on pellets density are reported in figure 4 and table 1.

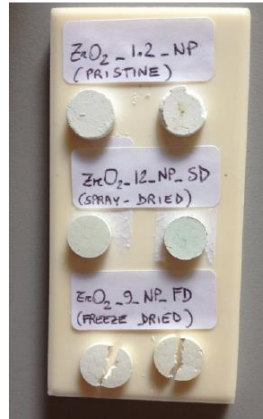


Figure 4 - Picture of the pellets obtained by pressing and sintering; from the top to the bottom: i) pristine CP ZrO₂_1_NP, ii) spray dried CP ZrO₂_9_NP_SD, and iii) freeze dried CP ZrO₂_12_NP_SD samples.

Table 1 - Pellets densities after cold die pressing or sintering

Sample Code	After cold die pressing		After sintering	
	Density [g/cm ³]	% Density*	Density [g/cm ³]	% Density*
CP ZrO ₂ _1_NP	2.1	36	3.5	59
CP ZrO ₂ _9_NP_SD	1.9	32	3.4	58
CP ZrO ₂ _12_NP_FD	2.4	41	2.9	49

* related to monoclinic ZrO₂ = 5.9 g/cm³

After pressing, modified CP ZrO₂_12_NP_FD sample displayed the higher density per cent followed by the pristine CP ZrO₂_1_NP and CP ZrO₂_9_NP_SD samples. This trend changed after sintering, pristine and modified pellet samples showed a similar density per cent, higher than that of the pellet obtained employing freeze dried ZrO₂ material. The small differences detected by comparing density per cent of ceramic pellet obtained by pristine and modified samples, did not allow to appreciate how the different drying process affected the final powder structure. From a visual observation, sintered pellet, obtained by freeze dried powder was broken by an extensive crack (Fig. 4, bottom). On the contrary, the modified ZrO₂_9_NP_SD powder best looked, because no crack or rift on the pellet was noted after sintering, as shown in figure 4.

3.3.1.3 Zircon pigment manufacturing

ZrO₂ NM was tested in a further ceramic application: the manufacturing of Zr-Pr pigment, one of the best yellow pigment for optical properties and chemical/physical stability in ceramic applications. The most important requirement was to display an intense and long-lasting coloration and in the case of zircon-based yellow pigments, these property strictly depended on the reaction yield. From this standpoint, the performances of pristine and modified material were evaluated in terms of colour obtained and reaction yield. Zr-Pr colour was measured by diffuse reflectance spectroscopy and data expressed as L*a*b* coordinates, where: L* defined the brightness (0 = black, 100 = white), while a* (+ red, - green) and b* (+ yellow, - blue) represented the chroma. In the colorimetric CIE L*a*b* space system, the b* parameter representing one of the axis (the b-b' axis) and its positive values described the yellow, while negative values denoted the blue. In table 2 are reported a summary of the colorimetric measurement performed on the investigated pigments.

Table 2 - Summary of the colorimetric measurement.

Sample Code	CIE L*a*b* parameters			
	L* Brightness	a* Chroma	b* Chroma	Cab* Saturation
ZrO ₂ _14_SilPr_NP	91.14 ± 0.02	-6.23 ± 0.01	37.51 ± 0.02	36.98 ± 0.02
ZrO ₂ _15_SilPr_NP_SD	90.92 ± 0.01	-7.73 ± 0.03	42.12 ± 0.04	42.74 ± 0.05

From the data obtained, the modified sample showed a more positive b* value, thus “more yellow shade”, in comparison with the pristine one. To better define the overall coloration of the sample was taken into account also the Cab* parameter, useful to evaluate the saturation or “color purity”. From both the values of Cab* and b* parameters, the modified sample ZrO₂_15_SilPr_NP_SD displayed a better coloration in comparison to the pristine one. The pigment reaction yield was investigate through PrZrSiO₄ crystalline phases determination; the XRD patterns of pristine and modified samples were reported in figure 5.

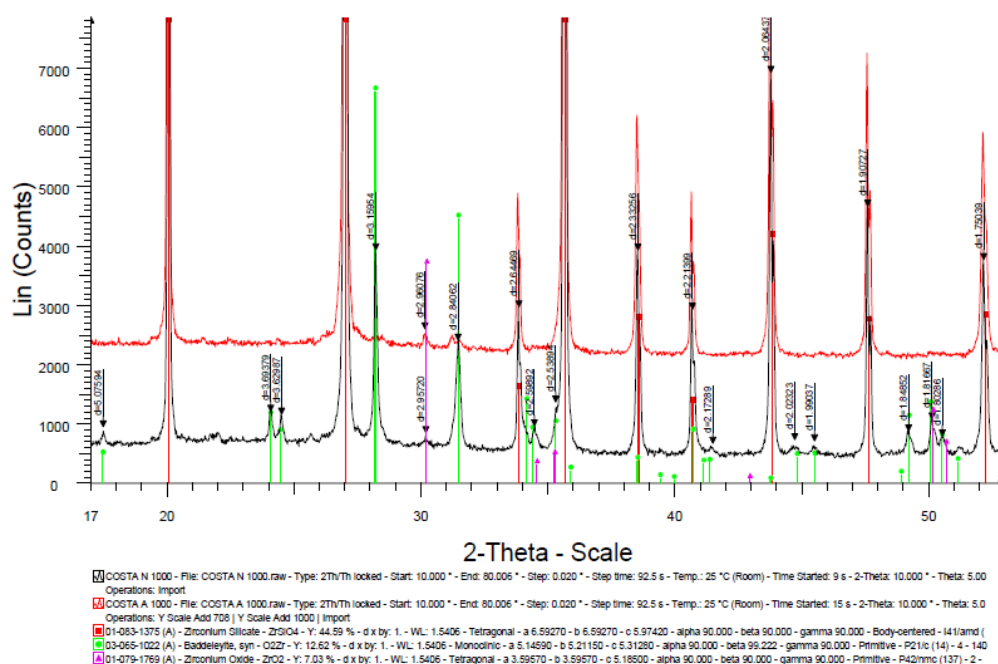


Figure 5 - XRD patterns of pristine ZrO₂_14_SilPr_NP (black) and modified ZrO₂_15_SilPr_NP_SD (red) pigments

Quantitative interpretation of pristine sample pattern (black pattern) showed a ~ 85 wt.% of yield in the desired Pr-ZrSiO₄ crystalline phase, accompanied by ~ 10 wt.% of ZrO₂ polymorphs (monoclinic ZrO₂ predominated over tetragonal ones) and, not discernible in the XRD pattern, a ~ 5 wt.% of silica-rich amorphous phase, expected on the basis of unreacted ZrO₂. The modified sample (red pattern) showed a nearly full reaction yield, as evidenced by the presence of Pr-ZrSiO₄ as main crystalline phase together with two very small peaks, attributed to tetragonal and monoclinic zirconia phases.

3.3.2 Exposure assessment: off-line measurement

To evaluate RRS of wet formulation drying by freeze or spray drying, EA were performed, focusing on contamination by NMs in air. INERIS performed a "basic measurement campaign" in GEA-Niro, industrial partner in the SANOWORK project, to evaluate if ZrO₂ NM was emitted in the workplace due to spray drying and associated operations. As demonstrated by INERIS, the spray drying did not cause a significant increase in the particulate count, therefore the introduction of spray drying process may be accepted as RRS.

Unfortunately, the same exposure measurement was not possible for the freeze drying process, but INERIS performed on all samples an off-line exposure experiment called "dustiness experiment", already adopted to investigate powder dustiness [16]. This off-line experiment simulated the emission of NMs during handling and allowed to compare their emissivity. The experimental set-up, schematized in figure 6, comprised a vortex shaker instrument which, by the combined effect of shaking and air flow, allowed the powder to be

tested to pass in the aerosol phase. The aerosol phase contains the inhalable fraction and for this reason it was considered for the analysis, collection and TEM observation of NMs.

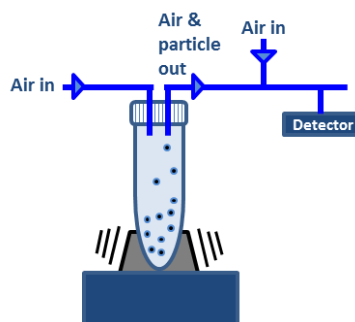


Figure 6 - Scheme of experimental set-up for dustiness test

To quantify the concentration of NMs released by each sample, two real-time measurement instruments were used: the CPC, that delivers a concentration in number of particles from 4 nm to 2.5 μm per cm^3 (reported as particle/ cm^3) and the APS, that take into account particles between 0.5 and 20 μm . The particles released during the experiments were sampled by a sampling pump on specific TEM grids employing a MPS. NM size and shape were investigated by TEM; representative TEM pictures were reported in figure 7.

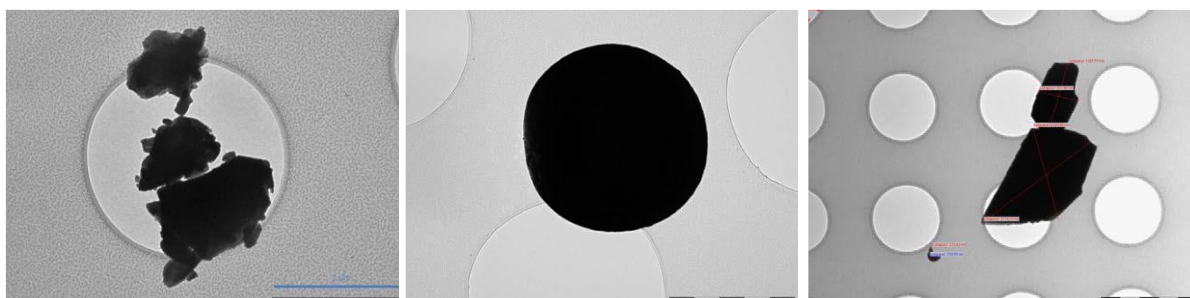


Figure 7 - ZrO_2 particles from aerosol generated from (left to right): i) pristine ZrO_2 _1_NP, ii) ZrO_2 _1_NP, ZrO_2 _9_NP_SD and iii) ZrO_2 _12_NP_FD samples.

As observed by TEM sampling grids, pristine sample ZrO_2 _1_NP was composed by particles with jagged and irregular outlines and an high percent of them was of size lower than 100 nm. In the spray dried sample ZrO_2 _9_NP_SD spherical shaped granules were observed, mainly bigger than 1 μm . The particle emitted from freeze dried sample were mainly bigger than 1 μm with irregular but smooth outlines. A summary of the results obtained by off-line dustiness tests are reported in table 3.

Table 3 - Summary of main results of the dustiness tests on ZrO₂ powders.

Sample Code	Average particles concentration		Dustiness		d _H by APS (0.5 μm - 20 μm)
	[particle/cm ³] by CPC (4 nm – 2.5 μm)	[particle/cm ³] by APS (500 nm - 20 μm)	Number conc. [particle/cm ³] (4 nm - 20 μm)	Number conc. [particle/cm ³] (4 nm - 330 nm)	
ZrO ₂ _1_NP	5 585	3 065	6 400	3 000	2.1
ZrO ₂ _9_NP_SD	21	32	46	< 10	3.1 – 4.7 – 6.2
ZrO ₂ _12_NP_FD	16	40	38	< 10	2.4

A significant difference in powder dustiness was measured during the experiments. From the average particle concentration observed both in the range 4 nm - 2.5 μm by CPC and 500 nm - 20 μm by APS, the pristine sample resulted the more emissive one. On the contrary, modified samples were of some orders of magnitude less emissive in comparison to the pristine one. The d_H of coarser particle measured by APS 0.5 μm - 20 μm, showed for both pristine and freeze dried samples the presence of particles of about 2 - 2.5 μm diameter, while in the spray dried sample were found bigger particles, composed by three population with 3.1 - 4.7 - 6.2 μm diameter.

3.4 Conclusions

NM surface control by both freeze and spray drying techniques were applied on ZrO₂ NM during formulation drying step and implemented at pilot-scale level by GEA-Niro. From the density percentages of green and sintered samples, it was not possible to establish if granulation process had improved the cold and hot consolidation of ZrO₂ NMs; nevertheless, it was hypothesized a better densification for the modified spray dried ZrO₂_9_NP_SD sample. The manufacturing of Zr-Pr pigment, showed that modified sample was produced with an higher reaction yield, and showed a more effective color evolution in comparison to the pristine sample, as confirmed by colorimetric determinations.

To evaluate a possible decrease in powder emissivity by freeze and spray drying as RRSs, a “basic measurement campaign” were performed at GEA-Niro during the spray drying operations of ZrO₂ NMs. The exposure measurement in workplace proved that spray drying process did not cause any significant increase in the particulate count and, therefore, the introduction of spray drying process as RRS may be promoted. The off-line dustiness experiment resulted a useful tool to compare, in an off-line setting, the emissivity of the involved samples and let to evaluate the efficiency of proposed drying techniques to decrease the nano aerosol dispersion ZrO₂ powders.

3.5 References

- [1]. P. Murugavel, M. Kalaiselvam, A. R. Raju and C. N. R. Rao, *J. Mat. Chem.*, **1997**, 7, 1433 - 1438
- [2]. N. C. Sagaya Selvam, A. Manikandan, L. J. Kennedy, J. J. Vijaya, *J. Colloid Interf. Sci.*, **2013**, 389, 91 - 98
- [3]. A. E. Bohè, J. Andrade-Gamboa, D. M. Pasquevich, A. J. Tolley, and J. L. Pelegrina, *J. Am. Ceram. Soc.*, **2000**, 83, 755 - 760
- [4]. A. E. Bohè and D. M. Pasquevich, *High-Temp. Mater. Sci.*, **1997**, 37, 1 - 16
- [5]. J. Duh, H. Dai, W. Hsu, *J. Mater. Sci.*, **1988**, 23, 2786 - 2791
- [6]. H. Armendàriz, M. A. Cortes, I. Hernández, J. Navarrete and A. Vázquez, *J. Mat. Chem.*, **2003**, 13, 143 - 149
- [7]. N. Zhao, D. Pan, W. Nie, and X. Ji, *J. Am. Chem. Soc.*, **2006**, 128, 10118 - 10124
- [8]. Y. Ohtsu, Y. Hino, T. Misawa, H. Fujita, K. Yukimura, M. Akiyama, *Surf. Coating Tech.*, **2007**, 201, 6627 - 6630
- [9]. L. La, H. Lu, H. Chen, B. Cheng, M. Lin, T. Chu, *J. Electron Spectrosc.*, **2005**, 144-147, 865 - 868
- [10]. S. Zhao, F. Ma, Z. Song, K. Xu, *Opt. Mater.*, **2008**, 30, 910 - 915
- [11]. Q. Zhang, Q. Du, M. Hua, T. Jiao, F. Gao, and B. Pan, *Environ. Sci. Technol.*, **2013**, 47, 6536 - 6544
- [12]. J. Chevalier, L. Gremillard, *J. Eur. Ceram. Soc.*, **2009**, 29, 1245 - 1255
- [13]. S. Ardizzone, L. Binaghi, G. Cappelletti, P. Fermo and S. Gilardoni, *Phys. Chem. & Chem. Phys.*, **2002**, 4, 5683 - 5689
- [14]. E. Ozel, S. Turan, *J. Eur. Ceram. Soc.*, **2007**, 27, 1751 - 1757
- [15]. M. Bengisu, *Engineering Ceramics* (ISBN 3-540-67687-2), Springer- Verlag, Berlin, Germany, **2001**, Chap. 3, pp. 85 - 205
- [16]. M. Morgeneyer, O. Le Bihan, A. Ustache, O. Aguerre-Chariol, *Powder Technol.*, **2013**, 246, 583 - 589

4. Processing line 3: electrospinning line (polyamide nanofibres)

4.1 Introduction

4.1.1 Polyamide nanofibres

Several fabrication techniques have been employed to produce NFs, ranging from, self-assembly ^[1, 2], template synthesis ^[3, 4], phase separation ^[5] and electrospinning ^[6]. Among them, electrospinning is the most widely studied technique for its industrial scalability and the potential for NFs mass production. Electrospun NFs were employed in different technological applications, including filtration membranes ^[7, 8], sensors ^[9], catalysis ^[10, 11], dye-sensitized solar cells ^[12, 13, 14] and fuel cells ^[15].

Recently, NFs received growing interest in the field of tissue engineering ^[16] for the possibility to tune their compositions and structures, mimic those of target tissues. NFs were employed as scaffolds for the repair of damaged tissues as cardiac ^[17], bone ^[18] and neural ^[19] tissue. The high surface area of nanofibrous network conferred oxygen permeability and prevented fluid accumulation at the wound site, making them ideal substrates for wound dressings and drug delivery ^[20, 21, 22].

PA was employed to fabricate NFs, either alone as filters material ^[23] or in composite NFs, together with lecithin ^[24], calcium lactate ^[25] or chitosan ^[26], for medical applications. Notwithstanding the biocompatibility of NF matrices and their wide employ in medical field, the industrial scale production raised occupational health and safety issues, due to the free fibres toxicity ^[27] and the possible release during handling ^[28], likely occurring also in related manufacturing operations.

4.1.2 Description of Processing line 3

PL 3 focused on a PA non-woven nanofibrous material, suitable for filtration purpose, obtained by the electrospinning process designed by Elmarco, that provided information on experimental procedure and set-up. Bayer was also involved in this PL as user of the Elmarco electrospinning machine. The main steps involved in PA NF production are reported in figure 1.

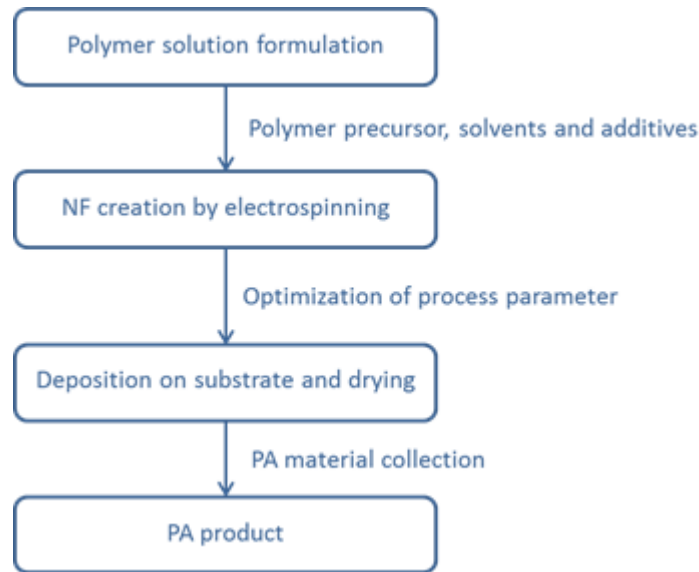


Figure 1 - Main step in PA electrospinning procedure

Electrospinning is a versatile process by which polymeric NFs, with diameters ranging from few nanometers to several micrometers, were produced by an electrostatically driven jet of polymer solution or polymer melt. For PA NFs, the precursor, Ultramid B27, was dissolved in acetic and formic acid and then stirred to homogenize the solution. Then, the polymer solution was feed into the electrospinning machine and process parameter optimized to obtain desired characteristics. Due to high voltage applied between electrodes, NFs were created and deposited onto a carrier substrate that allowed the solvent evaporation before to collect non-woven nanofibrous material on a roll. PA was deposited on a thin PP support, air dried and recovered.

4.1.3 Critical step identified and RRS proposed

A general scheme of the PL 3 was reported in figure 2.

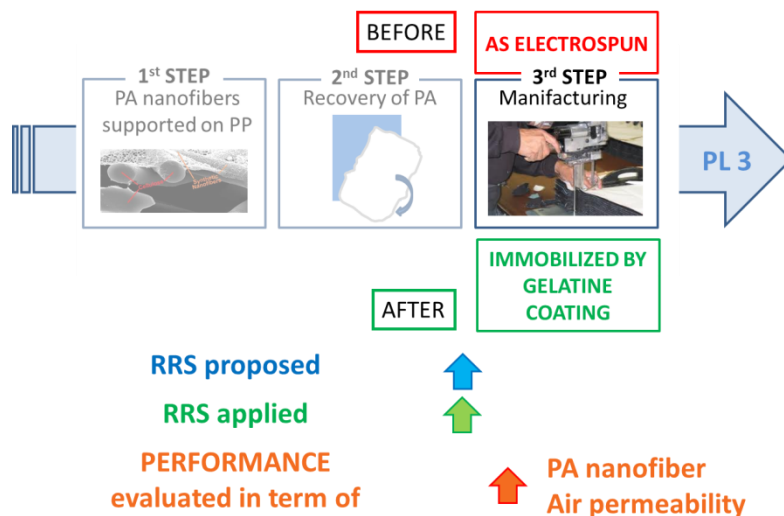


Figure 2 - Scheme of processing line 3, showing process step in which RRS were applied and evaluated

Along PL 3, the relevant steps for health hazard and EA were the recovery and manufacturing of the non-woven material (pleating, cutting, drilling) during product finalization. The two scenarios that took shape with the introduction of RRS were defined as BEFORE and AFTER.

4.1.3.1 Handling and manufacturing

The steps supposed to be critical for the potential of exposure to free NFs, were the recovery and manipulation operations, like the cutting of PA material, performed at the end of the PL. During these steps, the RRS of film coating deposition, employing the gelatin as protective layer, was proposed to avoid free fibre release. The gelatin layer removal from coated samples was also investigated, to maintain the same filtration performance of NFs after RRS application. The BEFORE scenario was represented by handling of the pristine PA non-woven materials, while the AFTER scenario was represented by the use of gelatin coated samples.

4.2 Experimental

4.2.1 Preliminary characterization of polyamide nanofibres

The materials used to test the non-woven manufacturing, were pristine PA NFs provided by Elmarco and encoded as **PA_1.1_NF**. Pristine sample morphology was observed by SEM taking images at different magnifications, while the air permeability, linked to filter efficiency, was measured by Elmarco.

4.2.2 Application of RRS at lab-scale level

4.2.2.1 Handling and manufacturing

To lower the possibility of free fibre inhalation during manufacturing step, a gelatin layer was deposited on PA non-woven. Samples involved are described below:

- Modified sample, encoded as **PA_4.1_gel**, was obtained by spraying on the pristine sample four layers of a gelatin solution (0.25 wt.% dissolved in 0.01 M PBS, pH = 7.4), using an automatic spray-coater equipment (X-CEL MULTITESTA, Aurel).
- Modified sample, **PA_4.1_gel_W1**, was obtained performing on PA_4.1_gel sample one washing treatment with warm water and then drying the sample at room temperature.
- Modified sample, **PA_4.1_gel_W2**, was obtained performing on PA_4.1_gel two washing treatments with warm water and then drying the sample at room temperature.

Samples washing procedures were optimized by Bayer, that perform SEM observations to evaluate the removal of the gelatin layers. Elmarco evaluate the filtration performance of the samples involved by measuring their air permeability.

4.3 Results and discussion

4.3.1 Preliminary Characterization of polyamide nanofibres

Pristine sample morphology was observed by SEM taking images at different magnifications. As shown in figure 3, most of NFs showed diameters around 100 nm, but also few fibres aggregates with diameter close to 1 μm , were found in the sample.

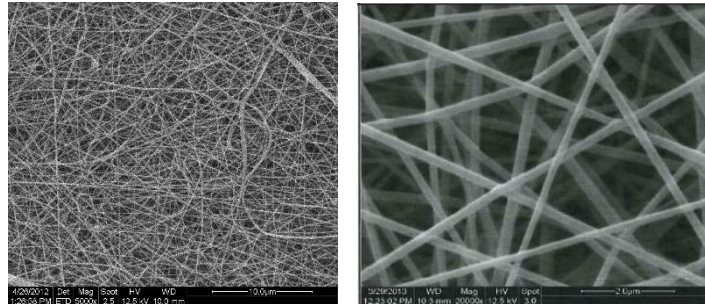


Figure 3 - Pristine PA_4.1_gel sample morphology by SEM images.

4.3.2 Application of RRS at lab-scale level

4.3.2.1 Handling and manufacturing

Modified sample obtained after the gelatine deposition were observed by SEM (Fig. 4).

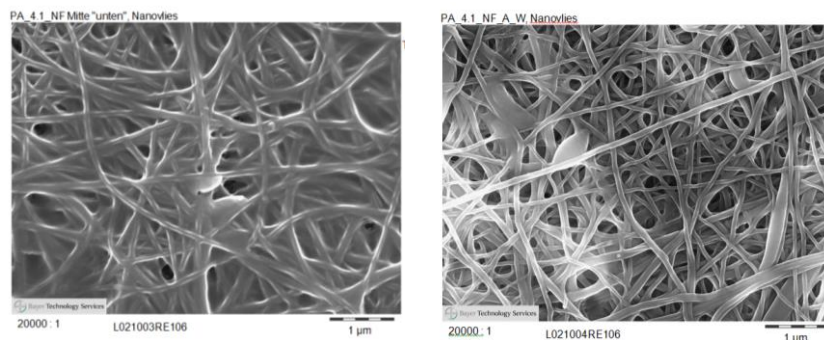


Figure 4 - Morphology of the gelatine coated PA_4.1_gel (left) and washed PA_4.1_gel_W1 (right) samples by SEM images.

The images obtained showed that the gelatine layer was homogeneously spread on the fibres surface, taking the shape of a continuous coating, especially in those region in which fibres were more closely arranged. After the gelatine washing, performed with warm water, only few spots of coating were found in the sample. However, observing the NF morphology, the heat treatment seemed to cure the fibres structure, reducing the space between fibres and, therefore, the porosity of the materials.

Air permeability of pristine PA_1.1_NF and modified PA_4.1_NF, PA_4.1_NF_W1, PA_4.1_NF_W2 samples was measured by Elmarco, according the European Standards for Filtration Materials (Table 1).

Table 1 - Summary of the air permeability measurement.

Sample code	Air permeability [m ³ /m ² /min]
PA_1.1_NF	2.44
PA_4.1_NF	0.97
PA_4.1_NF_W1	0.72
PA_4.1_NF_W2	0.03

The permeability of modified samples PA_4.1_NF was lower than that of pristine material due to gelatine film deposition. Unfortunately, as evidenced by the data collected, the washing treatment applied to check the NF structure recovery, after washing out the protective gelatine coating, was detrimental for the performance of the samples, because air permeability decreased with the number of applied treatments.

4.3.3 Exposure assessment: off-line and on-site measurements

EA started from a “basic measurement campaign” within Elmarco settings to verify the emission of PA NFs during the handling and manufacturing steps, supposed to be critical. To identify the presence of PA NFs, the N₂ was chosen as tracer element, being the component of NFs less commonly detected in the ambient air. Therefore, the exposure investigation was focused on fibrous N-containing materials. The instruments used by Ineris were the same used in the other measurement campaign to compare the results obtained. The real time CPC was used between the main potential sources and outlets, to determine the total particle concentration in number, in the range 10 nm – 1 µm. A TEM grid sampler was employed to measure the NPs near to the respiratory system, collecting them on specific TEM grids, which were observed.

The characterization of the background aerosol noise revealed a high number of particles, in the order of 3 000 particles/cm³, with d_H between 10 nm and 1 µm, such as oil droplets, soot and debris, that were commonly found in ambient air and typical of building materials, but N-containing fibres were not detected. During the cutting operations of the sheet of PA NFs, no significant increase was found in the particle count, that fluctuated between 3 000 and 4 500 particles/cm³. Despite a detailed study of the material found on the grids, no PA fibrous species were identified, the only particulates observed being the same found in the background aerosol.

Fibre release during cutting operations was further investigated by Bayer and Ineris in an off-line setting. To avoid interference by ubiquitous particles and perform safe experiments, the cutting experiments were carried out in a z-b box rebuilt into a glove box. The SMPS, the optical particle counter PDM and the NAS were connected to the z-b box and when PDM stably showed zero, the NAS was switched on to start the experiment. Prior to start, it was performed a measurement test in the glove box without tools and samples, just moving the gloves. Results gave an uncertainty of about ± 3 particles/cm³ smaller than 300 nm and ± 0.02 particles/cm³ bigger than 300 nm, depending on the user. After that the zero

background was reached again in the z-b box, the PA layer was detached from the substrate and cutted. During this operation, particles detected were $2/\text{cm}^3$ of diameter $< 100 \text{ nm}$ and $2.20/\text{cm}^3$ of diameter $< 300 \text{ nm}$. Therefore, from the data obtained, free NFs were not emitted, as shown by the insignificant change in their concentration during PA cutting operation. To investigate the morphology and composition of the emitted particles, sampling grids were subjected to TEM observation and particles found to EDS analysis (Fig. 5). From SEM image and EDS analysis, neither PA NFs were found in SEM image nor nitrogen was detected by EDS, confirming the absence of PA NFs emitted during the cutting.

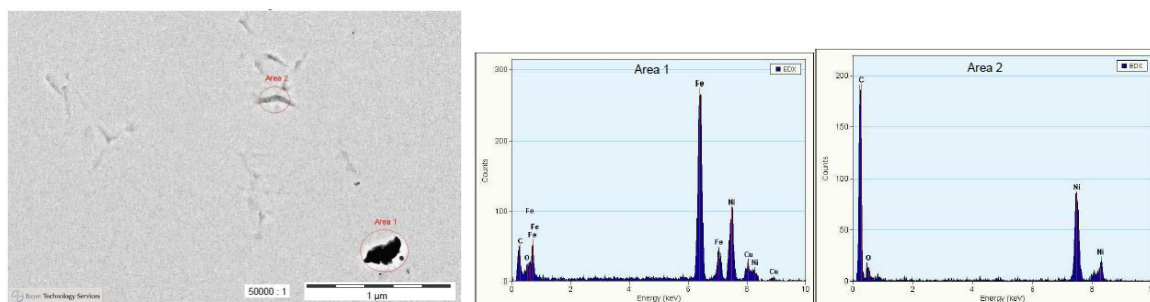


Figure 5 - Sampling grid image showing two area subjected to EDS analysis and respective spectra.

4.4 Conclusions

RRS of film coating deposition were applied on PA non-woven materials to control free fibre emission during handling operations. The gelatine coating process was successful, but air permeability of modified samples, both before and after washing treatment, was impaired. These results may be justified by the delicate structure of NF matrix, that may be easily damaged by coating and washing procedures, that worsened the properties of the final non-woven materials. In term of exposure, no PA NFs contamination in air was found in a basic measurement campaign, either in the background or during the cutting operations. This result was obtained also when cutting experiments were performed in the z-b box, confirming the unlikely exposure to PA NFs by the workers.

4.5 References

- [1]. J. D. Hartgerink, E. Beniash and S. I. Stupp, *Science*, **2001**, 294, 1684 - 1688
- [2]. M. B. Bannwarth, S. W. Kazer, S. Ulrich, G. Glasser, D. Crespy, and K. Landfester, *Angew. Chem. Int. Ed.*, **2013**, 52, 10107 - 10111
- [3]. L. Feng, S. Li, H. Li, J. Zhai, Y. Song, L. Jiang and D. Zhu, *Angew Chem. Int. Ed.*, **2002**, 41, 1221 - 1223
- [4]. C. R. Martin, *Chem. Mater.*, **1996**, 8, 1739 - 1746
- [5]. F. Yang, R. Murugan, S. Ramakrishna, X. Wang, Y. Ma and S. Wang, *Biomater.*, **2004**, 25, 1891 - 1900
- [6]. Z. Huang, Y. Z. Zhang, M. Kotaki and S. Ramakrishna, *Comp. Sci. Techn.*, **2003**, 63, 2223 - 2253

- [7]. R. Gopal, S. Kaur, Z. Ma, C. Chan, S. Ramakrishna, T. Matsuura, *J. Membr. Sci.*, **2006**, 281, 581 - 586
- [8]. W. W. Leung, C. Hung, P. Yuen, *Sep. Purif. Technol.*, **2010**, 71, 30 - 37
- [9]. B. Ding, M. Wang, X. Wang, J. Yu, G. Sun, *Mater. Today*, **2010**, 13, 16 - 27
- [10]. E. Formo, E. Lee, D. Campbell, and Y. Xia, *Nano Lett.*, **2008**, 8, 688 - 672
- [11]. Y. Dai, W. Liu, E. Formo, Y. Sun and Y. Xia, *Polym. Adv. Technol.*, **2011**, 22, 326 - 338
- [12]. J. Li, X. Chen, N. Ai, J. Hao, Q. Chen, S. Strauf, Y. Shi, *Chem. Phys. Lett.*, **2011**, 514, 141 - 145
- [13]. A. Sreekumaran Nair, R. Jose, Y. Shengyuan, S. Ramakrishna, *J. Colloid Interf. Sci.*, **2011**, 353, 39 - 45
- [14]. L. Yang and W. W. Leung, *Adv. Mater.*, **2013**, 25, 1792 - 1795
- [15]. T. Tamura, and H. Kawakami, *Nano Lett.*, **2010**, 10, 1324 - 1328
- [16]. X. Wang, B. Ding and B. Li, *Mater. Today*, **2013**, 16, 229 - 241
- [17]. A. Kumar, A. Patel, L. Duvalsaint, M. Desai and E. D. Marks, *J. Nanobiotech.*, **2014**, 12, 1 - 8
- [18]. H. Kim, J. Song, H. Kim, *J. Biomed. Mater. Res.*, **2006**, A 79, 698 - 705
- [19]. J. Xie, M. R. MacEwan, A. G. Schwartz and Y. Xia, *Nanoscale*, **2010**, 2, 35 - 44
- [20]. V. J. Reddy, S. Radhakrishnan, R. Ravichandran, S. Mukherjee, R. Balamurugan, S. Sundarrajan, S. Ramakrishna, *Wound Rep. Reg.*, **2013**, 21, 1 - 16
- [21]. K. S. Rho, L. Jeong, G. Lee, B. Seo, Y. J. Park, S. Hong, S. Roh, J. J. Choa, W. H. Park, B. Min, *Biomater.*, **2006**, 27, 1452 - 1461
- [22]. T. J. Sill, H. A. von Recum, *Biomater.*, **2008**, 29, 1989 - 2006
- [23]. Y. Guibo, Z. Qing, Z. Yahong, Y. Yin, Y. Yumin, *J. Appl. Polym. Sci.*, **2013**, 128, 1061 - 1069
- [24]. R. Nirmala, H. Park, R. Navamathavan, H. Kang, M. H. El-Newehy, H. Y. Kim, *Mater. Sci. and Eng.*, **2011**, C 31, 486 - 493
- [25]. H. R. Pant, P. Risal, C. H. Park, L. D. Tijing, Y. J. Jeong, C. S. Kim, *Colloid Surf.*, **2013**, B 102, 152 - 157
- [26]. R. Nirmala, R. Navamathavan, H. Kang, M. H. El-Newehy, H. Y. Kim, *Colloid Surf.*, **2011**, B 83, 173 - 178
- [27]. J. Muller, F. Huaux, N. Moreau, P. Misson, J. Heilier, M. Delos, M. Arras, A. Fonseca, J. B. Nagy, D. Lison, *Toxicol. Appl. Pharm.*, **2005**, 207, 221 - 231
- [28]. A. D. Maynard, P. A. Baron, M. Foley, A. A. Shvedova, E. R. Kisin and V. Castranova, *J. Toxicol. Env. Health*, **2004**, A 67, 87 - 107

5. Processing line 4: electrospinning line (TiO₂ nanofibres)

5.1 Introduction

5.1.1 TiO₂ nanofibres

Among several fabrication techniques reported to produce NFs, the electrospinning is the most widely studied for its industrial scalability and potential for mass production. Electrospun NFs of TiO₂ were employed in different technological applications; for example, in catalysis TiO₂ NFs decorated by Pt nanowires were employed to produce filtration membranes showing excellent catalytic activities for the hydrogenation of methyl red ^[1,2]. A catalyst with excellent sintering resistance was synthesized supporting Pt nanoparticles on TiO₂ NFs, followed by porous SiO₂ coating ^[3]. Moreover TiO₂ NFs doped by Ag NP ^[4] or with CNTs ^[5] were employed for dye-sensitized solar cells.

Electrospun TiO₂ NFs, employed as sensor ^[6], exhibited an exceptional sensitivity to NO₂. Nanograins of polyaniline enshased on electrospun TiO₂ NF surface were employed as ultrasensitive nanostructured sensor for NH₃ detection ^[7]. Furthermore an highly sensitive and stable humidity nanosensor based on LiCl-doped TiO₂ NFs was prepared through electrospinning and calcination techniques ^[8]. Recently, NFs received interest in the field of tissue engineering ^[9] for the possibility to tune their compositions and structures, mimic those of target tissues. Nanofibrous network, being able to confer oxygen permeability and prevent fluid accumulation at the wound site, has been employed especially for wound dressings and drug delivery ^[10,11,12]. Hybrid Polyurethane/ TiO₂ NP membrane ^[13] and silk fibroin/TiO₂ nanofibrous mats ^[14] were employed as wound dressing. Furthermore TiO₂ NFs containing hydroxyapatite ^[15] and Ag NP or TiO₂ NFs immobilized on TiO₂ plates ^[16] were investigated as future materials for implant applications.

Despite the biocompatibility of NF matrices and their employ in medical field, the industrial production raises occupational health and safety issues, due to free fibres hazardous properties ^[17] and the possible release during handling ^[18] and related manufacturing operations. Following the “fibre pathogenicity paradigm”, parameters as width, length and biopersistence, dictate whether or not a fibre will be pathogenic when inhaled from an airborne cloud ^[19]. Therefore in SbyD approach, these fibres parameters have to be controlled to lower the NF health hazard.

5.1.2 Description of the Processing line 4

PL 4 focused on a TiO₂ nanofibrous material, suitable for solar energy application, obtained by the electrospinning process designed by Elmarco, that provided information on experimental procedure and set-up. Bayer was also involved in this PL as user of the Elmarco electrospinning machine. The main steps involved in TiO₂ NF production are reported in figure 1.

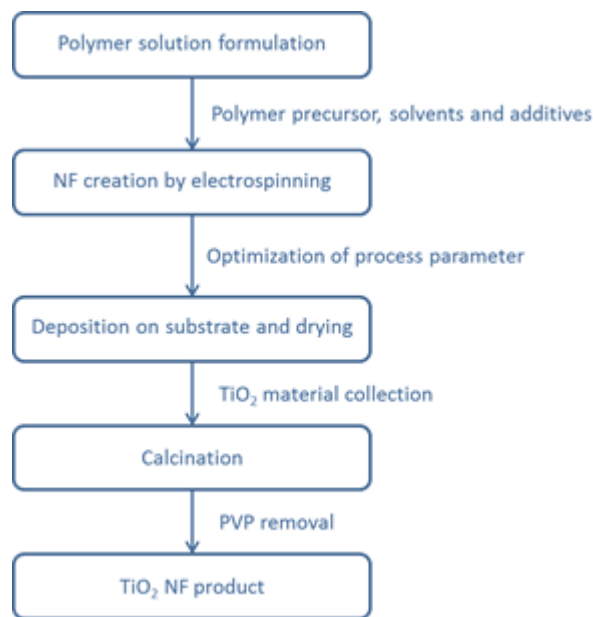


Figure 1 - Main steps in TiO₂ electrospinning procedure

Electrospinning is a versatile process by which polymeric NFs, with diameters ranging from few nanometers to several micrometers, were produced by an electrostatically driven jet of polymer solution or polymer melt. For TiO₂ NFs, the precursor, titanium butoxide, and the template, PVP K-90, were dissolved in ethanol and then stirred to homogenize the solution. Then, the polymer solution was feed into the electrospinning machine and process parameter optimized to obtain the desired NF characteristics. Due to high voltage applied between electrodes, NFs were created and deposited on a carrier substrate, that allowed the solvent evaporation before to collect non-woven nanofibrous material on a roll. TiO₂ was deposited on a thin PP support and air dried. To remove the PVP template, the electrospun non-woven was peeled off from the PP substrate and calcined, obtaining a white TiO₂ NF powder.

5.1.3 Critical step identified and RRS proposed

A general scheme of the PL 4 is reported in figure 2.

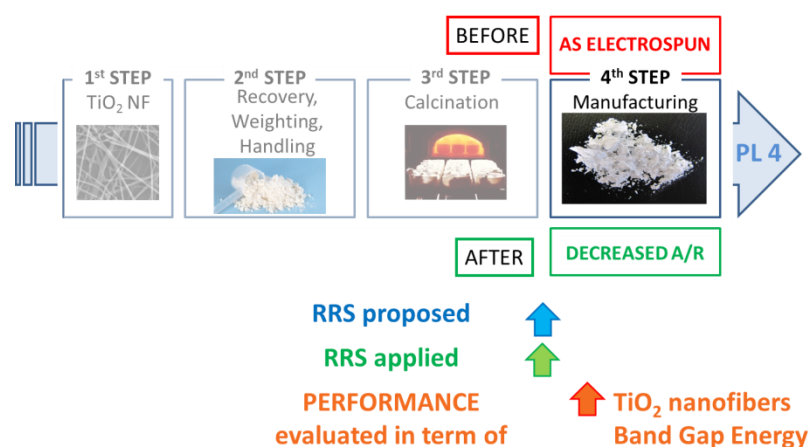


Figure 2 - Scheme of PL 4, showing the process step in which RRS were applied and evaluated

Along PL 4, the relevant steps for health hazard and EA were the recovery and handling of the NFs during product finalization. The two scenarios that took shape with the introduction of RRS were defined as BEFORE and AFTER.

5.1.3.1 Handling and manufacturing

The steps supposed to be critical for the potential of exposure to free NFs, were the recovery and manipulation operations, like the weighting of TiO₂, performed at the end of the PL. The RRS of wet milling was proposed to homogenize fibres AR (i.e. NF length /NF diameter) to decrease NF health hazard. The BEFORE scenario was represented by handling of the pristine TiO₂ NFs, while the AFTER scenario was represented by the use of wet milled samples.

5.2 Experimental

5.2.1 Preliminary characterization of TiO₂ nanofibres

The material used to test the TiO₂ handling was pristine TiO₂ NFs provided by Elmarco and encoded as **TiO₂_1_NF**. Pristine sample morphology was observed by HR-TEM (JEOL JEM-2100F, USA) and SEM-FEG (Zeiss, DE) taking images at different magnifications, used for particle size distribution. The thermal behavior of fibrous material was evaluated by TGA and DSC. Thermal analysis was performed in a simultaneous thermal analyzer STA 449C (Netzsch, GE) using a temperature ramp of 10 °C/min from 25 up to 1 000 °C. The E_g , selected as functional properties, was determinate by CNR-ISTEC through spectrophotometric method, employing a LAMBDA 35 spectrophotometer (Perkin Elmer, USA) equipped with integrating sphere LABSPHERE RSA-PE-20.

5.2.2 Application of RRS at lab-scale level

5.2.2.1 Handling and manufacturing

To decrease NM toxicity and lower the possibility of free fibre inhalation during manufacturing step, a wet milling was performed on TiO₂ NF. Samples involved are described below:

- Modified sample **TiO₂_8_sol_BM** was obtained by dispersing the pristine sample in acid (pH = 3) distilled water (nominal [TiO₂] 3 wt.%) and then ball milling the sample for 9 h using ZrO₂ beads of 3 mm diameter as grinding media.
- Modified sample, **TiO₂_9_sol_BM**, was obtained by dispersing the pristine sample in acid (pH = 3) distilled water (nominal [TiO₂] 3 wt.%) and then ball milling the sample for 2 h using ZrO₂ beads of 3 mm diameter as grinding media.
- Modified sample, **TiO₂_10_sol_BM**, was obtained by dispersing the pristine sample in acid (pH = 3) distilled water (nominal [TiO₂] 3 wt.%) and then ball milling the sample for 4 h using ZrO₂ beads of 3 mm diameter as grinding media.
- Modified sample, **TiO₂_11_sol_BM** was obtained by dispersing the pristine sample in acid (pH = 3) distilled water (nominal [TiO₂] 3 wt.%) and then ball milling the sample for 6 h using ZrO₂ beads of 3 mm diameter as grinding media.

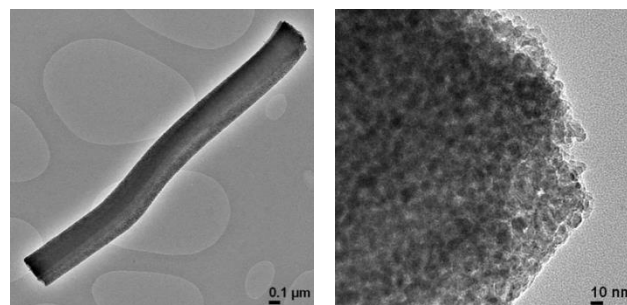
Samples were filtered under vacuum using a Buchner's filter and dried in an oven at 100 °C to regain the NFs in form of powder. After drying, further handmade grinding was not performed to avoid changes in the samples. The modified sample morphology and AR were assessed by SEM-FEG (Zeiss, DE) images and particle size distribution. The E_g of modified samples were investigated by CNR-ISTEC through spectrophotometric method, employing a LAMBDA 35 spectrophotometer (Perkin Elmer, USA) equipped with an integrating sphere LABSPHERE RSA-PE-20.

5.3 Results and discussion

5.3.1 Preliminary characterization of TiO₂ nanofibres

Pristine sample morphology was observed by HR-TEM and SEM-FEG, taking images at different magnifications (Fig. 3).

a)



b)

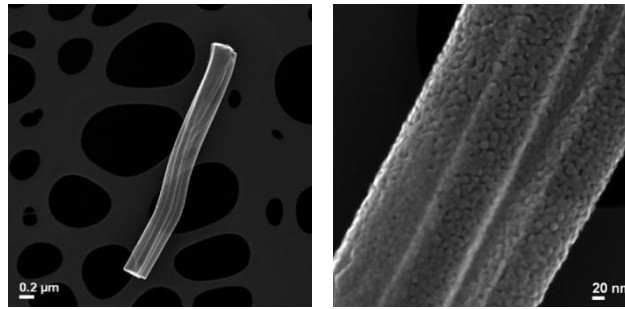


Figure 3 - Pristine TiO₂_1_NF sample morphology by a) TEM-BF and b) STEM- SE images.

From TEM-BF and STEM-HAADF images, pristine sample appeared to consist of discrete units of primary NPs. TEM-EDS spectra showed the presence of Ti and O. The primary NFs significantly varied in length and diameters because of the agglomeration of the fibres.

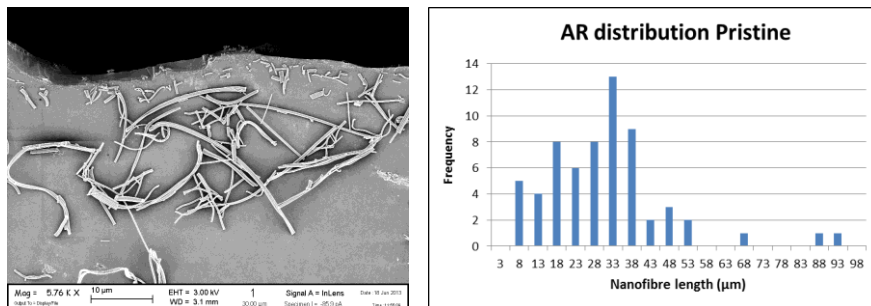


Figure 4 - Pristine TiO₂_1_NF sample morphology and AR distribution by SEM images.

SEM images showed that samples were agglomerated together (Fig. 4). Single fibre diameter was found to be between 20 - 30 nm, while agglomerated fibres showed a diameter of 150 - 500 nm, depending on the amount of single fibres connected. The average AR calculated for pristine sample was 28.5.

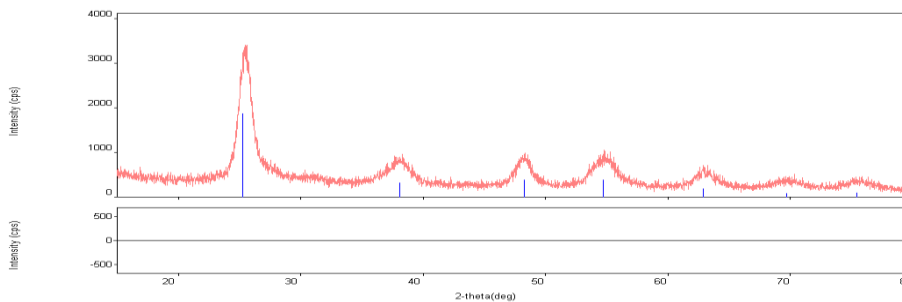


Figure 5 – XRD spectrum of pristine TiO₂_1_NF sample.

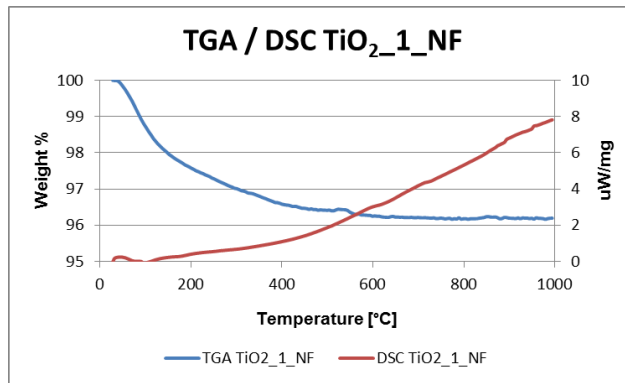


Figure 6 - TGA/DSC analysis of pristine TiO₂_1_NF sample.

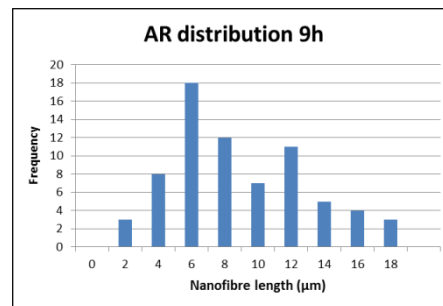
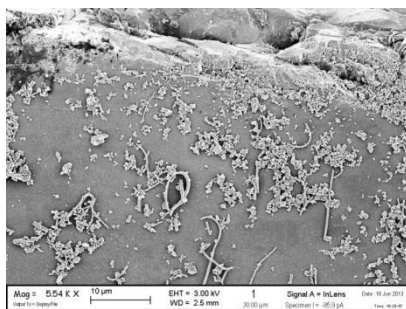
From XRD spectra provided from Elmarco (Fig. 5), the crystalline phase in pristine sample was anatase. The thermal analysis (Fig. 6) showed an overall weight loss of 4 wt.% ca. up to 1 000 °C, confirming that no PVP residue was present on pristine NFs after calcination.

5.3.2 Application of RRS at lab-scale level

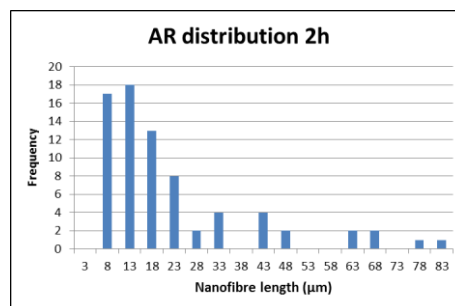
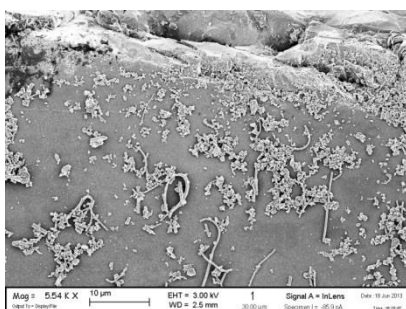
5.3.2.1 Handling and manufacturing

The fibrous shape of a NM has been considered as a “structural alert” as it is the cause of failed phagocytosis and the translocation in various biological compartments. Moreover, long fibres cannot be phagocytized and cleared, resulting in an higher toxic potential [19]. Therefore RRS of wet ball milling was proposed to homogenize and decrease NF length, and, as a consequence, their aspect ratio. Modified samples, obtained after different ball milling time, were observed by SEM-FEG (Fig. 7).

a)



b)



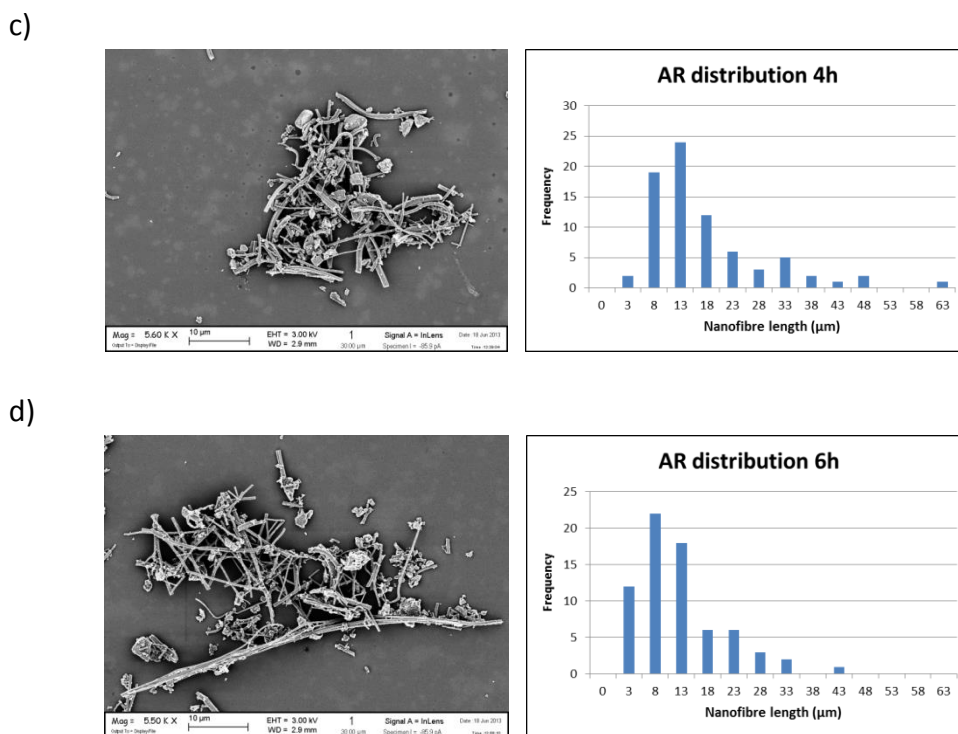


Figure 7 – Morphology of the ball milled a) TiO₂_8_NF, b) TiO₂_9_NF, c) TiO₂_10_NF, d) TiO₂_11_NF samples and their AR distributions calculated from SEM-FEG images.

The AR of pristine TiO₂_1_NF and modified samples was calculated from fibre length and diameter obtained by SEM-FEG images (Table 1).

Table 1 - Summary of AR determination for the TiO₂ NF samples.

Sample code	Milling time [h]	Average length [μm]	Average diameter [μm]	AR Min.	AR Ave.	AR Max.
TiO ₂ _1_NF	0	9.93	0.34	4.53	28.54	89.90
TiO ₂ _8_NF	9	2.78	0.36	4.11	7.82	16.93
TiO ₂ _9_NF	2	8.42	0.42	3.90	19.80	78.56
TiO ₂ _10_NF	4	5.84	0.38	2.67	15.09	60.55
TiO ₂ _11_NF	6	3.68	0.35	1.72	10.27	40.81

Thus, the process of ball milling seems to be an efficient method to homogenize and decrease NF AR. The pristine material showed a broad AR distribution, ranging from about 5 to 90. Increasing milling time, the NF length was reduced from 9.9 to 2.8 μm, giving a lower AR material. Following the “fibre pathogenicity paradigm”, a safe fibrous material should have a certain diameter and length and, moreover, to be not biopersistent^[19]. An aerodynamic diameter > 3μm, make the NM too thick to be inhalable, being the cut-off for inhalation in humans around 5 μm as aerodynamic diameter (for fibres, the aerodynamic diameter may be approximately evaluate as 3-times the actual diameter)^[20]. A fibre length < 5 μm was demonstrated to be a value that hinder frustrated phagocytosis^[20, 21]. Finally, a NF should be not biopersistent to undergo a rapid dissolution in the lungs. Modified samples maintained

the same diameter of pristine sample: 0.34 - 0.42 μm , below the safe range. Nevertheless NFs reached a length lower than 5 μm only after 6 h (TiO₂_11_NF) and 9 h (TiO₂_8_NF) of milling treatment. Due to the high inhomogeneity of the pristine sample, long fibres remained also after milling, affecting the value of the average AR. To remove the longer fibres, a preliminary filtration should be applied and coupled, if required, with a longer milling time.

The intrinsic production of ROS of TiO₂ NFs and the bench mark controls (crocidolite and P25 TiO₂) were assessed by co-incubation of the particles with a spin trap (Tempone-H) to detect the release of oxygen centered free radicals. The signal created by the production of ROS was compared to vehicle control (phosphate buffer) and a positive control (100 μM of pyrogallol), and the results are shown in figure 8, with some representative spectra shown in figure 9.

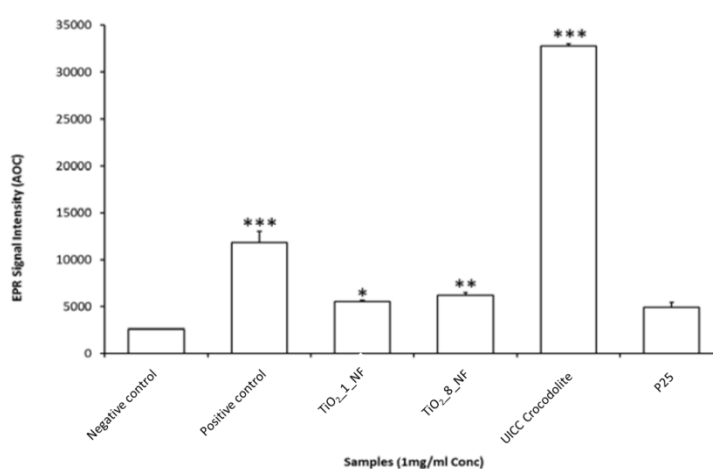


Figure 8 - EPR signal intensity after co-incubation with long TiO₂_1_NF, ball milled TiO₂_8_NF, UICC crocidolite and P25. Results are expressed as mean +/- standard error of the mean (sem) (n = 3). *** p < 0.001, ** p < 0.01, * p < 0.05 versus vehicle control.

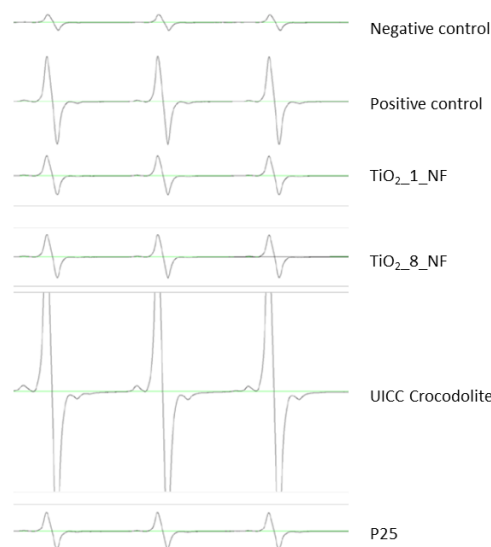


Figure 9 - Representative EPR spectra after co-incubation with long TiO₂_1_NF, ball milled TiO₂_8_NF, UICC crocidolite and P25.

The long and ball milled TiO₂ NFs did not induced significant ROS production above vehicle control, showing a signal not significantly different from that of P25, employed as benchmark material. These results suggested that the reactivity was primarily due to bulk chemistry, as demonstrated by the fact that there was no difference in ROS production between the long and ball milled TiO₂ NF with the same bulk chemistry, while crocidolite, characterized by different bulk chemistry, caused high levels of ROS production.

To evaluate if the RRS of wet milling preserved the functional properties of the material in energy applications, the NF E_g was evaluated through spectrophotometric method. As reported in literature the variations of E_g for NF sample may be attributed to their morphology and size [22,23,24] and usually an increase of E_g is expected decreasing the material size. This phenomenon, described as "quantum confinement effect", was mainly caused by the high surface energy of NF. The reference values of E_g for bulk TiO₂ materials were 3.2 eV for anatase phase and 3.0 eV for the rutile one. In table 2 are reported the particle size and E_g for pristine and modified samples.

Table 2 - E_g of the TiO₂ NF samples.

Sample code	Milling time [h]	Average length [μm]	AR Ave.	Band gap energy [eV]
TiO ₂ _1_NF	0	9.93	28.54	3.022
TiO ₂ _8_NF	9	2.78	7.82	3.108
TiO ₂ _9_NF	2	8.42	19.80	3.096
TiO ₂ _10_NF	4	5.84	15.09	3.064
TiO ₂ _11_NF	6	3.68	10.27	3.127

As general trend, extending milling time the fibres length decreased and their E_g became wider; therefore RRS of wet milling may be a good method to homogenize and reduce NF AR, increasing their functional properties. Basing on the AR, EPR and E_g results, the TiO₂_8_NF sample was selected for toxicity evaluation, being this sample expected to be less toxic (lower AR and ROS production) still maintaining a good functional performance.

5.3.3 Toxicity outcomes

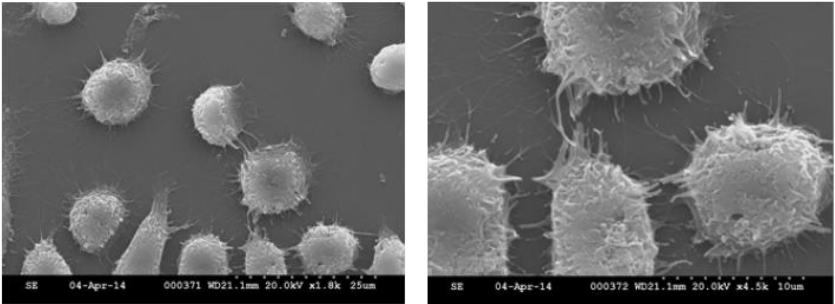
To evaluate the health hazard reduction following the introduction of RRS, the toxicological profile of TiO₂ NF and its modified, ball-milled, form were studied in vitro and compared. Cell lines employed have been chosen by biologists as a function of the involved industrial scenario and NM application. In all processing lines the exposure was supposed to occur mainly by inhalation, thus for viability and cytotoxicity tests, two cell lines were selected: A549 and RAW 264.7 cells, alveolar epithelial cells and macrophages, respectively. Both cell types were typically encountered by NMs after inhalation and their interaction determined the biological outcome of the exposure. For toxicity evaluation, UICC crocidolite and P25 were used as benchmark materials. UICC crocidolite significantly increased the EPR signal detected, suggesting its ability to self-generate ROS. However, neither ROS or signs of oxidative stress were found in the DCFH assay. On the contrary, the results of the tests performed, indicated that crocidolite significantly reduced the level of GSH in macrophages and increased the level of lipid peroxidation in both cell types, indicating an oxidative stress.

Pristine TiO₂_1_NF exhibited a marked cytotoxicity versus A549 epithelial cells, but was found to be only mildly toxic for RAW 264.7 macrophages. Both pristine and modified NFs gave a small EPR signal suggesting they may intrinsically produce ROS. However, in cell culture medium, no ROS production was evidenced employing the acellular DCFH assay and no sign of oxidative stress was evidenced by the DCFH assay in both macrophages and epithelial cells. The oxidative stress was associated with a significant decrease in the level of GSH in macrophages following incubation with the pristine, but not with the modified TiO₂_8_NF sample. Finally, a small signal for TBARs suggested that both pristine and remediated forms of TiO₂ NF may induce a slight lipid peroxidation in macrophages. The results obtained showed that ball milling procedures significantly reduced the cytotoxic effects of TiO₂_1_NF on epithelial cells, as well as their effects on the epithelial barrier and oxidative changes, thus confirming the relevant role of AR in determine the cytotoxicity of fibrous materials. On the other hand, the modified TiO₂_8_NF sample exhibited an higher capacity to activate macrophages and, therefore, it was expected to be more pro-inflammatory than the pristine sample.

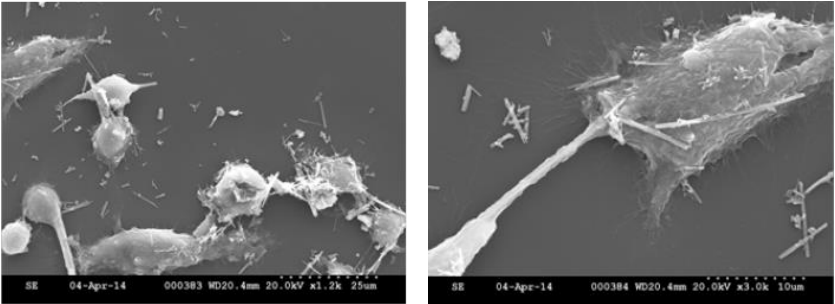
To study how cells interact with NF materials tested, IOM treated macrophages with sub-lethal concentration of the NF material involved, to observe cell morphology and sign of “frustrated phagocytosis” by SEM (Fig. 9). When macrophages were incubated with long crocidolite fibres, they tried to engulf the NF material by spreading along it. However, when crocidolite fibres were too long for being internalized, macrophages ended up in a “frustrated phagocytosis”. The same situation was observed when macrophages were treated with

pristine TiO₂_1_NF sample. On the contrary, when cells were treated with either Aeroxide® P25 or the ball milled TiO₂_8_NF sample (Fig. 10), they kept their round shape and no sign of “frustrated phagocytosis” was observed.

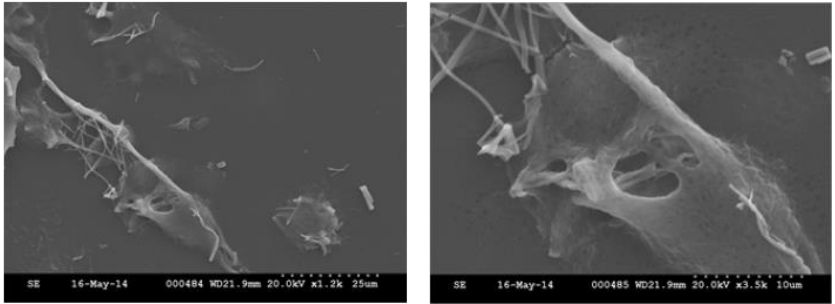
a)



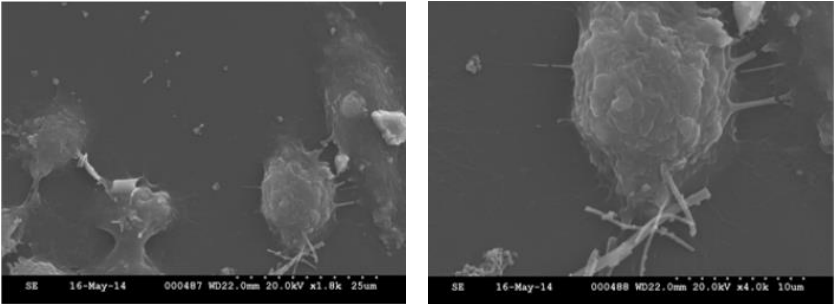
b)



c)



d)



e)

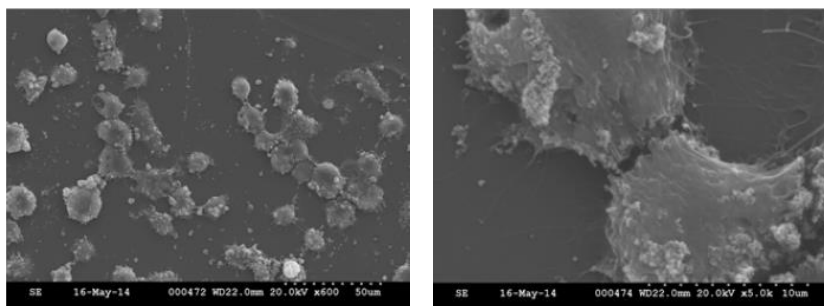


Figure 10 - Characterization of cell/materials interactions by SEM. Macrophages were seeded on coverslips and treated for 24 h with the indicated materials at $10 \mu\text{g}/\text{cm}^2$. The preparations were fixed and dehydrated before being mounted on stub for SEM analysis. Representative images at increasing magnification were taken a) untreated cells, b) UICC crocidolite, c) pristine TiO_2 _1_NF sample, d) modified TiO_2 _8_NF sample, e) P25

The ability of long fibres, or high AR materials, to engage with macrophages and to trigger “frustrated phagocytosis” was already extensively reported in the literature [25,26]. Altogether, these results showed that the pristine TiO_2 NF induced pathological “frustrated phagocytosis” in macrophage, unlike the modified form, suggesting a “remediation” of the material for this particular end-point. RRS strategy proposed seemed to significantly mitigate cytotoxicity, frustrated phagocytosis and oxidative stress, although producing a modified material with a greater pro-inflammatory activity, likely related to LPS contamination during the ball milling procedure.

To investigate the effect of prolonged exposure to TiO_2 NF, genotoxicity tests were performed with A549 and Balb/3T3 cells; in both cell lines, TiO_2 samples showed a genotoxic potential in vitro. Genotoxicity, evaluated by different endpoints, showed that TiO_2 _1_NF induced chromosome damage, DNA strand breaks and oxidation and cell morphological transformation, characteristic of tumorigenic cells. The modified TiO_2 _8_NF sample and the benchmark material Crocidolite resulted carcinogenic towards Balb/3T3 cells in vitro, showing that ball-milling did not affect the genotoxic potential of involved NF samples. Such as previously observed for the PL 1 and PL 5 NM, the solvent controls showed genotoxic and carcinogenic potential, suggesting that the effects observed may be not due exclusively to NMs, but also to their solvent, that may promote leaching phenomena or contain “toxic contaminants”.

5.3.4 Exposure assessment: off-line and on-site measurements

EA started from a “basic measurement campaign” in Elmarco settings to verify the emission of TiO_2 NFs during the handling and manufacturing steps, supposed to be critical. The exposure investigation was focused on Ti-containing fibrous. The instruments used by Ineris were the same used in the other measurement campaign to compare the results obtained. The real time CPC was used between the main potential sources and outlets, to determine the total particle concentration in number, in the range $10 \text{ nm} - 1 \mu\text{m}$. A TEM grid sampler was employed to measure the NPs near to the respiratory system, collecting them on specific TEM grids, which were observed by TEM.

The characterization of the background aerosol noise revealed an high number of particles, in the order of 3 000 – 4 000 particles/cm³. From TEM grid observation, these particles were mainly composed by oil droplets, soot and debris, commonly found in ambient air and typical of building materials. But from EDS analysis, none of these particles seemed to arise from TiO₂ NFs, because Ti was not detected. Different common handling operations were considered and evaluated, from the oven opening to the fibre transport, ground and packaging (Fig. 11).

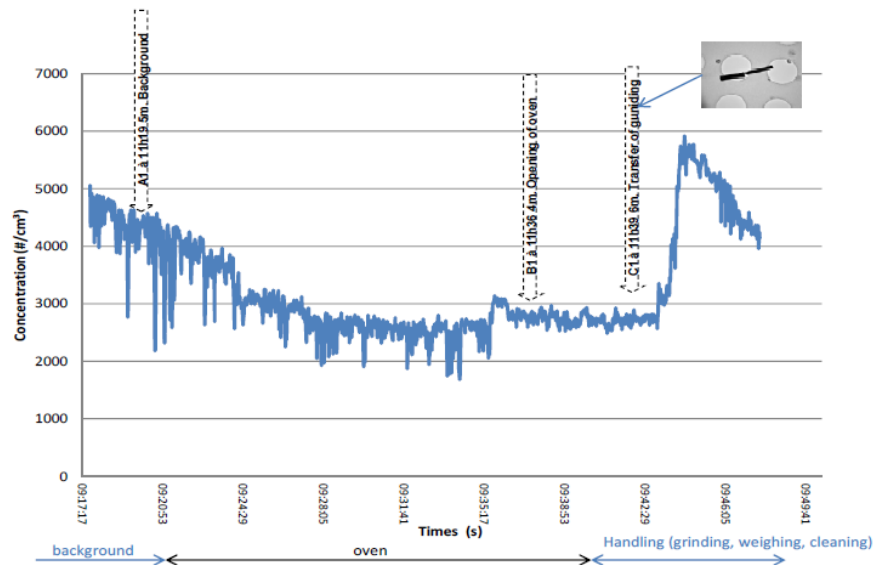


Figure 11 - Temporal monitoring of particle concentration evolution during preliminary campaign by Elmarco

The count increased sharply, reaching a maximum of nearly 6 000 particles/cm³, during NF handling operations. Concurrently with the increased particle count, from the observation and EDS analysis of sampling grids, the particles collected revealed the presence of TiO₂ NFs, that did not represent a numeric majority, but were immediately apparent due to their size. The TiO₂ fibres were generally of sub-micron length, whereas their diameter was generally between 150 nm and 500 nm.

5.4 Conclusions

To reduce the related health hazard, TiO₂ NF samples were subjected to a wet ball milling treatment as RRS. The milling procedure allowed to homogenize and reduce TiO₂ NF AR. From the evaluation of TiO₂ NF functional performance, an improvement of functional properties may be hypothesized, as extending the milling time the NF length decrease and their E_g become wider.

To evaluate an health hazard potential mitigation due to RRS application, pristine and modified samples toxicity were evaluated and compared. The RRS strategy proposed seemed to significantly mitigate cytotoxicity, frustrated phagocytosis and oxidative stress, although producing TiO₂ NF with a greater pro-inflammatory activity, likely referable to LPS

contamination. Ball milling significantly reduces the cytotoxic effects of TiO₂ NFs on epithelial cells as well as their effects on the epithelial barrier and oxidative changes, confirming the relevant role of AR in the cytotoxicity of fibrous materials. The modified TiO₂_8_ NF sample, exhibited an higher capacity to activate macrophages and, therefore, it was expected to be more pro-inflammatory than the pristine sample.

During preliminary exposure measurement campaign, no TiO₂ emission was detectable, neither by a particle count nor through sampling, until the TiO₂ NF material was manipulated. As soon as handling operations begun, under a switched-off fume hood, a significant peak was observed. The sample collected on sampling grid during the transfer and grinding operations, revealed the presence of TiO₂ NFs with diameter between 150 and 500 nm and sub-micrometer length.

5.5 References

- [1]. E. Formo, E. Lee, D. Campbell, and Y. Xia, *Nano Lett.*, **2008**, 8, 688 - 672
- [2]. R. Dan Li, Y. Yin, J. T. McCann, and Y. Xia, *Nano Lett.*, **2006**, 6, 1297 - 1302
- [3]. Y. Dai, B. Lim, Y. Yang, C. M. Cobley, W. Li, E. C. Cho, B. Grayson, P. T. Fanson, C. T. Campbell, Y. Sun, and Y. Xia, *Angew. Chem.* **2010**, 122, 8341 - 8344
- [4]. J. Li, X. Chen, N. Ai, J. Hao, Q. Chen, S. Strauf, Y. Shi, *Chem. Phys. Lett.*, **2011**, 514, 141 - 145
- [5]. L. Yang and W. W. Leung, *Adv. Mater.*, **2013**, 25, 1792 - 1795
- [6]. B. Ding, M. Wang, X. Wang, J. Yu, G. Sun, *Mater. Today*, **2010**, 13, 16 - 27
- [7]. J. Gong, Y. Li, Z. Hu, Z. Zhou, and Y. Deng, *J. Phys. Chem. C*, **2010**, 114, 9970 - 9974
- [8]. Z. Li, H. Zhang, W. Zheng, W. Wang, H. Huang, C. Wang, A. G. MacDiarmid, and Y. Wei, *J. Am. Chem. Soc.*, **2008**, 130, 5036 - 5037
- [9]. X. Wang, B. Ding and B. Li, *Mater. Today*, **2013**, 16, 229 - 24
- [10]. V. J. Reddy, S. Radhakrishnan, R. Ravichandran, S. Mukherjee, R. Balamurugan, S. Sundarrajan, S. Ramakrishna, *Wound Rep. Reg.*, **2013**, 21, 1 - 16
- [11]. K. S. Rho, L. Jeong, G. Lee, B. Seo, Y. J. Park, S. Hong, S. Roh, J. J. Choa, W. H. Park, B. Min, *Biomater.*, **2006**, 27, 1452 - 1461
- [12]. T. J. Sill, H. A. von Recum, *Biomater.*, **2008**, 29, 1989 - 2006
- [13]. L. Yan, S. Si, Y. Chen, T. Yuan, H. Fan, Y. Yao, and Q. Zhang, *Fiber. Polym.*, **2011**, 12, 207 - 213
- [14]. W. Jao, M. Yang, C. Lin and C. Hsu, *Polym. Adv. Technol.*, **2012**, 23, 1066 - 1076
- [15]. F. A. Sheikh, N. A. M. Barakat, M. A. Kanjwal, R. Nirmala, J. H. Lee, H. Kim, H. Y. Kim, *J. Mater. Sci. Mater. Med.*, **2010**, 21, 2551 - 2559
- [16]. J. I. Lim, B. Yu, K. M. Woo, Y. Lee, *Appl. Surf. Sci.*, **2008**, 255, 2456 - 2460
- [17]. J. Muller, F. Huaux, N. Moreau, P. Misson, J. Heilier, M. Delos, M. Arras, A. Fonseca, J. B. Nagy, D. Lison, *Toxicol. Appl. Pharm.*, **2005**, 207, 221 - 231
- [18]. A. D. Maynard, P. A. Baron, M. Foley, A. A. Shvedova, E. R. Kisin and V. Castranova, *J. Toxicol. Env. Health*, **2004**, 67, 87 - 10

- [19]. K. Donaldson, F. Murphy, A. Schinwald, R. Duffin and C. A. Poland, *Nanomedicine*, **2011**, 6, 143 - 156
- [20]. K. Donaldson, *Crit. Rev. Toxicol.*, **2009**; 39, 487 - 500
- [21]. K. Donaldson, F. A. Murphy, R. Duffin, C. A Poland, *Part. Fibre Toxicol.*, **2010**, 7:5, 1 - 17
- [22]. Y. Zhao, C. Li, X. Liu, F. Gu, H. Jiang, W. Shao, L. Zhang, Y. He, *Mater. Lett.*, **2007**, 61, 79 - 83
- [23]. K. M. Reddy, S. V. Manorama, A. R. Reddy, *Mater. Chem. Phys.*, **2002**, 78, 239 - 245
- [24]. J. Thomas, M. Yoon, *Appl. Catal. B Environ.*, **2012**, 111 - 112, 502 - 508
- [25]. F. A M., A. Schinwald, C. A. Poland and K. Donaldson, *Part. Fibre Toxicol.*, **2012**, 9:8, 1 - 15
- [26]. A. Schinwald, T. Chernova and K. Donaldson, *Part. Fibre Toxicol.*, **2012**, 9:47, 1 - 15

6. Processing line 5: spray coating line (Ag and TiO₂ nanosol)

6.1 Introduction

6.1.1 Ag and TiO₂ nanomaterials

The extensive literature on Ag NP synthesis and engineering, demonstrates an increasing attention on this material, already known and broadly used since long time for its strong antibacterial effects [1]. Nano Ag has been synthesized in different size and shape employing many methods, including chemical reduction [2, 3], polyol method [4, 5, 6] and more environmentally friendly methods such as photochemical [7], polysaccharide or biological methods [8]. Ag nanomaterial has been also synthesized in form of nanocomposite [9, 10], core shell [11, 12] and nanoalloy [13, 14].

The antibacterial activity of Ag material together with the possibility to obtain controlled size and shape, have been exploited in many field, first of all in biomedical application [15]. Nano Ag has been investigated as promising candidate in wound dressing [16], prosthetic device [17] and in bone repair composite [18]. As a further application, in recent years, nano Ag was investigated for antibacterial coating [19, 20] and as antibacterial additive in paint [21], by which the antibacterial property of Ag material was conferred to different substrate.

Different synthetic procedures have been developed and reported in literature to obtain nano TiO₂ dispersion and powders, including sol-gel [22, 23, 24] and modified sol-gel [25], hydrothermal [26], combustion [27] or flame [28] synthesis. TiO₂ is a semiconductor and photocatalytic oxide, that by interaction with light of comparable energy to its band gap, produces electron hole/pairs that reacts with adsorbed water and dissolved oxygen to produce ROS. These radicals oxidize materials adsorbed on the TiO₂ surface, leading to their degradation to CO₂ and H₂O [29]. For this property, enhanced by its nanoscale, TiO₂ has been extensively employed in catalysis, either alone, doped, or in nanocomposite, for water-splitting [30, 31], to oxidize organic matter [23] and to decompose environment pollutants [32, 33, 34]. Nanosized TiO₂ has been employed in many coating application. TiO₂ film has been used for air and water purification, heat transfer/dissipation and as anticorrosion agent [35]. TiO₂ allows to obtain antibacterial and self-sterilizing [36] surfaces. TiO₂ coating has been used in anti-fogging application because it can photo-induce hydrophilicity [37, 38, 39] on treated substrate. The ability to decompose organic molecules under UV irradiation suggested its employ as self-cleaning coating for different surfaces [40], especially for textile [41, 42].

When NM are involved in different applications in medical fields, their hazardous properties should be carefully considered. As reported, within toxicological paradigms nano size dimension [43], presence of contaminant [44], high aspect ratio shape [45], redox and acidic/basic properties as well as surface charge [46] may influence NM toxicity.

6.1.2 Description of Processing line 5

PL 5 consider the procedure owned by Colorobbia, that provided Ag and TiO₂ nanosols as well as information on synthetic and spray coating procedure, letting available the industrial scenario for the evaluation and implementation of RRS. The main steps of sol-gel synthetic procedure are reported in figure 1.

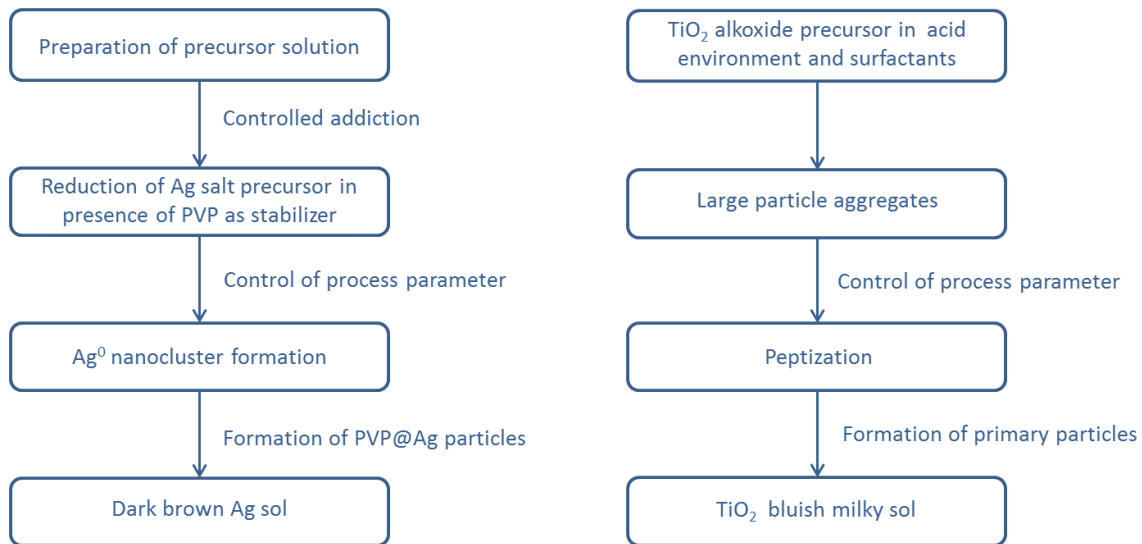


Figure 1 - Colorobbia Ag (left) and TiO₂ (right) nanosol synthetic scheme

Ag NPs were obtained by reduction of a solution of Ag salts in presence of PVP, glucose and NaOH. In the synthesis, the temperature control was critical for final Ag nanosol properties and characteristic. The final sol appeared as a dark-brown solution, due to the plasmon band of Ag NPs and their high concentration in the dispersion.

Titanium dioxide NPs were produced by low temperature sol-gel technique. The precursors were titanium alkoxide, inorganic acid, surfactants and water. The reaction temperature was a key parameter and had to be controlled to promote the peptization process of the large particle aggregates obtained at the beginning of the reaction. The sol obtained after a predefined reaction time appeared as a bluish milky sol, due to Tyndall's effect.

The sols, as they were synthesized, or after their dilution with water or alcohol, were sprayed on the surface of material to be coated by spray gun technique. The coated ceramic or glass tile was conveyed along an electric kiln where a thermal treatment allowed to fix the coating to the surface of the material. Depending on the nature of surface, the thermal treatment were carried out at temperature about 500 or 700 °C, for glass and ceramic tile respectively. At the end of process line, the tiles coming out from the oven were removed and let to cool.

6.1.3 Critical step identified and RRS proposed

A general scheme of PL 5 is reported in figure 2.

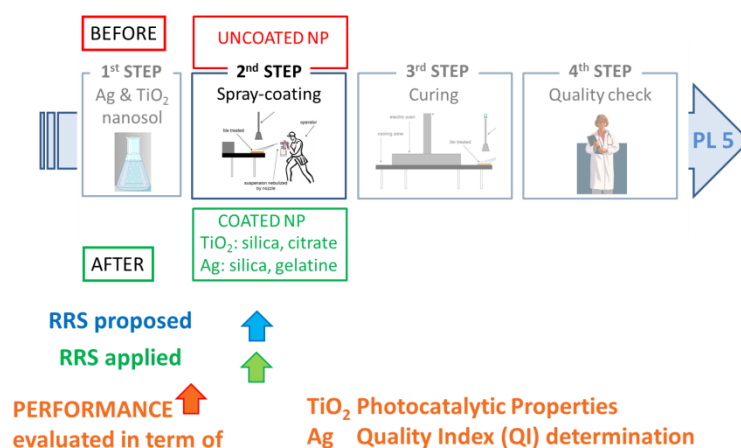


Figure 2 - Scheme of PL 5, showing process steps in which RRS were applied and evaluated

Along PL 5, the key step for health hazard and EA was the spray coating operation. The two scenarios that took shape with the introduction of RRS were defined as BEFORE and AFTER one, in relation to NMs employed.

6.1.3.1 Spray coating

The critical step to be monitored was the spray coating of the substrate, due to the potential NM emission that may imply a critical exposure spot for workers. During this step, different RRS were proposed both to decrease NM exposure and toxicity and maintain or improve NM technological performance. Ag was subjected to blending with colloidal SiO₂, purification and surface coating. TiO₂ was modified by blending with colloidal SiO₂, surface coating and spray drying. The BEFORE exposure scenario was represented by the spraying of the pristine sol, while in the AFTER exposure scenario modified sols were employed. For clearness, in the following paragraphs the experimental activity involving Ag and TiO₂ nanosols will be reported and discussed separately.

6.2 Experimental

6.2.1 Preliminary characterization of involved nanosols

6.2.1.1 Preliminary characterization of Ag sample

Pristine Ag, encoded as **Ag_1_sol**, was provided by Colorobbia and subjected to preliminary characterizations. NP size distribution, shape and presence of a crystalline phase were obtained by HR-TEM (JEOL JEM-2100F, USA). d_H and ZP were evaluated by a Zetasizer nano ZSP (Malvern Instruments, UK). XRF (Panalytical Axios Advanced, NL) or AAS (Perkin Elmer, USA) were employed to evaluate Ag concentration. To assess the presence and amount

of stabilizers, an aliquot of sol sample was dried and subjected to thermal analysis; TGA tests were performed in a PL-STA 1500 (PL Thermal Science, UK), using a temperature ramp of 10 °C/min from 25 up to 600 °C in air. Different techniques were employed to separate the Ag NPs from its cationic fraction; the SC (100 kDa, Merck Millipore) and the CFU (Amicon Ultra-15, 10 kDa, Merck Millipore) were employed, allowing to retain Ag NPs and filtrating the Ag⁺ ions.

Sample antibacterial activity against Escherichia Coli was selected as material functional property and assessed by Colorobbia laboratory. Escherichia Coli strain ATCC8739 was chosen as model microorganism for inactivation experiments. For the antibacterial activity assay the pristine and purified Ag samples were diluted with Mill-Q water and used as Ag stock solutions. The inoculum containing 1 ml of bacterial suspension (10⁶ cell/ml) in 9 ml of MilliQ-water was used for unexposed control, in the other test 1 ml of bacterial suspension (10⁶ cell/ml) was added to 9 ml of the Ag stock solution. After 2, 5 or 24 h, 1 ml from each sample was recovered, diluted, inoculated in a culture agar plate and incubated, then after 48 h the viable cell count was performed. The antibacterial activity of Ag nanosols was calculate using the following equations:

$$\mathbf{R \log = [\log(B/A) - (\log(C/A))] = [\log(B/C)]}$$

where:

R log: value of antibacterial activity

A: average of viable bacterial cells on untreated samples at 0 h of exposure time

B: average of viable bacterial cells on untreated samples at 24 h of exposure time

C: average of viable bacterial cells on Ag nanosol treated samples at 24 h of exposure time

$$\mathbf{R \% = 100 \times (B - A) \times B}$$

where:

R %: value of antibacterial activity

A: average of viable bacterial cells on Ag nanosol treated samples at 24 h of exposure time

B: average of viable bacterial cells on Ag nanosol untreated samples at 24 h exposure time

Before the antibacterial activity assay the total Ag concentration in the Ag stock solution was determined by a Liberty 200 ICP-OES (Varian, AU), as well as the Ag⁺ concentrations. The Ag⁺ content in the samples were obtained filtering an aliquot of these through CFU (Amicon Ultra-15, 10 kDa, Merck Millipore) and measuring the Ag concentration in the filtrate, being the filter able to retain Ag NPs. Each test was conducted in triplicate.

6.2.1.2 Preliminary characterization of TiO₂ sample

Pristine TiO₂, encoded as **TiO₂_6_sol**, was provided by Colorobbia and subjected to preliminary characterizations. HR-TEM (JEOL JEM-2100F, USA) was used to assess the particle size distribution and shape. Size and ZP were evaluated with a Zetasizer nano ZSP (Malvern Instruments, UK). XRF (Panalytical Axios Advanced, NL) were employed to measure TiO₂ concentration in the dispersion. Crystalline phase of TiO₂ was investigated by XRD (D8 ADVANCE, Bruker AXS, GE) on a dried sample.

Self-cleaning properties in pristine and modified samples were evaluated by the photodegradation efficiency of RhB dye, performing test on sols at room temperature. In each test, the total volume of the dispersion to be tested and its RhB and TiO₂ content, were kept constant respectively at 25 ml, 0.007 mg/ml and 3 wt.%. The sol samples TiO₂_6_sol, TiO₂_18_sil_sol or TiO₂_36_cit_sol or the TiO₂_15_NP_SD dispersion, were placed in a becker; then, under magnetic stirring, the RhB was added and the dispersion irradiated with an UV radiation intensity of 1.3 mW/cm² (Osram ULTRA-Vitalux lamp). The RhB degradation progress were monitored at regular times by collecting 3 mL of the dispersion and measuring the absorbance at $\lambda = 554$ nm in a quartz cuvette using an UV-vis single beam spectrophotometer S-22 (Boeco, GE). After UV determination, the measured aliquot was added again to the dispersion, to keep constant the total volume during the test. According to the Lambert-Beer law, the degradation or conversion rate of the RhB dyes was calculated by the formula:

$$\text{Conversion \%} = (C_0 - C_t) / C_0 \times 100 = (A_0 - A_t) / A_0 \times 100$$

where:

C₀: initial RhB concentration

C_t: concentration of RhB after the photocatalysis reaction

A₀: initial RhB absorbance

A_t: absorbance of RhB after the photocatalysis reaction

The photo degradation activities were compared by measuring the RhB conversion % at 60 min, also defined as RhB degradation efficiency %.

6.2.2 Application of RRS at lab-scale level

To decrease the potential toxicity of NMs involved and the potential emission during spray process, different surface engineering were applied, producing the samples described and listed below.

6.2.2.1 Ag samples

- Modified sample **Ag_15_sil_sol**, was obtained by mixing pristine Ag nanosol with commercial colloidal SiO₂ (SiO₂/Ag = 0.2 and [Ag] = 1.78 wt.%) and then ball milling for 24 h the sample to promote homogenization.

- Modified sample **Ag_31_sol_UF** was obtained starting from the diluted pristine Ag_{1.3_sol} ([Ag] = 1 wt.%) applying ultrafiltration treatments to remove the unreacted Ag⁺ cations.
- Modified sample **Ag_35_sil_sol** was prepared following Stöber's method ^[47], setting Ag:SiO₂ weight ratio 1:0.2 and Ag content equal to 0.08 wt.%. Pristine Ag sol was diluted up to 0.4 wt.% in water/ethanol (weight ratio = 1:4), followed by NH₄OH and TEOS addition. The mixture was magnetically stirred for 24 h at room temperature. Afterwards, synthesized nanosol underwent ultrafiltration with a SC to remove synthesis by-products and obtain neutral pH.

NP size distribution and shape were obtained by HR-TEM (JEOL JEM-2100F, USA). d_H and ZP were evaluated with a Zetasizer nano ZSP (Malvern Instruments, UK). Total Ag and SiO₂ content was measured by XRF (Panalytical Axios Advanced, NL) or AAS (Perkin Elmer, USA). SC (100 kDa, Merck Millipore) and CFU (Amicon Ultra-15, 10 kDa, Millipore) were used to separate the Ag⁺ fraction from Ag NP. Antibacterial activity of selected modified sample was assessed by Colorobbia laboratory against Escherichia Coli following the experimental condition explained in paragraph 6.2.1.1.

6.2.2.2 TiO₂ samples

- Modified sample **TiO₂_15_NP_SD** was prepared by spray drying of the pristine TiO₂ sample in a lab scale atomizer (spray dryer SD-05, Lab-Plant), obtaining a granulated powder.
- Modified sample **TiO₂_18_sil_sol**, was obtained by mixing pristine TiO₂ nanosol with commercial colloidal SiO₂ (SiO₂/TiO₂ = 3; total solid concentration 3 wt.%) and then ball milling for 24 h the sample to homogenize.
- Modified sample **TiO₂_36_cit_sol** was obtained by mixing pristine TiO₂ nanosol with trisodium citrate dihydrate (TiO₂/citrate weight ratio = 1.00/0.83 and [TiO₂] = 3 wt.%) and stirring overnight the dispersion.

HR-TEM (JEOL JEM-2100F, USA) was used to assess the particle size distribution and shape, EDS to evaluate the amount of SiO₂. XRF (Panalytical Axios Advanced, NL) was employed to measure TiO₂ and SiO₂ concentration in the dispersion. Size and ZP were measured with a Zetasizer nano ZSP (Malvern Instruments, UK). Spray dried sample was subjected to BET measurement of SSA by a Sorptly 1750, using N₂ as adsorption gas (Carlo Erba, I) to evaluate the presence of a nanostructured surface, then XPS AXIS 165 (Manchester, UK) was employed to assess the powder surface composition. Self-cleaning properties of the samples were evaluated by the photodegradation efficiency of RhB, following the experimental conditions reported in paragraph 6.2.1.2.

6.2.3 Implementation of RRS within the Processing line 5

Ag and TiO₂ modified samples showing the better functional properties at lab scale level, have been selected for the implementation within PL. Samples involved are described below.

6.2.3.1 Ag samples

- Pristine Ag sample **CT Ag_1_sol** was obtained by Colorobbia applying pristine Ag_1_sol by spray coating on ceramic tiles.
- Modified sample **CT Ag_31_sol_UF** was obtained by Colorobbia employing Ag_31_sol_UF for the spray coating of ceramic tiles.

Antibacterial activity of ceramic tiles coated by pristine and modified samples were assessed by Colorobbia laboratory against Escherichia Coli. Pristine and modified Ag samples, respectively Ag_1_sol and Ag_31_sol_UF, were diluted with Mill-Q water till a final Ag concentration of 0.1 wt.% and used to confer antibacterial properties; one ceramic tile for each Ag sample was prepared. Ag coating was applied by spray gun to obtain a nominal Ag content of 0.5 g on each tile. The coating was thermally treated using an electric muffle with a thermal cycle of 2.5 h ramp and 30 min dwelling at 700°C. Finally the tile surface was cleaned up with isopropyl alcohol 70 vol.%. The resulting tiles were used without further treatments for microbial tests. Culture plates were built on tile surface using a plastic hoop as plate outer limit, allowing the bacterial suspension to go in touch with the treated tile surface. The stock strain was sub-cultured in tryptic soy agar overnight. Then, for each test, the bacterial suspension was diluted in 10 ml of water reaching 10⁵ cell/ml concentration and used as inoculum. For each sample, three tests were performed. After 24 h, the inoculum from each sample was recovered, diluted, inoculated in a Plate Culture Agar and incubated; after 48 h the viable cell count was performed. The Ag coated tile antibacterial activity was calculate following the equations reported in paragraph 6.2.1.1.

The presence and distribution of Ag within the coated tiles were evaluated by Colorobbia employing a LA-ICP-MS X series 2 (Thermo Fischer Scientific, USA). One ceramic tile without treatment was measured for comparison, making two line raster composed by 9 measurement point. The coated tiles CT Ag_1_sol and CT Ag_31_sol_UF were analyzed making 5 line raster composed by different measurement point.

6.2.3.2 TiO₂ samples

- Pristine TiO₂ sample, encoded as **CT TiO₂_6_sol**, was obtained by Colorobbia applying pristine TiO₂_6_sol by spray coating on a ceramic tile.
- Modified sample **CT TiO₂_18_sil_sol** was obtained by Colorobbia employing TiO₂_18_sil_sol for the spray coating of a ceramic tile.
- Modified sample **CT TiO₂_36_cit_sol** was obtained by Colorobbia employing **TiO₂_36_cit_sol** for the spray coating of a ceramic tile.

Ceramic tiles coated by pristine and modified samples were assessed and compared by Colorobbia in term of photocatalytic degradation of NO and NO_x. Pristine and modified TiO₂ samples, respectively TiO₂_6_sol, TiO₂_18_sil_sol and TiO₂_36_cit_sol, were diluted with Milli-Q water till a TiO₂ final concentration of 1 wt.% and used to confer depolluting properties to the ceramic tiles. NM coating was applied by spray gun to obtain a nominal TiO₂ content of 0.5 g for each tile. The coating was thermally treated using an electric muffle with a thermal cycle of 2.5 h ramp and 30 min dwelling at 700°C. For depollution test, the coated ceramic tile was placed in a measurement chamber in which dry air, humid air and the pollutant NO were fed and recirculated using a peristaltic pump. A quartz windows above the chamber allowed the irradiation of the tile sample. The system conditions were controlled and managed by a software. A model 42i (NO-NO₂-NO_x) analyzer (ThermoScientific, USA) was connected to the system for the on-line monitoring of the NO, NO₂ and NO_x concentration versus reaction time.

6.2.4 Characterization of Ag and TiO₂ dispersion in biological media

Ag and TiO₂ samples tested by biologists for toxicological characterizations were also subjected to size and ZP measurement performed in biological relevant conditions, to understand the processes occurring during NMs-biological interactions. The dispersion state and colloidal stability, relevant parameters for the NMs-biological interactions, were investigated measuring size and ZP of pristine and modified nanosol, dispersed both in deionized water and cell culture media. d_H and ZP were obtained by DLS technique (Zetasizer nano ZSP, UK) following the standard operating procedure described hereafter. NM dispersion was ultrasonic treated for 15 min, then two sets of samples were prepared. For samples dispersed in culture medium, aliquots of NM dispersions were first added to BSA/PBS (0.05 vol.%) to obtain an intermediate that was added to cell culture medium supplemented with FBS (10 vol.%) to reach a final NM concentration of 128 µg/ml and 125 µg/ml, for Ag and TiO₂ samples respectively. The further set of samples were prepared diluting, with MilliQ water, Ag sol up to 128 µg/ml and TiO₂ up to 125 µg/ml. Dispersions were left to equilibrated for 1 h, then were vortex-mixed to ensure sample homogenization before size and ZP measurements.

d_H were obtained from DLS data expressed by intensity, in backscattering detection mode (scattering angle of 173 °) and setting measurement duration on automatic. After 2 min of temperature equilibration at 25 °C, 1 ml of sample volume was subjected to three consecutive measurements which were averaged to obtain d_H . After particle size determination, samples underwent ZP measurement by ELS. The Smoluchowski's approximation ^[48], consistent with the high dielectric constant of water, main component of all the above specified solvents, was applied to convert the electrophoretic mobility to ZP. Measurements were performed on 700 µl of sample, measurement duration, attenuator and applied voltage were set up automatically. After 2 min of temperature equilibration, samples underwent five measurements spaced out by 120 sec delay to avoid Joule heating. Before and after ZP analysis, a further size measurement was performed to check that the samples have not changed. ZP of NMs dispersed in cell culture medium was collected in monomodal mode due to the high medium conductivity, thus obtaining a mean ZP value.

6.2.4.1 Interaction between AgNPs and BSA

Furthermore during the research period at the University of Limerick, Ag NP tested by biologists, were investigated, studying the interaction between Ag NPs and BSA. The material used in the experiments was:

- BSA, MW= 66 000 g/mole, was obtained from Sigma Aldrich with 99% purity.
- Phosphate buffered saline (PBS) was freshly prepared using NaCl, KCl, KH_2PO_4 and $\text{Na}_2\text{HPO}_4 \cdot 2\text{H}_2\text{O}$ obtained from Sigma Aldrich to give pH 7 at 25 °C.
- BradfordUltra reagent was obtained from Expedeon and used to estimate the protein concentration. Bradford assay allow to shift the absorbance maximum of BSA from 280 nm to 595nm.
- MilliQ water was used in all experiments.

Preparation of BSA-Ag conjugated

To simulate the biological condition, for each Ag sample a series of BSA-Ag conjugates were prepared. The concentration series of BSA in PBS were prepared in 1 ml microcentrifuge tubes to obtain, after the addition of Ag sol under stirring, the appropriate BSA/Ag mass ratio. The investigated BSA/Ag mass ratio ranged from 0.5 to 300 (11 samples) and in each case, also one Ag sample only diluted in PBS (without BSA) was prepared for comparison. In all experiment the Ag concentration was kept constant at 0.1 mg/ml. Solutions were left to equilibrate for 1 h at room temperature in a biology shaker before analysis and separation experiments.

Separation of Ag NPs with strongly bound protein from the weakly interacting proteins

After 1, 24, 48 and 72 h of incubation with BSA, samples were subjected to 3 purification steps. During each step an aliquot of the solution was centrifuged in a micro-ultracentrifuge from 3 to 30 min at 10 000 rpm, then the supernatant were separated, the pellet collected and re-suspended in fresh PBS. This protocol allows to separate strongly bounded proteins from the weakly interacting or the excess of these. After different equilibration times, ranging from 1 to 72 h, the samples were subjected to different characterizations. UV-vis spectra were acquired with a NanoDrop 1000 Spectrophotometer in the 200-700 nm range to evaluate the BSA adsorption on Ag and to monitor the Ag SPR band in presence and absence of BSA. Ag-BSA conjugated were analyzed before and after the purification process. For the analysis, a solution drop (2 μ l) was pipetted at the end of a fibre optic cable and a second one was then brought into contact with the drop forming a liquid column acting as cuvette. ATR-IR spectroscopy were measured with a Spectrum 100 Series (Perkin Elmer, UK), to assess possible conformational changes in the secondary structure of BSA. For the study, a solution drop was placed directly on the crystal and 24 scans were recorded at a resolution of 4 cm^{-1} in the range 800-3 000 cm^{-1} . Raman spectra were recorded with a Dilor XY Labram spectrometer (Dilor/Jobin-Yvon/Horiba, USA) equipped with an Olympus BX40 confocal microscope and an ArHe 10 mW green laser, that were collected with a Peltier cooled CCD detector. Different

sets up were employed to test the opportunity to investigate a possible changes in the BSA secondary structure due to the interaction with Ag NP exploiting also a possible enhancement of the Raman signal. XPS were acquired with an AXIS 165 X-ray photoelectron spectrometer (Manchester, UK) using monochromatic Al K α radiation of energy 1 486.6 eV. For XPS study, spray dried sample was placed on stainless steel holder. C 1s peak at 284.8 eV was used as charge reference to determine core level binding energies. A survey spectrum was collected to show the elements present on the sample surface and to set up subsequent high-resolution XPS spectra acquisition.

6.3 Results and Discussion

6.3.1 Preliminary characterization of pristine Ag and TiO₂ nanosols

6.3.1.1 Ag sample

Pristine Ag nanosol was observed by HR-TEM with a field emission source operating between 40-300 kV. Figure 3 showed that pristine Ag sample was mainly composed by discrete particles, but few aggregates were also present (Fig. 3, image on the right). Particles with size below 20 nm appeared spherical, while among bigger particles, also truncated triangular shape was observed.

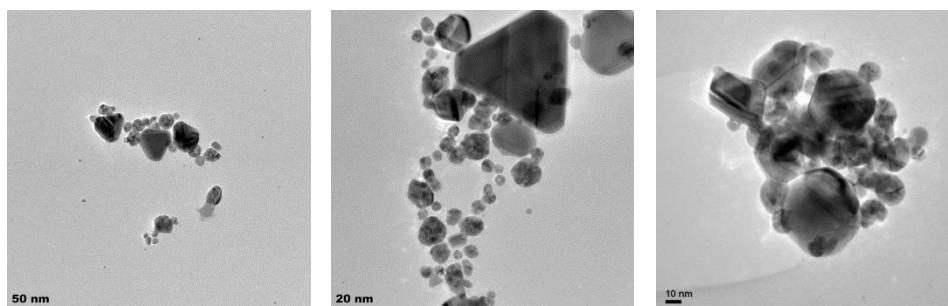


Figure 3 - HR-TEM images of pristine Ag nanosol

HR-TEM lattice images confirmed the presence of a crystalline phase (Fig. 4) and the TEM-EDS spectrum obtained by spot mode, showed the presence of Ag (Fig. 5).

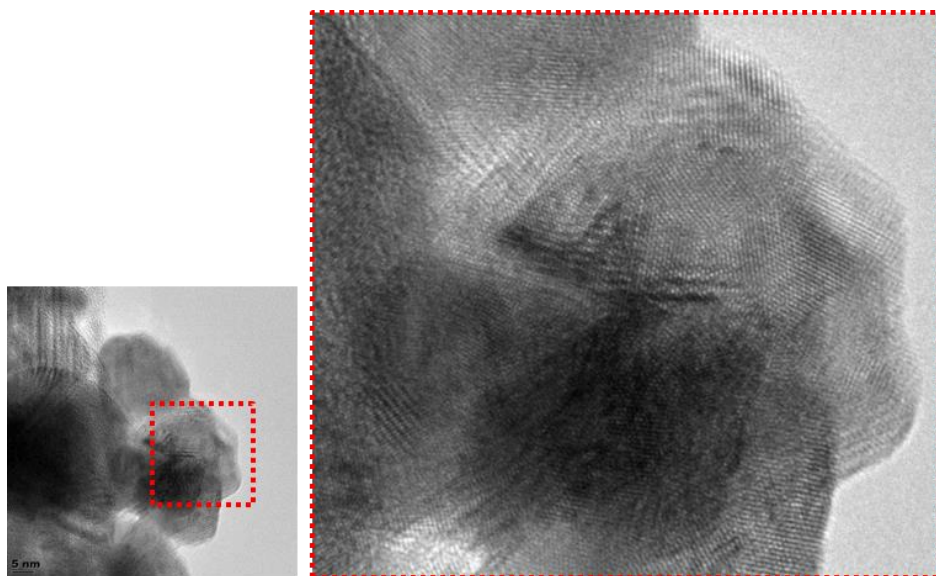


Figure 4 - HR-TEM image of pristine Ag (left) and its crystalline phase (right)

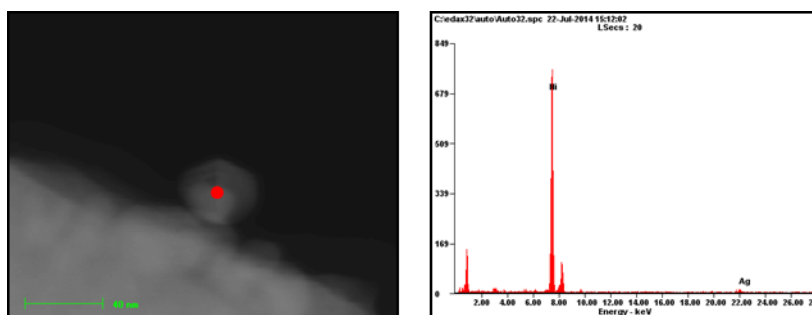


Figure 5 - HR-TEM image with underlined the spot used for EDS determination

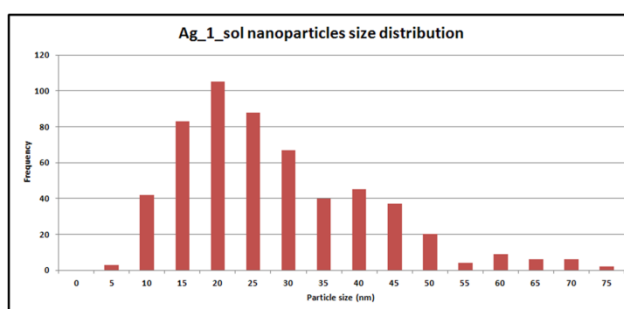


Figure 6 – Particle size distribution based on HR-TEM images

The size of the particles varied between 3.4 nm to 73.4 nm among the considered distribution (Fig. 6) of 557 NPs. The size and ZP of pristine sample were measured by DLS after dilution with water up to 128 µg/ml. Sample showed a monomodal particle size distribution, obtaining an average value d_H of 130 ± 2 nm and a Pdl of 0.2 ± 0.02 . At pH = 3.9 achieved after water dilution, the sample ZP was -14 ± 0.2 mV.

Despite the mechanism whereby Ag exert antibacterial and toxic actions is still under debate^[49,50], Ag⁺ has been considered one of the major responsible. Therefore the Ag⁺ content was investigated, being a relevant parameter to understand Ag reactivity and toxicity mechanism. The total silver, Ag NP and Ag⁺ contents in pristine sample were measured by XRF. The separation of cationic silver fraction were carried out using two different methods to obtain more sound data and evaluate if the separation technique may influence the Ag amount detected in the filtrate. For the ultrafiltration by the SC (Fig. 7), pristine sample were diluted up to 1 wt.% with water, placed in the cell and maintained under stirring.

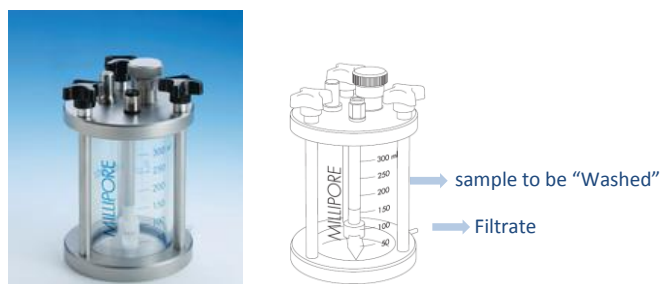


Figure 7 - Image of SC device

A slight over-pressure (0.3 bar) was applied to force the sample to pass through the filtration membrane placed on the bottom of the cell. Four washing steps were performed and in each step, the output stream (filtrate) was collected in a graduate beaker and an equal amount of fresh solvent was added into the cell, continuing with the following washing steps. The washed sample was collected from the cell and analyzed by XRF, to know the Ag⁰ NP content; the filtrate of each step was measured calculating the total amount of Ag⁺ washed (Table 1).

Table 1 – XRF measurement of total and ionic Ag content in pristine sample

Sample code	Ag _{tot} [wt.%]	Ag ⁺ [wt.%]*	Ag ⁰ [wt.%]	Ag ⁺ /Ag _{tot} %
Ag_1_sol	1.00	0.55	0.44	55

From the difference between Ag_{tot} and Ag⁰ in the washed sample, the Ag⁺ should be about 0.56 wt.%. This value correlate very well with the sum of Ag⁺ measured in the filtrate of each washing step, that gave a value of 0.55 wt.%. Thus, from the data obtained using the SC, 55 % of the Ag in pristine sample was in the cationic form. The filtration was carried out also in the CFU (Fig. 8), in a one-step filtration.

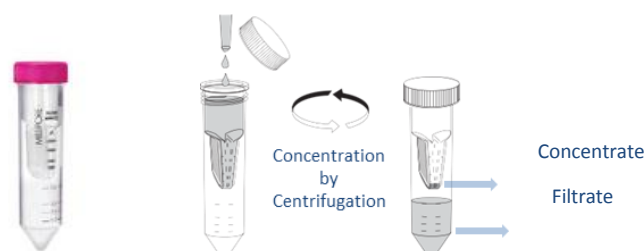


Figure 8 - Image of CFU device

The pristine sample was diluted up to 0.50 wt.% with water and loaded on the filtration device on the top of the vial, that was closed and subjected to centrifugation for a fixed time. The Ag_{tot} concentration in pristine sample and Ag^+ in the filtrate were measured by XRF (Table 2).

Table 2 - XRF measurement of total and cationic Ag content in pristine sample

Sample code	Ag_{tot} [wt.%]	Ag^+ [wt.%]*	Ag^+/Ag_{tot} %
Ag_1_sol	0.50	0.28	56

From the Ag^+ revealed in the filtrate and Ag_{tot} present in the sample before the filtration, the Ag^+/Ag_{tot} ratio was calculated to be around 56 %, value in agreement with the previous one obtained by SC ultrafiltration. 4F separation technique was also used, exploiting its separation channel as an on-line purification membrane. During the analysis, samples smaller than membrane cut-off exit from it and may be collected from the cross-flow line and analyzed by AAS. Carrying out the Ag^+ separation in 4F, the Ag^+/Ag_{tot} ratio was found to be about 50 %^[51]. Therefore, the separation technique did not influence the Ag^+ content detected in pristine sample.

The thermal analysis (Fig. 9) was performed on a dried aliquot of the sample, showing an overall weight loss of 60.0 wt.% at 600 °C, attributable to the decomposition of PVP used as stabilizer and synthesis by-products. Figure 9 shows a slow weight loss of 3.0 wt.% ca. up to 100 °C, due to water evaporation, then in the temperature range 200-350 °C, the sample lost 15.5 wt.% plus 15.5 wt.% ca.; these weight losses may be associated with two exothermic peaks due to the glucose thermal decomposition^[52]. Another weight loss of 10.0 wt.% ca. at 400 °C, was associated with an exothermic peak generated by the PVP combustion^[53]. Between 500 and 600 °C, it was detected a further weight loss of 17.0 wt.% ca., associated with an exothermic peak due to nitrate thermal decomposition. The residue at 600 °C was about 40.0 wt.%.

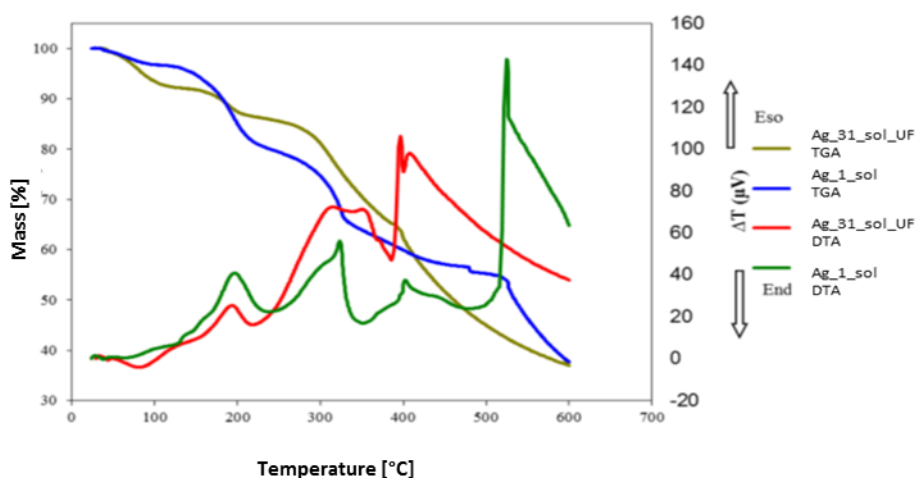


Figure 9 - DTA-TGA analysis of pristine and purified Ag sample

For comparison, also the DTA-TGA of purified sample Ag_31_sol_UF were reported. Purified sample showed a greater weight loss of 7.0 wt.% ca. due to water and a lower weight lost, about 5.5 wt.%, associated with glucose decomposition. Moreover around 400 °C may be noted two exothermic peaks, while no other peaks were detected, with a residue at 600 °C of 40.0 wt.%. The different thermal behaviors of pristine and purified samples were consistent with the purification procedure, that should lower the amount of synthesis by-products in the purified sample.

6.3.1.2 TiO₂ sample

Pristine nanosol was observed by HR-TEM with a field emission source operating between 40-300 kV. Figure 10 shows that pristine TiO₂ sample was mainly composed by discrete spherical particles with size below 5 nm.

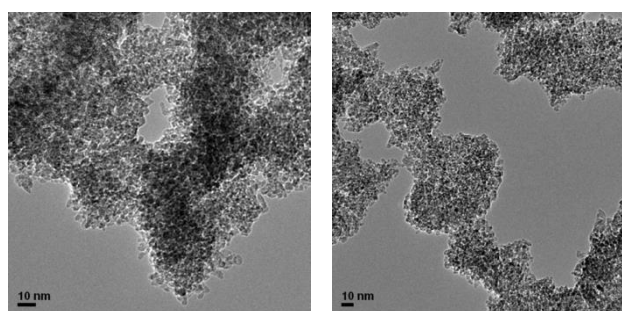


Figure 10 - Pristine Ag nanosol shape by HR-TEM images.

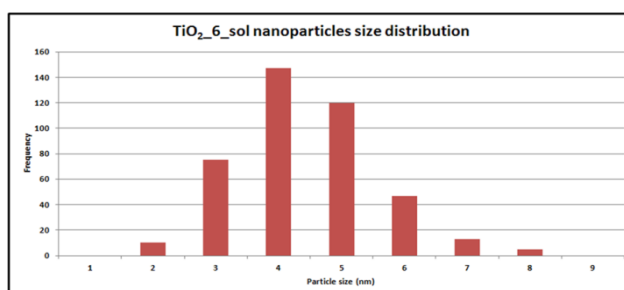


Figure 11 - Particle size distribution from HR-TEM images

The size of the particles (Fig. 11) was found to be very small and agglomerated. The size of the primary particles varied in the range of 1.2 nm - 7.6 nm. The size and ZP of pristine sample were measured by DLS after dilution with water up to 125 µg/ml (Table 3).

Table 3 – DLS measurement of pristine TiO₂ sample

Sample code	pH	Z-ave size [d. nm]	Pdi	ZP [mV]
TiO ₂ _6_sol	3.9	45 ± 1	0.48 ± 0.09	41.2 ± 0.0

Sample showed a two different peak in the intensity particle size distribution, therefore to evaluate the relative amount of each peak in the distribution, the volume particle size distribution was considered. From this latter, the relative volume of the population at 4 800

nm diameter (Peak2, % PD = 15) was found to be the 2 %, suggesting the presence of a little amount of aggregate particles in the pristine sample. Pristine TiO₂ sol sample was subjected to XRF to check the atomic composition and to XRD for the phase determination, for this latter an aliquot of the sample was dried (Table 4).

Table 4 – XRF and XRD results of pristine TiO₂ sample

Sample code	XRF		XRD	
	Nominal TiO ₂ [wt.%]	TiO ₂ [wt.%]	Anatase %	Brookite %
TiO ₂ _6_sol	3.00	3.39	84	16

The TiO₂ concentration measured by XRF was slightly higher than the nominal one declared by the producer, probably due to aging phenomena, for example the evaporation of the solvent. From the XRD the main crystalline phase detected in the pristine samples was anatase, together with a few percent of brookite.

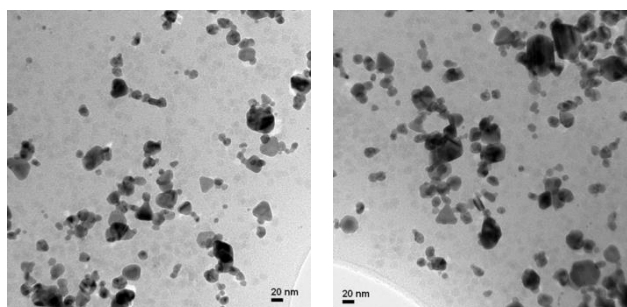
6.3.2 Application of RRS at lab-scale level

6.3.2.1 Ag samples

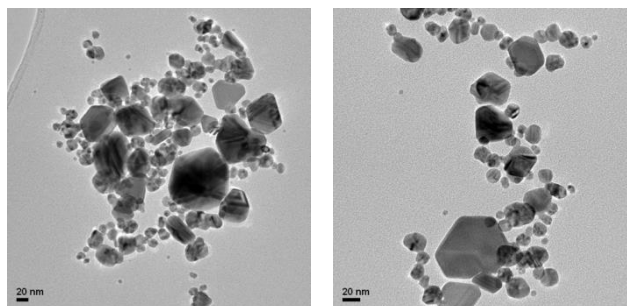
Ag toxicity towards biological systems was commonly correlate with the release of toxic Ag⁺ ions from the surface, that mainly arised from the oxidation of the exposed Ag⁰ NP surface, due to the cooperative effects of dissolved oxigen and protons [54]. Therefore, the different surface modification were focused on the possibility to decrease, control or block the release of toxic Ag⁺. The SiO₂ has been selected as possible coating material to reduce the toxicity of silver [55] and other NMs [56, 57]. Ag_15_sil_sol, was obtained by blending with SiO₂, by this way Ag⁺ ions may interact with the negatively charged SiO₂ surface, reducing the availability of free Ag⁺ ions in the system. Ag_35_sil_sol sample were synthetized with core shell structure, in which the compact silica shell was aimed to isolate the Ag surface and, therefore, to avoid Ag⁺ release. The sample Ag_31_sol_UF, was obtained removing by ultrafiltration the Ag⁺ excess present in the pristine sample, allowing Ag NP surface to establish a new Ag⁺ equilibrium and, therefore, concentration in the solution.

The modified samples were observed by HR-TEM (Fig. 12), to obtain the morphology and mean size of Ag particles.

a)



b)



c)

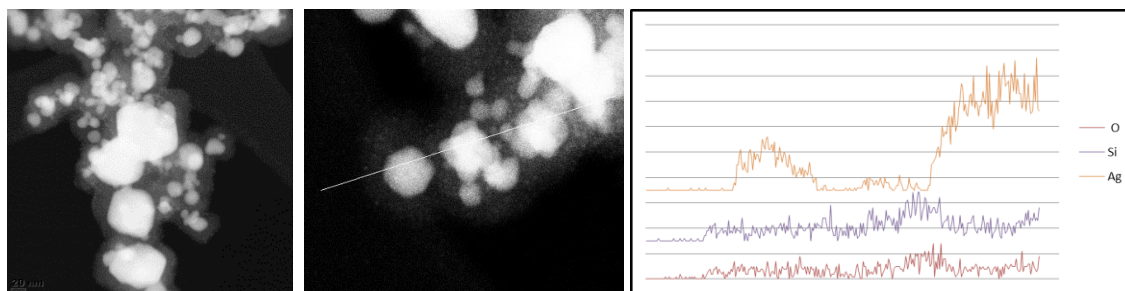


Figure 12 - Images by HR-TEM of modified Ag samples: a) Ag_15_sil_sol, b) Ag_31_sol_UF, c) Ag_35_sil_sol and its related EDS pattern

In Ag_15_sil_sol sample (Fig. 12 panel a), the colloidal silica, light grey spherical object, and the darker Ag NPs appeared homogeneously dispersed. As expected, purified sample Ag_31_sol (Fig. 12 panel b) showed particle shape and size similar to those of the pristine material, being obtained by the removal of silver ion from it. Ag_35_sil_sol (Fig. 12 panel c) showed the Ag core and the SiO₂ shell structure and EDS showed Ag particles coated by silica. From TEM images, the particle size distribution was calculate and the data obtained are reported in table 5.

Table 5 - Primary particle size distribution data obtained from TEM images

Sample code	Size distribution [peack at]	Average size [nm]	Typical size range, MAX [nm]	Typical size range, MIN [nm]
Ag_1_sol	20	24	74	3
Ag_15_sil_sol	21	18	72	3
Ag_31_sol_UF	18	15	158	3
Ag_35_sil_sol	40	38	140	20

The pristine Ag_1_sol and modified Ag_15_sil_sol and _Ag_31_sol_UF samples showed similar particles size distribution and average size, with diameters around 20 nm. Only the silica core shell sample Ag_35_sil_sol showed bigger particle dimensions, with an average size of 40 nm. Mean d_H and ZP were measure by DLS on diluted samples, obtaining the data reported in table 6.

Table 6 - Mean d_H , Pdl and ZP of modified Ag samples diluted up to 128 $\mu\text{g/ml}$ in deionized water.

Sample code	pH	d_H [nm]	Pdl	ZP [mV]
Ag_15_sil_sol	3.2	169 \pm 1	0.24 \pm 0.02	-3.2 \pm 0.1
Ag_31_sol_UF	4.5	103 \pm 2*	0.24 \pm 2.00*	-16.3 \pm 0.4
Ag_35_sil_sol	6.5	184 \pm 0	0.21 \pm 0.02	-34.6 \pm 1.1

* Bimodal size distribution, size of each peak and relative volume of the two populations such as reported in the discussion below.

According to the data obtained, silica modified samples (Ag_15 and Ag_35) showed a monomodal size distribution with similar value of the mean d_H (or Z-average) and Pdl. Ag⁺ purified sample, Ag_31_sol_UF was characterized by a bimodal size distribution, therefore the intensity of particle size distribution should be considered for the assignment of the size of each peak. Ag_31_sol_UF sample showed a peak centered on 140 nm (Peak 1, %PD = 43) and another on 20 nm (Peak 2, %PD = 14). Being the intensity size distribution really sensitive to the presence of aggregates and large particles, because scattered light intensity is proportional to the sixth power of scattering particle diameter, to estimate the relative amount of each peak in the distribution, the volume particle size distribution was considered. From this latter, the relative volume of the two populations at 140 nm (Peak 1, %PD = 43) and 20 nm (Peak 2, %PD = 14) resulted almost the same, being respectively 49 % and 51 %. From the ZP measured, the Ag_15_sil_sol and Ag_31_sol_UF resulted the less stable, while the core and shell modified samples Ag_35_sil_sol showed a good colloidal stability, being the absolute value of its ZP above 30 mV^[58]. The increasing of ZP negative value in silica modified samples may be justified by the presence of silica coating that showed a negative ZP at the pH investigated, being its isoelectric point around pH 2. Thus, the comparison between the two silica coated samples confirmed the expected presence of an homogeneous and compact silica coating in the case of Ag_35_sil_sol, on the contrary Ag_15_sil_sol showed an homogeneous dispersion of Ag NP and colloidal silica.

The cationic Ag content, was measured and compared with that of pristine sample, to understand the influence of the surface modification on the Ag⁺ amount detected in the sample. The separation of Ag⁺ from Ag_{tot} was performed by SC or CFU and samples obtained were analyzed by XRF or AAS, where specified (Table 7).

Table 7 - Results of Ag⁺ separation and determination in pristine and modified Ag samples.

Sample code	Ag _{tot} [wt.%]	Ag ⁺ [wt.%]*	Ag ⁰ [wt.%]	Ag ⁺ /Ag _{tot} %	Filtration method
Ag_1_sol	1.00	0.55	0.44	55	SC
Ag_15_sil_sol	0.88	0.57	0.31	65	SC
Ag_31_sol_UF	0.44	0.0137 *	-	3	MFU
Ag_35_sil_sol	0.075 *	2.2 x 10 ⁻⁵ *	-	0	MFU

* Measured by AAS

From the analysis of data reported, the silica blending seemed to increase the Ag⁺ ions in the modified sample Ag_15_sil_sol in comparison to pristine Ag_1_sol. On the contrary Ag⁺ purification by ultrafiltration gave the expected results, decreasing the Ag⁺ content in Ag_31_sol_UF sample. In the core and shell sample Ag_35_sil_sol, the low amount of Ag⁺ detected (0.02 ppm by AAS) suggested that the synthetic procedures, that ended up with an ultrafiltration procedures, eliminated synthesis by-products and Ag⁺ eventually present in the sample. Moreover, allowed to hypothesize that the presence of silica shell controls the Ag⁺ release in the final Ag_35_sil_sol, because the sample was analyzed at t = 0 and after few days after its preparation and no increase in the Ag⁺ amount detected was observed. Thus, RRS of purification by ultrafiltration and silica coating by chemical synthesis were so effective to decrease the Ag⁺ content in related samples.

Sample Ag_31_sol_UF was selected for antibacterial tests, because maintained a certain amount of Ag⁺, necessary to exploit the antibacterial activity. Moreover purified sample allowed an easier comparison with the pristine one, differing from it mainly for the Ag⁺ content. The antibacterial tests were performed by Colorobbia to evaluate if RRS may be detrimental for an antibacterial activity and, therefore, for the performances expected within industrial spray coating application. Before the antibacterial tests, the total Ag_{tot} and Ag⁺ concentration in the Ag stock solution was determined. Samples for the determination of Ag⁺ content were obtained filtering an aliquot of stock solution through CFU and measuring the Ag concentration in the filtrate. A summary of the results of antibacterial activity assay of Ag, concentration in stock solutions and their Ag⁺ content, are reported in table 8.

Table 8 - Data of Ag samples employed and antibacterial activity results

Sample code	Starting conc. [wt.%]	Ag dispersion used for the antibacterial tests			Antibacterial test			
		Dilution	Ag _{tot} [ppb]	Ag ⁺ [ppb]	Inoculum	24h [cell/ml]	R%	R [log]
Unexposed control	0		0		11.5 x 10 ⁵	85 x 10 ⁵	-	-
Ag_1_sol	4	1:10 ⁶	39.4	22.10	11.5 x 10 ⁵	31 x 10 ²	99.90	3.2
Ag_31_sol_UF	0.44	1:10 ⁵	44.7	1.53	11.5 x 10 ⁵	44 x 10 ⁵	0	0
Ag_31_sol_UF	0.44	1:10 ⁴	447	15.3	11.5 x 10 ⁵	34 x 10	99.96	4.4
Ag_31_sol_UF	0.44	1:10 ³	4 470	153	11.5 x 10 ⁵	<10	>99.99	>5
Ag_31_sol_UF	0.44	1:10 ²	44 700	1 530	11.5 x 10 ⁵	<10	>99.99	>5

The amount of Ag⁺ revealed in the pristine Ag_1_sol sample was about the 56 wt.% of total Ag content, value that correlated well with that detected in a previous separation experiment. This relevant Ag⁺ content detected may be attributed to an unreacted fraction of starting reagent (AgNO₃). In the modified Ag_31.3_sol_UF sample, the Ag⁺/Ag_{tot} was around 3 wt.%, in accordance with other data obtained, especially considering the really low concentration involved. In this sample the Ag⁺ content may be ascribed to a Ag⁺ fraction still remaining in the sample or due to a new equilibrium between the AgNP surface and released Ag⁺. In fact, during Ag_31_sol_UF preparation, the Ag⁺ excess was removed and AgNP came

in touch with fresh water, in aerobic conditions. Therefore, Ag NP remaining in the sample may release further Ag⁺ to restore the equilibrium between the Ag⁺ ions adsorbed on Ag NP surface and those dissolved in the water dispersion.

Observing the data of antibacterial assay, the pristine sample Ag_1_sol, with 39 ppb of total silver and about 22 ppb of Ag⁺, showed a full antibacterial activity. Comparing the pristine sample with the Ag_31_sol_UF having a close Ag_{tot} concentration of 45 ppb, the modified samples did not show any antibacterial activity. On the contrary, comparing the two samples with close Ag⁺ content (22 ppb and 15 ppb, for Ag_1_sol and Ad_31_sol_UF respectively) they exerted comparable antibacterial activities. These results suggested an Ag⁺ dependent antibacterial activity rather than a particle specific activity as previously reported for other Ag NP [59]. Considering these data, the ultrafiltration strategy resulted detrimental for the antibacterial activity of modified Ag_31_sol_UF sample. However, it was decided to further investigate the antibacterial activity of sol samples within their real industrial application, that is the functionalization of ceramic tile through spray coating and thermal treatment. During this latter in fact, the Ag⁺/Ag_{tot} ratio could be modified, affecting the antibacterial properties of the final ceramic tile.

6.3.2.2 TiO₂ samples

The photocatalytic activity [29] of TiO₂ was commonly correlated with the ROS production, that may cause oxidative damage of a range of key structures and components of cells including DNA, proteins and lipids, leading to significant functional changes to the cell, cell death, induction of inflammatory pathways or alterations in terms of cell signaling or communication [60].

For these reasons, the ROS production was taken into account as relevant parameter in TiO₂ NP induced toxicity and therefore the different surface modifications were focused on the possibility to decrease and control the formation and/or release of ROS and other active species. The SiO₂ was selected as coating material being known to reduce the toxicity of TiO₂ [61] and other NMs [55, 56, 57]. TiO₂_15_NP_SD spray dried sample, was produced to lower the pristine material emissivity, although maintaining a nanostructured surface that should guarantee an highly reactive material. TiO₂_18_sil_sol was obtained by blending with SiO₂, by this way the photocatalytic activity of TiO₂ could be improved as demonstrated for the rattle-type TiO₂@void@SiO₂ composite particles [62], where the improvement of photocatalytic activity was ascribed to void space and presence of silica, that allowed active sites of TiO₂ to contact more dye molecules, as well as to the better dispersibility of the composite in comparison to the original TiO₂ NMs. In a recent paper [63] the addition of SiO₂ in the production of a thin TiO₂/SiO₂ film, resulted in an improvement of the optical properties and photocatalytic activity. The promoting effect of SiO₂ was ascribed to an increase of the roughness of the TiO₂/SiO₂ thin film, with consequent increase of the active surface area, and/or to the capacity of SiO₂ to act as an adsorbent for the test molecule used in photocatalytic tests. The citrate layer on TiO₂_36_cit_sol sample may shield the active sites of TiO₂ particles or react with ROS and/or other intermediates, controlling the production and/or

availability of these active species in the system. The above mentioned modified samples were observed by HR-TEM (Fig. 13) to obtain the morphology and mean size of NPs.

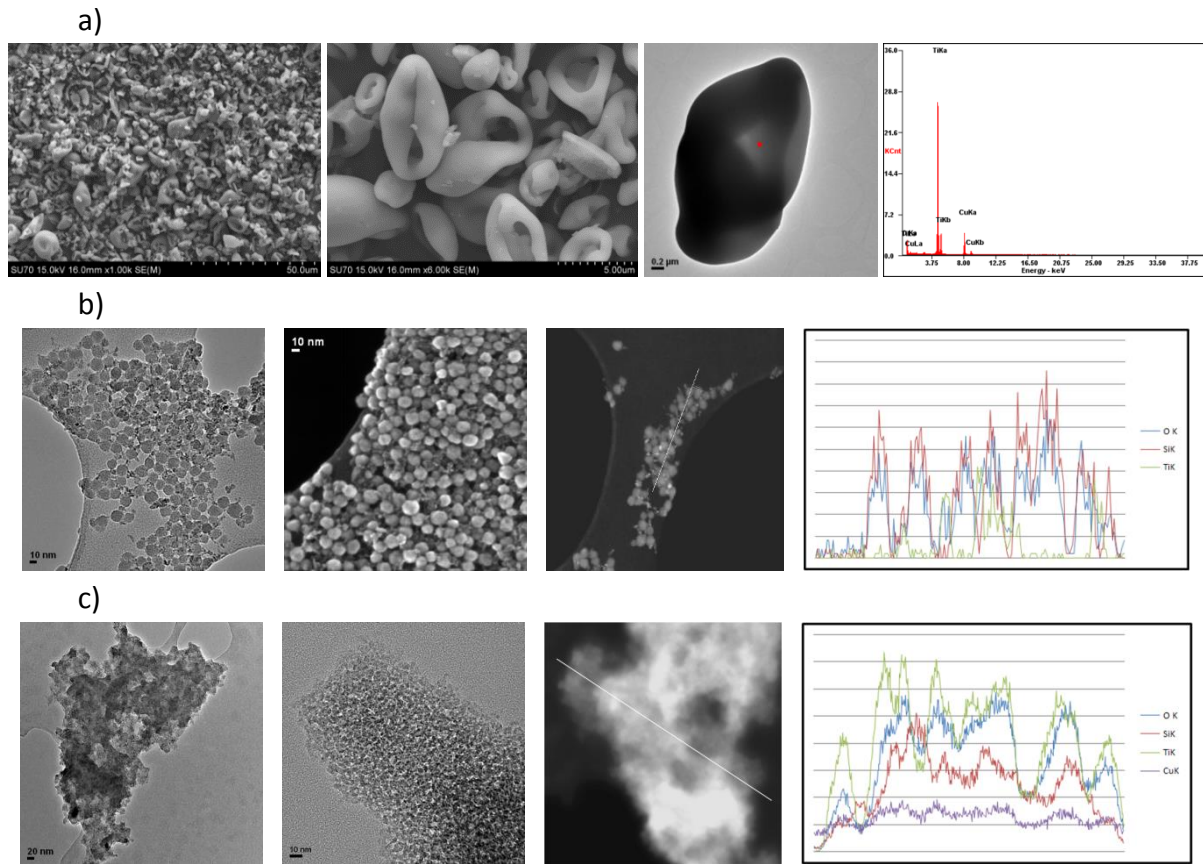


Figure 13 - Modified TiO₂ sample, a) SEM-FEG, bright field TEM and EDS of TiO₂_15_NP_SD, b) bright field TEM, STEM-HAADF images and STEM-EDS line scan of TiO₂_18_sil_sol, c) bright field TEM, STEM-HAADF images and STEM-EDS line scan of TiO₂_36_cit_sol

TiO₂_15_NP_SD sample was composed by micro-sized particles with irregular morphology, as observed by SEM-FEG. From the TEM-EDS spot mode, the presence of Ti and O in the secondary micro-particles was confirmed. TEM images of TiO₂_18_sil_sol samples showed the presence of discrete units of different primary NP homogeneously dispersed. In the images (Fig. 13 panel b) the bigger spherical particles were the colloidal SiO₂, with diameters around 20 nm, while the smaller were those of TiO₂. STEM-EDS line scan showed the presence of Ti along with Si and O. TiO₂_36_cit_sol samples showed particles size and morphology close to those obtained for pristine sample, composed by small primary NPs with diameter around 4 nm, that formed nanometre sized agglomerates. From TEM images, the particle size distribution was calculate (Table 9).

Table 9 - Primary particle size distribution data obtained from TEM images

Sample code	Size distribution [peak at]	Average size [nm]	Typical size range, MAX [nm]	Typical size range, MIN [nm]
TiO ₂ _6_sol	4	4	8	2
TiO ₂ _15_NP_SD	-	3 000	5 000	900
TiO ₂ _18_sil_sol	16	15	24	10
TiO ₂ _36_cit_sol	4	5	9	2

The pristine TiO₂_6_sol, and modified TiO₂_36_cit_sol samples showed similar particles size distribution and average size, with diameters around 4 nm. The SiO₂-blended sample TiO₂_18_sil_sol showed bigger particle dimensions, with an average size of 15 nm. The TiO₂_15_NP_SD sample, showed micron sized particles typical of spray dried materials. Mean d_H and ZP were measure by DLS on diluted samples (Table 10).

Table 10 - Mean d_H, Pdl and ZP of modified TiO₂ samples diluted up to 125 µg/ml in deionized water

Sample code	pH	d _H [nm]	Pdl	ZP [mV]
TiO ₂ _6_sol	2.3	45 ± 1 *	0.48 ± 0.09	41.2 ± 0.5
TiO ₂ _18_sil_sol	4.8	156 ± 22 *	0.11 ± 0.00	3202 ± 4.1
TiO ₂ _36_cit_sol	5.5	39 ± 1 **	0.28 ± 0.00	-34.2 ± 1.2

* Presence of aggregates ** Bimodal size distribution, size of each peak and relative volume of the two populations such as reported in the discussion below.

According to the data obtained, SiO₂-modified sample TiO₂_18_sil_sol showed a peak on 156 nm together with a peak at higher size, similar to that found in the pristine sample, for both peak size and relative volume population (2 %). Citrate coated TiO₂_36_cit_sol sample was characterized by a bimodal size distribution, therefore the intensity particle size distribution was considered for the assignment of the size of each peak. These were centered on 14 nm (Peak 1, %PD = 8) and 60 nm (Peak 2, %PD = 56). To estimate the relative amount of each peak in the distribution, the volume particle size distribution was considered. From this latter, the relative volume of the population at 14 nm (Peak 1, %PD = 8) was 100 % suggesting the presence of only few bigger aggregate (Peak 2, d.= 60 nm, %PD = 56, vol% = 0). From the ZP measured, all samples showed a good colloidal stability, being the absolute value of its ZP above 30 mV^[58].

To evaluate the presence of a nanostructure on granule surface, the spray dried TiO₂_15_NP_SD sample underwent BET and XPS analysis (Fig. 14 and Table 11).

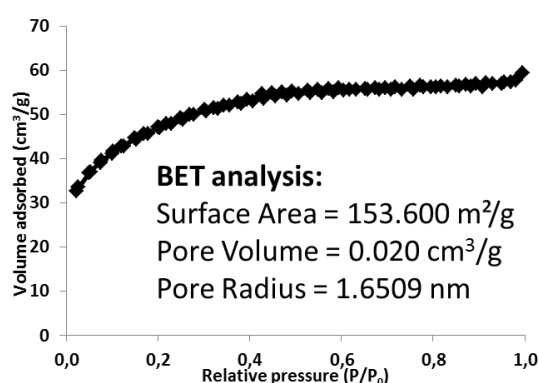


Figure 14 - BET analysis of spray dried TiO₂_15_NP_SD sample

Table 11 - Summary of BET and XPS data for the spray dried TiO₂_15_NP_SD sample.

Sample Code	BET specific surface area [m ² /g]	BET pore radius [nm]	BET pore volume [cm ³ /g]	XPS [atomic %]
TiO ₂ _15_NP_SD	153.6	1.65	0.02	Ti:17.9, O:50.9, C:31.2

The high value of SSA obtained by BET analysis confirmed the nanostructure of the powder surface, while XPS analysis confirmed the presence of Ti, O and C.

The pristine and modified sample ROS production was investigated, being related to the TiO₂ NM photocatalytic activity and the ability to induce oxidative stress. The intrinsic production of ROS of pristine and modified TiO₂ samples was assessed by IOM. Involved NMs were co-incubated with a spin trap (Tempone-H) to detect the release of oxygen-centered free radicals. The signal created by the production of ROS was compared to vehicle control (phosphate buffered saline) and a positive control (100 μM of pyrogallol). The result and representative spectra are shown in figure 15 and figure 16, respectively.

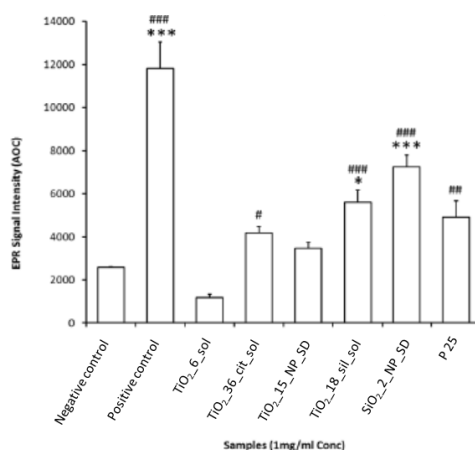


Figure 15 - EPR signal intensity after co incubation with pristine TiO₂_6_sol and modified TiO₂_36_cit_sol, TiO₂_15_NP_SD, TiO₂_18_sil_sol samples. Signal intensity of a silica SiO₂_2_NP_SD sample and the benchmark control Aerioxide® P25 were also reported for comparison. Results were expressed as mean +/- standard error mean (n = 3). *** P < 0.001, **P < 0.01, * P < 0.05 vs. vehicle control; ###P < 0.001, ## P < 0.01 vs. pristine TiO₂_6_sol.

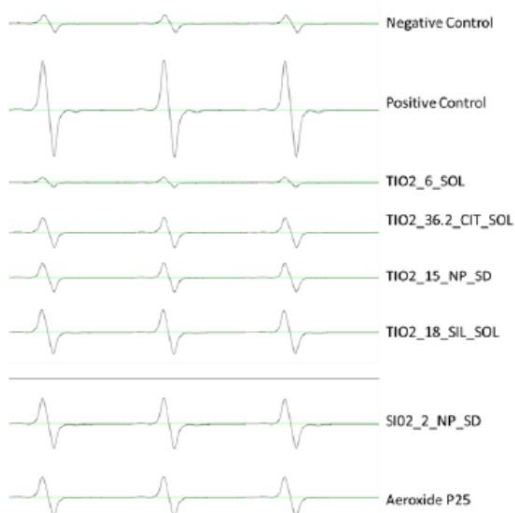


Figure 16 - Representative EPR spectra after 1 h of co-incubation of the spin trap Tempone-H with pristine TiO_2 _6_sol and modified TiO_2 _36_cit_sol, TiO_2 _15_NP_SD, TiO_2 _18_sil_sol samples. Spectra of the silica SiO_2 _2_NP_SD sample and the benchmark Aeroxide® P25 were also reported for comparison.

From the lower to the higher quantity of ROS detected, samples may be classified, as follow: TiO_2 _6_sol < TiO_2 _15_NP_SD < TiO_2 _36_cit_sol < TiO_2 _18_sil_sol sample. Pristine TiO_2 _6_sol sample showed a low level of intrinsic ROS production, with a signal intensity below that of the vehicle control and significantly lower than that of benchmark material P25. TiO_2 spray dried TiO_2 _15_NP_SD sample produced moderate levels of ROS, although higher than those observed for pristine sample. The presence of the citrate layer in TiO_2 _36_cit_sol increased the ROS production. Highest level of ROS production was found in presence of SiO_2 in the sample TiO_2 _18_sil_sol. Form data obtained by EPR, all RRS applied enhanced ROS production of involved TiO_2 materials. However as recently reported ^[64] the amount of radical species detected with a methodology may be not predictive of the photocatalytic activity exerted, being this latter dependent from many other factor that may strongly affect the final functional properties of the material produced.

To test the selected nanomaterial functional properties, pristine and modified sample photocatalytic activity were evaluated in a model system measuring of the photo-degradation efficiency of RhB by UV-visible light. The graph of RhB degradation efficiency % versus time and RhB degradation efficiency % after 60 min were reported respectively in figure 17 and table 12.

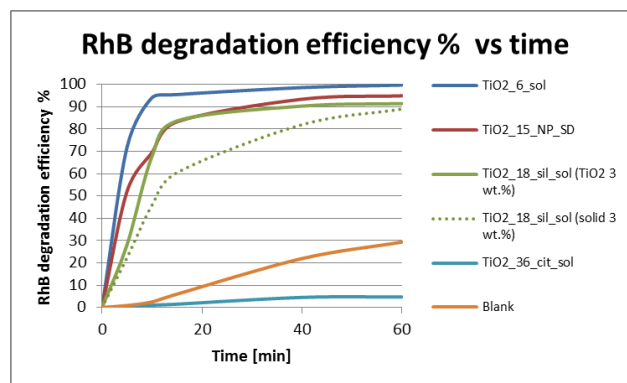


Figure 17 - RhB degradation efficiency % of pristine TiO₂_6_sol and modified TiO₂_15_NP_SD, TiO₂_18_sil_sol (TiO₂ 3 wt.%), TiO₂_18_sil_sol (solid 3 wt.%) and TiO₂_32_cit_sol samples.

Table 12 - RhB degradation efficiency % after 60 min of reaction of pristine TiO₂_6_sol and modified TiO₂_15_NP_SD, TiO₂_18_sil_sol (TiO₂ 3 wt.%), TiO₂_18_sil_sol (solid 3 wt.%) and TiO₂_36_cit_sol samples.

Sample code	pH	Efficiency %
TiO ₂ _6_sol	2.3	99.7
TiO ₂ _15_NP_SD	-	94.9
TiO ₂ _18_sil_sol (TiO ₂ 3 wt.%)	4.8	91.4
TiO ₂ _18_sil_sol (solid 3 wt.%)	4.8	89.0
TiO ₂ _36_cit_sol	5.5	4.7
Blank	6.7	29.3

Pristine sample TiO₂_6_Sol showed best photocatalytic performances under these experimental conditions, raising a RhB conversion % more than 90% in the first 10 min and close to 100 % after 1 h of reaction time. The spray dried TiO₂_15_NP_SD sample, containing nanostructured micrometer-sized granules of TiO₂, performed a good photocatalytic activity, with a final RhB conversion of about 95%. The presence of SiO₂ was evaluated keeping constant at 3 wt.% both the TiO₂ content and the total solid content, i.e. TiO₂ and SiO₂, investigating TiO₂_18_sil_sol (TiO₂ 3 wt.%) and TiO₂_18_sil_sol (solid 3 wt.%) samples, respectively. These samples showed similar photocatalytic activities, lower in comparison with that of pristine sample, with a RhB degradation efficiency around 90% after 1 h of reaction. The presence of the citrate coating in TiO₂_36_cit_sol sample, dramatically decreased the sample photoreactivity, that was found to be lower than that of the reference sample (blank). From the comparison of ROS production and photocatalytic activity observed, it may be noted that pristine sample with the lower level of ROS detected showed best photocatalytic activity, suggesting that different factors, more than ROS production, may influence the TiO₂ sample photocatalytic reactivity.

6.3.3 Implementation of RRS within Processing line 5

6.3.3.1 Ag samples

Pristine Ag_1_sol and purified Ag_31_sol_UF samples, diluted up to 0.1 wt.% with water, were employed to coat ceramic tiles within the industrial setting. The typical set up for microbial test on treated ceramic tiles are shown in figure 18.

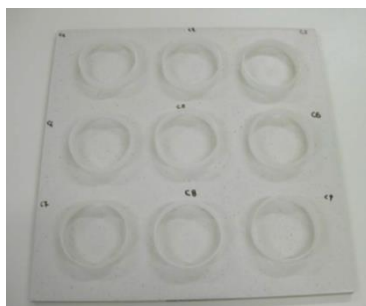


Figure 18 - Typical set up for microbial tests on treated ceramic tiles

Table 13 - Data obtained for microbial tests on treated ceramic tiles

Sample Code	INOCULUM (cell/ml)	RECOVER 24 h (cell/ml)	R %	R log
Control	49.5×10^5	29.2×10^5		
Ag_1_sol	49.5×10^5	95.6×10^4	67.3	0.48
Ag_31_sol_UF	49.5×10^5	26.2×10^5	10.3	0.05

From antibacterial tests performed on tiles coated with the same Ag_{tot} concentration (Table 13), the pristine material conferred a higher antibacterial activity to ceramic tiles in comparison to the modified sample Ag_31_sol_UF. Nevertheless, in the antibacterial tests performed on Petri plate, using almost total Ag concentration, Ag_1_sol showed antibacterial activity, unlike purified Ag_31_sol_UF sample. When the Ag samples were applied on the ceramic tiles at the same total Ag content, it is noteworthy that Ag_1_sol showed only 10 times higher antibacterial activity (R log) in comparison to that of tile treated with Ag_31_sol_UF. This result suggested that during application and thermal treatment, the sprayed Ag may be involved in different process, that modified the total Ag content and/or the Ag^+/Ag_{tot} ratio in final coated ceramic tiles. The possible hypothesis were:

- different Ag amounts were sprayed and, therefore, immobilized on the tile surface;
- part of the Ag^+ ions in pristine sample were reduced to Ag^0 , leading to a more close Ag NP content in both coated tiles;
- part of the excess of Ag^+ in pristine sample were involved in a coordination complexes within the ceramic matrix, or were lost during the final washing treatment that did Ag^+ not available to exert antibacterial effects.

In both hypothesis the antibacterial grade of the two treated tiles should become less marked as in the experiment reported below. To better understand the mechanism involved, the Ag present on the coated tiles was estimated by LA-ICP-MS on the tile surface to check the Ag coating homogeneity and the possible presence of Ag under the tile surface. In all spectra, the signal intensity was reported as a function of the ablation time and each peak corresponded to a sampling point in the line raster. The spectrum obtained analyzing an uncoated tile sample, considered as blank, was reported in figure 19.

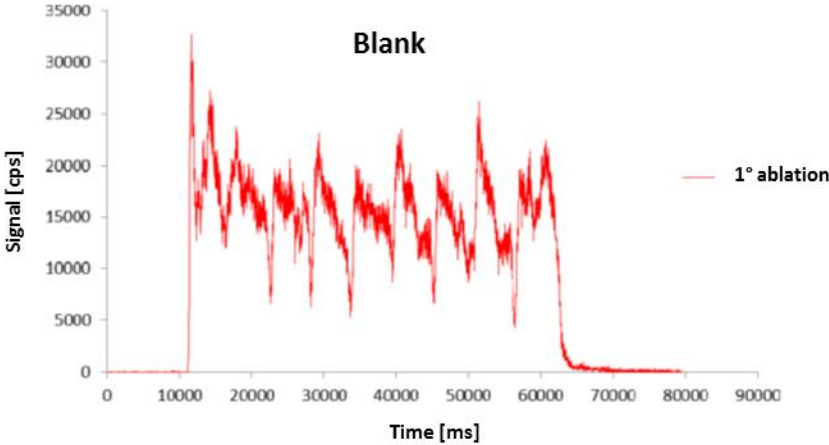
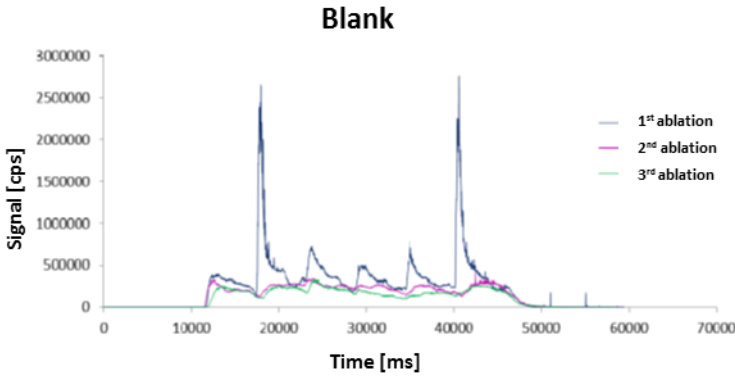


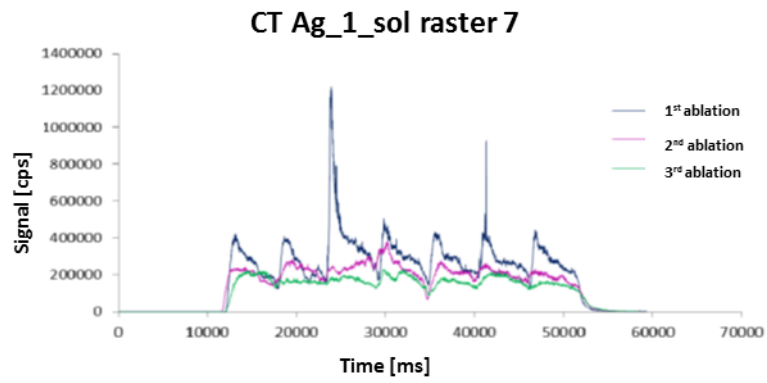
Figure 19 - Uncoated ceramic tile spectra (blank), 9 measurement point belonging to one line raster

For CT Ag_1_sol sample, different area were analyzed through 5 line raster, each one composed respectively by 6, 7, 8, 9, 10 points. Three consecutive ablation on same sampling points, were performed for each line raster (Fig. 20).

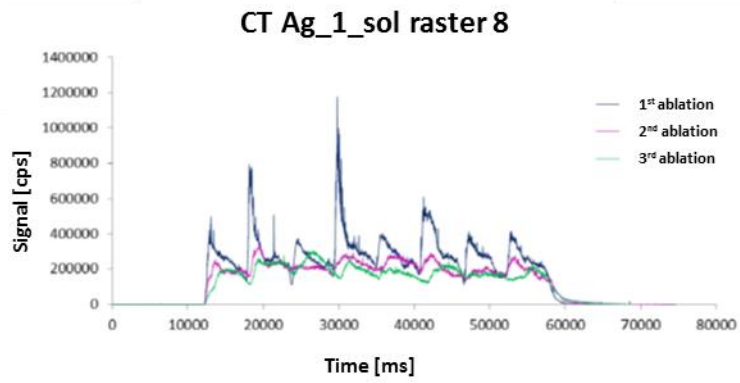
a)



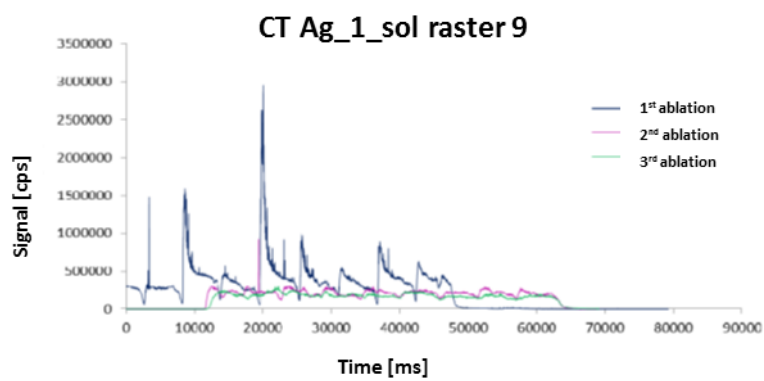
b)



c)



d)



e)

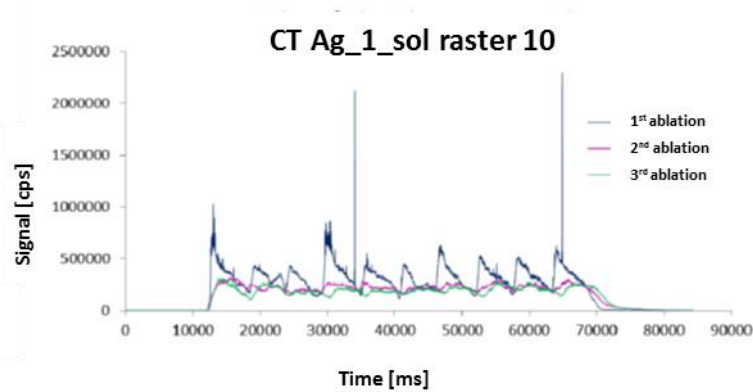


Figure 20 - CT Ag_1_sol spectra, a) 6 point line raster, b) 7 point line raster, c) 8 point line raster, d) 9 point line raster, e) 10 point line raster. Three consecutive ablations for each raster were reported.

In all spectra obtained, comparing consecutive ablations on the same measurement point, the Ag signal in the first ablation was of high intensity, decreasing and becoming comparable, during the second and third ablations. This result may be attributed to different concentration of the Ag coating, that was mainly located on the tile surface.

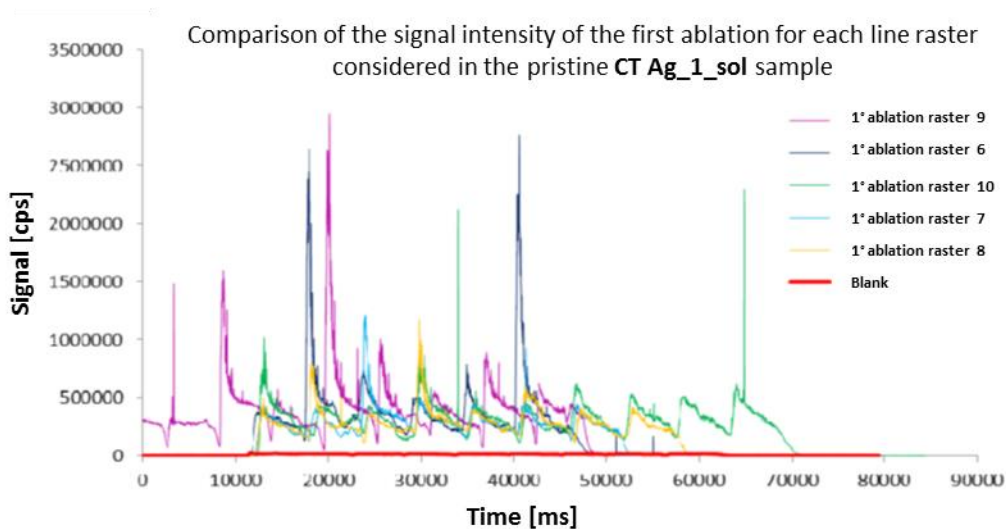
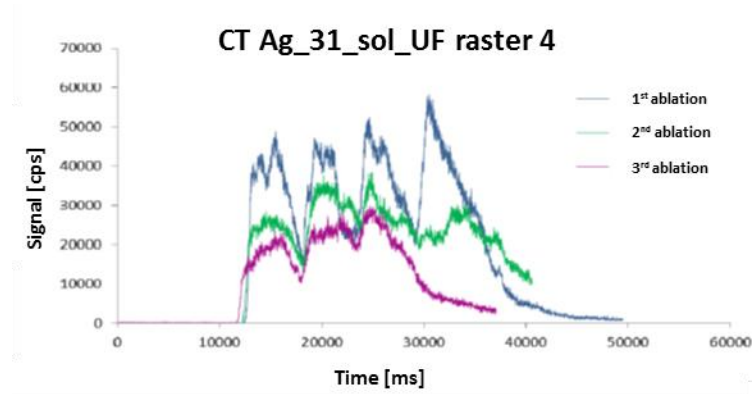


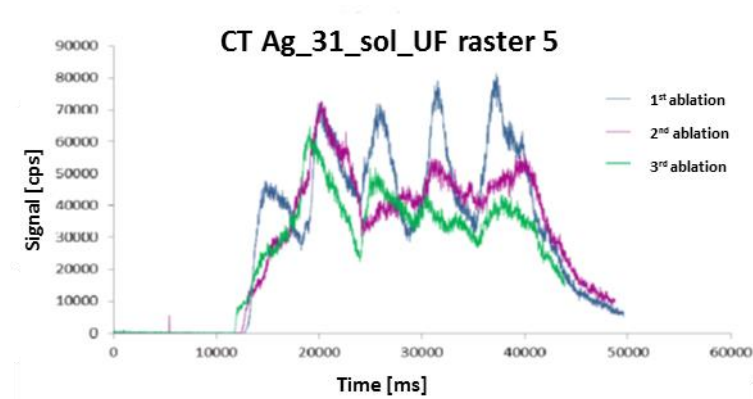
Figure 21 - Comparison of the signal intensity of the first ablation for each line raster considered in the pristine CT Ag_1_sol sample.

From the comparison of the signals relative to the first ablations of blank and coated tile CT Ag_1_sol, showed in figure 21, it may be noted the presence of the Ag coating in CT Ag_1_sol sample, as showed by the significantly higher intensity signal obtained. Anyway CT Ag_1_sol showed different signal intensity in relation to the ablation point considered, indicating that the Ag coating was not homogeneous in the area considered. For CT Ag_31_sol sample, different area were analyzed through 5 line raster, each one composed respectively by 4, 5, 6, 7, 8 measurement point. Three consecutive ablation on the same sampling points, were performed for each line raster (Fig. 22).

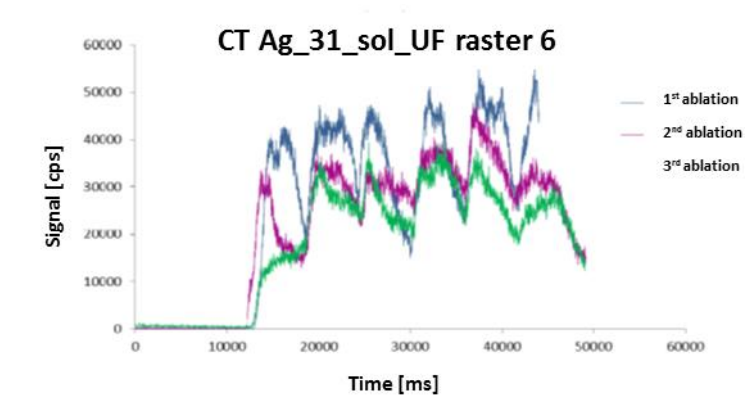
a)



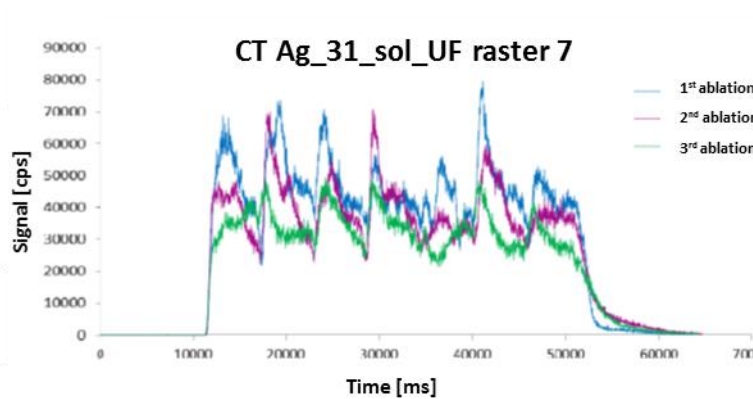
b)



c)



d)



e)

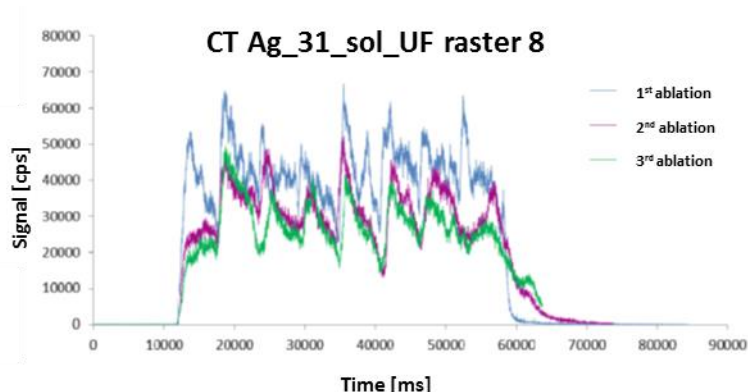


Figure 22 - CT Ag_{31_sol} spectra, a) 4 point line raster, b) 5 point line raster, c) 6 point line raster, d) 7 point line raster, e) 8 point line raster. Three consecutive ablations for each raster were reported.

In the CT Ag_{31_sol}_UF sample, comparing consecutive ablations on the same measurement point, the Ag signal collected during consecutive ablations was of low intensity. Plotting the intensity signal of the first ablation for pristine CT Ag_{1_sol}, modified CT Ag_{31_sol}_UF and blank sample (Fig. 23), the signal of CT Ag_{31_sol}_UF was comparable of that obtained for the blank, suggesting a low Ag concentration, probably due to some drawbacks during Ag coating application.

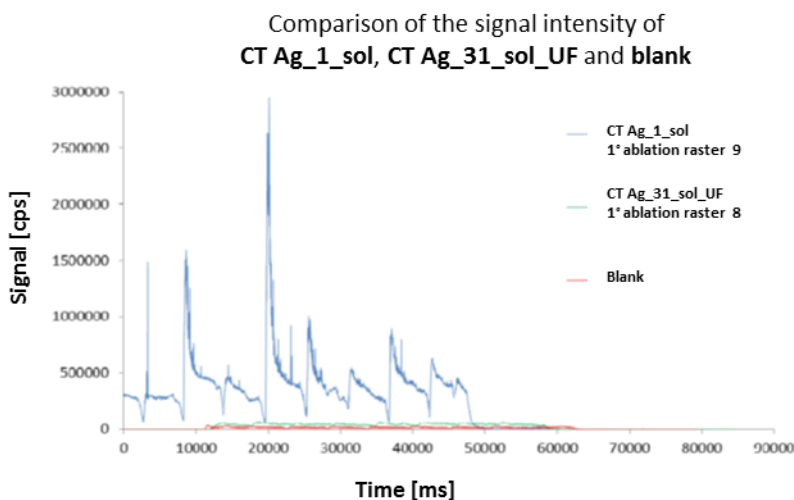


Figure 23 – Comparison of the signal intensity of CT Ag_{1_sol}, CT Ag_{31_sol} and blank.

These data were in agreement with the antibacterial activity showed by the coated tiles, but not allowed to hypothesize different fates of sprayed Ag during the application. Further tiles will be coated to perform antibacterial and laser ablation test, in order to obtain a larger panel of data and best understand the effectiveness of the purification strategy within real industrial applications.

6.3.3.2 TiO₂ samples

To further investigate the NM functional properties within the industrial applications, the pristine TiO₂_6_sol and modified TiO₂_18_sil_sol and TiO₂_36_cit_sol samples, diluted up to 1 wt.% of TiO₂ content by water, were employed to coat ceramic tiles within the industrial setting let available from Colorobbia. The functional properties of coated tiles obtained were evaluated in term of NO and NO_x degradation (Fig. 24).

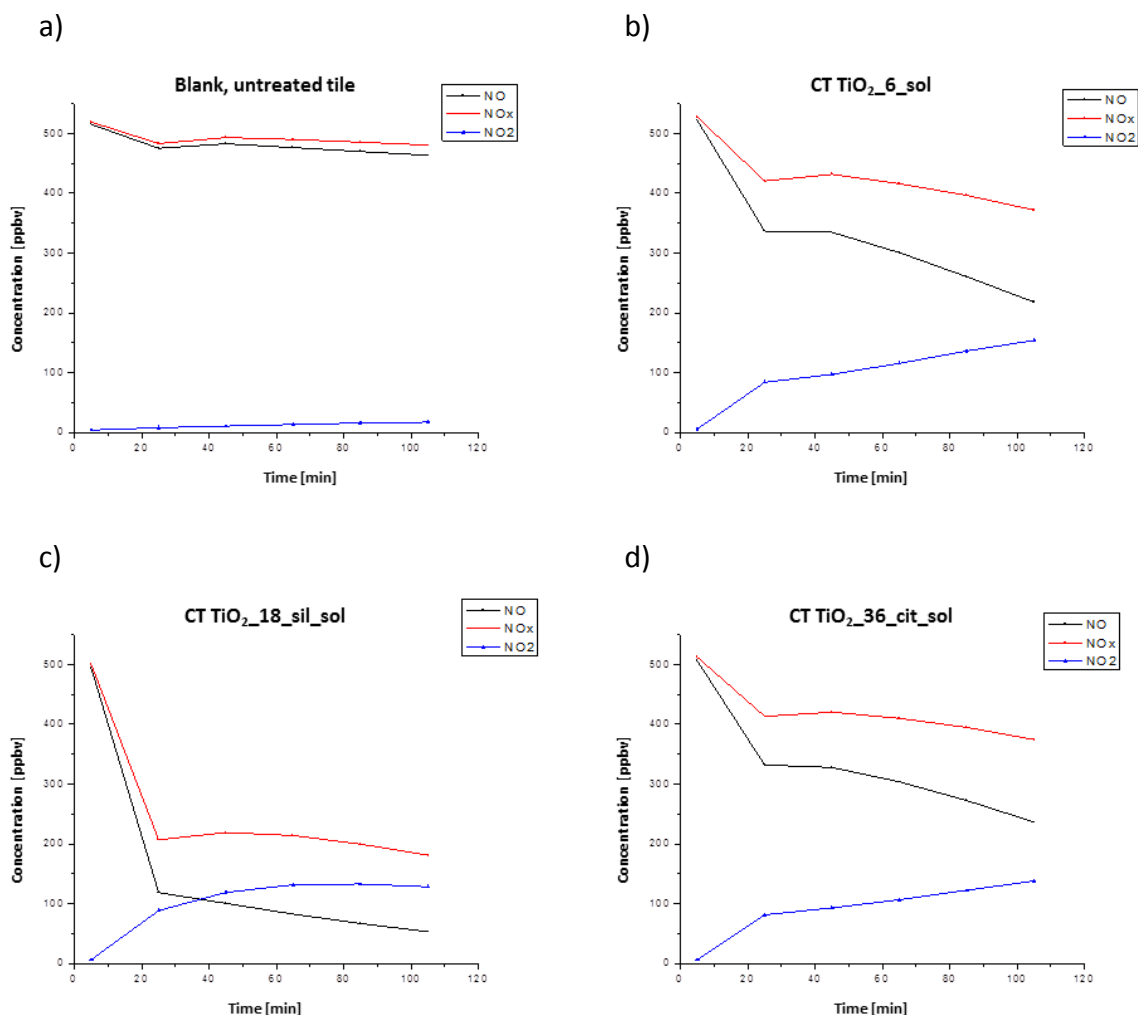


Figure 24 - NO and NO_x conversion tests on treated ceramic tiles: a) Blank, uncoated tile, b) CT TiO₂_6_sol, c) CT TiO₂_18_sil_sol and d) CT TiO₂_36_cit_sol.

Considering the NO and NO_x conversion, the silica coated sample CT TiO₂_18_sil_sol showed best photocatalytic activity, with a degradation efficiency higher than those of pristine and citrate coated samples. As previously reported, the improvement of photocatalytic performance due to the presence of SiO₂ may be ascribed to different factors such as the increase the NM surface roughness, with consequent increase of the active surface area, the increase of NM hydrophilicity and the favored adsorption of the test molecule on TiO₂ surface. To deepen investigate results obtained, further tests have been performed to compare the pristine and the silica blended CT TiO₂_18_sil_sol samples, at constant solid content (Fig. 25).

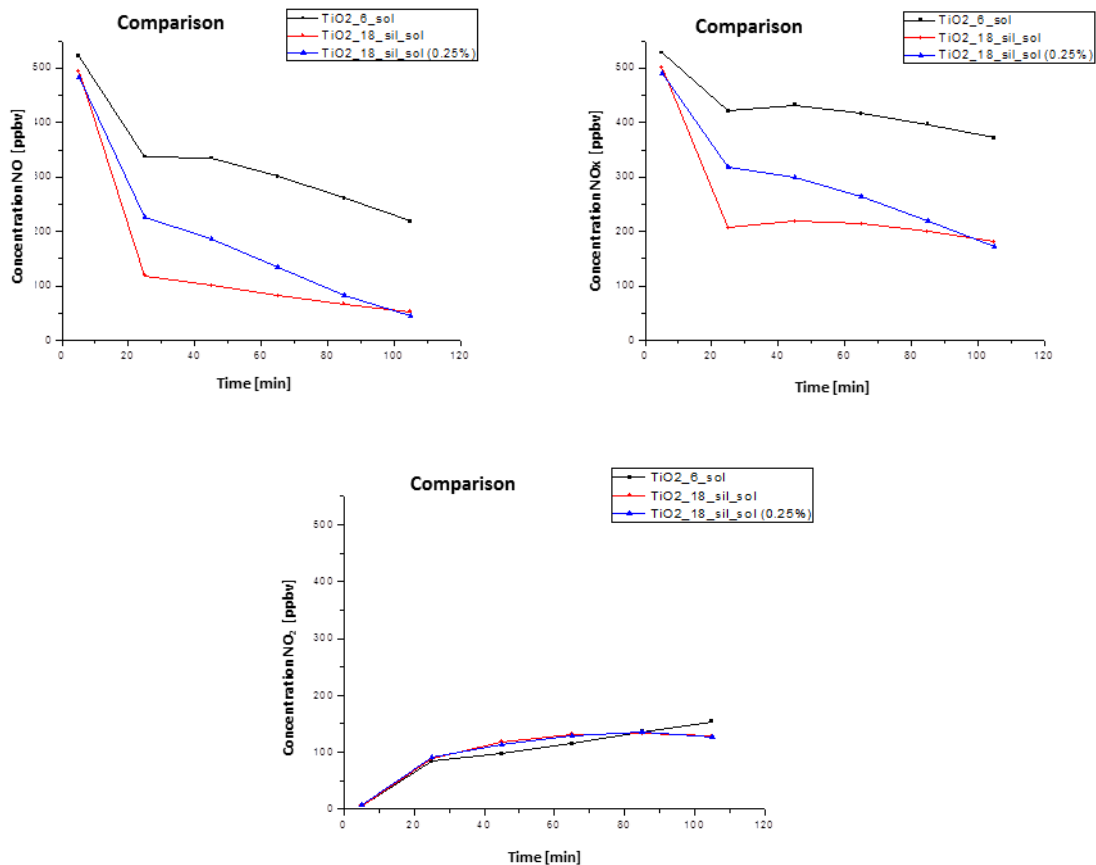


Figure 25 - NO and NO_x conversion tests on treated ceramic tiles coated with pristine TiO₂_6_sol (TiO₂ content 1 wt.%, black), modified TiO₂_18_sil_sol (TiO₂ content 1 wt.%, red) and CT TiO₂_18_sil_sol (total solid content 1 wt.%, TiO₂ content 0,25 wt.%, blue).

As demonstrated by the graphs obtained, both silica modified samples, even at constant solid content and therefore at TiO₂ concentration of 0,25 wt.%, showed an higher degradation efficiency in comparison with that of pristine sample. On the data obtained, RRS implementation at industrial scale level resulted in a relevant product performance improvement.

6.3.4 Toxicity outcomes

An important parameter to evaluate the health hazard reduction following the introduction of RRS was the toxicity of pristine and modified NMs towards cells. Cell lines employed were chosen by biologists as a function of the involved industrial scenario and NM application. In all processing lines the exposure was supposed to occur mainly by inhalation, thus for viability and cytotoxicity tests, two cell lines were selected: alveolar epithelial cells and macrophages, A549 and RAW 264.7 cells, respectively. Both cell types were typically encountered by NMs upon inhalation and their interaction determined the biological outcome of the exposure. To evaluate the effect of the prolonged exposure to NMs, genotoxicity tests were performed with mouse embryonic fibroblasts, Balb/3T3 cells.

6.3.4.1 Ag samples

Different Ag samples, including Ag_1_sol, Ag_15_sil_sol, Ag_31_sol_UF and Ag_35_sil_sol, owing to this processing line were in-vitro tested by biologists partners of SANOWORK EU project. Ag materials, along the range of dose tested, exerted different toxicity towards epithelial cells A549, more evident for macrophages RAW 264.7 (Fig. 26).

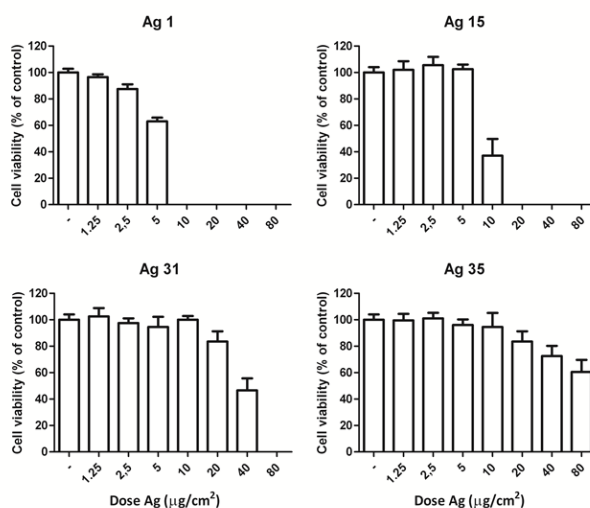


Figure 26 - Cell viability, measured by Resazurin assay using RAW 264.7. Cells were exposed for 24 h to increasing concentrations (1.25 – 80 µg/cm²) of PL 5 Ag NM.

Ag_15_sil_sol sample exhibited very similar cytotoxic effects compared with the pristine sample in both RAW 264.7 and A549 cell lines, indicating that this modification did not mitigate Ag NM toxicity. Ag_35_sil_sol showed a significant lower cytotoxic effect if compared with that of pristine material. Strongest mitigating effect was observed with purified Ag_31_sol_UF sample, that exerted a very low toxicity, suggesting that most of the toxic effects exhibited by Ag_1_Sol was due to its relevant content of Ag⁺ ions. The presence of Ag gave rise to interferences with LDH assay, therefore it was difficult to make an accurate estimation of the relative cytotoxicity of both forms.

The oxidative stress, defined as an imbalance between anti-oxidant and oxidant in cells, was also taken into account in the toxicity evaluation. The pristine Ag NPs Ag_1_Sol and the purified Ag_31_sol_UF sample gave a not significant signal by EPR, also in cell free conditions, suggesting that they did not generate ROS. Ag_1_sol strongly reduced the level of glutathione in both cell types, indicating a significantly induced oxidative stress. On the contrary, it was required a much higher concentration of the ultra-filtrated Ag_31_sol_UF sample to observe a reduction in glutathione level, suggesting that Ag⁺ ions may be involved in both the cytotoxicity and oxidative stress observed. Altogether these results suggested an high cytotoxicity and signs of oxidative stress following treatment with pristine Ag NMs; on the contrary, the Ag_31_sol_UF sample, was found to be much less cytotoxic than the pristine one towards both macrophages and epithelial cells, suggesting an efficient remediation of the toxicity of involved Ag NMs.

6.3.4.2 TiO₂ samples

Both pristine and modified TiO₂ NM, in the dose range tested, displayed only very low toxicity in terms of membrane integrity or cell viability for both A549 and RAW 264.7 cell lines (Fig. 27).

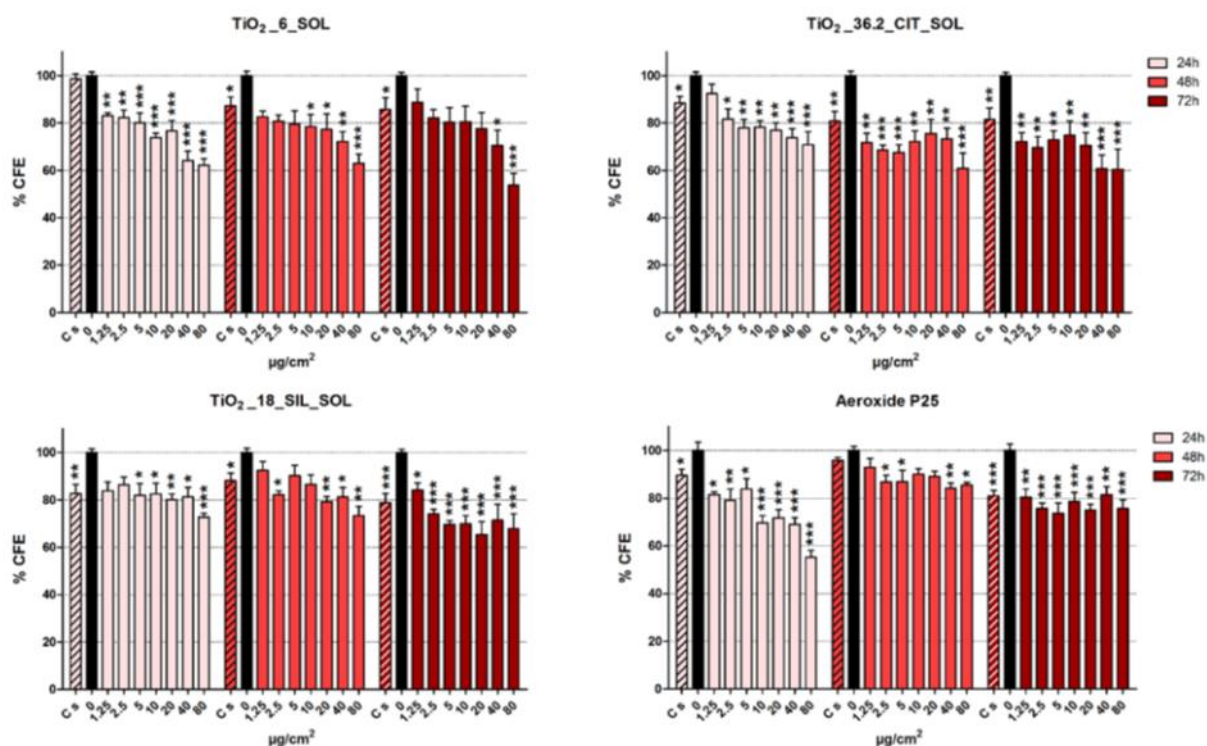


Figure 27 - Cell viability, measured by CFE assay, in A549. Cells were exposed for 24, 48 and 72 h to increasing concentrations (1.25 – 80 µg/cm²) of TiO₂ NMs. Data are graphically presented as mean % CFE values normalized to the untreated control (0 µg/cm²; black bar) ± standard error mean (SEM); n = 9. * p > 0.05; ** p < 0.01; *** p < 0.001. C+: 1µM Na₂CrO₄ that induced 0 % CFE (data not shown).

P25 was employed as a benchmark material to compare toxicological profiles of all the TiO₂-based materials investigated. P25 has no or low toxicity, as determined with LDH, resazurin or calcein/ethidium methods, although clear cut toxicity is seen with CFE and Cytome assays. The ability of pristine and modified TiO₂ sample to induce oxidative stress were evaluated by measuring ROS production in cell free condition by EPR and DCFH, or in presence of cell by GSH and TBARs. P25 produced a small amount of ROS as detected by EPR, while no ROS were detected in the acellular DCFH assay. This latter showed that P25 slightly induced oxidative stress in macrophages after 24 h incubation and this effect was associated with the detection of TBARs, index of lipid peroxidation. In alveolar epithelial cells, P25 reduced the level of the anti-oxidant GSH, indicative of oxidative stress.

Pristine TiO₂_6_sol sample showed a low levels of intrinsic ROS by EPR, but produced a slightly increased the level of oxidative stress in macrophages which was also associated with a reduction in the cellular GSH content. Modified samples TiO₂_18_sil_sol was able to generate ROS as detected by EPR, but no ROS production was found in the acellular DCFH

assay. Spray dried sample TiO₂_15_NP_SD significantly decreased the level of GSH in macrophages. TiO₂_36_cit_sol slightly increase oxidative stress in alveolar epithelial cells and decreased the level of GSH in macrophages. The inflammogenic potential of all the modified TiO₂ samples tested, assessed in terms of stimulation of NO production and cytokine secretion by macrophages, was clearly stronger than those of pristine or benchmark materials.

To investigate the effect of prolonged exposure to TiO₂ NM, genotoxicity tests were performed with A549 and Balb/3T3 cells. In both cell lines, TiO₂ samples showed a genotoxic potential in vitro. Genotoxicity, evaluated by different endpoints, showed that all TiO₂ samples induced chromosome and DNA damage, and morphological transformation, characteristic of tumorigenic cells. Similarly, and as previously observed for the solvent controls of PL 1 and PL 4 NMs, the solvent controls showed genotoxic and carcinogenic potential, suggesting that the effects observed might not be due exclusively to NMs, but also to their solvent that may contain toxic contaminants.

6.3.5 Characterizations of Ag and TiO₂ in biological media

6.3.5.1 Ag samples

A further goal was to find a relationship between toxicological response and chemical-physical property (as size and ZP) of NMs tested in biological systems. In the last few years, some have been identified and related to the reactivity of NPs toward biological components. These hazard-specific properties are usually investigated and determined by classical physicochemical characterization. Physicochemical characterization of nanomaterials may be divided into three categories based on the physical state of the nanomaterial (i.e., dry, wet, or in a test system) that can be referred to as primary, secondary, and tertiary phase [65]. Primary characterization was performed on particles or materials as dry powders. Secondary characterization was performed on particles or materials in the wet phase (solution or suspension) as in solvents, ultrapure water, environmental water (ground, fresh, marine), buffered solution (phosphate buffered saline) or cell culture media. Tertiary characterization was performed on particles or materials either in vivo or ex vivo, including characterization in cells and tissues (e.g., blood, lung fluid, liver, and kidney) as well as interactions with proteins, lipids, or specific cell types during or after treatment. Secondary characterization seems to be fundamental to predict biological reactivity, but it was usually limited to common solvents like water. Nevertheless, specific biological conditions, such as low NPs concentration, type / pH of the medium and presence of biological entities, could play a crucial role on the physical characteristic that are measured. It is well known that when NM have been dispersed in the cell culture medium, a water solution of salts, sugars, lipids, aminoacids and proteins, their surface was spontaneously coated by serum protein giving rise to the NPs PC formation [66, 67] as depicted in figure 28.

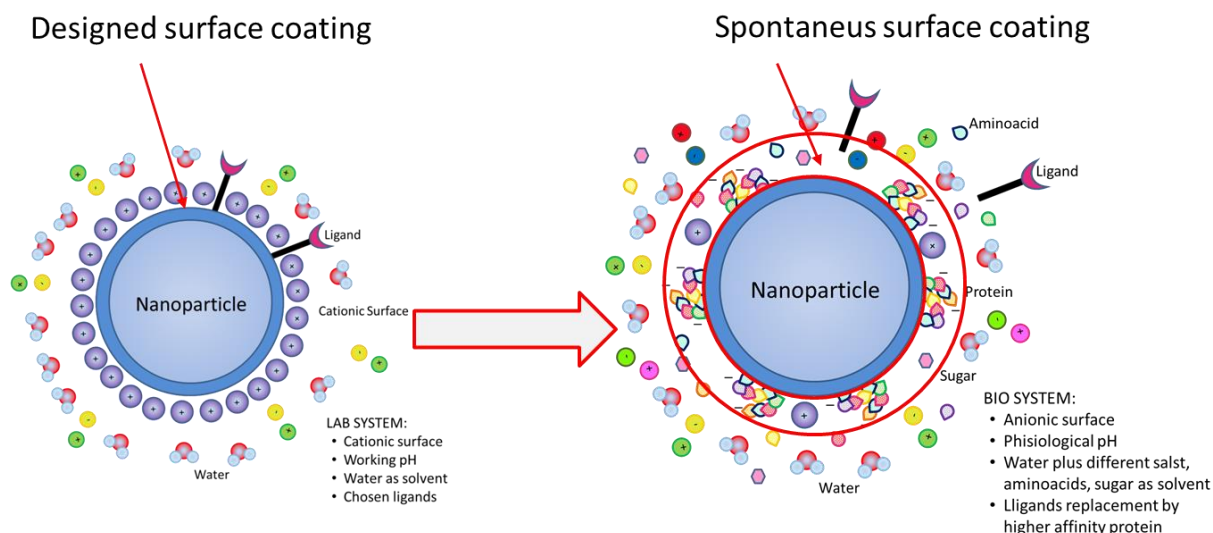


Figure 28 - Schematic representation of PC formation moving from a lab-system to a bio-system

Therefore characterizations conducted in the lab-scale system may be not fully representative of the properties shown by NMs in bio-systems, where they effectively move and react, with a consequent wrong information, that hinders the definition of sound structure-reactivity mechanisms and limit the success of safe by design approach. To obtain more useful data and to understand a possible PC formation and its modification due to introduced design surface coatings, NMs and NPs were dispersed, at the same concentration, in water or cell culture media. Then, both d_H and ZP were measured and compared. All Ag samples in both solvents, gave reproducible and sound size data. In most of the samples only one size population were detected, with a Pdl around 0.2. When dispersed in biological media, Ag samples displayed an excellent colloidal stability and maintained practically unmodified their d_H and Pdl, as evidenced by the size graphs (Fig. 29) and data (Table 14) obtained by DLS.

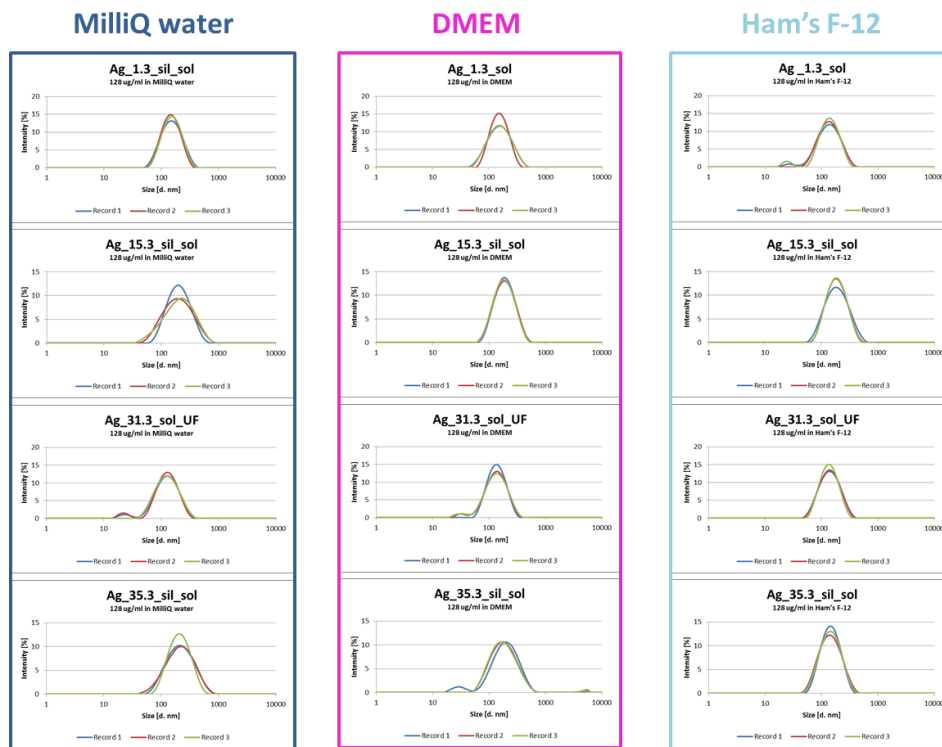


Figure 29 - DLS sizes of Ag samples dispersed in Milli-Q water, DMEM and Ham's F-12. For each solvent, from the top to the bottom, the samples were Ag_1_sol, Ag_15_sil_sol, Ag_31_sol_UF and Ag_35_sil_sol

Table 14 - pH, ZP, mean size diameter by intensity and Pdl of Ag samples dispersed at 128 µg/ml in deionized water and complete culture media DMEM and Ham's F-12.

Sample Code	MilliQ water				DMEM				Ham's F-12			
	pH	ZP [mV]	d _H [nm]	Pdl	pH	ZP [mV]	d _H [nm]	Pdl	pH	ZP [mV]	d _H [nm]	Pdl
Ag_1_sol	3.9	-14.0	130	0.20	7.8	-7.5	131	0.21	8.0	-9.9	113	0.23
Std. Dev.		0.2	2	0.02		0.3	0	0.02		0.3	0	0.00
Ag_15_sil_sol	3.2	-3.2	169	0.24	7.8	-7.5	162	0.19	7.7	-7.5	160	0.20
Std. Dev.		0.1	1	0.02		0.4	1	0.01		0.5	1	0.01
Ag_31_sol_UF	4.5	-16.3	103	0.24	8.0	-8.6	114	0.19	8.1	-9.8	118	0.19
Std. Dev.		0.4	0	0.00		1.2	2	0.01		0.5	1	0.02
Ag_35_sil_sol	6.5	-34.6	184	0.21	8.0	-7.8	146	0.29	7.9	-9.1	118	0.23
Std. Dev.		1.1	2	0.02		0.4	3	0.01		0.3	2	0.01

For Ag sample, the maintenance of the NM d_H in water and culture media suggested a non-interaction between NM and biological component. However, d_H did not depend only on the surface composition of a NM, but also on the ionic strength of the medium in which NM was dispersed, that may affect the NM diffusion rate by changing the thickness of its electric double layer (i.e. Debye length). Likely in our case the adsorption of small biological entities, may be masked by the higher ionic concentration of the cell culture media, that compressed

the electric double layer and reduced the measured d_H . Therefore, it was hypothesized that the combined presence of adsorbed moieties on Ag NP surface and the high ion concentration in the media, acting in opposite way, resulted in an apparent maintenance of both d_H and Pdl. Unfortunately, in these cases the data obtained did not allow any considerations on PC thickness, although ZP levelling supported the formation of protein coatings. ZP of Ag samples dispersed were leveled off around -7.5 mV in DMEM and -9/-10 mV in Ham's F-12, in agreement to the value expected by serum protein at the same pH [67].

6.3.5.1.1 Interaction between AgNPs and BSA

The observed ZP encouraged to investigate other parameter inherent to NMs-biological interactions, such as quantity, identity and secondary structure of adsorbed proteins, that may be related to the presence of designed surface modification and toxicity by NMs [68]. In this contest it was begun a collaboration with Limerick University (IRL) on the possibility to deeply characterize NP in biological condition. During the stage in those Laboratories, it was performed an investigation on the interaction between Ag NPs and BSA, a small globular protein that is one of the main in plasma, being of significant relevance as reference model. Ag NPs were conjugated with BSA using different BSA/Ag mass ratio, optimizing a protocol of purification (Fig. 30) and investigating the formation of BSA corona by different techniques.

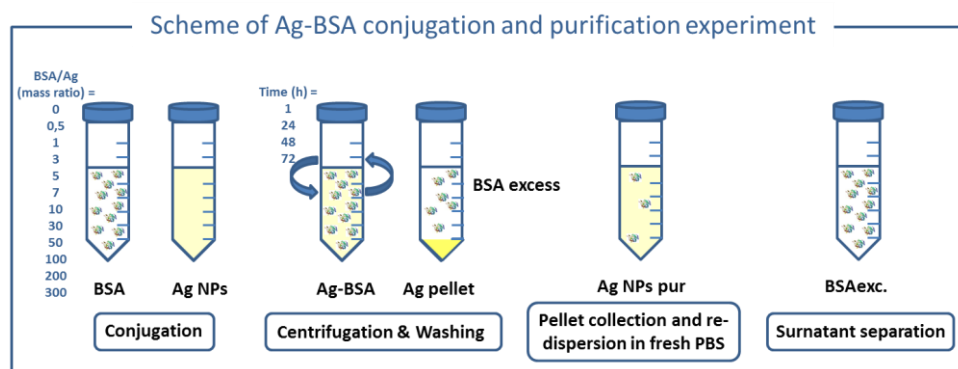


Figure 30 - Scheme of Ag-BSA conjugation and purification tests

UV-vis spectroscopy was employed to estimate the BSA absorption on NPs, measuring the intensity of its band at 280 nm before and after the purification experiment, that allowed to separate Ag associated protein from non-associates one. Unfortunately, all Ag NPs considered showed a shoulder around 280 nm that overlapped to the band of BSA. Especially for the lower BSA/Ag mass ratio tested, the signal of Ag NP was stronger than that of BSA hindering to obtain an adsorption isotherm. To avoid the overlapping of the Ag signal, Bradford's assay [69] was employed, a common method for protein quantification allowing to shift maximum of peaks. The Bradford reagent contain Coomassie dye, that binded the proteins leading to an immediate shift in absorption maximum to 595 nm with a concomitant color change of the solution that became blue. Unfortunately, the HF contained in the Bradford reagent dissolved the Ag NPs retained in the supernatant after ultracentrifugation, releasing

in solution the absorbed BSA molecules and doing impossible a correct protein quantification. For this reason, it was not possible to make a quantitative estimation of BSA adsorbed by UV-vis spectroscopy. However, the UV-vis spectroscopy in case of metallic NPS allowed to study also the surface alteration because of characteristic SPR peak, that is due to the collective oscillation of the metallic surface electrons. It is well known that the SPR peak maximum is very sensitive to changes in the close environment of NP and its change may be used to monitor the PC formation [66, 70]. All samples involved and their Ag-BSA adduct were analyzed before (Fig. 31) and after (Fig. 32) the above described purification process (after 1, 24, 48 and 72 h). The SPR peak of Ag sample (Ag 0) and Ag-BSA samples (from Ag 1 to Ag 11) were monitored at 0, 24, 48 and 72 h.

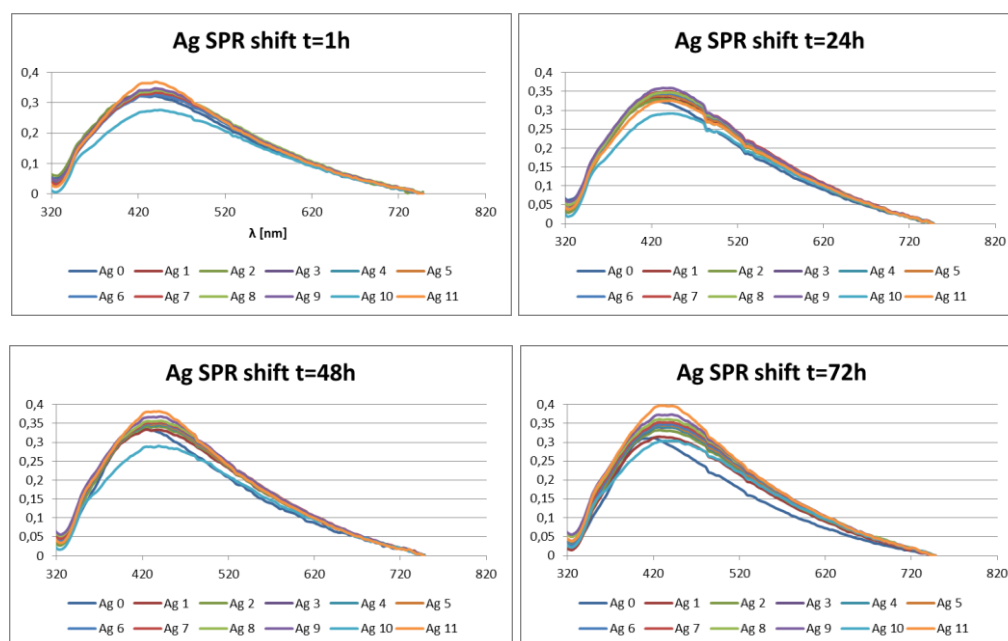


Figure 31 - UV-vis spectra of Ag and Ag-BSA samples after 0, 24, 48, 72 h of interaction with BSA

Ag sample dispersed in PBS in absence of protein (Fig. 31) showed SPR peak maxima at 421 nm and by further addition of BSA, the SPR peak broadened and shifted to higher wavelength (433 nm), suggesting a protein adsorption. For all Ag-BSA samples the SPR shift was already evident from the first hour of interaction with BSA, slowly shifting towards red during the 72 h.

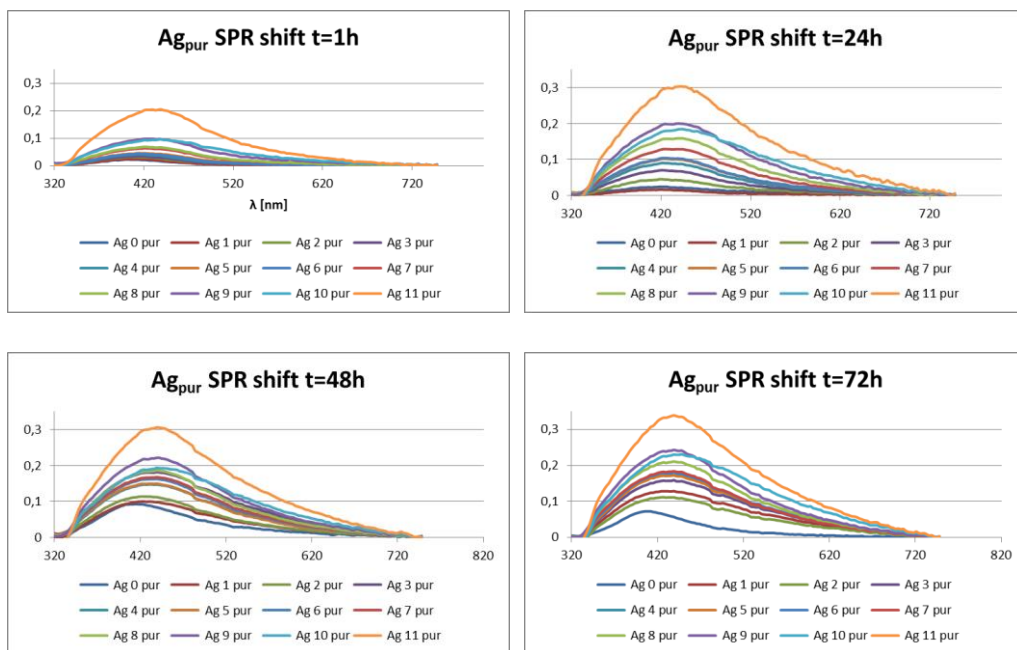


Figure 32 - UV-vis spectra of purified Ag and Ag-BSA samples after 0, 24, 48, 72 h of interaction with BSA

In the SPR peaks of Ag sample (Ag 0 pur) and Ag-BSA samples (from Ag 1 pur to Ag 11 pur) after purification (Fig. 32), the shift was observed a very different intensities, that may be related to the colloidal stability of the samples. In fact, during the purification, that comprise 3 cycles of centrifugation and re-dispersion, the sample prepared in absence of BSA (Ag 0 pur) hardly tolerated the centrifugation, showing a strong aggregation, that reflected a broadening and a drop in the SPR peak intensity. Increasing the amount of BSA added, the SPR peak intensity slowly increase and its maximum shifted towards red, suggesting a stabilizing effect of BSA towards AgNPs. For all purified Ag-BSA samples, the SPR shift was evident in the first hour of interaction with BSA and further shifted up to 24 h, leveling off for the rest of experiment.

ATR-IR spectroscopy was used to monitor conformational changes of BSA secondary structures by interaction with different Ag NPs. Protein infrared spectra showed peaks arising from amide bond vibrations, important bands for protein conformational studies being were sensitive to changes in protein secondary structure. Amide I was a broad band and its overall shape was determined by many secondary structure components of the analyzed protein, as α -helix, β -sheets, turns and random coil. Its characteristic absorption band, centered at 1 600–1 700 cm^{-1} , was largely due to C=O stretching vibrations. The amide II band, centered at 1 500–1 600 cm^{-1} , was related to on plane vibrations of the N-H bending and C-N stretching vibrations of the amide bond, although this band is less sensitive to conformational changes in comparison to the amide I band [71]. In ATR-IR study in solution, H₂O absorption was a problem because it directly overlap to amide I band. H₂O has a strong IR absorbance around 3 400 cm^{-1} (O-H stretching), 2 125 cm^{-1} (H₂O association combination band) and 1 640 cm^{-1} (H-O-H bending), whereas D₂O has no absorption band in the region where amide I and amide II bands were observed [72]. Although challenging, it was decided to study BSA conformational changes in presence of water, because it is well known that proteins may lose their original secondary

structure if dried or affected by H-D exchanges in the peptide linkages [73]. To collect information on the changes in protein secondary structures, the spectra of bare BSA and BSA-Ag in their PBS solution were recorded and bands in amide I and II regions compared. Unfortunately the really low Ag and BSA concentration employed, gave rise to a bad spectra with a low signal-to-noise ratio, doing impossible any sound interpretation. Thus, to check the possibility to obtain more clearly interpretable results, some samples with higher Ag and BSA concentration were prepared and analyzed.

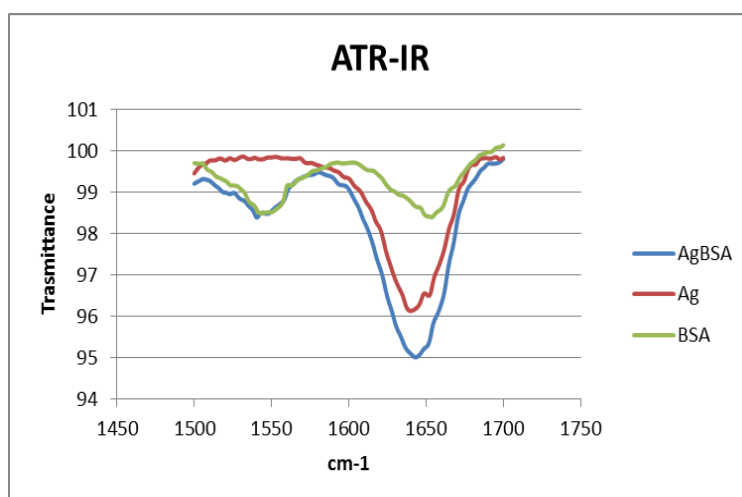


Figure 33 - ATR-IR spectrum of Ag and Ag-BSA samples after 24 h of interaction with BSA

Focusing on the amide I and II region (Fig. 33), in the case of pristine Ag, the spectrum showed a peak at 1640 cm^{-1} due to the C=O bond of the PVP used as capping agent. The BSA dispersed in PBS displayed signals at 1654 cm^{-1} (amide I region) and 1547 cm^{-1} (amide II region). The spectrum of Ag-BSA showed bands at 1643 cm^{-1} (amide I region) and 1543 cm^{-1} (amide II region). Both amide I and amide II absorption peaks of Ag-BSA were slightly shifted to lower wavelength in comparison to those of pure BSA, suggesting some changes in the secondary structures of BSA. Also the data collected for the surface modified Ag samples suggested subtle differences in the orientation of BSA when conjugated with Ag NPs, that has to be further investigated by a concentration series study.

Raman spectroscopy may successfully monitor variations in the secondary structure of proteins after adsorption on NPs. It is known that some surfaces, for example those of metals, may enhance the Raman signal of the molecules adsorbed, due to the so called SERS. The increase of the Raman intensity may be in the order of 10^{10} - 10^{11} [74], but for some systems, it can reach also higher values. In our case the Raman study was performed to understand if the BSA molecules displaced the PVP used as capping, close to the Ag surface. For the Raman investigation, the liquid samples were analyzed either using a liquid sample holder or directly making a drop of the solution under the laser beam, trying to enhance the Raman signal. Ag NPs, BSA solutions and Ag-BSA conjugates were analyzed, but all the exhibited low intensities and were quite noisy, due to the low concentration. Also changing the spectrometer set up and focus, the expected SERS was not present, suggesting the presence of a certain amount

of oxide on Ag surface that hinders the SERS [75]. This was confirmed by XPS analysis, that can determine the surface concentration of elements present and their oxidation state. The XPS may identify the elements present in the outer 10 nm of a sample down to 0.1 atomic percent. However for that metallic NPs it require powdered material and therefore a spray dried sample of pristine Ag was subjected to XPS (Table 15 and 16). Area highlighted in violet corresponded to overall concentration and below each, it was reported the synthetic components of the transition and possible species responsible for it. Data obtained, justified the absence of SERS, showing that the Ag NP surface was mainly composed by C from PVP and, moreover, half of the Ag detected on NM surface was present as oxide.

Table 15 - Quantification from survey XPS spectra

Sample Code	O 1s	C 1s	N 1s	Na 1s	Ag 3d
Ag_1_sol	24.1	63.2	8.8	1.4	2.5

Table 16 - Quantification from HR-TEM XPS spectra

Name	Position	FWHM	R.S.F.	% Conc.	Possible Compounds
O 1s	531.77	2.517	2.93	23.9	
Ag 3d	367.82	1.221	18	5.4	
C 1s	284.77	1.904	1	70.7	
O 1s	531.35	1.776	2.93	11.2	Metal Oxides
O 1s	532.51	2.000	2.93	12.6	O from Organics
Ag 3d	367.86	1.385	10.7	2.6	Ag ₂ O
Ag 3d	373.87	1.294	7.38	2.5	
Ag 3d	369.54	1.180	10.7	0.1	Ag Cluster
Ag 3d	375.54	1.155	7.38	0.1	
C 1s	284.80	1.639	1	56.3	C-C, C-H
C 1s	286.99	1.662	1	14.4	C-O, C-OH

6.3.5.2 TiO₂ samples

To understand a possible PC formation and its modification due to introduced design surface coatings, TiO₂ NMs were dispersed, at the same concentration, in water or cell culture media, then both d_H and ZP were measured and compared (Fig. 34 and Table 17).

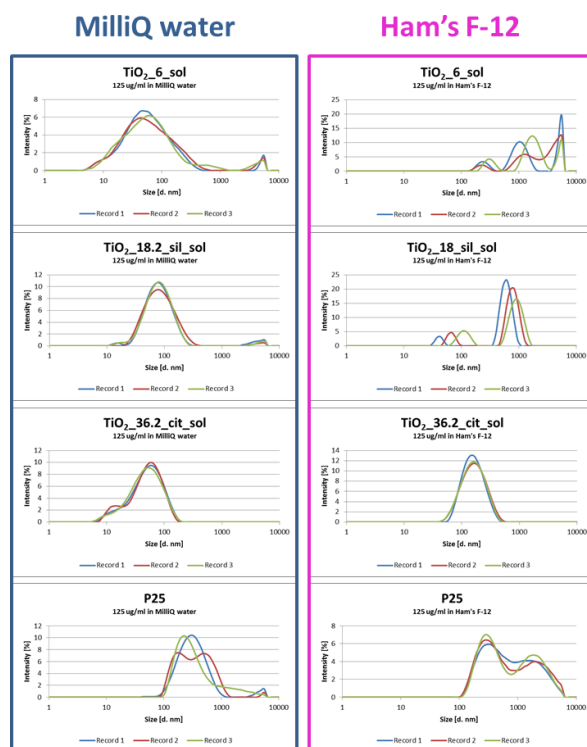


Figure 34 - DLS size graph of TiO₂ samples dispersed in Milli-Q water, DMEM and Ham's F-12. For each solvent, from top to bottom, the samples were TiO₂_6_sol, TiO₂_18_sil_sol, TiO₂_36_cit_sol and P25

Table 17 - pH, ZP, mean size diameter by intensity and Pdl of TiO₂ samples dispersed at 125 µg/ml in deionized water and complete culture medium DMEM. Data in *italics*, of not of sufficiently good quality data, were reported only to evidence a general trend.

Sample Code	MilliQ water				DMEM			
	pH	ZP [mV]	d _H [nm]	Pdl	pH	ZP [mV]	d _H [nm]	Pdl
TiO ₂ _6_sol	2.3	41.2	45	0.48	7.2	-12.2	1 829	0.64
Std. Dev.		0.5	1	0.09		0.9	100	0.05
TiO ₂ _18_sil_sol	4.8	32.2	156	0.11	7.7	-10.8	479	0.77
Std. Dev.		4.1	22	0.00		0.6	44	0.15
TiO ₂ _36_cit_sol	5.5	-34.2	39	0.28	7.6	-10.9	138	0.21
Std. Dev.		1.2	1	0.00		0.2	1	0.01
P25	4.1	37.4	286	0.30	7.7	-11.5	468	0.43
Std. Dev.		0.9	4	0.04		0.4	16	0.02

Although it was impossible to obtain sound size data for TiO₂_6_sol, TiO₂_18_sil_sol and P25 samples dispersed in medium, due to the presence of different size population and large, settling particles during the analyses, a general trend may be established. Comparing the data obtained for TiO₂ NPs dispersed in water or in complete culture medium, a size enlargement and ZP potential levelling may be noted. The size enlargement, attributable to poor stability and strong aggregation of TiO₂ samples in cell culture medium, may be justified considering that all TiO₂_6_sol, TiO₂_18_sil_sol and P25 samples cross their IEP to reach culture medium buffered pH, with consequent NP destabilization.

The modification of d_H was especially noticeable for the pristine sample that underwent a fivefold d_H increase and partially precipitated in cell culture medium. Therefore it was challenging to obtain sound size data due to poor samples stability and polydispersion, that reduced the measurement reproducibility, as shown by in the DLS size graph (Fig. 34, upper graph). Three peaks were present in the particle size distribution by intensity, centered at 2 346 nm (Peak 1, %PD = 28), 3 901 nm (Peak 2, %PD = 18) and 263 nm (Peak 3, %PD = 21), which relative amount in the volume particle size distribution were 10 %, 90 % and 0 %, respectively, confirming the presence of aggregates.

Both TiO₂_18_sil_sol and P25 samples showed a bimodal size distribution, therefore the intensity particle size distribution was considered for the assignment of the size of each peak. Sample TiO₂_18_sil_sol showed peaks centered at 74 nm (Peak 1, %PD = 52) and 780 nm (Peak 2, %PD = 23) with a relative amount of 52 % and 23 % respectively in the volume particle size distribution. Sample P25 showed a bimodal distribution, with overlapping peak. Peaks were centered at 803 nm (Peak 1, %PD = 56) and 2 198 nm (Peak 2, %PD = 38), with a relative amount of 56% and 38% respectively in the “volume” particle size distribution. Citrate coated sample TiO₂_36_cit_sol, gave good and reproducible analyses also when dispersed in cell culture media, showing a monomodal size distribution (Fig. 34, bottom graph) centered at 138 nm. This sample underwent the low d_H increase, probably due to the electro-steric contribution of citrate coating and, having no IEP, maintained negative its ZP over the involved pH range.

Regarding the ZP, as previously reported for Ag and ZrO₂ NMs, the leveling occurring in culture medium were consistent with the protein absorption on NM surfaces. In DMEM the ZP of all measured samples level off at about -11 mV, value in accordance with those of serum protein at the same pH [67]. The different dispersion of TiO₂ sample in cell culture media, detected in condition close to those employed by biologists, did not allow to meet relationships with the toxicity data. Anyway, measurement performed for pristine and P25 sample were exploited in an investigation carried out by biologists on the pro-inflammatory responses of RAW 264.7 murine macrophages co-administered with LPS [76], observing that the simultaneous exposure to LPS and TiO₂ NPs may exacerbate the inflammatory response in vivo.

6.3.6 Exposure assessment: on-site measurements

Being inhalation one of the main way of exposure to NMs, in all processing lines the EA was focused on contamination by NMs in air. EA started from a "basic measurement campaign" also in PL 5 to measure the exposure to NMs during the steps supposed to be critical. Measurements were carried out in Colorobbia workplace, during the spray coating of the ceramic tiles by Ag ant TiO₂ sols. The instruments used were the same as in the other preliminary campaign and were the CPC and the TEM grid sampler system. The CPC was used between main potential sources and outlets, to determine in real time the total particle concentration in number, in the range 10 nm - 1 μm. The TEM grid sampler was used to measure particles near to the respiratory system; in this instrument, through a sampling pump, particles were sampled on specific TEM grids, which were observed and analyzed by EDS.

The background ambient aerosol was measured before to start with the spraying operations, to discern the specific contribution by the process to air pollution. During CPC measurement of the ambient aerosol, the background noise gave an average particle concentration of 13 500 particles/cm³ (standard deviation = 850 particles/cm³). From TEM observation of sampling grids and EDS analyses on the particles collected, the background was composed by soot particles and submicron oil droplets, in addition to large particles of calcite and alumina. The presence of some metal particles suggested that the proximity of the welding workshop gave rise to particle contamination due to co-activity. However no particle containing the involved Ag and TiO₂ NMs were detected in the grid analysis. Considering the full spray coating operation, a slow increase in the count was observed, followed by a sharp increase in the particle concentration few minutes after that Ag dispersion was sprayed (Fig. 35).

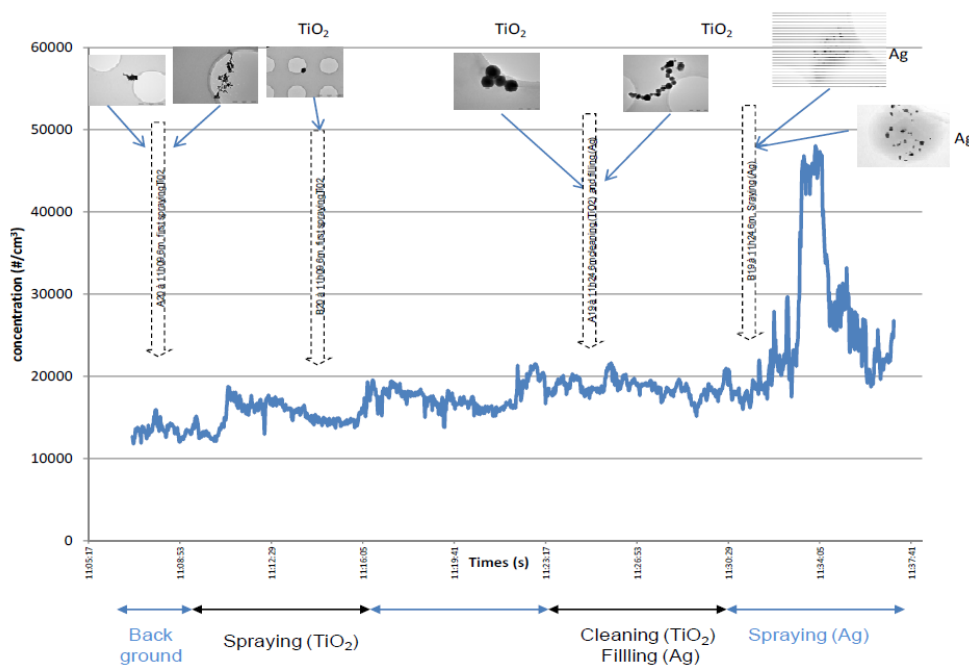


Figure 35 - Evolution of the particle calculation (particles/cm³) during spray coating operation and TEM images of the particles in each step

During the spraying of the TiO₂ dispersion, the concentration in number of particle increased over the period. Anyway, from TEM observation the only objects containing a low percentage of Ti (1-2 wt.%) were particles with diameter < 1 μm characterized by an high K or Si content. Although the background noise showed no trace of Ti, it was difficult to attribute these particles to the spraying operation, due to the low Ti concentration and the shape of the particles. During the spraying of Ag dispersion, the particle count by CPC increased (Fig. 35). From the observation and EDS analysis of sampling grids, the particles collected were organic clusters containing a large amount of Ag. During firing and cooling of treated tiles the particle count decreased over the period, raising the background level, although during cooling of Ag coated tiles, some particle containing Ag aggregates were observed (data not shown).

6.3.7 Cost/benefit analysis

A qualitative cost/benefit analysis for PL 5, was carried out by UL in collaboration with partners involved in SANOWORK project. Tables 18 and 19 showed hazard, exposure, risk and associated cost data in relation to the spraying operation, that was considered an high risk exposure step. Exposure data for the pristine material, Ag_1_sol and TiO₂_6_sol, were taken from the measurement campaign carried out by INERIS, while toxicity data derived from the tests performed by biologists. Functional properties were evaluated together with the industrial partner Colorobbia, as well as production time and costs.

Table 18 - Toxicity, exposure and risk data and remediation costs for the spraying operation of Ag NPs in PL5, considered a high risk task for workers.

Sample Code	Ag_1_so	Ag_31_sol_UF
RRS	None, unmodified Ag NPs in solution	Purification, Ag NPs purified through ultrafiltration
Exposure	1.6 x 10 ⁴ particles/cm ³ GM: 0.089 (mg/m ³) φ 100 nm	?
Toxicity	Very toxic	Much less toxic
Risk	Likely unacceptable in worst case in which all the particles in the exposure measurement contain Ag	?
Functional Change	None by definition	Significantly less antibacterial
Cost [€/Kg]	60	90
Production Time [h/Kg]	Externally procured	0.4

Spray coating operation of Ag NM within PL5 showed a relevant occupational risk. The RRS of purification gave a modified material Ag_31_sol_UF with a markedly reduced toxicity

in comparison to that of pristine sample, but the antibacterial activity, at same total Ag content, was decreased as well. Anyway the low toxicity of the purified, the low production time and cost, suggested that the material may be used at higher concentration to obtain the desired antibacterial effect.

Table 19 - Toxicity, exposure and risk data and remediation costs for the spraying operation of TiO₂ NPs in PL5, considered a high risk task for workers.

Sample Code	TiO ₂ _6_sol	TiO ₂ _15_NP_SD	TiO ₂ _18_sil_sol	TiO ₂ _36_cit_sol
RRS	None , pristine TiO ₂ NPs in solution for spraying	SD , spray dried TiO ₂ re-dispersed for tile spraying	SiO₂ blending , TiO ₂ NPs blended with colloidal silica for spraying	Citrate surface coating , TiO ₂ NPs coated with for spraying
Exposure during spraying operation	8 195 particles/cm ³ GMD: 0.018 (mg/m ³) φ 100 nm (However, all only a tiny fraction are expected to be TiO ₂ particles)	-	-	-
Toxicity	Comparable to bench mark material P25	Oxidative stress comparable to pristine material. Stronger inflammogenic potential compared to pristine material	Oxidative stress comparable to pristine material. Stronger inflammogenic potential compared to pristine material	Oxidative stress comparable to pristine material. Stronger inflammogenic potential compared to pristine material
Risk	Health risk in worst case, i.e. assuming exposure levels are entirely attributable to TiO ₂ .	-	-	-
Functional Change	None by definition	Slightly less photo-catalytic than pristine material	Higher photo-catalytic than pristine material	Significantly less photo-catalytic than pristine material
Cost [€/Kg]	13.5 (procurement)	18 (production)	4 (production)	15 (production)
Production Time [h/Kg]	Externally procured	2	24	0.032

Although spray coating operation of TiO₂ NMs within PL5 showed a low occupational risk, the RRS of SiO₂ blending was noteworthy. The modified material TiO₂_18_sil_sol showed a higher photocatalytic activity in comparison to that of pristine material. The improvement of functional properties of TiO₂ NM together with the simple and cost effective industrial implementation, may justify the long production time required.

6.4 Conclusions

RRS were developed and applied to nano Ag and TiO₂ sols used and tested in the production of antibacterial and photocatalytic coatings. Technological, safety and economics aspects were taken into account to evaluate their effectiveness. For Ag NM, RRS of silica blending and core-shell coating as well as purification by ultrafiltration were successfully applied on pristine Ag NMs. Among obtained samples, the Ag_31_sol_UF was selected as a function of its low toxicity for the implementation within PL 5. The pristine and Ag_31_sol_UF samples were employed to spray-coat ceramic tiles, that were tested for antibacterial properties, to evaluate the final product functional properties. Pristine material conferred a higher antibacterial activity to ceramic tiles in comparison with the modified sample CT Ag_31_sol_UF; however in laser ablation test, employed to check the coating homogeneity, no Ag was detected in this latter, suggesting trouble during Ag coating application. Therefore, further tiles will be coated to make antibacterial and laser ablation test repeated, to obtain a larger set of data and better understand the effectiveness of purification strategy in the industrial application.

For TiO₂ NM, RRS silica blending and core-shell coating as well as citrate coating were applied. Among obtained samples, TiO₂_18_sil_sol and TiO₂_36_cit_sol were selected for the implementation within PL 5 and employed to spray coat ceramic tiles. To evaluate the final properties of functionalized tiles, de-pollution test were performed. From NO and NO_x degradation, the SiO₂ coated sample CT TiO₂_18_sil_sol showed best photocatalytic activity, with a degradation efficiency higher than those of pristine and citrate coated samples.

To evaluate the health hazard potential mitigation due to RRS application, pristine and modified samples toxicity were evaluated and compared. Through an extensive study of the toxicity exhibited by tested Ag samples, biologists identified a sample with highly reduced toxicity, Ag_31_Sol_UF. Results suggested a high cytotoxicity and signs of oxidative stress following treatment with pristine Ag_1_sol, while the ultra-filtered Ag_31_sol_UF sample was found to be much less cytotoxic than the pristine one, in both macrophages and epithelial cells, suggesting an efficient remediation of the toxicity of involved Ag NMs.

As assessed by biologists, TiO₂ pristine and modified samples exhibited a comparable toxicity. Therefore RRS of silica blending of TiO₂_18_sil_sol or citrate coating of TiO₂_36_cit_sol did not attenuate the modest oxidative stress elicited by the pristine TiO₂_6_sol material, while showed a markedly greater inflammatory potential. Moreover, TiO₂ samples and their respective solvent controls induced both genotoxic and carcinogenic effects.

To find a relationship between toxicological response and NM chemical-physical properties, size and ZP of both Ag and TiO₂ NMs were investigated in biological condition. For Ag sample, the maintenance of the NM d_H in water and culture media allowed to hypothesized that the combination of adsorbed moieties on Ag NP surface and high ion concentration in the media, acting in opposite manner, resulted in an apparent maintenance of both d_H and Pdl. Otherwise ZP levelling supported the formation of protein coating. The observed ZP suggest

to investigate other parameters inherent to NMs-biological interactions, such as quantity, identity and secondary structure of adsorbed proteins. In this contest it was started a collaborative study with the Limerick University (IRL) on the possibility to deeply characterize Ag NP in biological conditions. Ag NPs were conjugated with BSA, as a model protein, using different BSA/Ag mass ratio and optimizing a protocol of purification. UV-vis analysis let to estimate the Ag SPR peak red-shift, already evident from the first hour of interaction with BSA. Using ATR-IR and Raman spectroscopy it was tried to understand possible protein conformation changes after the interaction with NPs. This background characterizations let to identify advantages and limits of the techniques available to understand the interactions between NPs and biological media proteins, improving knowledge about the influence of the designed surface coatings on PC formation.

For TiO₂ samples, size data showed an aggregation and destabilization in biological medium, with the exception of TiO₂_36_cit_sol sample. The ZP levelling, that underwent the samples after dispersion in cell culture media, suggested the formation of PC. The different dispersion of TiO₂ samples in cell culture media, detected in condition near to those employed by biologists, do not allowed to found a relationship with the toxicity data. Anyway measurement performed for pristine and P25 sample were exploited in an investigation carried out by biologists on the pro-inflammatory responses of RAW 264.7 murine macrophages co-administered with LPS, founding that the simultaneous exposure to LPS and TiO₂ NPs may exacerbate the inflammatory response in vivo.

In term of exposure, no Ag or TiO₂ NM contamination in air were found during the background measurement. Throughout the entire spray coating operations performed with pristine NM, a slow increase in the count was observed, followed by a sharp increase in particle concentration few minutes after that Ag dispersion was sprayed. This result underlined the need of RRS for this latter NM, especially considering the potential toxicity.

A qualitative cost/benefit analysis for PL 5, was carried out by UL in collaboration with partners involved in SANOWORK EU project. The spray coating operation of Ag NM within PL5 showed a relevant occupational risk. The RRS of purification gave a modified material, Ag_31_sol_UF, with a markedly reduced toxicity in comparison of that of pristine sample, but the antibacterial activity, at same total Ag content, decreased as well. Anyway, the low toxicity of the purified sample, the low production time and cost, suggested that the material may be used at higher concentration to obtain the desired antibacterial effect. Although the spray coating operation of TiO₂ NM within PL5 showed a low occupational risk, the RRS of SiO₂ blending was noteworthy. The modified material TiO₂_18_sil_sol showed an higher photo-catalytic activity in comparison of that of pristine sample, that justifies a reduction of the operative volumes . The improvement of the TiO₂ NM functional properties together with the easy and cost effective industrial implementation, may justify an increase of the time required for the production of silica modified samples.

6.5 References

- [1]. B. Nowack, H. F. Krug, and M. Height, *Environ. Sci. Technol.*, **2011**, 45, 1177 - 1183
- [2]. N. Leopold, and B. Lendl, *J. Phys. Chem. B*, **2003**, 107, 5723 - 5727
- [3]. T. Yonezawa, S. Onoue, and N. Kimizuka, *Langmuir*, **2000**, 16, 5218 - 5220
- [4]. A. Tao, P. Sinsersuksakul, and P. Yang, *Angew. Chem. Int. Ed.*, **2006**, 45, 4597 - 4601
- [5]. Y. Sun and Y. Xia, *Adv. Mater.*, **2002**, 14, 833 - 837
- [6]. B. Wiley, T. Herricks, Y. Sun, and Y. Xia, *Nano Lett.*, **2004**, 4, 1733 - 1739
- [7]. B. Pietrobbon and V.r Kitaev, *Chem. Mater.*, **2008**, 20, 5186 - 5190
- [8]. V. K. Sharma, R. A. Yngard, Y. Lin, *Adv. Colloid Interf.*, **2009**, 145, 83 - 96
- [9]. R. Pasricha, S. Gupta, and A. K. Srivastava, *Small*, **2009**, 5, 2253 - 2259
- [10]. S. A. Amin, M. Pazouki, A. Hosseinnia, *Powder Techn.*, **2009**, 196, 241 - 245
- [11]. Z. Zheng, B. Huang, X. Qin, X. Zhang, Y. Dai and M. Whangbo, *J. Mater. Chem.*, **2011**, 21, 9079 - 9087
- [12]. C. Huang, Z. Yang, and H. Chang, *Langmuir*, **2004**, 20, 6089 - 6092
- [13]. D. A. Slanac, W. G. Hardin, K. P. Johnston, and K. J. Stevenson, *J. Am. Chem. Soc.*, **2012**, 134, 9812 - 981
- [14]. Y. Herbani, T. Nakamura, and S. Sato, *J. Phys. Chem. C*, **2011**, 115, 21592 - 21598
- [15]. K. Chaloupka, Y. Malam and A. M. Seifalian, *Trends Biotechnol.*, **2010**, 28, 580 - 588
- [16]. K. Madhumathi, P. T. S. Kumar, S. Abhilash, V. Sreeja, H. Tamura, K. Manzoor, S. V. Nair, R. Jayakumar, *J. Mater. Sci. Mater. Med.*, **2010**, 21, 807 - 813
- [17]. G. Gosheger, J. Harges, H. Ahrens, A. Streitburger, H. Buerger, M. Erren, A. Gonsel, F. H. Kemper, W. Winkelmann, C. Von Eiff, *Biomater.*, **2004**, 25, 5547 - 5556
- [18]. Z. Zheng, W. Yin, J. N. Zara, W. Li, J. Kwak, R. Mamidi, M. Lee, R. K. Siu, R. Ngo, J. Wang, D. Carpenter, X. Zhang, B. Wu, K. Ting, C. Soo, *Biomater.*, **2010**, 31, 9293 - 9300
- [19]. A. Sadeghnejad, A. Aroujalian, A. Raisi, S. Fazel, *Surf. Coat. Technol.*, **2014**, 245, 1 - 8
- [20]. L. Guo, W. Yuan, Z. Lu, C. M. Li, *Colloid Surf. A*, **2013**, 439, 69 - 83
- [21]. R. D. Holtz, B. A. Lima, A. G. Souza Filho, M. Brocchi, O. L. Alves, *Nanomed. Nanotech. Biol. Med.*, **2012**, 8, 935 - 940
- [22]. D. P. Macwan, P. N. Dave, S. Chaturvedi, *J. Mater. Sci.*, **2011**, 46, 3669 - 3686
- [23]. C. Su, B. Hong, C. Tseng, *Catal. Today*, **2004**, 96, 119 - 126
- [24]. S. Watson, D. Beydoun, J. Scott and R. Amal, *J. Nanopart. Res.*, **2004**, 6, 193 - 207
- [25]. G. Li, L. Li, J. Boerio-Goates, and B. F. Woodfield, *J. Am. Chem. Soc.*, **2005**, 127, 8659 - 8666
- [26]. H. Yin, Y. Wada, T. Kitamura, S. Kambe, S. Murasawa, H. M. Takao Sakata and S. Yanagida, *J. Mater. Chem.*, **2001**, 11, 1694 - 1703
- [27]. K. Nagaven, G. Sivalingam, M. S. Hegde, and G. Madras, *Environ. Sci. Technol.*, **2004**, 38, 1600 - 1604
- [28]. J. R. McCormick, B. Zhao, S. A. Rykov, H. Wang, and J. G. Chen, *J. Phys. Chem. B*, **2004**, 108, 17398 - 17402

- [29]. M. Pelaez, N. T. Nolan, S. C. Pillai, M. K. Seery, P. Falaras, A. G. Kontos, P. S. M. Dunlop, J. W. J. Hamilton, J. A. Byrne, K. O'Shea, M. H. Entezari, D. D. Dionysiou, *Appl. Catal. B Environ.*, **2012**, 125, 331 - 349
- [30]. A. Fujishima and K. Honda, *Nature*, **1976**, 238, 37 - 38
- [31]. M. Ni, M. K. H. Leung, D. Y. C. Leung, K. Sumathy, *Renew. Sust. Energ. Rev.*, **2007**, 11, 401 - 425
- [32]. S. Roy, M. S. Hegde, N. Ravishankar, and G. Madras, *J. Phys. Chem. C*, **2007**, 111, 8153 - 8160
- [33]. Y. Zhang, Z. Tang, X. Fu, and Y. Xu, *ACS Nano*, **2010**, 4, 7303 - 7314
- [34]. W. Zhao, W. Ma, C. Chen, J. Zhao, and Z. Shuai, *J. Am. Chem. Soc.*, **2004**, 126, 4782 - 4783
- [35]. A. Fujishima, X. Zhang, D. A. Tryk, *Surf. Sci. Rep.*, **2008**, 63, 515 - 582
- [36]. Y. Ohko, Y. Utsumi, C. Niwa, T. Tatsuma, K. Kobayakawa, Y. Satoh, Y. Kubota, A. Fujishima, *J. Biomed. Mater. Res.*, **2000**, 58, 97 - 101
- [37]. R. Wang, K. Hashimoto, A. Fujishima, M. Chikuni, E. Kojima, A. Kitamura, M. Shimohigoshi, T. Watanabe, *Nature*, **1997**, 388, 431 - 432
- [38]. J. C. Yu, W. Ho, J. Lin, H. Yip, and P. Wong, *Environ. Sci. Technol.*, **2003**, 37, 2296 - 2301
- [39]. Antonio Tricoli, M. Righettoni, and S. E. Pratsinis, *Langmuir*, **2009**, 25, 12578 - 12584
- [40]. H. Yaghoubi, N. Taghavinia, E. K. Alamdari, *Surf. Coat. Technol.*, **2010**, 204, 1562 - 1568
- [41]. C. Colleoni, M.R. Massafra, G. Rosace, *Surf. Coat. Technol.*, **2012**, 207, 79 - 88
- [42]. D. Wu, M. Long, J. Zhou, W. Cai, X. Zhu, C. Chen, Y. Wu, *Surf. Coat. Technol.*, **2009**, 203, 3728 - 3733
- [43]. G. Oberdörster, J. Ferin, and B. E. Lehnert, *Env. Health Persp.*, **1994**, 102, 173 - 179
- [44]. K. Donaldson, D. M. Brown, C Mitchell, M Dineva, P. H. Beswick, P. Gilmour, and W. MacNee, *Env. Health Persp.*, **1997**, 105, 1285 - 1289
- [45]. Dufresne, M. Harrigan, S. Massé, R. Bégin, *Am. J. Ind. Medicine*, **1995**, 27, 581 - 592
- [46]. Nagy, A. Steinbrück, J. Gao, N. Doggett, J. A. Hollingsworth, and R. Iyer, *ACS Nano*, **2012**, 6, 4748 - 4762
- [47]. W. Stöber, A. Fink, *J. Colloid. Interface Sci.*, **1968**, 26, 62 - 69
- [48]. M. Smoluchowski, *Ann. Phys.*, **1906**, 21, 756 - 780
- [49]. X. Chen, H. J. Schluesener, *Toxicol. Lett.*, **2008**, 176, 1 - 12
- [50]. C. N. Lok, C. M. Ho, R. Chen, Q. Y. He, W. Y. Yu, H. Sun, P. K. H. Tam, J. F. Chiu, C. M. Che, *J. Biol. Inorg. Chem.*, **2007**, 12, 527 - 534
- [51]. V. Marassi, S. Casolari, B. Roda, A. Zattoni, P. Reschiglian, S. Panzavolta, T. Syed, S. Ortelli, C. Delpivo, M. Blosi, A. L. Costa, *J. Pharm. Biomed.*, **2015**, 106, 92 - 99
- [52]. F. Örsi, *J. Therm. Anal. Calorim.*, **1973**, 5, 329 - 335
- [53]. A. E. Jablonski, A. J. Lang, S. Vyazovkin, *Thermochim. Acta*, **2008**, 474, 78 - 80
- [54]. J. Liu, D. A. Sonshine, S. Shervani, and R. H. Hurt, *ACS Nano*, **2010**, 4, 6903 - 6913
- [55]. G. A. Sotiriou, T. Sannomiya, A. Teleki, F. Krumeich, J. Vörös, and S. E. Pratsinis, *Adv. Funct. Mater.*, **2010**, 20, 4250 - 4257

- [56]. J. Kim, H. S. Kim, N. Lee, T. Kim, H. Kim, T. Yu, I. C. Song, W. K. Moon, and T. Hyeon, *Angew. Chem. Int. Ed.*, **2008**, 47, 8438 - 8441
- [57]. R. A. Jalil, Y. Zhang, *Biomater.*, **2008**, 29, 4122 - 4128
- [58]. P. R. Mishra, L. Al Shaal, R. H. Müller, C. M. Keck, *Int. J. Pharm.*, **2009**, 371, 182 - 189
- [59]. Z. Xiu, Q. Zhang, H. L. Puppala, V. L. Colvin, and P. J. J. Alvarez, *Nano Lett.*, **2012**, 12, 4271 - 4275
- [60]. M. Valko, D. Leibfritz, J. Moncola, M. T.D. Cronin, M. Mazura, J. Telser, *Int. J. Biochem. Cell. Biol.*, **2007**, 39, 44 - 84
- [61]. X. Feng, S. Zhang, X. Lou, *Colloid Surf. B*, **2013**, 107, 220 - 226
- [62]. Y. Ren, M. Chen, Y. Zhang, and L. Wu, *Langmuir*, **2010**, 26, 11391 - 11396
- [63]. R. Fateh, R. Dillert, and D. Bahnemann, *Langmuir*, **2013**, 29, 3730 - 3739
- [64]. S. Ortelli, M. Blosi, C. Delpivo, D. Gardini, M. Dondi, I. Gualandi, D. Tonelli, V. Aina, I. Fenoglio, A. A. Gandhi, S. A. M. Tofail, A. L. Costa, *J. Photochem. Photobiol. A*, **2014**, 292, 26 - 33
- [65]. M. Hull, D. Bowman, *Nanotechnology Environmental Health and Safety: Risks, Regulation and Management*, Elsevier NL, 2009, Chap. 1.
- [66]. M. Mahmoudi, I. Lynch, M. R. Ejtehadi, M. P. Monopoli, F. Baldelli Bombelli, and S. Laurent, *Chem. Rev.*, **2011**, 111, 5610 - 5637
- [67]. E. Casals, T. Pfaller, A. Duschl, G. J. Oostingh, and V. Puntès, *ACS Nano*, **2010**, 4, 3623 - 3632
- [68]. Lynch, K. A. Dawson, *Nanotoday*, **2008**, 3, 40 - 47
- [69]. M. M. Bradford, *Anal. Biochem.*, **1976**, 72, 248 - 254
- [70]. A. Gebregeorgis, C. Bhan, O. Wilson, D. Raghavan, *J. Coll. Interface Sci.*, **2013**, 389, 31 - 41
- [71]. P. Roach, D. Farrar, and C. C. Perry, *J. Am. Chem. Soc.*, **2006**, 128, 3939 - 3945
- [72]. A. Bouhekka, T. Bürgi, *Appl. Surf. Sci.*, **2012**, 369 - 374
- [73]. P. Cioni, G. B. Srambini, *Biophys. J.*, **2002**, 82, 3246 - 3253
- [74]. B. Sharma, R. R. Frontiera, A. Henry, E. Ringe, and R. P. Van Duyne, *Mater. Today*, **2012**, 15, 16 - 25
- [75]. Y. Han, R. Lupitsky, T. Chou, C. M. Stafford, H. Du, and S. Sukhishvili, *Anal. Chem.*, **2011**, 83, 5873 - 5880
- [76]. M. G. Bianchi, M. Allegri, A. L. Costa, M. Blosi, D. Gardini, C. Delpivo, A. Prina-Mello, L. Di Cristo, O. Bussolati and E. Bergamaschi, *Toxicol. Res.*, **2015**, 4, 385 - 398

7. Processing line 6: plastic composite line (CNT)

7.1 Introduction

7.1.1 CNT

CNT were firstly obtained in form of MWCNT^[1] and from their discovery, CNTs were immediately synthesized in large-scale^[2] and in form of SWCNT^[3]. Since then, CNT have emerged to be one of the most intensively investigated nanostructure and the research in this field is in continuous evolution^[4].

Arc-discharge, laser ablation and chemical vapor deposition are the three main methods used for CNT synthesis^[5]. CNT are a form of the C element, organized, as in fullerene and graphite, in layers of hexagonal rings having conjugated double bond. CNT could be made by one or more graphene sheets which have been rolled up into a cylindrical shape, giving rise respectively to the so called SWCNT or MWCNT. The length of CNT are usually in the size of micrometers with diameters from few up to 100 nm^[6].

Because of their extraordinary properties, CNT can be considered as attractive candidates in many different technological applications. CNT have been employed together with polymers or precursor resins to obtain nano-composite material with increased stiffness, strength and toughness^[7]. Depending on their chirality and diameter, CNT was found to be metallic or semiconducting^[8, 9]. The semiconducting CNTs have been used to build molecular field-effect transistors, while metallic CNTs to build single-electron transistors^[10]. Furthermore CNT have been widely employed for energy conversion and storage^[11]. Recently, CNTs received growing interest as components of biosensors^[12] and medical devices^[13], motivated by the dimensional and chemical compatibility of CNTs with biomolecules, such as DNA and proteins.

Despite the biocompatibility of CNT and their employ in medical field, the industrial scale production raised occupational health and safety issues^[4], due to free fibres hazardous properties^[14, 15]. Moreover CNT toxicity were compared to those exerted from asbestos fibres and it was reported that injection of large quantities of MWNTs into the lungs of mice could cause asbestos-like pathogenicity^[16].

Therefore in SbyD approach, CNT geometry and surface chemistry should be engineered to improve CNT biocompatibility and biodegradability^[17]. Moreover, to lower the exposure to airborne CNTs, they could be consolidated into micron-size granules employing granulation processes like as spray drying^[18] and freeze spray drying. CNT granules could retain a nanostructured surface and could be handled in a safer way during subsequent production process. Furthermore a proper engineering of the material to be dried could allow to re-disperse the granules into individual nano-sized particles^[19].

7.1.2 Description of Processing line 6

PL 6 is focused on extrusion of polymeric matrix charged with CNTs, to obtain high-strength and high-stiffness polymer composite. This PL was owned by Leitao, that provided information on experimental set-up and let available the exposure scenario. The main steps involved in PNC production are reported in figure 1.

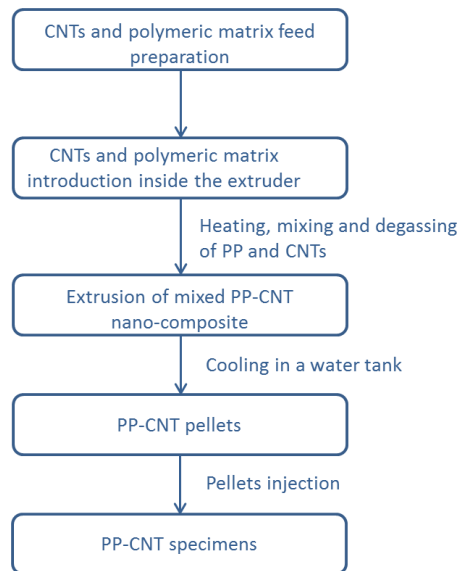


Figure 1 - Main step in PNC production

In a PNC production, CNTs and PP matrix were introduced inside the extruder through an hopper. Inside the extruder, CNT and PP were heated to melt the PP and mix both materials, employing six resistances and some kneading. During the extrusion, a gas outlet valves allowed the molten polymer degassing during the process and facilitate the removal of water vapor. PNC finally came out of the system with the aid of the rotating action of the screw and were deposited on a water tank for rapid cooling. The solid PP - CNT PNC was broken by a mill into pellets. The pellets were then injected to obtain PP - CNT PNC specimens.

7.1.3 Critical step identified and RRS proposed

A general scheme of the PL 6 was reported in figure 2.

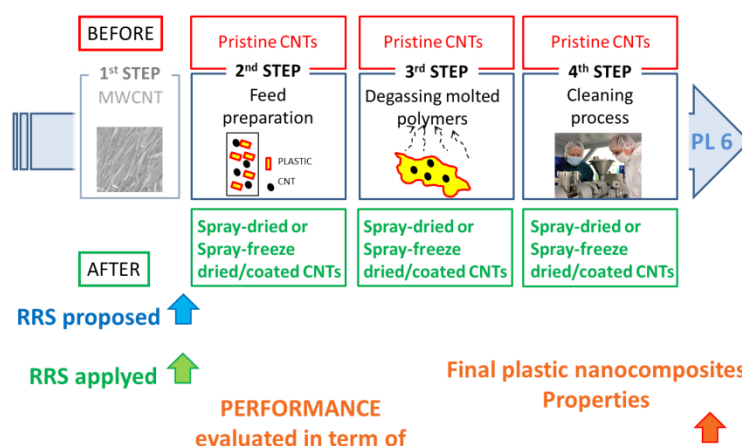


Figure 2 - Scheme of processing line 6, showing process step in which RRS were applied and evaluated.

Along PL 6, the relevant steps for health hazard and EA were the feed preparation, the degassing of molten polymers and the final cleaning operations. The two scenarios that took shape with the introduction of RRS were defined as BEFORE and AFTER.

7.1.3.1 Feed preparation, degassing molten polymers and cleaning process

The steps supposed to be critical for the potential of exposure to free CNTs, were the feed preparation, degassing molten polymers and cleaning process, performed along the PL 6. During these steps, the RRS of spray drying and freeze spray drying, were proposed to decrease possible CNTs emission in the workplace. The BEFORE scenario was represented by the employ of the pristine CNTs, whilst in the AFTER the spray dried or freeze spray dried CNTs were used as nano-filler.

7.2 Experimental

7.2.1 Preliminary characterization of CNTs

Pristine CNTs were obtained from commercial source and encoded as **C_1_NT**. Pristine sample morphology was observed by HR-TEM (JEOL JEM-2100F, USA) and SEM-FEG (Zeiss, DE) taking images at different magnifications, used for particle size distribution. Pristine sample was subjected to BET measurement of SSA, using nitrogen as adsorptive gas to evaluate the presence of a nanostructured surface.

7.2.2 Application of RRS at lab-scale level

To decrease CNTs toxicity and lower the possibility of free CNTs inhalation during manufacturing step, a poloxamer coating and spray drying or freeze spray drying were performed on pristine CNTs. Samples involved are described below:

- Modified sample, **C_3_FG**, was prepared dispersing the pristine CNTs powder (nominal [CNTs] 9 wt.%) with the aid of a poloxamer ([pol] 3 wt.%, CNTs/pol = 3) in distilled water and then ball milling the sample overnight to promote CNTs dispersion. The dispersion was freeze spray dried, obtaining a dried granulated materials.
- Modified sample, **C_4_SD**, was prepared dispersing the pristine CNTs powder (nominal [CNTs] 9 wt.%) with the aid of a poloxamer ([pol] 3 wt.%, CNTs/pol = 3) in distilled water and then ball milling the sample overnight to promote CNTs dispersion. The dispersion was spray dried, obtaining a dried granulated materials.

Modified samples morphology was observed by HR-TEM (JEOL JEM-2100F, USA) and SEM-FEG (Zeiss, DE) taking images at different magnifications, used for particle size distribution. Modified sample was subjected to BET measurement of SSA, using nitrogen as adsorptive gas to evaluate the presence of a nanostructured surface.

7.2.3 Application of RRS at lab-pilot scale level

For further validation of the introduced RRS, the pristine and modified CNTs were used as nano-filler material to test their employment, in a real application, during the steps of feed preparation, degassing of molten polymers and final cleaning procedures.

CNTs were introduced in PP polymer by extrusion process obtaining a PNC in the form of pellets. Samples involved are described below:

- Pristine sample, **PP-pCNTs**, were obtained by the introduction of pristine CNTs in PP matrix by extrusion process, obtaining a nano-composite in the form of pellets.
- Modified sample, **PP-mCNTs**, were obtained by the introduction of modified C_4_SD in PP matrix by extrusion process, obtaining a nano-composite in the form of pellets.

For the RRS validation, different pellets properties were evaluate by Leitat. The nano-composite crystallinity and thermal behavior were investigated by TGA and DSC. The distribution of the CNTs filler in the pellet nano-composite surface were observed employing SEM or TEM.

The pellets obtained were injected to obtain specimens upon which perform tests to evaluate the final PNC properties. Samples involved are described below:

- Pristine sample, **SPEC PP-pCNTs**, were obtained by the injection of pristine pellets PP-pCNTs to obtain specimen.
- Modified sample, **SPEC PP-mCNTs**, were obtained by the injection of modified pellets PP-mCNTs to obtain specimen.

The specimens functional performance were evaluated in term of functionality of the final PNC product, including mechanical strength, flexural and flame retardant properties.

7.3 Results and discussion

7.3.1 Preliminary characterization of CNT

Pristine sample morphology was observed by HR-TEM and SEM, taking images at different magnifications, as shown in figure 3.

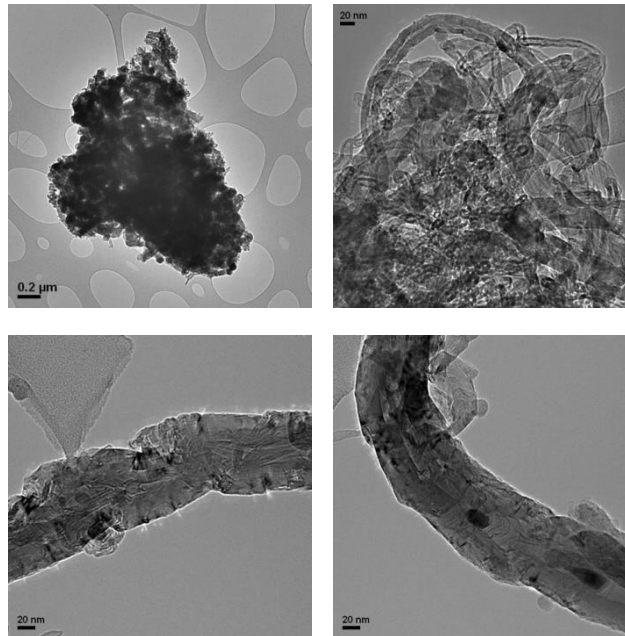


Figure 3 - Pristine CNT sample morphology by HR-TEM images.

From TEM images, pristine sample appeared to consist of both free CNT and aggregate. These latter, were composed by a large number of single CNT closely connected together in a bundle-like morphology. CNT aggregate dimensions were found to be mainly in the micron range. As shown in figure 3, single CNT diameter ranged from 20 to 50 nm. To investigate the presence of bigger aggregates, sample morphology was observed by SEM as shown in figure 4.

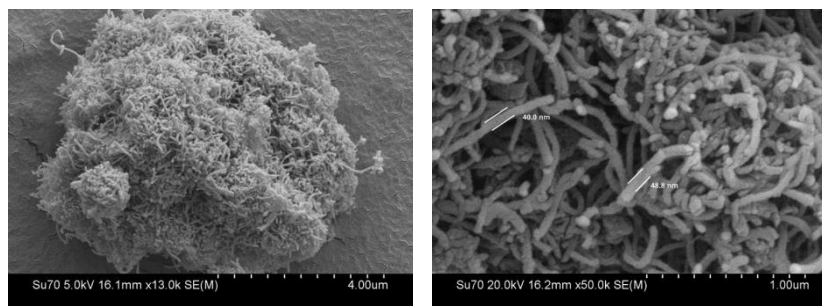


Figure 4 - Pristine CNT sample morphology by SEM images.

SEM images confirmed the high level of agglomeration of the sample, revealing the presence of different size aggregates, often bigger than 10 μm.

To evaluate the surface area extent, pristine C_1_NT sample underwent BET analysis, which results are reported in table 1.

Table 1 - Summary of BET results of pristine C_1_NT sample.

Sample Code	Surface Area [m ² /g]	Pore Volume [cm ³ /g]	Pore Radius [nm]
C_1_NT	39.2	0.37	1.84 nm

In accordance with the presence of micron sized aggregate, BET emphasized the low surface area of the sample, resulting from the strong agglomeration of single CNT that were mainly present as tightly packed bundle-like aggregate.

7.3.2 Application of RRS at lab-scale level

CNT has been considered as hazardous NM due to the fibre shape, or high aspect ratio, that hinders phagocytosis and clearance mechanisms, resulting in an higher toxic potential [15]. Therefore RRS of spray drying and freeze spray drying were proposed to lower the CNT emissivity through the obtainment of micron sized granules. Modified samples obtained were observed by TEM and SEM-FEG as shown in figure 5.

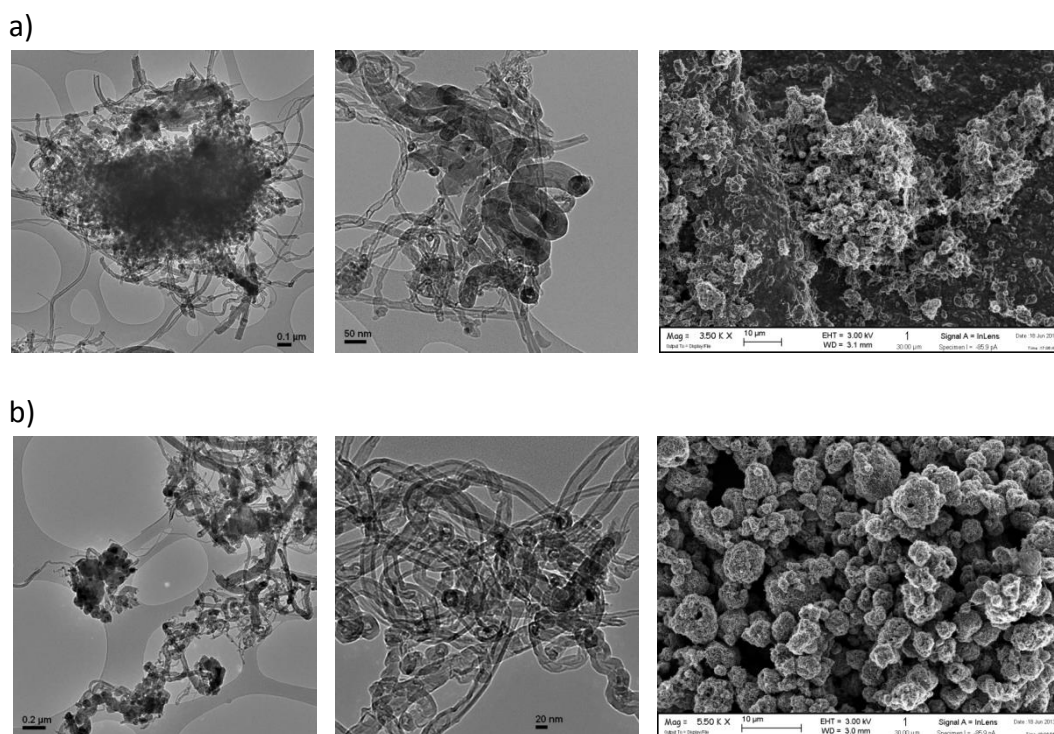


Figure 5 - Morphology of modified a) freeze dried C₃FG and b) spray dried C₄FG samples from TEM and SEM-FEG images.

From SEM observation, both spray dried and freeze spray dried samples were composed mainly by aggregates, but also some free CNT have been observed by TEM. Freeze dried C₃FG samples (Fig. 5, panel a) showed the presence nearly spherical agglomerates, similar to those found in pristine sample, but more spherical packed, with an average diameter of

~ 3 μm . Spray dried samples C_4_SD (Fig. 5, panel b) observation underlined a different aspect of the aggregate, characterized by a ceno-spherical shape typical of spray dried powders, with an average diameter of ~ 3.5 μm . From TEM images, together with CNT aggregate also some free CNT were observed. From free CNT fibre length and diameter, the AR of free CNT in pristine and modified samples were calculated, data obtained are summarized in table 2.

Table 2 - Summary of the CNT samples AR determination.

Sample code	Average diameter [nm]	Typical d range, MAX [nm]	Typical d range, MIN [nm]	Average AR
C_1_NT	19.8	50	4	14.3
C_3_FG	21.6	48	8	19.4
C_4_SD	23.5	64	8	14.7

Basing on results obtained, both drying processes did not affected free CNT AR, but produced different granulate powder, with diameter above the cut-off for inhalation in humans, that is around 3 μm of aerodynamic diameter^[15]. Following the fibre pathogenicity paradigm, a fibrous material, to be considered less hazardous for the health, should have a certain diameter ($d > 3 \mu\text{m}$), length ($l < 5 \mu\text{m}$) and moreover it should not be biopersistent^[15]. Considering the aerodynamic diameter of free CNT, evaluate as three-times the actual diameter^[20], they resulted to be inhalable fibres. But on the other hand, free CNT length was found to be lower than 5 μm , value that usually avoid frustrated phagocytosis^[20, 21].

Modified sample surface area were evaluated by BET analysis and results obtained are reported in table 3.

Table 3 - Summary of BET results of modified CNT samples.

Sample code	Specific surface area [m^2/g]	Pore Radius [nm]	Pore Volume [cm^3/g]	Diameter from BET SSA [μm]
C_3_FG	13.7	2.3	0.06	1.75
C_4_SD	1.8	30.2	0.06	13.3

Both modified samples showed a low surface area, due to the spray drying and freeze drying techniques that produced granulated, micron sized powder. Despite the similar aggregate size, the spray dried C_4_SD samples showed a lower surface area probably due to its more tightly packed granules.

The intrinsic production of ROS of pristine and modified CNT samples was assessed by IOM, being related to the ability of samples to induce oxidative stress. Involved NMs were co-incubated with a spin trap (Tempone-H) to detect the release of oxygen-centered free radicals. The signal created by the production of ROS was compared to vehicle control (phosphate buffered saline) and a positive control (100 μM of pyrogallol). The result and representative spectra are shown in figure 6 and figure 7, respectively.

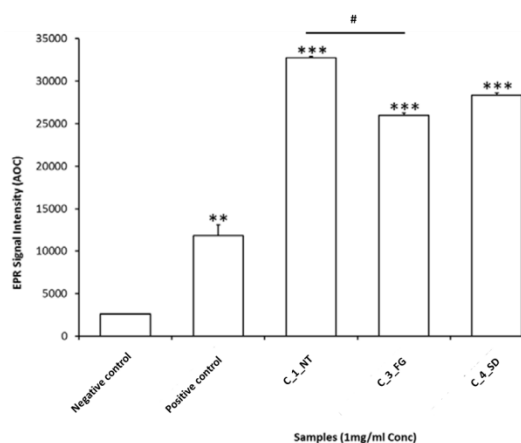


Figure 6 - EPR signal intensity after co incubation with pristine C_1_NT or modified forms C_3_FG and C_4_SD. Results are expressed as mean +/- sem (n=3). *** p<0.001, **p<0.01, vs. vehicle control; # p<0.05 vs. Pristine (C_1_NT).

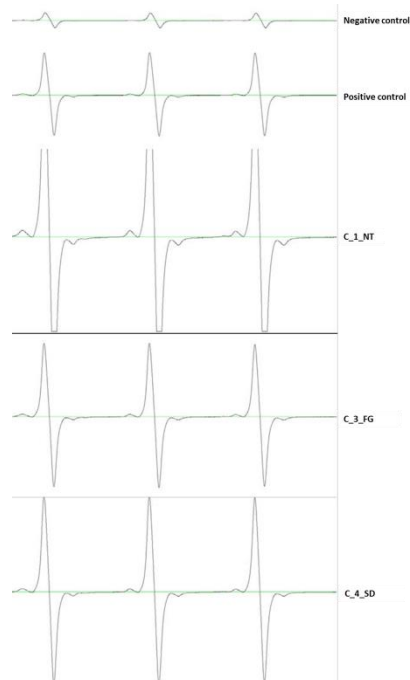


Figure 7 - Representative EPR spectra after 1 h of co-incubation of the spin trap Tempone-H with pristine C_1_NT and modified, C_3_FG and C_4_SD, samples.

The results showed that all CNT samples produced high levels of ROS at the dose of 1 mg/ml, which in the case of the pristine material C_1_NT, was above the detection limit of the assay. The RRS application, appeared to significantly reduce the level of intrinsic oxidant production although this was still significantly above the vehicle control and the positive control of the assay. This suggested that RRS application were effective at ameliorating the intrinsic CNT reactivity, but did not remove it completely.

7.3.3 Application of RRS at pilot-scale level

The polymer employed to obtain final PNC was a PP, (Ultra polymers. Moplen 501H, Lyondellbasell), with the following properties: density: 0.9 g/cm³, melt flow rate = 6.0 g/10 min (230°C/2.16 Kg), tensile modulus=1 500 MPa, tensile stress at yield= 34 MPa, tensile strain at break > 50 % and tensile strain at yield = 9 %. Pristine C_1_NT and modified C_4_SD samples were mixed together with PP and extruded in a co-rotating twin screw extruder, to obtain a PNC in form of pellets charged with 3 wt.% of CNT. Pellet obtained using pristine and spray dried CNT as filler were encoded respectively as PP - pCNT and PP - mCNT. The distribution of CNT in the pellet surface was evaluate by SEM while the inner part of the sample was investigated by TEM, as shown in figure 8.

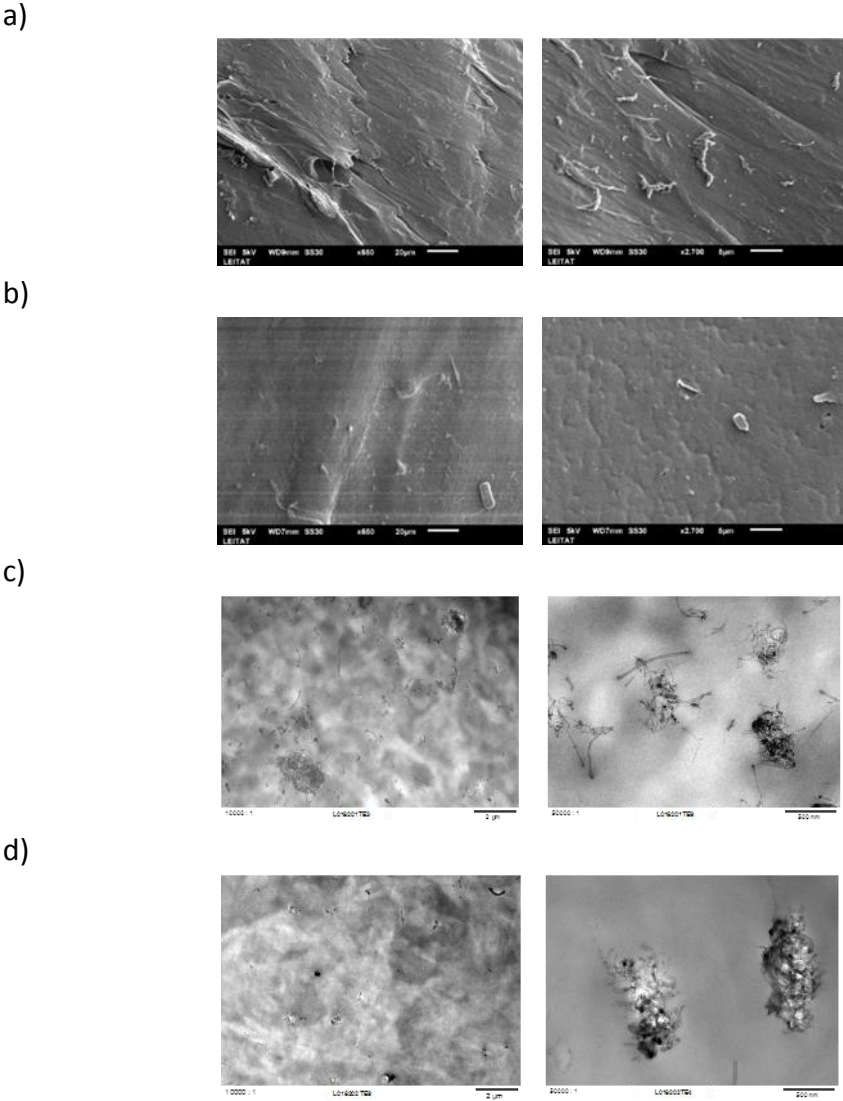


Figure 8 - SEM images of a) pristine PP-pCNT pellet surface by SEM, b) modified PP-mCNT pellet surface by SEM c) inner part of pristine PP-pCNT pellet by TEM and d) inner part of PP-mCNT pellet by TEM.

From images obtained, a different distribution of CNT on the pellet surface and in its section were observed. Pristine PP-pCNT pellet presented an homogenous distribution of CNT on pellet surface (Fig. 8, panel a), where isolated CNT could be found. Conversely in the surface

of pellet obtained employing spray dried CNT (Fig. 8, panel b), isolated CNT were hardly observed. From the investigation of the inner part of the pellet performed by TEM, in the pristine sample PP-pCNT both free and aggregated CNT were observed, whilst in the modified PP-mCNT pellet, CNT were only observed as aggregates.

The pellet thermal behavior were evaluated by TGA and DSC, graph and data obtained are reported respectively in figure 9 and table 4.

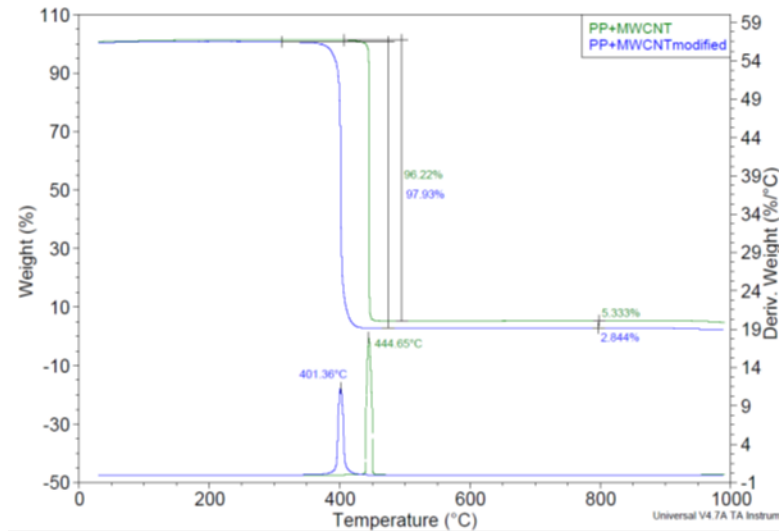


Figure 9 - TGA analysis of pristine C_1_NT (green pattern) and modified C_4_SD (blue pattern) samples.

Table 4 - Summary of the main parameters in DSC.

Sample Code	Midpoint T^a_c [°C]	ΔH_{cc} [J/g]	Midpoint T^a_m [°C]	ΔH_{cm} [J/g]	Cristallinity %
PP - pCNTs	127.81	98.97	166.24	11.45	3.78 ± 0.04
PP - mCNTs	122.53	82.98	164.83	87.06	1.23 ± 0.04

Crystallization (T^a_c) and melting (T^a_m) temperatures, glass transition and crystallization kinetics were determined for each PNC. From data obtained the PNC crystallinity decreases when modified CNT were used as nano-fillers in PP matrices, probably due to the surfactant, the poloxamer, used to disperse the CNT in water. From TGA analysis (Fig. 9), both pristine and modified pellet sample showed a similar thermal behavior, but the PP - mCNT started to lost weight 40 °C sooner than PP - pCNT sample, suggesting a lower thermal stability of PNC filled with modified CNT.

To further investigate the effect of the nano-filler on the properties of the final PNC material, pellets previously obtained were injected to obtain specimens upon which perform tests to evaluate the final PNC properties. The mechanical properties of PNC were determined following the standard UNI-EN ISO 178:2011 which describes the methodology to determine the flexural properties of rigid and semi-rigid plastic materials under defined conditions. Before the experiment the specimens were conditioned to a specific temperature ($23^\circ\text{C} \pm 2^\circ\text{C}$) and humidity ($50\% \pm 5\%$ r.h.) for 24 hours. The testing machine Instron, was used to asses flexural properties of involved specimens, obtaining results shown in table 5.

Table 5 - Summary of result obtained on PNC flexural properties.

Sample Code	Flexural Modulus (MPa)	Flexural Strength (MPa)	Deformation (%)
SPEC PP - pCNT	1 019.97 ± 42.19	37.55 ± 0.25	7.01 ± 0.33
SPEC PP - mCNT	1 015.21 ± 32.17	36.21 ± 0.50	7.30 ± 0.27

From data reported flexural properties were very similar in both samples. Comparing both PNC with neat PP, it can be observed that the introduction of pristine and modified CNT as nano-filler into PP matrix, led to a less rigid material (flexural modulus of PP: 1448 MPa) but with a greater flexural strength (flexural strength of PP: 33.58 MPa). Furthermore the tensile properties of the specimen were investigated, obtaining data reported in table 6.

Table 6 - PNC tensile properties.

Sample Code	Strength [MPa]	Strain at strength [%]	Yield stress [MPa]	Elongation at yield stress [%]	Strength at break [MPa]	Tensile Modulus [MPa]
SPEC PP - pCNT	28.24 ± 0.45	10.70 ± 0.41	28.05 ± 0.42	12.94 ± 0.52	25.84 ± 0.81	1 020 ± 30.10
SPEC PP - mCNT	29.03 ± 0.19	11.01 ± 0.31	29.00 ± 0.18	11.76 ± 0.55	17.16 ± 1.66	1 120 ± 39.70

The results showed that similar strength was needed to deform both specimens. However comparing these values to that obtained by neat PP (strength: 22.2 MPa) it can be concluded that the introduction of both pristine and modified CNT in PP matrix, improved the PNC tensile strength. Considering the strength at break, the introduction of pristine CNT in PP (SPEC PP - pCNT) contributes to obtain a tensile resistant material (strength at break of plain PP: 22.2 MPa) but lowered the strength at break of SPEC PP - mCNT.

The specimens tensile modulus were evaluated employing the universal testing machine ZWICK. During this test the tensile modulus of PP - mCNT PNC was found to be slightly higher than PNC including pristine CNT. Finally to evaluate possible flame retardant properties due to the presence of CNT, specimens underwent to flame retardant assay (data not shown), but unfortunately both PNC showed the same flammability and physical behavior typical of neat PP polymer. Therefore, the use of pristine or modified CNT as nano-filler did not provided flame retardant property to PP polymer.

7.3.4 Toxicity outcomes

To evaluate the health hazard reduction following the introduction of RRS, the toxicological profile of pristine and modified CNT were tested in vitro and compared. Cell lines employed, A549 and RAW 264.7 respectively alveolar epithelial cells and macrophages, have been chosen by biologists because both cell types were typically encountered by NMs upon inhalation and therefore could represent a model of respiratory exposure.

In alveolar epithelial cells A549 and macrophages, both pristine and modified CNT samples showed no or very low cytotoxicity as assessed by the LDH assay. In contrast, viability

data, obtained with the resazurin assay, indicated that C_1_NT sample caused a significant loss of viability, which was more evident in airway epithelial cells (Fig. 10, upper panel) than in macrophages.

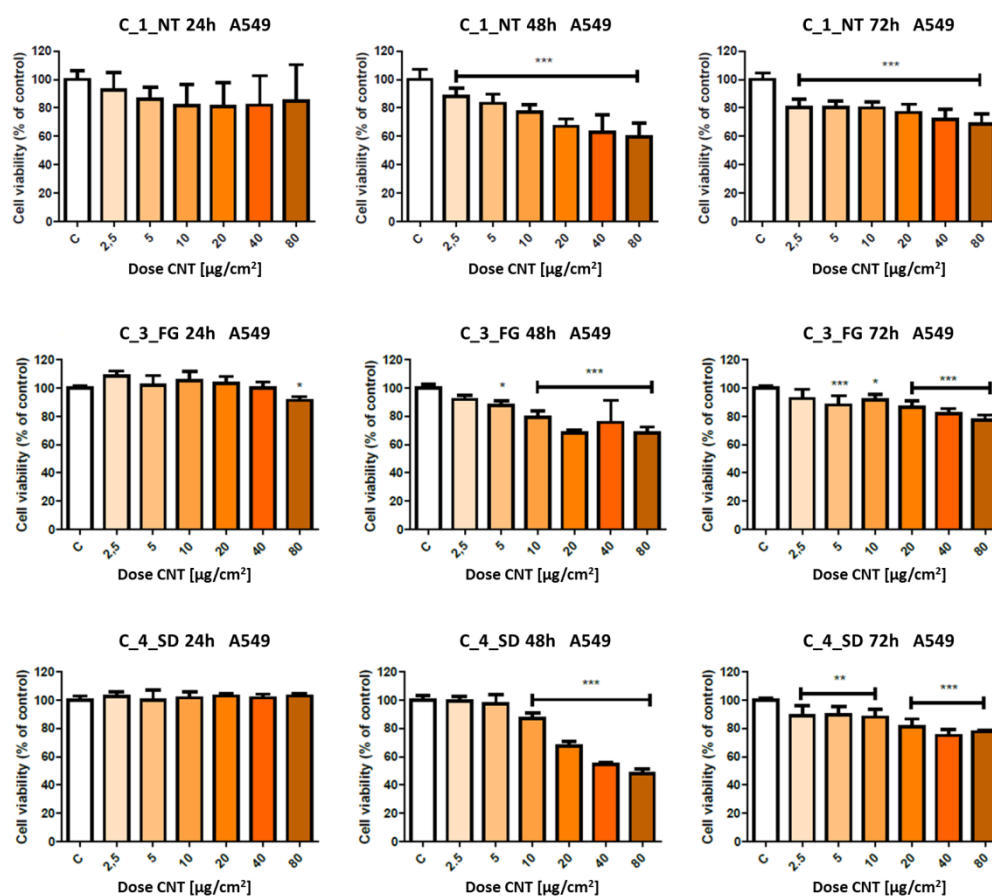


Figure 10 - Cell viability in cells treated with pristine C_1_NT. Resazurin. Data are average of 18 determinations in 3 separate experiments. *** $p < 0.001$ (upper panel). Cell viability in cells treated with modified C_3_FG and C_4_SD samples. Resazurin. Data are average \pm SD of 6 determination. *, **, *** $p < 0.05$, $p < 0.01$, $p < 0.001$.

As shown in figure 10, from cells viability test evaluated by resazurin assay in A 549, RRS partially mitigate the toxic effects of CNT materials.

EPR analysis showed that both pristine and modified CNT were able to generate ROS, although modified forms produced ROS in a lower amount. Similarly, in the acellular DCFH assay, all samples were able to generate ROS. In terms of oxidative stress, both pristine and modified CNT samples induced oxidative stress as assessed by the DCFH assay and GSH level. Similar effects were observed in alveolar epithelial cells but to a slightly lower extent than in macrophages. Finally, no effect on lipid peroxidation was evidenced following treatment with the three different CNT samples.

Overall C_1_NT, C_3_FD and C_4_SD displayed very similar toxicological profile. However, towards macrophages the modified materials exhibited a smaller activating effect and, therefore, were expected to exert a smaller pro-inflammatory activity in vivo.

7.3.5 Exposure assessment: off-line and on-site measurements

EA started from a "basic measurement campaign" within Leitat to verify the emission of CNT during the PNC production steps, supposed to be critical. The instruments used by Ineris were the same used in the other measurement campaign to compare the results obtained. The real time CPC was used between the main potential sources and outlets, to determine the total particle concentration in number, in the range 10 nm - 1 µm. A TEM grid sampler was employed to measure the NPs near to the respiratory system, collecting them on specific TEM grids, which were observed.

The characterization of the background aerosol noise revealed an high number of particles, that varied from 27 000 to 10 000 particles/cm³. From TEM grid observation, these particles were mainly composed by oil droplets and soot, commonly found in ambient air and presumably come from urban background noise, like as engine combustion processes. Anyway, no CNT fibre was observed on the sample grid before the start-up of the extrusion process. Different common handling operation have been monitored along the PL 6, from the CNT weighting to the extrusion and cleaning operation, as shown in figure 11.

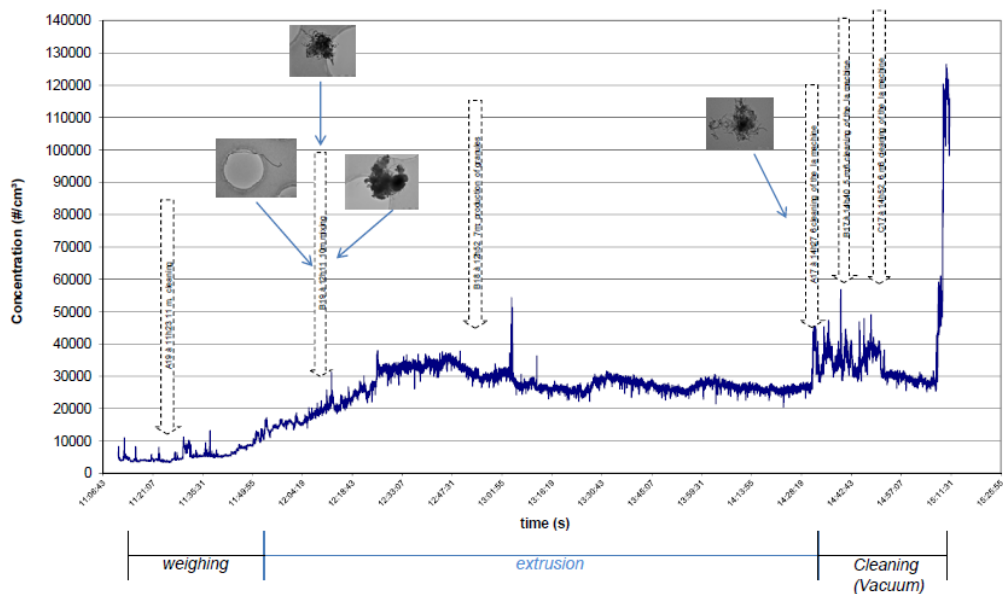


Figure 11 - Temporal monitoring of particle concentration evolution during preliminary campaign at Leitat

During the extrusion process, the particle count showed a long and slow increase, that ranged from 10 000 particles/cm³ to more than 30 000 particles/cm³. Concurrently with the increased particle count, from the observation and EDS analysis of sampling grids, the particles collected revealed the presence of CNT fibres and aggregate, furthermore some rare CNT fibres linked to PP particles were also observed. The vacuum-cleaning operation, led to a sharp increase in the particle count, with a maximum of 57 000 particles/cm³, but the analysis of TEM grids revealed polymer particles and very few CNT.

For this PL an intensive measurement campaigns were carried out, measuring the ambient aerosol generated during the extrusion process of PP charged with pristine C₁_1_NT

and modified C_4_SD samples. Unfortunately, the sampling of the aerosol did not showed any significant differences between the employ of pristine and modified CNT, in both cases in fact were found similar shape, size and amount of CNT. Probably the specificities of the site did not allowed a real quantification of the emissions due to the dilution condition, dimension of the workplace and, in some cases, presence of co-activities.

All these factor illustrates the complexity encountered during on-site measurement that could hinder a sound evaluation of samples emissivity, therefore to evaluate the introduction of the RRS in term of CNT exposure, INERIS performed on both pristine and modified samples an off-line experiment, the dustiness tests ^[22], aimed to simulates the powder emission during handling and to compare the emissivity of the involved samples. The experimental set-up comprise a vortex shaker instrument which, by the combined effect of shaking and air flow, allow the powder to be tested to pass in the aerosol phase. The aerosol phase, that contain the inhalable fraction, was considered for the analysis. To quantify the concentration of NMs released by each sample, two real-time measurement instruments were used: the CPC, that delivers a concentration in number of particles from 4 nm to 2.5 μm per cm^3 (reported as particles/ cm^3) and the APS, that take into account particles between 0.5 and 20 μm . The particles released during the experiments were sampled by a sampling pump on specific TEM grids employing a MPS. In table 7, a summary of the results obtained by dustiness tests, are reported.

Table 7 - Summary of the main results on the dustiness tests on pristine C_1_NT and modified CNT

Sample Code	Dustiness	Nano-structure (mass collected from TEM grids)		
	Number concentration [particles/ cm^3] range 4 nm – 20 μm	d [nm]	Bundles	Free CNT
C_1_NT	1 060	~50 nm	Yes	Yes
C_3_FG	< 10	~45 nm	Yes	Yes
C_4_SD	< 10	-	Yes	Yes

Considering data obtained during dustiness tests, the three CNT samples displayed different degrees of dustiness, but all sample produced aerosol containing free CNT and their aggregates. Both granulated C_3_FG and C_4_SD samples obtained after RRS application emitted slightly less than 10 particles/ cm^3 during tests, while the pristine sample (C_1_NT) exerted one hundred times higher particle emission in number concentration. The trend obtained was less distinct based on the mass collected from the filters (data not shown) and observed by TEM (Fig. 12). In this case the pristine C_1_NT sample remained the most highly emissive in term of the mass quantification of the aerosol produced during the experiments, followed by C_4_SD and C_3_FG.

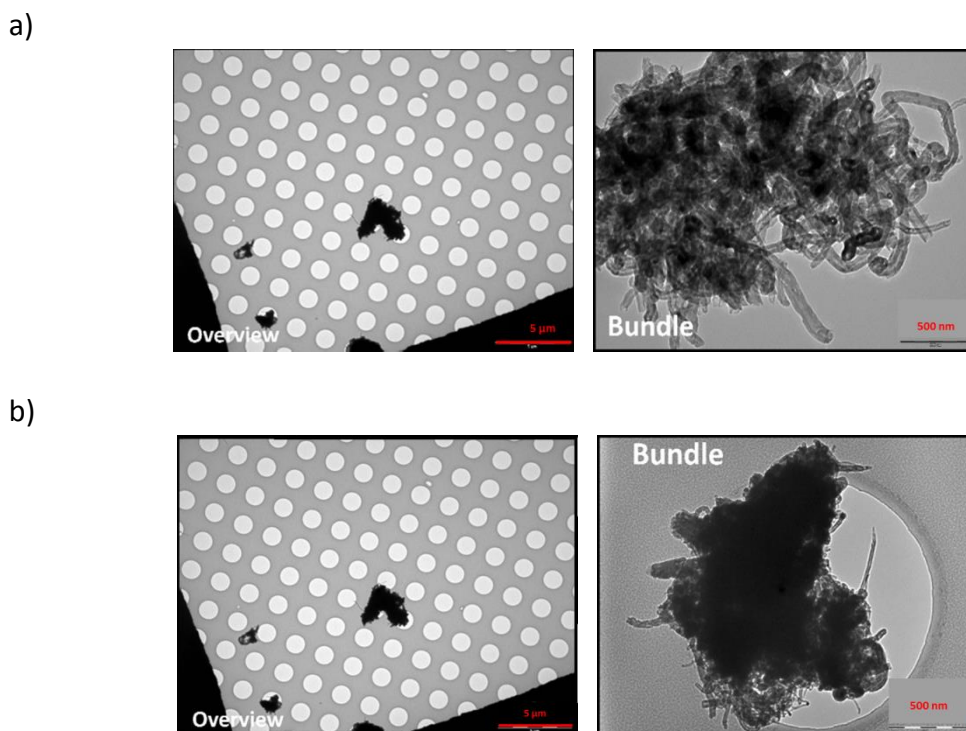


Figure 12 - CNT particles from aerosol generated from a) pristine C₁_NT and b) modified C₃_FG samples.

The observation of materials on the sampling grids, (Fig. 12) showed the presence of bundles and free fibres in all samples considered. However, the higher number of these objects, were found in grid relative to the pristine C₁_NT sample (Fig. 12, panel a), while the lower number of CNT fibres and aggregate were found in grid used for freeze spray dried C₃_FG sample (Fig. 12, panel b). The off-line dustiness tests allowed to compare, in an off-line setting, the emissivity of the involved CNT materials, and to justify the introduction of RRS of granulation because the CNT generated after their introduction resulted to be the less emissive samples.

7.3.6 Cost/benefit analysis

A qualitative cost/benefit analysis for PL 6, was carried out by UL in collaboration with partners involved in SANOWORK project. Table 8 show hazard, exposure, risk and associated cost data in relation to the spray drying and freeze spray operation, that were employed to produce modified nano-filler used in the extrusion process of PP-CNT PNC. Exposure data for the pristine, C₁_NT, and modified C₃_FG and C₄_SD materials were taken from the measurement campaign carried out by INERIS, while toxicity data derived from the tests performed by biologists. PNC properties, production time and costs were evaluated together with the partner Leitat.

Table 8 - Toxicity, exposure and risk data and remediation costs for the spraying operation of Ag NPs in PL5, considered a high risk task for workers.

Sample Code	C_1_NT	C_3_FG	C_4_SD
RRS	None, unmodified CNT	Freeze spray drying, CNT consolidated in granules of micron size dimension.	Spray drying, CNT consolidated in granules of micron size dimension.
Exposure from dustiness tests	250 particles/cm ³ GM: 0.00028 (mg/m ³) φ 100 nm	100 times less emissive than pristine sample	100 times less emissive than pristine sample
Toxicity	Induced higher ROS levels than the reference material	Expected to be less inflammatory in vivo than pristine material. Produced slightly less ROS than pristine material	Expected to be less inflammatory in vivo than pristine material. Produced slightly less ROS than pristine material
Risk	Health risk present	Substantially reduced	Substantially reduced
Functional Change	None by definition	No significant impact	No significant impact
Cost [KWh/Kg]	32	60	35
Production Time [h/Kg]	Externally procured	2	11

For processing lines 6, that presented an health risk due to airborne CNT, the RRS were largely effective and relatively simple to implement and scale up at pilot scale level. The RRS of freeze spray drying and spray drying gave a modified materials with an expected lower inflammatory activity in comparison to that of pristine sample. Moreover from dustiness tests, modified samples showed a lower exposure that could justify the higher production times and costs.

7.4 Conclusions

To reduce the free CNT fibre health hazard, pristine C_1_NT sample was subjected to freeze spray drying and spray drying as RRS. Both the drying techniques allowed to consolidate CNT in micron sized granules. RRS application showed no significant impact on PNC properties obtained employing pristine C_1_NT and modified, C_3_FG and C_4_SD, samples.

To evaluate an health hazard potential mitigation due to RRS application, the toxicological profile of pristine CNT was compared to those of CNT prepared by spray drying or freeze granulation. Although the toxicological profile of the three CNT samples was found to be comparable, partial mitigation of effects on cell viability and macrophage activation was achieved through RRS.

During preliminary exposure measurement campaign at Leitao, CNT emissions were detectable during extrusion and cleaning operations. The implementation of PL 6 were performed at pilot-scale level, thus letting available an exposure scenario for Ineris

quantitative EA campaign. For this aim, other extrusion experiments were performed using both pristine C_1_NT and modified C_4_SD samples as nano-filler in the PP matrix. Unfortunately data collected did not showed differences in the CNT emitted. Anyway the off-line dustiness experiments allowed to justify the introduction of RRS of granulation because the granulated CNT, generated after their introduction, resulted to be the less emissive samples.

The cost/benefit analysis, carried out by UL in collaboration with partners involved in SANOWORK EU project, underlined that RRS were largely effective to lower sample inflammatory activity and exposure, moreover RRS were found to be cost effective and simple to implement and scale up at pilot-scale level.

7.5 References

- [1]. S. Iijima, *Nature*, **1991**, 354, 56 - 58
- [2]. T. W. Ebbensen and P. M. Ajayan, *Nature*, **1992**, 358, 220 - 222
- [3]. S. Iijima and T. Ichjhashi, *Nature*, **1993**, 363, 603 - 605
- [4]. M. F. L. De Volder, S. H. Tawfick, R. H. Baughman, A. J. Hart, *Science*, **2013**, 339, 535 - 539
- [5]. H. Dai, *Acc. Chem. Res.*, **2002**, 35, 1035 - 1044
- [6]. H. Dai, *Surf. Sci.*, **2002**, 500, 218 - 241
- [7]. T. Chou, L. Gao, E. T. Thostenson, Z. Zhang, J. Byun, *Compos. Sci. Technol.*, **2010**, 70, 1 - 19
- [8]. J. W. G. Wildöer, L. C. Venema, A. G. Rinzler, R. E. Smalley, and C. Dekker, *Nature*, **1998**, 391, 59 - 62
- [9]. T. Wang Odom, J. Huang, P. Kim, and C. M. Lieber, *Nature*, **1998**, 391, 62 - 64
- [10]. R. Martel, T. Schmidt, H. R. Shea, T. Hertel, and P. Avouris, *Appl. Phys. Lett.*, **1998**, 73, 2447 - 2449
- [11]. L. Dai, D. W. Chang, J. Baek, and W. Lu, *Small*, **2012**, 8, 1130 - 1166
- [12]. T. Kurkina, A. Vlandas, A. Ahmad, K. Kern, and K. Balasubramanian, *Angew. Chem. Int. Ed.*, **2011**, 50, 3710 - 3714
- [13]. S. Y. Hong, G. Tobias, K. T. Al-Jamal, B. Ballesteros, H. Ali-Boucetta, S. Lozano-Perez, P. D. Nellist, R. B. Sim, C. Finucane, S. J. Mather, M. L. H. Green, K. Kostarelos and B. G. Davis, *Nat. Mater.*, **2010**, 9, 485 - 490
- [14]. J. Muller, F. Huaux, N. Moreau, P. Misson, J. Heilier, M. Delos, M. Arras, A. Fonseca, J. B. Nagy, D. Lison, *Toxicol. Appl. Pharm.*, **2005**, 207, 221 - 231
- [15]. K. Donaldson, F. Murphy, A. Schinwald, R. Duffin and C. A. Poland, *Nanomedicine*, **2011**, 6, 143 - 156
- [16]. C. A. Poland, R. Duffin, I. Kinloch, A. Maynard, W. A. H. Wallace, A. Seaton, V. Stone, S. Brown, W. Macnee and K. Donaldson, *Nat. Nanotechnol.*, **2008**, 3, 423 - 428
- [17]. A. Bianco, K. Kostarelos and M. Prato, *Chem. Commun.*, **2011**, 47, 10182 - 10188
- [18]. J. S. Lindeløv and M. Wahlberg, *J. Phys.: Conf. Ser.*, **2011**, 304, 012083
- [19]. B. Faure, J. S. Lindeløv, M. Wahlberg, N. Adkins, P. Jackson, L. Bergström, *Powder Technology*, **2010**, 203, 384 - 389
- [20]. K. Donaldson, *Crit. Rev. Toxicol.*, **2009**; 39, 487 - 500

[21]. K. Donaldson, F. A. Murphy, R. Duffin, C. A Poland, *Part. Fibre Toxicol.*, **2010**, 7:5, 1 - 17

[22]. M. Morgeneyer, O. Le Bihan, A. Ustache, O. Aguerre-Chariol, *Powder Technol.*, **2013**, 246, 583 - 589

8. Final Conclusions

In this PhD thesis, different RRS based on NM surface engineering were proposed, starting from the existing paradigms on exposure and hazard mechanisms. RRS were developed and applied within real case studies, represented by the involved processing lines, and their effectiveness were evaluated considering NM final product performances, exposure risk and hazard potential.

It was demonstrated that although several processing lines presented a certain level of occupational risk, simple cost effective RRS may be proposed to highly reduce risks associated to NMs. For instance, the RRS of CFC, applied to improve ZrO₂ water dispersion, increased the washing efficiency of synthesis reactor, allowing to reduce NM contamination in wastewater and perform an efficient recycling procedure of the NM recovered, with a final reduction of production self-costs by 7%.

The granulation techniques of freeze drying and spray drying, employed to promote NM aggregation, were proved to be effective to reduce NM exposure potential, still maintaining their functionality and reactivity. The wet ball milling resulted to be a possible method to reduce and homogenize NM aspect ratio, leading to a significant mitigation of TiO₂ NF toxicity. On the other hand, the purification strategy strongly reduced Ag NM toxicity. The dispersion in a SiO₂ phase, applied for TiO₂ NM, improved the NM depolluting performance, still maintaining its toxicity profile.

The investigation of engineered NMs in relevant biological conditions, aimed to understand the interaction between NPs and biological entities, let to identify advantages and limits of available characterization techniques, obtaining new insights to design safer NMs.

Curriculum Vitae

Born in 1985, I obtained my Research Master Degree in “Products, Processes and Materials for Industrial Chemistry” at Faculty of Industrial Chemistry of University of Bologna in March 2010, working on the field of organic chemistry, with a Thesis entitled “From abiotic chemistry of phosphorous to the prebiotic one: synthesis of nitrogen heterocycles by condensation in water”, under supervision of Prof. G. Baccolini, Prof. C. Boga and Dott. G. Micheletti.

From 27, May, 2010 to 27, January, 2011 I obtained a Research Fellowship for a “Technology Transfer Project” on hair dyeing from vegetable origin from Spinner Consortium, performing my research activity at the Department of organic chemistry “A. Mangini” - Faculty of Industrial Chemistry of University of Bologna (IT) - in collaboration with the company Ilios (Cesena, IT).

From 2012 to 2015 I was PhD student under the Department of Industrial Chemistry “Toso Montanari” University of Bologna (IT), performing my activity mainly at CNR-ISTEC, Faenza (IT), with a research fellowship on nanomaterials engineering. My doctoral research activity focused on the design of engineered nanomaterial for occupational health and safety, within the European project “SANOWORK”, coordinated by Dr. Anna Costa (CNR-ISTEC). Besides the nanomaterials surface engineering and their implementation within involved processing line, my contribution was to investigate nanomaterials in biological relevant condition. In this contest, thanks to a Marco Polo grant, I spent a period of 3 month at the Limerick University (Irl) to study the interaction occurring at the NM-protein interface.

My doctoral research activity has been documented by 7 participation at national and international conference, in which I contributed with oral (4) or poster (3) presentations; I co-authored 4 papers published in peer reviewed journals and I’m working on 3 papers on NM toxicity and their characterization in biological media. In years 2013 and 2014, I presented 2 lectures on surface engineering of NM and their characterization at the course of Industrial Chemistry (Chemistry and technologies for the environment and materials, Faenza).

Work in progress based on this thesis

C. Delpivo, S. Ortelli, M. Allegri, M. Blosi, M. G. Bianchi, O. Bussolati, T. Syed, A. Costa, E. Bergamaschi, **Wet state characterization of nanomaterials within biological media in a safety by design approach**, Article manuscript in progress, to be submitted for publication in **summer 2015**

A. Costa, D. Gardini, M. Blosi, C. Delpivo, S. Ortelli, M. G. Bianchi, M. Allegri, O. Bussolati, E. Bergamaschi, **Nanosilver: an innovative paradigm to promote its safe and active use**, Article manuscript in progress, to be submitted for publication in **summer 2015**

C. Uboldi, S. Di Bucchianico, C. Delpivo, F. Coppedè, M. Blosi, A. Costa and L. Migliore, **Remediated titania nanoparticles to reduce lung exposure at work places: an in vitro study**, Article manuscript to be submitted for publication in **summer 2015**

Peer-reviewed publication based on this thesis

M. G. Bianchi, M. Allegri, L. Di Cristo, A. L. Costa, M. Blosi, D. Gardini, C. Delpivo, A. Prina-Mello, O. Bussolati, E. Bergamaschi, **Titanium dioxide nanoparticles enhance macrophage activation by LPS through a TLR4-dependent intracellular pathway**, *Toxicology Research*, **2015**, 4, 385 - 398

V. Marassi, S. Casolari, B. Roda, A. Zattoni, P. Reschilgian, S. Panzavolta, T. Syed, S. Ortelli, C. Delpivo, M. Blosi, A. L. Costa, **Hollow-fiber flow field-flow fractionation and multi-angle light scattering investigation of the size, shape and metal-release of silver nanoparticles in aqueous medium for nano-risk assessment**, *Journal of Pharmaceutical and Biomedical Analysis*, **2015**, 106, 92 - 99

S. Ortelli, M. Blosi, C. Delpivo, D. Gardini, M. Dondi, I. Gualandi, D. Tonelli, V. Aina, I. Fenoglio, A. Gandhi, T. Syed, A.L. Costa, **Multiple approach to test nano TiO₂ photo-activity**, *Journal of Photochemistry and Photobiology A: Chemistry*, **2014**, 292, 26 - 33

D. Gardini, M. Blosi, C. Delpivo, S. Ortelli, A. L. Costa, **Silica-coating as protective shell for the risk management of nanoparticles**, *Journal of Physics: Conference Series*, **2013**, 012052

Conference presentation based on this thesis

C. Delpivo, S. Ortelli, M. Blosi, A. Vaccari, T. Syed, A. L. Costa, **Wet State Characterization As Key Step in a Safety by Design Approach**, *Oral presentation delivered at Nanosafe 2014*, Grenoble (FR), November, **2014**

C. Delpivo, S. Ortelli, M. Blosi, A. L. Costa, S. Albonetti, A. Vaccari, **Safety by design strategy on CNT**, *Poster presentation delivered at The XXV National Congress of the Italian Chemical Society*, Arcavacata di Rende (IT), September, **2014**

C. Delpivo, S. Ortelli, M. Blosi, A. L. Costa, S. Albonetti, A. Vaccari, **Zirconia nanomaterial production drawback: integraton of risk remediation strategy**, *Poster presentation delivered at The Day of Chemistry of Emilia Romagna*, Bologna (IT), December, **2013**

C. Delpivo, S. Ortelli, M. Blosi, A. L. Costa, A. Vaccari, M. Dondi, **Towards a promising future in the safe industrial use of nanomaterials**, *Oral presentation delivered at Nanotechnology 2013*, Thessaloniki (GR), July, **2013**

C. Delpivo, A. L. Costa, M. Blosi, D. Gardini, S. Albonetti, A. Vaccari, M. Dondi, **Nanoparticle surface engineering: challenging properties of silica coatings**, *Oral presentation delivered at The Day of Chemistry of Emilia Romagna*, Ferrara (IT), December, **2012**

A. L. Costa, C. Delpivo, M. Blosi, D. Gardini, S. Ortelli, S. Albonetti, A. Vaccari, G. Baldi, A. Barzanti, M. Dondi, **Silica coating of nanosurfaces: strategy for risk control and process improvement**, *Poster presentation delivered at NanotechItaly 2012*, Venezia (IT), November, **2012**

C. Delpivo, A. Costa, D. Gardini, M. Blosi, S. Albonetti, A. Vaccari, **Silica-coating as protective shell for risk management of nanoparticles**, *Oral presentation delivered at The XVIII National Congress of Industrial Chemistry Division of the Italian Chemical Society*, Firenze (IT), June, **2012**

Other peer-reviewed publication

C. Boga, G. Micheletti, C. Delpivo, M. Mazzacurati, **A simple route to new cyclic (Chloroalkyl)phosphane-, diphosphane-, and aminophosphane derivatives**, *Heteroatom Chemistry*, 24, **2013**, 392-397

C. Delpivo, C. Boga, G. Micheletti, **A green synthesis of quinoxalines and 2,3-dihydropyrazines**, *Synthesis*, 45, **2013**, 1546 - 1552

G. Micheletti, C. Delpivo, G. Baccolini, **A green synthesis of glycoluril derivatives in aqueous solution with recycle of the waste**, *Green Chemistry Letters And Reviews*, 6, **2013**, 135 - 139

C. Boga, C. Delpivo, B. Ballarin, M. Morigi, S. Galli, G. Micheletti, S. Tozzi, **Investigation on the dyeing power of some organic natural compounds for a green approach to hair dyeing**, *Dyes and Pigments*, 97, **2013**, 9 - 18

G. Baccolini, C. Delpivo, G. Micheletti, **Wittig reaction: role of steric effects in explaining the prevalent formation of Z olefin from nonstabilized ylides**, *Phosphorus, Sulfur, and Silicon and the Related Elements*, 187, **2012**, 1291 - 1302

G. Baccolini, C. Boga, C. Delpivo, G. Micheletti, **Facile synthesis of hydantoins and thiohydantoins in aqueous solution**, *Tetrahedron Letters*, 52, **2011**, 1713 - 1717